Doctoral Thesis (Abridged)

博士論文（要約）

Numerical analysis of variable-density flow and mass transport in unsaturated-saturated media: prediction of seawater intrusion problem under future tsunami scenarios at the Niijima Island, Japan

(地下の飽和−不飽和領域における密度流・物質輸送に関する数値解析的研究：新島における将来的な津波被害に伴う地下水の塩水汚染の予測を事例として)

劉 佳奇

Liu Jiaqi

Department of Environment Systems
Graduate School of Frontier Sciences
The University of Tokyo

2020

Doctoral Thesis (abridged)

博士論文（要約）

Numerical analysis of variable-density flow and mass transport in unsaturated-saturated media: prediction of seawater intrusion problem under future tsunami scenarios at the Niijima Island, Japan

(地下の飽和−不飽和領域における密度流・物質輸送に関する数値解析的研究：新島における将来的な津波被害に伴う地下水の塩水汚染の予測を事例として)

Adviser: Professor Tomochika Tokunaga

劉 佳奇

Liu Jiaqi

Chapter 4 of this thesis is to be submitted and published in a journal, hence Chapter 4 is removed from this version of thesis. The relevant content is scheduled to be published within 3 years.

ABSTRACT

Tsunamis cause vertical infiltration of seawater from land surface to coastal aquifers, i.e., tsunami-induced seawater intrusion (TSWI), which can threaten the quality of groundwater resources. Numerical modeling is a useful tool and has been used in previous studies to understand TSWI processes based on the major tsunami disaster in 2004 and 2011. However, little work has been done to predict TSWI under future tsunami scenarios, especially in the vicinity of seismically active zones like Japan. Furthermore, the interpretations of the simulation results of TSWI can be problematic due to a series of model uncertainties with respect to tsunami inundation scenarios, site specific aquifer properties, anthropogenic activities, and so on. Therefore, this study tends to numerically simulate TSWI in coastal aquifers under future tsunami scenarios and examine the impacts of model uncertainties on simulation results. For this purpose, both a conceptual problem and a field-based case were studied by numerical modeling using the code FEFLOW, which solves variable-density flow and mass transport in unsaturated-saturated porous media.

First, a conceptual problem was designed, in which saltwater was injected vertically from the top into a 2-D vertical cross-section of an unconfined aquifer under horizontal groundwater flow conditions. In total, 158 numerical simulation cases were designed with various configurations of horizontal groundwater flow, solute injection, aquifer properties, and dispersivity. Three end-member flow regimes were identified that were dominated by the horizontal hydraulically-driven flow, the vertical hydraulically-driven flow, and the vertical density-driven flow, respectively. The flow regimes and parameter sensitivity were explained by boundary-conditions-based and element-based dimensionless numbers. The understanding based on the simulations of this conceptual problem provided a basic reference for interpretation of saltwater migration in TSWI problems.

Next, the numerical approach was applied to predict TSWI in a real site. The Niijima Island, Japan, was selected to be the case, because groundwater is the only source for freshwater in the island but facing high risks of TSWI under the future Nankai earthquake scenarios. Both 2-D and 3-D numerical models of the groundwater system in the Niijima Island were developed and calibrated. A series of simulation cases were designed for studying the impacts of model uncertainties including tsunami inundation conditions, aquifer properties, rainfall recharge settings, numerical parameters, and groundwater abstraction activities. The element-based dimensionless numbers were applied to analyze the temporal changes of flow patterns. The simulated tsunami inundation of 15 m a.m.s.l. (above mean sea-level) would cause seawater, with a volume scale of 10^6 m^3, to infiltrate into subsurface within several tens of minutes, and groundwater salinization would persist for about eight years. An extreme tsunami of 20 m a.m.s.l. could cause a broader seawater flooding zone, and as a result, TSWI may deteriorate the groundwater quality even in no-inundated zones, which would require a period of more than 18 years to be recovered by the natural rainfall recharge. The field settings including unsaturated zone properties, groundwater flow path and travel time, and bedrock surface topography, had important influences on simulation results, and they can provide useful information with respect to the estimation of the total amount of seawater infiltration, direction of contaminant migration, and total time for recovery of polluted aquifers. Simulation results indicated that some groundwater in the southeastern part of the island would be survived from seawater intrusion, and this survived portion of groundwater resource had the potential to provide water supply in an equivalent amount of the pre-tsunami level (3.7×10^5 m^3/year), and did not worsen the recovery processes.

This study is expected to provide a more comprehensive understanding of TSWI processes and a better strategy to perform numerical modeling approaches to solve coastal hydrological processes.

ACKNOWLEDGEMENTS

First and foremost, I would wish to express my deepest gratitude to my supervisor Prof. Tomochika Tokunaga, Department of Environment Systems, Graduate School of Frontier Sciences, The University of Tokyo, for his continuous support of my doctoral study, for his patience, motivation, enthusiasm, and immense knowledge. His guidance helped me in all the time for research, fieldwork, attending conferences, and writing this thesis. He has been a great source of inspiration during tough times, for which, I am indebted to him.

I sincerely thank Prof. Tomochika Tokunaga (The University of Tokyo), Prof. Shigeru Tabeta (The University of Tokyo), Prof. Jun Sasaki (The University of Tokyo), Prof. Masaatsu Aichi (The University of Tokyo), and Prof. Takeshi Hayashi for serving as thesis committee members and their valuable comments on my findings, which incented me to improve and widen my research from various perspectives.

I am extremely grateful to Dr. Isobe Ichiyo of Niijimamura Museum for helping in field investigations and sharing geohydrological knowledge of the Niijima Island which enormously supported this research.

I also would like to acknowledge the Niijima Village Office for selflessly assisting the fieldworks and providing important data for this research.

I am hugely indebted to Mr. Hayashi Hisao of Geo-X Consultants Corporation, Japan for conducting microtremor survey and analyzing the data.

My thanks and appreciation go to Mr. Makoto Inoue, Global Info-tec., for his collaboration by conducting resistivity surveys, data analysis, and interpretation to support my doctoral study.

I acknowledge Department of Environment Systems, Graduate School of Frontier Sciences, The University of Tokyo, for providing an opportunity to work in a learning environment that will always be an inspiration to me. I thank all departmental and administrative staff members who facilitated my research and life.

My sincere thank goes to Mr. Katsuro Mogi for his help in the laboratory and fieldworks. Many thanks to all the members of Toku-Lab for the camaraderie, discussions and help in all aspects of life during my stay in Japan.

I would like to express my appreciations for the financial support and research funds I received for my Ph.D. study from the Japan Society for the Promotion of Science (JSPS). I also thank the Todai Fellowship provided by The University of Tokyo.

I would like to dedicate this work to my parents for their unconditional love, support, believe and guidance, spiritual teachings and for everything that inspired me to achieve my goals in my professional and personal life.

TABLE OF CONTENTS

LIST OF TABLES ..... **vii**

LIST OF FIGURES ..... **viii**

LIST OF ABBREVIATIONS ..... **xv**

LIST OF UNITS OF MEASUREMENTS ..... **xvi**

LIST OF SYMBOLS ..... **xvii**

CHAPTER 1: INTRODUCTION **1**
1.1 Background 1
1.2 Objectives 4
1.3 Strategy and Structure of the Thesis 4

CHAPTER 2: LITERATURE REVIEW **6**
2.1 Introduction 6
2.2 Density-Driven Flow (DDF) 6
2.2.1 Physical Experiments 7
2.2.2 Benchmarks and Numerical Modeling 9
2.2.3 Dimensionless Number Analysis 11
2.3 Tsunami-Induced Seawater Intrusion (TSWI) 13
2.3.1 Environmental Observation and Monitoring 13
2.3.2 Physical Experiments 16
2.3.3 Numerical Modeling 18
2.4 Summary 22

CHAPTER 3: FUNDAMENTAL THEORY FOR NUMERICAL MODELING OF DENSITY-DRIVEN FLOW IN UNSATURATED-SATURATED MEDIA **25**
3.1 Analytical Solution for Saltwater-Freshwater Interface 25
3.2 Governing Equations of Numerical Modeling 28
3.2.1 Heads in Groundwater for DDF 28
3.2.2 Parameters for Variably Saturated Porous Media 32
3.2.3 Governing Equations for Fluid Flow 33
3.2.4 Governing Equations for Mass Transport 36
3.3 General Descriptions of Boundary Conditions (BCs) and Initial Conditions (ICs) 40
3.4 Criteria for Model Discretization 42
3.5 Numerical Modeling Code 43
3.6 Validation of the FEFLOW Code (Modeling Sandbox Experiments) 44
3.6.1 Sandbox Experiment I (Sinking Plume with Static Water Table) 44
3.6.2 Sandbox Experiment II (Sinking Plume with Lateral Water Flow) 45

CHAPTER 4: 2-D MODEL OF A CONCEPTUAL PROBLEM: FLOW REGIMES AND DIMENSIONLESS NUMBER ANALYSIS **48**
4.1 Introduction 48
4.2 Methods 48
4.2.1 ICs and BCs 48
4.2.2 Spatial and Temporal Discretization 49
4.2.3 Parameterization of Simulation Cases 50
4.2.4 Dimensionless Numbers 52
4.3 Results and Discussions 54
4.3.1 Classification of Flow and Transport Regimes Based on Simulation Results 54
4.3.2 BC-Based Dimensionless Number Analysis 57

4.3.3 Element-Based Dimensionless Numbers Analysis 62
4.3.4 Parameter Sensitivities 66
4.4 Summary 68

CHAPTER 5: THE STUDY SITE: THE NIIJIMA ISLAND, JAPAN 70
5.1 Location and Climate 70
5.2 Social Background 71
5.3 Geological Settings 72
5.4 Hydrogeological Settings 74
5.5 Tsunami Disaster Risks 75
5.5.1 The Anticipated Nankai Earthquake and Tsunami Scenarios 75
5.5.2 Local Preparedness 78

CHAPTER 6: 2-D MODEL OF THE NIIJIMA ISLAND: PROCESSES AND UNCERTAINTIES 79
6.1 Introduction 79
6.2 Methods 79
6.2.1 ICs and BCs 79
6.2.2 Spatial and Temporal Discretization 82
6.2.3 Parameterization of Simulation Cases 83
6.2.4 Measurable Indicator and Element-Based Dimensionless Numbers 88
6.3 Results and Discussions 90
6.3.1 TSWI Processes 90
6.3.2 Element-Based Dimensionless Number Analysis 94
6.3.3 Uncertainties of Tsunami Inundation Scenarios 97
6.3.4 Uncertainties of Rainfall Recharge BCs 102
6.3.5 Uncertainties of Aquifer properties 103
6.3.6 Uncertainties of Numerical Parameters 112
6.4 Summary 117

CHAPTER 7: 3-D MODEL OF THE NIIJIMA ISLAND: PREDICTION OF TSWI AND POST-DISASTER WATER SUPPLY 119
7.1 Introduction 119
7.2 Methods 119
7.2.1 ICs and BCs 119
7.2.2 Spatial and Temporal Discretization 122
7.2.3 Parameterization 124
7.3 Results and Discussions 126
7.3.1 Prediction of TSWI 126
7.3.2 Long-Term Water Supply in Response to Tsunami Disasters 132
7.3.3 Effect of Pumping Saltwater Out 133
7.4 Recommendations and Implications 134
7.4.1 Field Indicators for Assessing the Vulnerability of Coastal Aquifers to TSWI. 134
7.4.2 Strategies for Securing Water Supply in Post-Disaster Period 136
7.5 Summary 137

CHAPTER 8: CONCLUSIONS 139

CITED REFERENCES 141

APPENDIX 154

LIST OF TABLES

Table 2.1 Summary of observations and environmental monitoring data on TSWI due to the tsunami disasters in 2004 and 2011. 15

Table 2.2 Summary of model setups and results by numerical studies on TSWI due to the tsunami disasters in 2004 and 2011. 21

Table 3.1 Unsaturated versus saturated porous media conditions 32

Table 3.2 Summary of parameters of Sandbox Experiment I and numerical model by FEFLOW. 45

Table 3.3 Summary of sandbox experiment setups and parameters in FEFLOW model. 46

Table 4.1 Summary of simulation parameters 51

Table 6.1 Summary of simulation parameters in the baseline case 84

Table 6.2 Configurations of the simulation cases for uncertainty analysis 87

Table 7.1 Summary of simulation parameters in the baseline case 125

LIST OF FIGURES

Figure 1.1 A vertical conceptual cross-section showing a coastal groundwater system under (a) normal conditions and (b) tsunami inundation conditions. Modified after Mahmoodzadeh and Karamouz (2019). 1

Figure 1.2 Measurements of electrical conductivity of groundwater before and after (a) the 2004 Indian Ocean tsunami (Illangasekare et al., 2006) and (b) the 2011 Tohoku tsunami (Mori et al., 2012). Data are compared with the drinking water quality standards by WHO (2004). 2

Figure 1.3 Global map of tsunami hazard (after UNISDR, 2009) 3

Figure 1.4 An example of fingering patterns observed in sandbox experiments, in which dense solute was injected from the top of a container filled with sands and water (Simmons et al., 2002). 4

Figure 1.5 Schematic diagram showing the methodology and structure of the thesis. 5

Figure 2.1 Sandbox experiments by Oostrom et al. (1992): (a) experiment settings and (b) plume outline curves. 8

Figure 2.2 (a) Settings of the Elder problem (Elder, 1967); (b) concentration contours are shown for the single (s1), double (s2), and triple (s3) bifurcation solutions (van Reeuwijk et al., 2009). 10

Figure 2.3 (a) Settings of the salt lake problem: an unstable saline boundary layer formed by uniform evaporation along AB. Along CD, there is uniform recharge which is at constant pressure. Boundaries BC, DE, EF, and FA are assumed impermeable. Dashed lines are streamlines. (b)Development stages of unstable puma behavior in the salt lake problem (Simmons et al., 1999). 10

Figure 2.4 A vertical conceptual cross-section showing the sources of TSWI: (1) direct vertical infiltration of seawater through the land surface; (2) infiltration from ponding seawater; (3) infiltration from open dug wells; and (4) landward shift of freshwater-saltwater interface (modified after Vithanage et al., 2012). 17

Figure 2.5 Physical model of tsunami injection and infiltration into a shallow coastal sandy aquifer at (a) 2, (b) 5, (c) 11, and (d) 19 min. The pre-tsunami seawater wedge is dyed green, and the pre-tsunami fresh water flowing from right to left is light brown. Infiltrated tsunami water, dyed red, is injected across the top of the aquifer. Tsunami water is also immediately injected into the aquifer through the open borehole. Dense seawater quickly develops into plumes that reach the preexisting seawater wedge (Hogan, 2006; Illangasekare et al., 2006). 18

Figure 2.6 Vithanage et al. (2012): (a) model domain and boundary conditions; (b) simulation results. 20

Figure 3.1 The saltwater-freshwater interface in a homogeneous, unconfined coastal aquifer: (a) the Ghyben-Herzberg principle (modified after Freeze and Cherry (1979)); (b) the Dupuit-Ghyben-Herzberg principle considering an impermeable bottom of the aquifer (modified after Guo and Jiao (2007)). 25

Figure 3.2 (a) Definition of the Henry problem; (b) Concentration distribution obtained by Henry (1964) from his semianalytical solution compared with the Ghyben-Herzberg solution of the sharp interface (modified after Diersch (2013)). 27

Figure 3.3 Heads in groundwater for variable-density condition modified after Lusczynski (1961). 29

Figure 3.4 Typical plots of (a) retention cure, and (b) relative permeability curve (Diersch, 2013). 33

Figure 3.5 Microscopic and macroscopic domains and the representative elementary volume V_3 (Freeze and Cherry, 1979). 34

Figure 3.6 Representative elementary volume (REV). 34

Figure 3.7 REV for development of the advective transport equation. 36

Figure 3.8 (a) Schematic figure showing theoretical variation of velocity within an individual pore; (b) Schematics showing tortuous branching and reconnection of microscopic flow path in a porous media; (c) Results of tracer movement; (d) Tracer transport showing as the sum of advective and dispersive components. Figures were modified after Zheng and Bennett (2002). 38

Figure 3.9 Longitudinal dispersivity versus scale of observation reported by Gelhar et al. (1992). 39

Figure 3.10 Stages of model development using the code FEFLOW (Diersch, 2013). 43

Figure 3.11 (a) Setups of Sandbox Experiment I (Simmons et al., 2002); (b) Model domain and BCs using FEFLOW. 44

Figure 3.12 Comparisons between Sandbox Experiment I and FEFLOW modeling results (black line indicating the water table or the line of pressure zero). 45

Figure 3.13 (a) Schematic figure showing experimental setup illustrating saltwater contaminant from a saltwater plume infiltrating into a porous medium (modified after Hogan, 2006); (b) Model domain and BCs by FEFLOW for simulating the sandbox experiments (white line indicating the water table). 46

Figure 3.14 Comparison between Sandbox Experiment II and FEFLOW modeling results (black line indicating the water table or the line of pressure zero). 47

Figure 4.1 (a) Model domain and BCs; (b) ICs of saturation and mass concentration distributions. See text in detail. 49

Figure 4.2 The temporal changes of streamlines and mass concentrations in the example simulation cases depicting each flow and transport regime. The white arrows show the flow directions. 56

Figure 4.3 The 1-D diagrams of (a) M_x^{BC}, (b) M_z^{BC}, and (c) Ra_d^{BC} showing the plots of simulation cases with flow and transport regimes. 58

Figure 4.4 The 3-D diagrams of M_x^{BC}, M_z^{BC}, and Ra_d^{BC} showing (a) the plots of simulation cases with the flow and transport regimes, and (b) the approximate zones of VH, HH, VD, and DD. White dashed lines show the boundaries based on estimation which may have large uncertainties..... 60

Figure 4.5 Plots of the laboratory experiments by (a) Oostrom et al. (1992) and (b) Hogan (2006) on the 3-D diagrams of M_x^{BC}, M_z^{BC}, and Ra_d^{BC} in comparison with the flow regime distributions based on numerical simulation results in Figure 4.4b. Note that L^{BC} = 0.01 m was assumed for the point source described by Hogan (2006).. 62

Figure 4.6 Spatial distributions of element-based dimensionless numbers M_x^E, M_z^E, Ra_d^E, and the locations of the plume cores in the saturated zone for the flow regime HH, VH, and VD. See the corresponding simulation results in Figure 4.2. The plume cores were delineated by the zones which had mass concentrations greater than 50% of the highest concentration in the saturation zone.. 63

Figure 4.7 Plots of the element-based dimensionless numbers M_x^E, M_z^E, and Ra_d^E for (a) the whole plume and (b) the plume cores. 64

Figure 4.8 (a) Plume cores and (b)temporal changes of the element-based dimensionless numbers M_x^E, M_z^E, and Ra_d^E at the plume cores for the case No. 73 (HH-VD regime Figure 4.2e). 65

Figure 4.9 The changes of the mass concentration distributions and regime shift on the diagram of M_x^{BC}, M_z^{BC}, and Ra_d^{BC} by increasing J^{BC}, q_z^{BC}, C_s^{BC}, L^{BC}, K, and K_z/K_x, H^{BC}, and α_L..... 67

Figure 5.1 (a) A location map of the Niijima Island; (b) Satellite image of Niijima Island showing the location of the Honson Village (by Google Earth). 70

Figure 5.2 Average monthly precipitation and temperature of year 2011 ~ 2015 at the Niijima Island. Data source: Japan Meteorological Agency (2017). 71

Figure 5.3 (a) Trends in population by age of Niijima Island 1960-2015; (b) Trends in Population by Age of Japan, 1960-2015 (data source: http://www.stat.go.jp). 71

Figure 5.4 Number of visitors to the Niijima Island by month, 2012 and 2013. Data from Oshima Subprefecture of Tokyo (2014). 72

Figure 5.5 Geology of the Niijima Island: (a) topography map showing land surface elevations (Ministry of Land, Infrastructure, Transport and Tourism, 2015), bedrock surface elevations (Construction Section of Niijima Village, 2001; Isobe and Nakashima, 2001; Shindo, 1980), sea bottom elevations (Nakaoka and Suzuki-Kamata, 2015) and anticipated tsunami hazard zone (Tokyo Disaster Management Council, 2013); (b) geologic map with the location of public water supply wells; (c) schematic geologic cross-sections of N-S (vertical exaggeration by a factor of 2) and W-E (vertical exaggeration by a factor of 10). Modified from Shindo (1980) and Isshiki (1987).. 73

Figure 5.6 The bedrock surface elevations of the Niijima Island based on the resistivity survey results by Shindo (1980) (white lines), the ones based on the microtremor survey results (red

points), and the ones based on borehole data by Niijima Village Office (2015) (B1 and B2) and by Construction Section of Niijima Village (2001) (B3). 74

Figure 5.7 The results of 1-D electrical sounding. See the location of the measurement in Figure 5.6. The data was analyzed and provided by Kiso-jiban Consultants Co.,Ltd., Japan..... 75

Figure 5.8 (a) Boundaries of tectonic plates surrounding Japan and location of Niijima Island (source: https://www.newscientist.com); (b) Estimated maximum seismic intensity by the Nankai earthquake and location of Niijima Island (intensity level in Japan Meteorological Agency seismic intensity scale) (source: http://www.forbes.com); (c) Average wave height and maximum wave height in different coastal sites in the worst scenario of the estimated Nankai Earthquake. Black arrow indicates the condition of Niijima Island (Cabinet Office of Japan, 2011)..... 76

Figure 5.9 The scenario of tsunami inundation at the Niijima Island: (a) simulated height of tsunami waves and inundation area (b) Tsunami wave displacement at the sea surface near the Maehama coast of the Niijima Island under the Nankai earthquake and tsunami scenario simulated by Tokyo Metropolitan Government (2013). A tide level of 0.73 m a.m.s.l. was considered in the simulation. 77

Figure 6.1 ICs of ST-1, and BCs of ST-1 to ST-4. Vertical exaggeration is by a factor of 10.80

Figure 6.2 Fitting results for parameterization: (a) The modeled water retention curve using the van Genuchten model (van Genuchten, 1980) based on the measured data by Shindo (1980). (b) Comparison of the simulated results (at the end of ST-1) and observed water table elevations. The observed data are projected positions to the line W-E. The measured data are plotted with the fluctuation ranges based on the historical records of water table elevations provided by the Niijima Office and by Aichi et al. (2011). 85

Figure 6.3 Varied settings for uncertainty analysis: (a) The settings of time-variable tsunami inundation elevation $h_T(t)$ during ST-2. (b) The setting of the recharge rate $R(t)$ with daily variances (annually cyclic). Keeping the annual recharge of 883 mm/yr, $R(t)$ was set to be proportional to the daily rainfall amount on the Niijima Island in 2017 (Japan Meteorological Agency, 2017). (c) The model domain showing the scenario of the bedrock with the concave up shape. (d) The model domain included the aquifer layer and the bedrock layer. (d) The model domain included the tsunami deposits layers at land surface at the beginning of ST-4..... 89

Figure 6.4 The simulation results showing the temporal changes of mass concentrations, water table, and streamlines in the baseline case: (a) ST-1, (a) to (d) ST-2, (d) to (g) ST-3, and (g) to (l) ST-4. The white lines with arrows are streamlines. Note that the streamlines in (a) show the route of water flows at the quasi-steady-state while the ones in (b) to (l) illustrate the directions of flow at the given time during the transient simulation period. The grey lines are the concentration isoline of 0.33 kg/m^3 NaCl which is equivalent to the concentration limit of 0.2 kg/m^3 Cl^- in Japanese drinking water standards (Ministry of Health, Labor and Welfare, 2015) . *T* indicates the time elapsed from the beginning of ST-2 when the tsunami inundation event started. Vertical exaggeration is by a factor of 10. 93

Figure 6.5 The temporal changes of *TM* during (a) ST-2, (b) ST-3, and (c) ST-4 in the baseline case. Note the scale of the *TM* axis in (b) is different from those in (a) and (c). 94

Figure 6.6 Spatial distributions of the element-based dimensionless numbers M_x^E, M_z^E, Ra_d^E, and the plume cores for the simulations results of the baseline case at 10 minutes, 80 days, and 2 years. See the corresponding simulation results in Figure 6.4. 95

Figure 6.7 The plots of the element dimensionless numbers at the plume cores for the simulation results of the baseline case at 10 minutes, 80 days, and 2 years on the diagram of M_x^E, M_z^E, and Ra_d^E. 96

Figure 6.8 The temporal changes of *TM* during ST-2 and ST-4 for the simulation cases with varied settings of tsunami inundation scenarios: (a) $h_T(t)$ was varied from 5 m a.m.s.l. to 25 m a.m.s.l. while $h_T(t)$ was kept constant over time in each case; and (b) $h_T(t)$ of 15 m a.m.s.l. was kept constant for 10, 40, and 120 minutes; and (c) $h_T(t)$ was temporally varied over time during ST-2 (see details in Figure 6.3a). 98

Figure 6.9 The simulation results showing the temporal changes of concentrations, water table, and streamlines in ST-4 for the case of $h_T(t)$ = 25 m a.m.s.l. (the case T-H4). Vertical exaggeration is by a factor of 10. 99

Figure 6.10 The simulation results showing the temporal changes of mass concentrations and water table in ST-4 for the case T-HD5 which set $h_T(t)$ according to the tsunami wave displacement that was simulated by Tokyo Metropolitan Government (2013) (Figure 5.9b). Vertical exaggeration is by a factor of 10. 101

Figure 6.11 The temporal changes of *TM* during ST-2 and ST-4 for the simulation cases with varied settings: (a) the duration of ST-3 was varied from 1 to 30 days; and (b) $R(t)$ was varied from 662 to 1104 mm/yr while the ratio *R/K* was kept constant, and $R(t)$ with daily and seasonal variation. 103

Figure 6.12 The temporal changes of *TM* during ST-2 and ST-4 for the simulation cases with varied settings of aquifer properties: (a) the ratio K_z/K_x was varied from 0.1 to 1; (b) *K* of the aquifer materials was varied from 1.1×10^{-3} m/s to 1.1×10^{-4} m/s; (c) the bedrock surface topography in a concave up shape with $h_T(t)$ of 15 and 25 m a.m.s.l.; (d) the effect of a bedrock layer with *K* of 1.1×10^{-13} m/s and 1.1×10^{-7} m/s; and (e) the effect of the tsunami deposits layers with *K* of 1.1×10^{-13} m/s and 1.1×10^{-7} m/s. 105

Figure 6.13 The simulation results showing the temporal changes of mass concentrations, water table, and streamlines in (a) ST-2, and (b) to (f) ST-4 for the case with K_z/K_x = 0.1 (the case A-Kz1). Vertical exaggeration is by a factor of 10. 106

Figure 6.14 The simulation results showing the temporal changes of mass concentrations and water table during ST-4 for the case with $K = 1.1 \times 10^{-4}$ (the case A-K1). Vertical exaggeration is by a factor of 10. 107

Figure 6.15 The simulation results showing the temporal changes of mass concentrations, water table, and streamlines with the setting of in a concave up bedrock shape with (a) $h_T(t)$ = 15 m a.m.s.l. (the case A-BS1) and (b) $h_T(t)$ = 25 m a.m.s.l. (the case A-BS2). Vertical exaggeration is by a factor of 10. 109

Figure 6.16 The simulation results showing the temporal changes of mass concentrations, water table, and streamlines during ST-4: (a) a bedrock layer with $K = 1.1 \times 10^{-13}$ m/s (the case A-

BK1); and (b) a bedrock layer with $K = 1.1 \times 10^{-7}$ m/s (the case A-BK2). Vertical exaggeration is by a factor of 10. 110

Figure 6.17 Plots of horizontal and vertical fluid velocity v_x and v_z of the nodes at the interface between the aquifer layer and the bedrock layer for the simulation cases A-BK1 and ABK2 at 1 year after the tsunami. See the location of the selected interface at the red frame in Figure 6.16. The plots were compared with the average slope of the selected interface..... 111

Figure 6.18 The simulation results showing the temporal changes of mass concentrations and water table during ST-4: (a) tsunami deposits layers with $K = 1.1 \times 10^{-13}$ m/s (the case A-T1); and (b) tsunami deposits layers with $K = 1.1 \times 10^{-7}$ m/s (the case A-T2). Vertical exaggeration is by a factor of 10. 112

Figure 6.19 The simulation results showing the temporal changes of mass concentrations, water table, and streamlines during ST-4 with varied settings of seawater density: (a) $\rho_s = 1000$ kg/m^3 (M-S1), (b) $\rho_s = 1002.5$ kg/m^3 (M-S2), and (c) $\rho_s = 1250$ kg/m^3 (M-S3). The white lines with arrows are streamlines. Vertical exaggeration is by a factor of 10. 113

Figure 6.20 The temporal changes of *TM* during ST-4 for the simulation cases with varied seawater density settings from 1000 kg/m^3 to 1250 kg/m^3. 114

Figure 6.21 Comparison of the simulation results showing mass transport patterns at 100 days after the tsunami with element size Δl that ranged from 0.43 m to 9.93 m. No convergence was obtained in the case M-E7. Vertical exaggeration is by a factor of 10. 115

Figure 6.22 Box and whisker plots of downward velocities of the elements at the plume cores at 100 days after the tsunami with element size Δl that ranged from 0.43 m to 9.93 m. The plume cores were defined as the regions where the concentration was higher than 50% of the maximum concentration of the plume in the saturated zone. 116

Figure 7.1 (a) Domain and discretization of the 3-D model; BCs and ICs for simulation of (b) the pre- and post-tsunami periods and (c) the tsunami inundation period. Vertical exaggeration is by a factor of 5. 120

Figure 7.2 Layer configurations of the 3-D model. 124

Figure 7.3 Comparison of measured and computed data: (a) The modeled saturation curve using the van Genuchten model (van Genuchten, 1980) based on the measured data by Shindo (1980); (b) Spatial distribution of computed hydraulic head contours and measured hydraulic heads; (c) Comparison of computed and measured hydraulic heads. The measured data are plotted with the fluctuation ranges based on the historical records of water table elevations provided by the Niijima Office and by Aichi et al. (2011). 126

Figure 7.4 Cross-sections showing temporal changes of mass concentration distributions under the condition that prior to the arrival of the tsunami, and at 10, 30, and 120 minutes during tsunami inundation of $h_T = 15$ m a.m.s.l.. Vertical exaggeration of the cross-sections is by a factor of 10. See the location of the cross-section in Figure 5.5. The mass concentration of 0.33 kg/m^3 NaCl is equivalent to the concentration limit of 0.2 kg/m^3 Cl^- in Japanese drinking water standards (Ministry of Health, Labor and Welfare, 2015). 127

Figure 7.5 Temporal changes of accumulated volume of seawater that was intruded through land surface during the tsunami inundation of 15 and 20 m a.m.s.l. 128

Figure 7.6 3-D views of modeling results: (a1) mass concentration distributions and (a2) flowlines showing directions and remaining travel time of groundwater which discharges out to the sea at the normal quasi-steady state (before the tsunami) of the Niijima Island. The aquifer recovery process after the tsunami of (b)15 m a.m.s.l. and (c) 20 m a.m.s.l.. Dashed lines show the location of the vertical cross-sections in Figure 11. Vertical exaggeration is by a factor of 10. 130

Figure 7.7 Temporal changes of the loss of freshwater resource with time after tsunami of 15 and 20 m a.m.s.l. under pumping and no pumping conditions..... 131

Figure 7.8 Vertical cross-sections comparing the distribution of mass concentration at one year after the tsunami of (a) 15 m a.m.s.l. and (b) 20 m a.m.s.l.. See the locations of the cross-section in Figure 7.6. Vertical exaggeration of the cross-sections is by a factor of 10. 131

Figure 7.9 Simulations results of pumping fresh groundwater after (a) h_T = 15 m a.m.s.l. tsunami and (b) h_T = 20 m a.m.s.l. tsunami and pumping the intruded saltwater after (c) h_T = 20 m a.m.s.l. tsunami. 133

Figure 7.10 Conceptual vertical cross-sections showing the patterns of saltwater plume with bedrock structures (a) convex upward and (b) convex downward, respectively. 135

LIST OF ABBREVIATIONS

1-D	one-dimensional
2-D	two-dimensional
3-D	three-dimensional
a.m.s.l.	above sea-level
BCs	BCs
DDF	density-driven flow
HH	horizontal hydraulically-driven flow
ICs	ICs
Mt.	mountain
REV	representative elementary volume
SWI	seawater intrusion
TM	total mass of the solute
TSWI	tsunami-induced seawater intrusion
VD	vertical density-driven flow
VH	vertical hydraulically-driven flow

LIST OF UNITS OF MEASUREMENTS

kg/m^3	kilogram per cubic meter
km	kilometer
km^2	square kilometer
L	liter
m	meter
m^3	cubic meter
mg/L	milligram per liter
min	minute
mm/yr	millimeter per year
m/s	meter per second
M_W	moment magnitude
°C	degree Celsius

LIST OF SYMBOLS

Roman Letters

Symbol	Unit	Description
c	ML^{-3}	mass concentration;
c_c	ML^{-3}	pre-defined constant mass concentration;
c_f	ML^{-3}	mass concentration of freshwater;
c_m	ML^{-3}	mass concentration of seawater;
C_s	L^{-1}	specific moisture capacity;
C_s^{BC}	ML^{-3}	mass concentration at fluid injection boundary;
D_{ij}	L^2T^{-1}	dispersion coefficient tensor;
D_d	L^2T^{-1}	coefficient of molecular diffusion;
g	LT^{-2}	gravitational acceleration;
h	L	hydraulic head;
h_c	L	pre-defined constant hydraulic head;
h_s	L	piezometric head related to seawater;
H_0	L	thickness of the saturated zone;
H_0	L	depth of aquifer bottom;
H_f	L	fresh-water head;
H_n	L	environmental-water head;
H_p	L	point-water head;
i	-	unit vector in a horizontal plane;
j	-	unit vector in a horizontal plane;
k_{ij}	L^2	permeability;
k	-	unit vector directed upward along vertical;
$\boldsymbol{k}$	L^2	permeability tensor;
K_x	LT^{-1}	horizontal hydraulic conductivity;
K_{ij}	LT^{-1}	hydraulic conductivity tensor;
K_{ij}^s	LT^{-1}	hydraulic conductivity tensor of saturated porous media;
K_z	LT^{-1}	vertical hydraulic conductivity;
K^r	-	relative permeability;
L^{BC}	L	solute injection length;
L_h	L	distance from groundwater divide to coastline;
m	-	fitting parameter for van Genuchten model;
M_w	-	moment magnitude scale of an earthquake;
M	-	convective ratio
M_x^{BC}	-	BC-based convective ratio;

M_x^E	-	element-based convective ratio;
M_z^{BC}	-	BC-based convective ratio;
M_z^E	-	element-based convective ratio;
n	-	pore size distribution index for van Genuchten model;
p	$ML^{-1}T^{-2}$	pressure;
Pe_m	-	mesh Peclet number;
q_i	LT^{-1}	component of Darcy flux in *i* direction;
q_p	LT^{-1}	pre-defined Darcy flux;
$\mathbf{q}$	-	Darcy flux vector;
Q	LT^{-1}	total flux;
Q_n	LT^{-1}	integral boundary balance flux;
R	L	recharge depth;
Ra	-	Rayleigh number;
Ra_d^{BC}	-	BC-based Rayleigh number;
Ra_d^E		element-based Rayleigh number;
s	-	saturation (fluid volume per void volume);
s_e	-	effective saturation;
s_r	-	residual saturation;
s_s	-	maximum saturation;
S_s	L^{-1}	specific storage coefficient;
t	T	time;
$\mathbf{v}$	-	average linear velocity vector;
v_i	LT^{-1}	component of average linear velocity in *i* direction;
W_i	$ML^{-2}T^{-1}$	component of dispersive flux in *i* direction;
x, y, z	L	coordinates;
z_s	L	depth of freshwater-saltwater interface below datum;
z_w	L	elevation of water table;
Z	L	elevation;
Z_r	L	elevation of reference point;

Greek Letters

Symbol	Unit	Description
α	L^{-1}	fitting parameter for van Genuchten model;
α_L	L	longitudinal dispersivity;
α_T	L	transverse dispersivity;

β	-	control factor;
ε	-	porosity;
θ	-	volumetric water content;
μ	$ML^{-1}T^{-1}$	viscosity;
ρ	ML^{-3}	fluid density;
ρ_a	ML^{-3}	average density of water between Z_r and Z;
ρ_f	ML^{-3}	density of freshwater;
ρ_s	ML^{-3}	density of seawater;
χ_s	1	density ratio between seawater and freshwater;
ψ	L	pressure head;

CHAPTER 1: INTRODUCTION

1.1 Background

In the hydrological cycle at coastal areas, precipitation in the form of rainfall or snowmelt reaches to land surface or ocean. Once water reaches to the ground, water evapotranspirates into the atmosphere, some infiltrates into the soil and recharges groundwater, or some flows into lakes or rivers and finally discharges into the ocean. At the coastal areas, fresh groundwater flowing from inland areas meets with seawater, which can be described by a saltwater-freshwater mixing zone (Figure 1.1a). Because seawater contains a higher concentration of dissolved components than freshwater, it has a higher density than freshwater, which causes that the denser seawater is situated beneath the lighter fresh groundwater. Coastal groundwater systems are of great research interest because of their important roles of supplying freshwater for drinking, domestic, industrial and agricultural uses and maintaining ecosystem function.

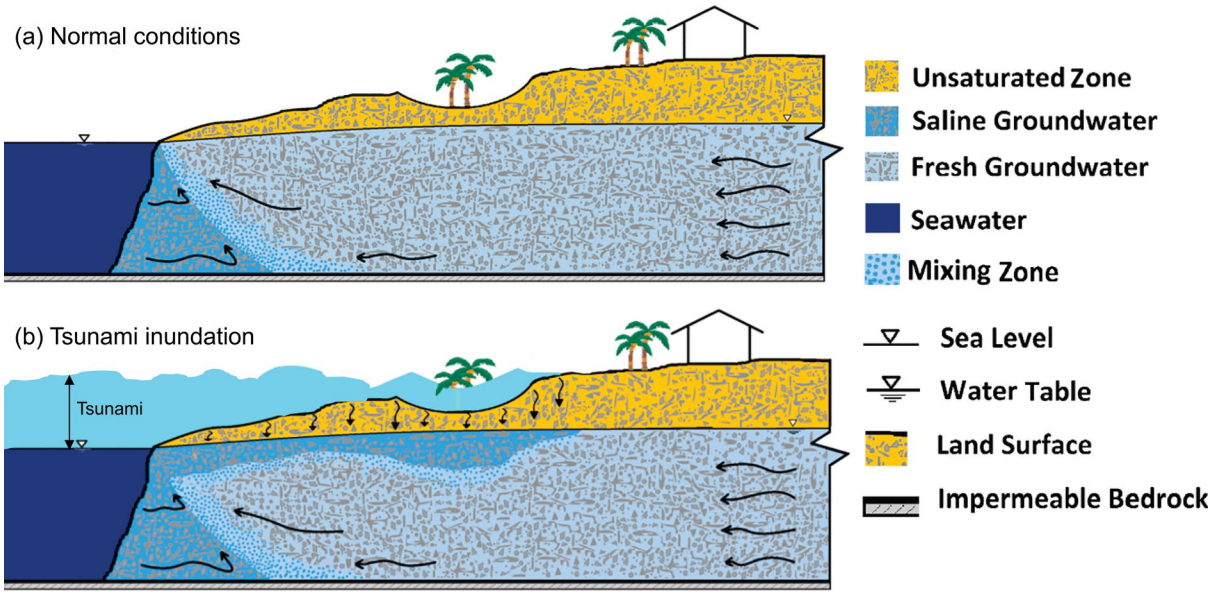

Figure 1.1 A vertical conceptual cross-section showing a coastal groundwater system under (a) normal conditions and (b) tsunami inundation conditions. Modified after Mahmoodzadeh and Karamouz (2019).

Coastal groundwater systems are affected by seawater intrusion (SWI) which can threaten the quality of freshwater resources. Besides SWI caused by lateral shifts of saltwater-freshwater mixing zone towards inland due to climate change and sea-level rise (Ketabchi et al., 2016; Werner and Simmons, 2009) or due to intensive groundwater abstraction activities (Werner et al., 2013), SWI can occur vertically from land surface due to large-scale seawater flooding caused by tsunamis, i.e., tsunami-induced seawater intrusion (TSWI) (Illangasekare et al., 2006; Nakagawa et al., 2013) (Figure 1.1b). As shown in Figure 1.2, increases of groundwater salinity over the drinking water quality standards due to TSWI have been reported in many coastal areas after the major tsunamis in 2004 and 2011 (Illangasekare et al., 2006; Mori et al., 2012). The disturbance of water supply persisted for several years due to the remained saltwater in aquifers (Sivakumar and Elango, 2010; Violette et al., 2009; Vithanage et al., 2012). Furthermore, many coastal areas around the globe are facing tsunami risks (Figure 1.3), especially in the vicinity of seismically active zones, such as Japan, Indonesia, Chile, and Peru (UNISDR, 2009) . Therefore, understanding TSWI processes and predicting future TSWI are critical to strengthen groundwater resources resilience in tsunami-prone zones.

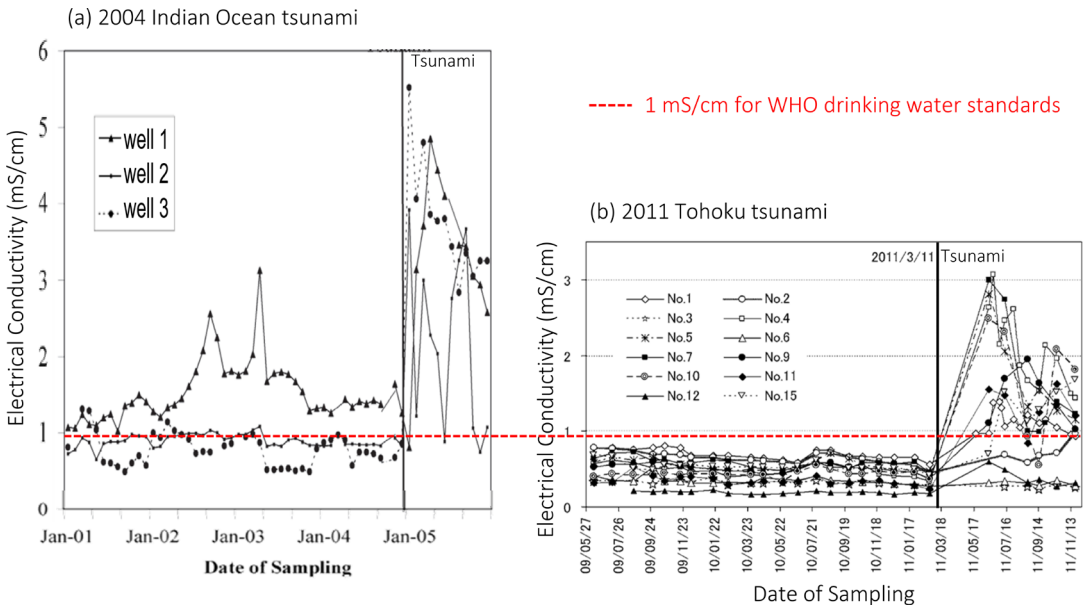

Figure 1.2 Measurements of electrical conductivity of groundwater before and after (a) the 2004 Indian Ocean tsunami (Illangasekare et al., 2006) and (b) the 2011 Tohoku tsunami (Mori et al., 2012). Data are compared with the drinking water quality standards by WHO (2004).

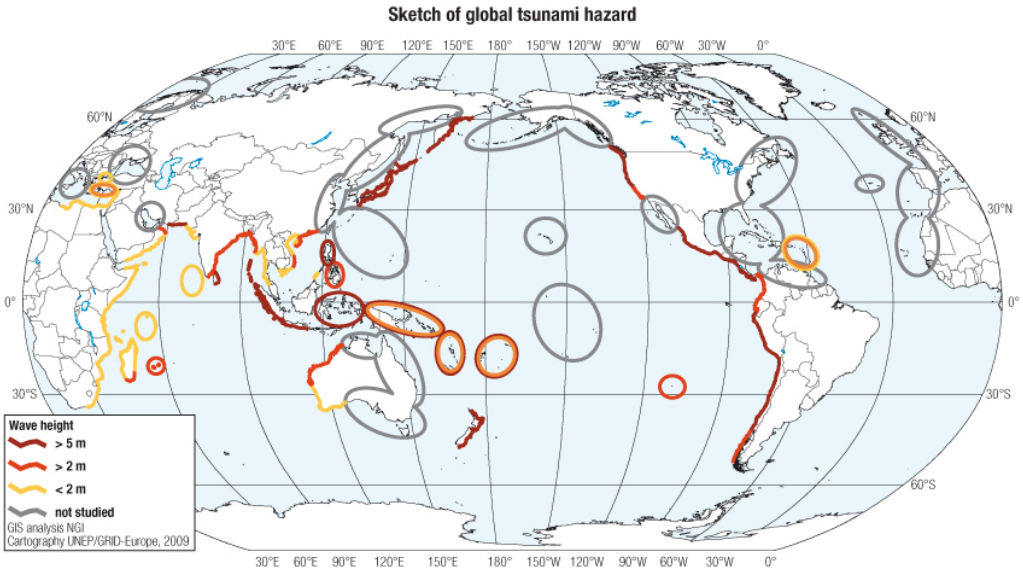

Figure 1.3 Global map of tsunami hazard (after UNISDR, 2009)

TSWI has been previously studied to understand its density-driven mechanism and its environmental impacts on coastal aquifers (see the detailed literature review in Chapter 2). The problem of TSWI involves variable-density flow and mass transport processes in unsaturated-saturated media. When saltwater infiltrates through unsaturated soil and overlies on top of fresh groundwater, the density differences between saltwater and freshwater groundwater can result in fingering flow patterns (Figure 1.4). This fingering phenomenon has been studied through many physical, numerical simulations, and theoretical analysis for its important impacts on concentration distributions and contaminant migration. Moreover, TSWI based on the major tsunami disaster in 2004 and 2011 has been studied to quantify their impacts on coastal groundwater system using techniques including environmental monitoring and numerical modeling. These studied provided important theoretical knowledge and field-based information for understanding processes of TSWI. Especially, numerical modeling has been extensively used in these studies and could be a very useful tool for predicting TSWI under future tsunami scenarios. However, accurate interpretations of modeling results require a comprehensive understanding of a series of uncertainties of model settings, including tsunami inundation scenarios, geological and hydrological settings, anthropogenic disturbance, and so on.

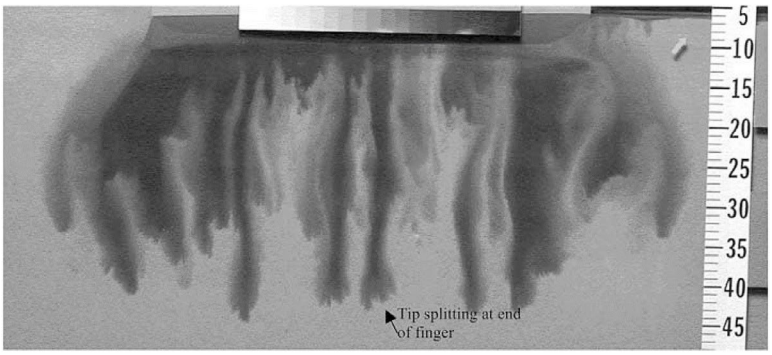

Figure 1.4 An example of fingering patterns observed in sandbox experiments, in which dense solute was injected from the top of a container filled with sands and water (Simmons et al., 2002).

1.2 Objectives

The objectives of this study were set to be:

(1) to numerically simulate TSWI processes in unconfined coastal aquifers under future tsunami scenarios;

(2) to investigate the impacts on simulation results of TSWI caused by the model uncertainties, including tsunami scenarios, hydrogeological factors, and anthropogenic activities.

1.3 Strategy and Structure of the Thesis

The methodology and structure adopted in this thesis are schematically shown in Figure 1.5. Chapter 2 presents a literature review concerning previous studies on variable-density flow and mass transport, and studies on the TSWI problems based on the major tsunami disaster in 2004 and 2011. The thesis adopted a numerical modeling approach to solve variable-density flow and mass transport in unsaturated-saturated media using the code FEFLOW. Chapter 3 describes the basic theories of the modeling approach and general settings of numerical simulations. The main investigations began with simulations of a conceptual problem (Chapter 4), in which a dense solute was continuously injected from the top into an unconfined, homogenous aquifer with horizontal groundwater flow. A series of numerical experiments were conducted using various values of the parameters and boundary conditions. Three dimensionless numbers were adopted to understand the driving forces of the flow regimes, and

to support the analysis of parameter sensitivity. The conceptual problem was designed to provide a basis for understanding the behavior of dense solute with respect to sinking and mixing patterns. Next, the modeling approach was applied to simulate TSWI under future tsunami scenarios in a real coastal site. The Niijima Island, Japan, was selected to be the example, because groundwater is the only source of freshwater in the island, and the island is facing high risks of TSWI under the Nankai earthquake and tsunami scenarios. Chapter 5 provides information on the Niijima Island including social, geological, hydrogeological settings, and tsunami scenarios, which was obtained by fieldworks and from sources including online databases, literature, and government offices. In Chapter 6, TSWI processes in the Niijima Island were simulated on a 2-D vertical cross-section. The settings of the tsunami inundation scenarios, the rainfall recharge conditions, and the aquifer properties, were varied to investigate their impacts on the simulation results. In Chapter 7, the numerical model was extended to 3-D and was applied to test the impacts and reliability of the unpolluted portion of groundwater as a freshwater resource in the post-disaster period. Finally, Chapter 8 summarizes the findings and gives suggestions for future research.

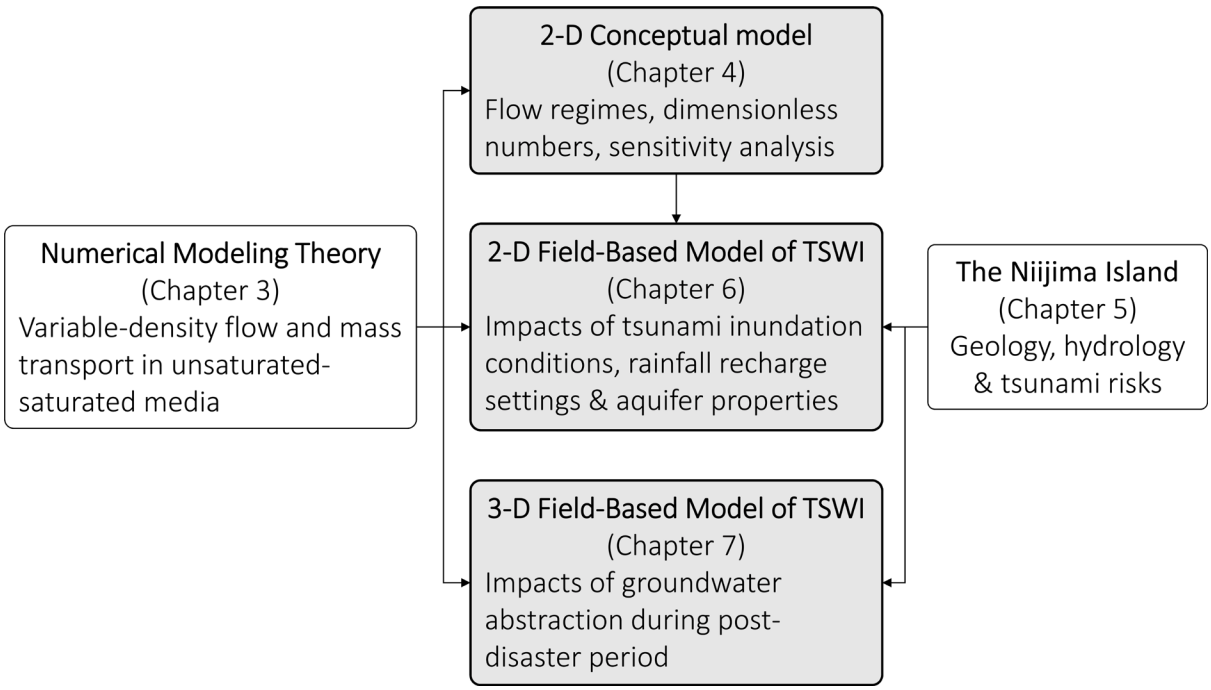

Figure 1.5 Schematic diagram showing the methodology and structure of the thesis.

CHAPTER 2:LITERATURE REVIEW

2.1 Introduction

This chapter presents a literature review for studying TSWI based on two aspects:

(1) The problem of TSWI involves variable-density flow and mass transport processes in porous media. Relevant studies on the mechanism of these processes were reviewed in Section 2.2;

(2) Previous studies on TSWI based on the 2004 Indian Ocean earthquake and tsunami and the 2011 Tohoku earthquake and tsunami were reviewed in Section 2.3.

2.2 Density-Driven Flow (DDF)

Fluid flow problems in which density influences flow patterns in porous media are commonly referred to as density-driven flow (DDF) problems. In the last few decades, there has been growing interest in the research on DDF processes because of their wide existence in environmental issues and their essential effects on contaminant mixing processes. Besides TSWI (Illangasekare et al., 2006; Vithanage et al., 2012), examples evolving variable-density flow include leakage from waste disposal sites (Liu and Dane, 1996; Schincariol and Schwartz, 1990; Zhang and Schwartz, 1995), dynamics of seawater-freshwater mixing zones in coastal aquifers (Henry, 1964; Post and Kooi, 2003; Smith, 2004), DNAPL studies (Lemke et al., 2004), and heat and fluid flow in geothermal research (Gvirtzman et al., 1997; Oldenburg and Pruess, 1999). In these problems, when the invading plume has a significantly higher density than that of the ambient groundwater, the mixing would occur in the form of lobe-shaped instabilities or fingers, which is referred as free convection (Schincariol and Schwartz, 1990). This density induced instability is vital for three main reasons (Simmons et al., 2001): (1) the total amount of solute transport involved in free convection is typically more significant than that in diffusion; (2) the mixing speed is greatly accelerated; and (3) the solute spreads over much larger distances. Therefore, understanding the mechanism of variable-density flow and mass

transport is important for predicting the fate of groundwater contamination and taking appropriate countermeasures.

Previous studies have adopted physical experiments, numerical modeling, and dimensionless number analysis, to understand DDF phenomenon, which has been reviewed by Simmons et al. (2001), Diersch and Kolditz (2002), and Nield and Bejan (2006).

2.2.1 Physical Experiments

One of the first attempts to investigate the mixing behavior of two stratified fluids of different densities was carried out by List (1965). This experiment discovered that if a dense fluid flows horizontally above a lighter one the flow would always be unstable, unless the growth rate of the unstable waves was low enough so that the flow could be considered quasi-stable. List (1965) interpreted the mixing of unstable patterns as the convection caused by flow was relatively much larger than the pore scale diffusion, and hence, the problem is referred to as convection dominated problem. List (1965) pointed out that the instability growth rate would be high if the plume descends faster than its dispersion, namely, the plume should be stable when the dispersion velocity is higher than the velocity of descent.

Oostrom et al. (1992) conducted laboratory sandbox experiments by injecting a solute into homogeneous, unconfined aquifer model under horizontal flow conditions (Figure 2.1). Results showed that contaminant plumes with a density larger than the ambient groundwater were either stable or unstable. The unstable flow patterns were featured with lobe-shaped, transient, 3-D perturbations. They found that the level of instabilities would be increased with a larger density difference. Furthermore, a large velocity of horizontal groundwater flow reduced the likelihood of the occurrence of instabilities, while this likelihood was increased with a larger solute injection rate or a larger value of hydraulic conductivity.

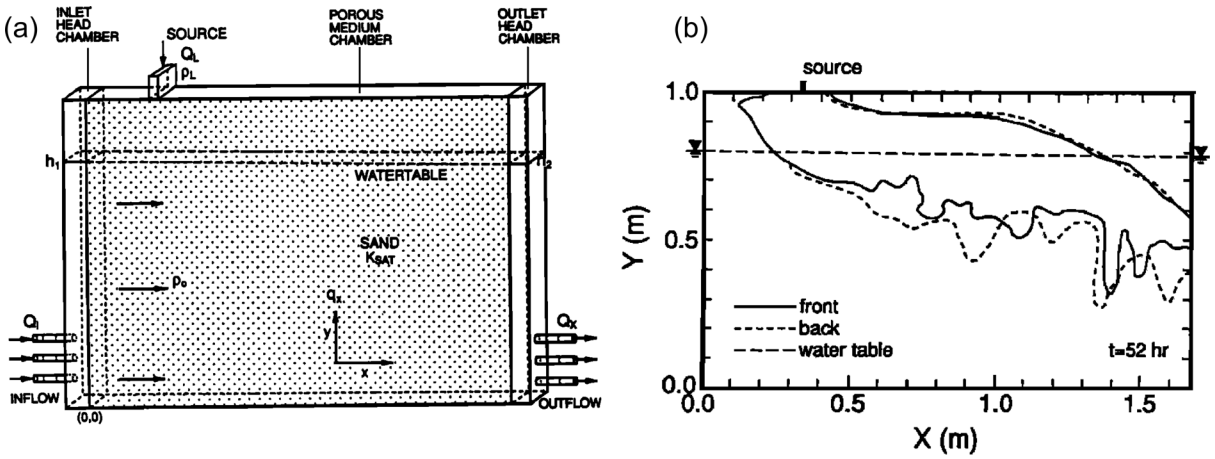

Figure 2.1 Sandbox experiments by Oostrom et al. (1992): (a) experiment settings and (b) plume outline curves.

Paschke and Hoopes (1984) conducted experiments based on a sand tank which involved hydrodynamic dispersion, buoyancy involved vertical motion and the horizontal groundwater flow. They found that the plume would continue to move vertical downward and mix with the horizontal groundwater flow until the plume became significantly diluted so that downward movement became very small. Once this situation was achieved, density effect was minimized and the trajectory, concentration, and boundary of the plume can be adequately calculated by the advection-dispersion equations for non-buoyant fluids.

In the physical experiments by Schincariol and Schwartz (1990), a homogeneous, layered, and lenticular porous medium was considered. This study was trying to understand the influence of the heterogeneous structure of the porous medium on the development of DDF. They found a density difference as small as 0.8 kg/m^3 was enough to produce gravitational instabilities in a homogeneous media. When the layered and lenticular system was introduced, the behavior of DDF became much more complex. It was concluded that unstable convective mixing is a nonlinear dynamic process which is very sensitive to small changes in the initial conditions of the experiments. For example, Schincariol and Schwartz (1990) found it difficult to reproduce the experiment results due to the sensitivity of the system. Besides causing the fingering patterns, DDF was found to result in different directions and speeds of plume movement due to the existence of barriers in the porous medium. For example, their

experiments with dipping beds showed that when this component of flow was aligned with the direction of the horizontal flow, the plume would move at greater than expected velocities.

Simmons et al. (2002) presented experiments carried out in a sand filled glass flow container under both fully saturated and variably-saturated conditions and focused on the processes that occurred at the capillary fringe and below the water table, as affected by a dense contaminant plumes migration through the unsaturated zone. Their experiments discovered that volumetric water content appeared critical in the variably-saturated laboratory runs. Plume behavior at the water table depended on the density of the fluid that accumulates there. They suggested that the unsaturated zone and position of the water table should be considered in contaminant studies in order to predict the migration pathways, rates and fate of dense plumes.

2.2.2 Benchmarks and Numerical Modeling

Besides laboratory physical experiments, many numerical modeling approaches have been developed and used for analyzing DDF related instabilities. To test the reliability of the numerical codes, a series of test cases and benchmarks have been developed, for example, the most often referred Elder natural convection problem (Elder, 1967; Voss and Souza, 1987) and the salt lake problem (Simmons et al., 1999). The classic Elder problem, established by Elder (1967) is an experimental heat transport problem aiming at producing thermal convection in a Hele-Shaw cell. The Elder problem has since been modified into a mass transport problem by Voss and Souza (1987). This is an unstable transient problem consisting of dense fluid circulating downwards under buoyancy forces from a region of high specific concentration along the top boundary (Figure 2.2a). The salt lake problem was first introduced by Simmons et al. (1999) which describes a transient system in which an evaporation and density-driven fingering process evolves downwards in an area of upward-discharging groundwater in a Hele-Shaw cell experiment (Figure 2.3).

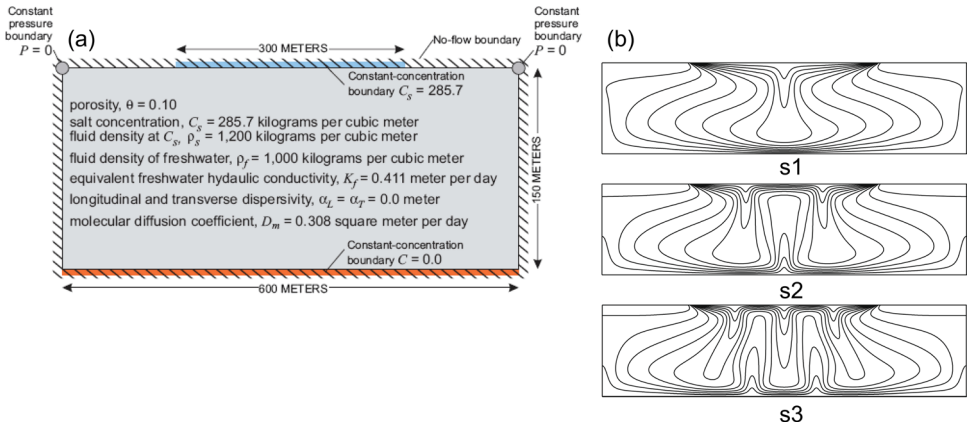

Figure 2.2 (a) Settings of the Elder problem (Elder, 1967); (b) concentration contours are shown for the single (s1), double (s2), and triple (s3) bifurcation solutions (van Reeuwijk et al., 2009).

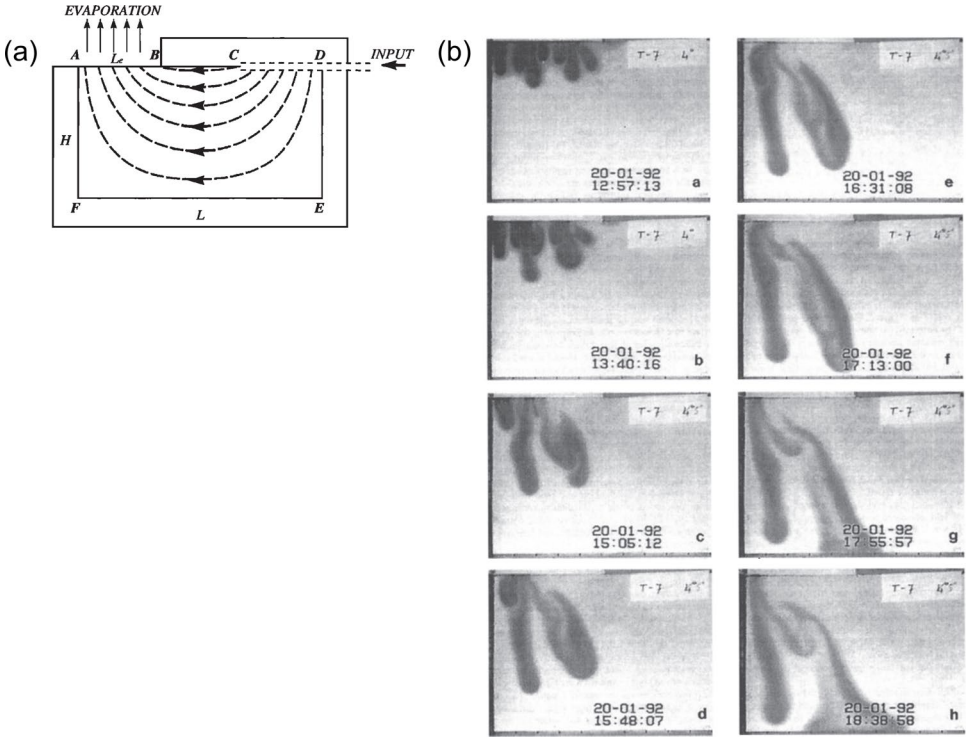

Figure 2.3 (a) Settings of the salt lake problem: an unstable saline boundary layer formed by uniform evaporation along AB. Along CD, there is uniform recharge which is at constant pressure. Boundaries BC, DE, EF, and FA are assumed impermeable. Dashed lines are streamlines. (b)Development stages of unstable puma behavior in the salt lake problem (Simmons et al., 1999).

The limited number of analytical solutions of DDF problems makes numerical modeling an important tool for this topic. The Elder problem and salt lake problem have been used for validating many numerical simulators. Numerical codes such as FEFLOW (Diersch, 2013), HYDROGEOSPHERE (Therrien et al., 2004), SUTRA (Voss and Provost, 1984), TOUGH2 (Pruess et al., 1999), and SEAWAT (Guo and Langevin, 2002) were summarized by

Simmons et al. (2010). Based on these benchmarks, many other studies conducted numerical simulations and found that the numerical solutions of DDF can be problematic because: (1) the onset and development of instability can be altered by choice of spatial discretization; (2) multiple solutions may exist; (3) the modeling results are sensitive to small perturbations. For example, the study by van Reeuwijk et al. (2009) used the pseudospectral method to avoid numerical error associated with spatial discretization, and proved that multiple steady states are indeed an intrinsic characteristic of the Elder problem (Figure 2.2b). Mazzia et al. (2001) concluded that grid convergence in the salt lake problem could not be achieved due to the sensitivity to numerical errors (e.g., truncation errors) when they investigated the reliability of the salt lake problem for the verification of numerical codes. Diersch and Kolditz (2002) agreed with the difficulty in predicting precise finger number, finger sizes, and descending pathways of fingers. Cremer and Graf (2015) found the number of fingers can be influenced due to the perturbation including spatial and temporal distribution of boundary conditions and heterogeneity of hydraulic conductivity field.

2.2.3 Dimensionless Number Analysis

Two dimensionless numbers, the convective ratio *M* and the Rayleigh number *Ra*, were commonly used to indicate the plume stability in DDF problems in porous media (Elder, 1967; Simmons et al., 2010; Wood et al., 2004; Wooding et al., 1997). The Rayleigh number *Ra* is an indicator to express whether density-driven instability is likely to occur in simple free convective systems, and was defined as the ratio between density-driven forces and the resisting forces caused by diffusion (Wooding, 1989):

$$Ra = \frac{\text{Density-driven forces}}{\text{Diffusion}} = \frac{\overline{H}K\left(\rho_s - \rho_0\right)/\rho_0}{\varepsilon D_d} \qquad \text{Eq 2.1}$$

under the condition that the effects of mechanical dispersion caused by the ambient flow were not considered, and $\overline{H}$ is the characteristic length scale (e.g., the plume thickness defined by

Oostrom et al., 1992), K is hydraulic conductivity, ρ_s is saltwater density, ρ_0 is freshwater density, ε is porosity, and D_d is the coefficient of molecular diffusion. By definition, a higher value of *Ra* reflects a higher degree of plume instability due to the density effect, while a lower value means the enhancement of diffusion which inhibits density-driven instability. Theoretically, density-driven instability is likely to occur when *Ra* is greater than $4\pi^2$ (Horton and Rogers, 1945; Lapwood, 1948), e.g., *Ra* = 400 in the classic Elder problem (Elder, 1967; Voss and Souza, 1987), *Ra* > 1800 in a saline disposal basin, *Ra* = 4870 in the salt lake problem (Wooding et al., 1997), and $Ra \approx 5000$ in a TSWI site (Illangasekare et al., 2006). However, the application of the Rayleigh number has limitations due to: (1) homogenous media and steady-state condition is assumed in the Rayleigh number (Simmons, 2005); (2) the choice of characteristic length scale $\overline{H}$ in the Rayleigh number is often difficult and ambiguous (Simmons et al., 2001); and (3) mechanical dispersion is excluded in the definition of *Ra* in Eq 2.1.

If the system to be studied is a mixed convective system where free convection (driven by density difference) and forced convection (driven by hydraulic head difference) together operate the processes, the convective ratio *M* is used for evaluating the relative strength between free and forced convection. The original convective ratio *M* is the ratio between free convective speed and forced convective speed, and was defined as (Bear, 1972):

$$M = \frac{\text{Free convective speed}}{\text{Forced convective speed}} = \frac{\left(\rho_s - \rho_0\right)/\rho_0}{\Delta h / \Delta L} \qquad \text{Eq 2.2}$$

where Δh is the hydraulic head difference over a length ΔL. When $M \gg 1$, free convection dominated transport process occurs. When $M \ll 1$, by contrast, forced convection is dominant. As *M* approaches 1, two processes are of comparable magnitude. In the laboratory experiments conducted by Oostrom et al. (1992), when $M > 0.3$, the free convection driven by the vertical

solute injection began to overwhelm the forced convection driven by the horizontal groundwater stream, and the plume behavior became unstable.

2.3 Tsunami-Induced Seawater Intrusion (TSWI)

Salinization of coastal groundwater systems has been reported by observations and environmental monitoring data after the major tsunami disasters in 2004 and 2011. On 26 December, 2004, an earthquake of moment magnitude (M_w) 9.3 occurred off the western coast of northern Sumatra (Liu et al., 2005). The generated tsunami affected the coastal areas of 14 countries in Asia and Africa. For example, about 750 km of the coast in India was inundated by the tsunami (Violette et al., 2009). On 11 March, 2011, an earthquake of M_w 9.0 occurred off the Pacific coast of Tohoku area, Japan. About 561 km^2 of coastal areas up to 0.5 to 1 km inland in Japan were submerged by seawater at the time of tsunami (Inui et al., 2012; Sugita, 2012). The tsunami reached to a maximum run-up elevation of 39.7 m a.m.s.l. (above mean sea-level) at Miyako city (Mori et al., 2012). TSWI of the major tsunamis in 2004 and 2011 have been understood through environmental observation and monitoring, physical and numerical modeling.

2.3.1 Environmental Observation and Monitoring

Table 2.1 summarizes the results of observation and monitoring studies after the major tsunami disasters in 2004 and 2011. The coastal areas investigated were mostly in relatively low elevation (< 15 m a.m.s.l.) with the aquifer materials to be high permeability (hydraulic conductivity on the order of 10^{-4} and 10^{-5} m/s). Annual precipitation of these tsunami-affected areas ranged from 1000 to 3000 mm/yr. The tsunami height of 3 to 12 m a.m.s.l. resulted in the tsunami inundation elevation of 5 to 29 m a.m.s.l. and the occurrence of seawater flooding 0.5 to 2 km inland from the coastline. Tsunami inundation continuously affected those coastal zones for a few hours. As for the consequences of seawater inundation, the maximum groundwater salinity measured at one month after the tsunami can be as high as 5.10 kg/m^3 Cl^-,

which is near the one-third of the seawater salinity. Even three years after the tsunami, groundwater salinity was still reported as high as in the level of around 2.84 kg/m^3 Cl^-, which is ten times higher than the acceptable limit of drinking water (0.2 kg/m^3 Cl^- in Japanese drinking water quality standards (Ministry of Health, Labor and Welfare, 2015) . Moreover, the recovery of groundwater salinization took several years. It is important to note that a simple comparison among the data summed up in Table 2.1 shows no clear correlation among the local hydrogeological settings, the tsunami inundation conditions, and the consequences of the SWI. Therefore, it can be interpreted that SWI and recovery processes are very likely under the joint influence of multiple factors including local hydrogeological settings (e.g., hydraulic conductivity and rainfall), tsunami inundation condition (e.g., inundation elevation and duration), and anthropogenic impacts (e.g., post-tsunami groundwater pumping). Therefore, knowing the TSWI processes in a specific site needs approaches that take into account the local hydrogeological information, tsunami inundation conditions, and human activities.

Water supplies in many coastal areas were strongly affected by TSWI. For example, after the disaster in 2004, over 40,000 drinking water wells up to 1.5 km inland from the coastline were damaged or polluted (Illangasekare et al., 2006; Villholth et al., 2005), which caused 80,000 people living in the settlement close to the coastline without secure drinking water (Villholth, 2007). As reported after the 2004 Indian Ocean earthquake and tsunami, in some areas, local people initiated well cleaning activities including removal of sands, debris, and pumping saline water out, but it was proven to be ineffective for recovering polluted wells or sometimes even prolonged the salinity level in wells (Illangasekare et al., 2006; Vithanage et al., 2009) or causing upconing of saltwater (Villholth et al., 2005).

Table 2.1 Summary of observations and environmental monitoring data on TSWI due to the tsunami disasters in 2004 and 2011.

Tsunami disaster	Reference	Study site				Inundation conditions				Consequences	
		Location	Elevation (m a.m.s.l.)	Hydraulic conductivity (m/s)	Annual rainfall (mm/yr)	Wave height (m)	Inundation elevation (m a.m.s.l.)	Distance from coast (km)	Inundation duration (hour)	Groundwater salinity (kg/m^3 Cl^-)	Recovery time (year)
2004 Indian Ocean earthquake and tsunami	Illangasekare et al. (2006)	Sri Lanka	< 15	-	1000 ~ 1700	3-8	15	1.5	1.5	1.68* (1 M)	> 1
	Villholth (2007)	East coast, Sri Lanka	-	-	1500	-	-	1	-	1.83* (1 M)	1.5
	Lyllon (2008)	East coast, Sri Lanka	-	-	-	-	5	< 1	-	5.10* (1 M)	-
	Piyadasa et al. (2009)	South coast, Sri Lanka	-	-	1167	-	-	-	few	-	> 4
	Kume et al. (2009)	Southeastern coast, India	-	-	1200	-	-	0.5 ~ 2	few	2.84 (40 M)	1.5
	Chidambaram et al. (2010)	Southeastern coast, India	-	1.6×10^{-4} ~ 2.7×10^{-4}	1662	-	29	0.5 ~ 1	-	3.22 (9 M)	-
	Vithanage et al. (2012)	East coast, Sri Lanka	< 4	0.9×10^{-4} ~ 1.4×10^{-4}	1200 ~ 1900	5 ~ 12	7	1	-	1.08* (10 M)	1 ~ 1.5
	Marohn et al. (2012)	Northern Sumatra, Indonesia	< 5	-	> 3000	-	-	1.5	< 5	2.44* (29 M)	-
2011 Tohoku earthquake and tsunami	Sugita (2012)	Asahi-city, Japan	< 5	5.0×10^{-4}	-	7.6	-	0.5 ~ 1	-	3.25* (2 M)	-
	Mori et al. (2012)	Sendai Plain, Japan	< 3	8.2×10^{-5}	-	-	> 10	4	-	1.53* (8 M)	-
	Nakagawa et al. (2013)	Minamisanriku town, Japan	-	-	-	-	16.1	-	-	1.33 (1 M)	-

- for data not provided;
* for salinity value converted from electrical conductivity at 20 °C;
M for months after tsunami;

Lyllon (2008) and Vrba and Salamat (2007) claimed that there is a need to find appropriate local safe drinking water resources that could be used immediately for emergency situations. After the disaster in 2004, freshwater was mainly provided by distributing packed water (polybags or PET bottles) and transporting tanked water in tsunami-affected areas. However, related issues, as reported by Shaw et al. (2006), are: (1) the water supply was only temporary with a limited quantity; (2) a large amount of used packs and empty PET bottles became solid wastes; and (3) sometimes proper disinfections were not applied to the tanked water. After the 2011 Tohoku earthquake, 27,000 bottles of drinking water were distributed to tsunami inundation areas within one day after the tsunami (Ministry of Agriculture, Forestry and Fisheries, 2011) . However, for the remote islands in tsunami-prone zones, the transportation of packed freshwater from the mainland could be very expensive and unsustainable. Compared with other freshwater sources, groundwater has advantages such as reliable and good quality, readily available on the spot and on demand. Therefore, assessing groundwater vulnerability to tsunami disasters and evaluating the capacity of unpolluted groundwater resources to provide post-disaster water supply can be beneficial for local disaster preparedness.

2.3.2 Physical Experiments

As shown in Figure 2.4, Illangasekare et al. (2006) and Vithanage et al. (2012) suggested that there were four sources of saltwater intrusion induced by tsunami inundation: (1) direct vertical infiltration of seawater through the land surface; (2) infiltration from ponding seawater; (3) infiltration from open dug wells; and (4) landward shift of saltwater-freshwater interface. Among these four sources, direct infiltration from land surface into unsaturated zone was likely the primary contribution of intruded seawater for the case where highly permeable sands exist and extents of the inundation area are large. Illangasekare et al. (2006) suggested that the surcharge of hydraulic head due to tsunami inundation could have led to a forced convection

regime at the initial stage of tsunami inundation, while as the surcharged head dissipated, free convection of seawater in aquifer could then dominate the mixing process.

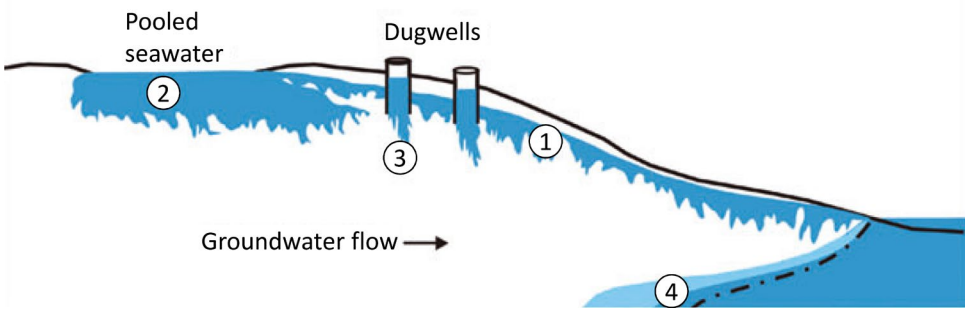

Figure 2.4 A vertical conceptual cross-section showing the sources of TSWI: (1) direct vertical infiltration of seawater through the land surface; (2) infiltration from ponding seawater; (3) infiltration from open dug wells; and (4) landward shift of freshwater-saltwater interface (modified after Vithanage et al., 2012).

Based on TSWI occurred at a coastal aquifer in Sri Lanka after the tsunami in 2004, Hogan (2006) and Illangasekare et al. (2006) conducted laboratory experiments to study the TSWI from three sources: (1) beach surface infiltration, (2) slow infiltration through inundated coastal lagoons and ponds, and (3) open well injection (Figure 2.5). This study tried to describe the mixing and transport of saltwater in a coastal aquifer discharged from multiple sources. The results indicated that the tsunami water penetrated the porous medium relatively quickly from the beach face infiltration and from injection through an open well. The well source penetrated the aquifer rapidly but migrated horizontally due to the fast groundwater flow. There was very little mixing of the intruded saltwater with the saltwater wedge. It took a much longer time for the contaminant that reached the wedge to leave the system. They found that a noticeable increase in the amount of fingering was observed in an experiment with slower horizontal groundwater flow. Their simulation of saltwater transport from the ponded source showed that there are two convective processes which are occurring, the downward convection due to density differences between the tsunami water and the horizontal convection due to the groundwater flow. However, these experiments were performed in a highly idealized system, of which the settings may not be reasonably representative for a real TSWI problem at a field.

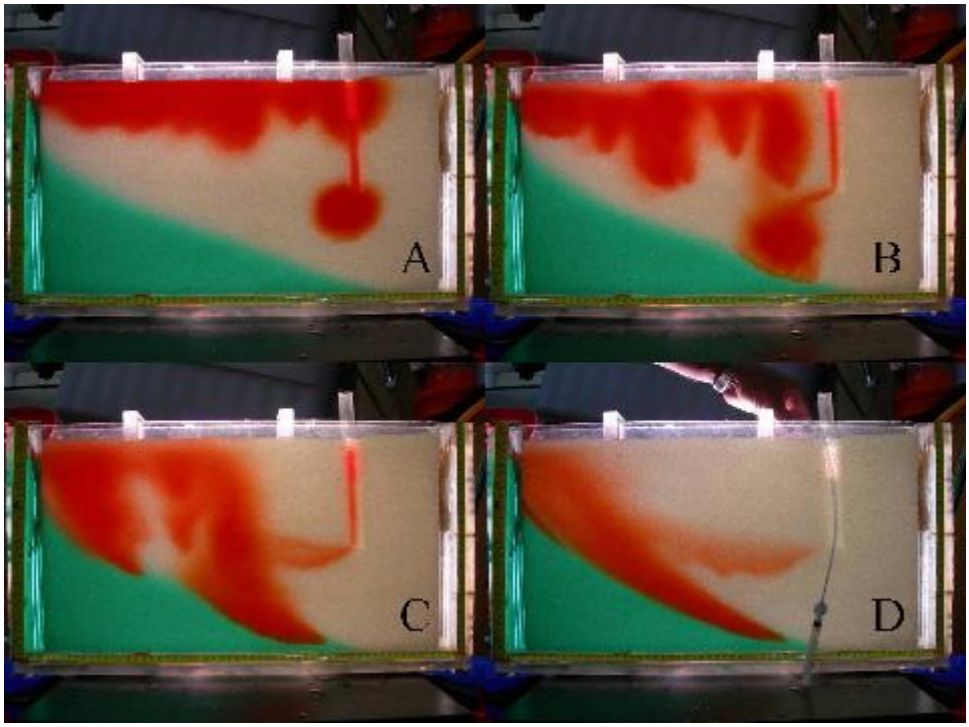

Figure 2.5 Physical model of tsunami injection and infiltration into a shallow coastal sandy aquifer at (a) 2, (b) 5, (c) 11, and (d) 19 min. The pre-tsunami seawater wedge is dyed green, and the pre-tsunami fresh water flowing from right to left is light brown. Infiltrated tsunami water, dyed red, is injected across the top of the aquifer. Tsunami water is also immediately injected into the aquifer through the open borehole. Dense seawater quickly develops into plumes that reach the preexisting seawater wedge (Hogan, 2006; Illangasekare et al., 2006).

2.3.3 Numerical Modeling

A summary of the studies on the numerical simulations of TSWI based on the tsunamis in 2004 and 2011 are presented in Table 2.2. The simulation results with respect to the recovery time of the polluted aquifer varied with different model properties (e.g., scale, porosity, and dispersivity) and different tsunami inundation conditions and rainfall recharge.

Essink (2005) developed numerical models by using the code MOCDENS3D to simulate the impacts of TSWI on the coastal aquifers of Maldives. They found that the simulated TSWI affected the upper part of the freshwater resource, and then, the intruded saltwater descended in the aquifer. The groundwater system was recovered by fresh rainfall recharge after about 10 years after the tsunami. However, in their simulations, the effect of the mixing of saltwater with freshwater due to the pressure of the tsunami waves was not considered.

Based on the tsunami inundation in India in 2004, Violette et al. (2009) conducted unsaturated zone modeling and saturated flow simulation by using Hydrus-1D code and MODFLOW, respectively. Their analyses suggested that pre-tsunami groundwater mixed with 5% tsunami seawater was enough to explain the observed salinity increase that occurred within one month of the tsunami. Both seawater infiltration during the tsunami and the infiltration through filled depressions were responsible for the observed salinity increase. The salinity change in groundwater was faster in monsoon seasons compared with that in dry seasons. However, DDF was not considered in this study, which may cause large uncertainties for interpretations of the simulation results.

In the modeling work by Vithanage et al. (2012), TSWI processes in unsaturated and saturated zones were modeled by using the codes Hydrus-1D and HST3D, respectively (however, not fully coupled) (Figure 2.6). A model of a layered, anisotropic aquifer was developed and calibrated based on measured water table elevations. The simulations showed a rapid initial decrease in salinity just after the tsunami, which was in agreement with observations due to the flow of the denser fluid and subsequent recharge by freshwater. The simulations suggested that it took about five years to recover the water quality in the upper 6 m of the aquifer and that the aquifer would recover totally through flushing of saltwater approximately within 15 years. However, this model excluded the simulation of saltwater-freshwater interactions, which may have important influences of discharge processes of the intruded saltwater. Though the bedrock structure was included in the model design, the impacts of bedrock on saltwater migration were not discussed.

In the numerical simulations by Sivakumar and Elango (2010), the numerical model by using FEFLOW was calibrated and reasonably matched with the measured groundwater table levels. However, the model design was limited to relatively a coarse mesh size (720 nodes and 639 elements), which may significantly affect the calculation of mass transport processes.

Furthermore, this study assumed no density effect in a horizontal 2-D model, which may be the reason why a relatively fast aquifer recovery time of 2 years was obtained.

Ministry of Agriculture, Forestry and Fisheries (2017) performed 3-D numerical simulations using the codes MODFLOW and SEAWAT based on the 2011 Tohoku earthquake and tsunami. Both MODFLOW and SEAWAT simulators produced simulation results of hydraulic head and groundwater salinity distributions in a good agreement with their measured data using the resistivity survey method after the tsunami. By using the model they forecasted the future recovery processes of groundwater quality, and found that a period of more than 10 years is required for the aquifer to be recovered by natural rainfall recharge. However, the initial conditions for the aquifer recovery processes were directly assigned based on their field measurements after the tsunami, rather than conducting simulations according to the tsunami inundation conditions.

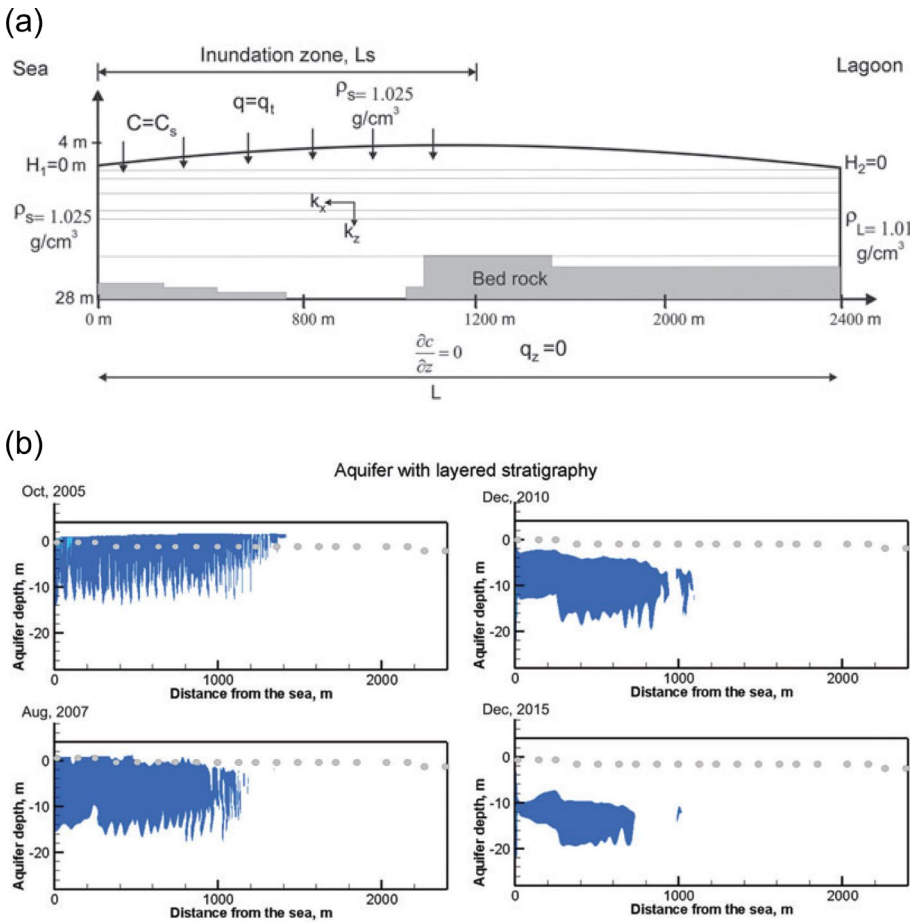

Figure 2.6 Vithanage et al. (2012): (a) model domain and boundary conditions; (b) simulation results.

Table 2.2 Summary of model setups and results by numerical studies on TSWI due to the tsunami disasters in 2004 and 2011.

Reference, Location, Scale	**Model features**			**Model setting**						**Results**
	Modeling code (dimensions)	**DDF**	**Unsaturated**	**Inundation duration (hour)**	**Inundation elevation (m a.m.s.l.)**	**Rainfall recharge (mm/yr)**	ε	**Hydraulic conductivity (m/s)**	α_L, α_T **(m)**	**Recovery time (years)**
Essink (2005), Maldives, 0.4 km long, 7 m deep	MOCDENS3D (2-D)	Yes	No	2	3	300	0.35	4.63×10^{-4}	0.1, 0.01 m	10
Violette et al. (2009), Southeastern coast, India, 21 km long, 12 m deep,	MODFLOW HYDRUS-1D (1- and 2-D)	No	Yes	0.08 (5 min)	0.1	200	0.3	7.44×10^{-5}	-	6 ~ 10
Sivakumar and Elango (2010), Southeastern coast, India, 2 km long, 15 m deep	FEFLOW (2-D)	No	No	-	-	300	0.17 ~ 0.25	3.13×10^{-4} ~ 5.09×10^{-4}	5.0 ~ 12.5, 0.5 ~ 1.2	2
Vithanage et al. (2012), East coast, Sri Lanka, 2.4 km long, 32 m deep	HST3D, HYDRUS-1D (1- and 2-D)	Yes	Yes	1	7	654	0.35	1.51×10^{-5} ~ 6.78×10^{-5}	0.5, 0.0625	15
Ministry of Agriculture, Forestry and Fisheries (2017) Japan, 240 km^2, 100 m deep	MODFLOW, SEAWAT (3-D)	Yes	No	-	-	1274	0.03 ~ 0.27	2.31×10^{-10} ~ 2.31×10^{-5}	-	> 10
Alsumaiei and Bailey (2018), Maldives, 0.2 ~ 10.1 km^2	SEAWAT (3-D)	Yes	No	8	1 ~ 1.8	1095 ~ 1825	-	1.16×10^{-4}	-	2

ε : porosity;

α_L, α_T : longitudinal and transverse dispersivities;

-: data not provided;

2.4 Summary

The understanding of DDF processes and TSWI problems from the literature introduced above are summarized as:

(1) Accurately and precisely modeling of the distributions of instabilities in DDF problems is currently extremely difficult, because the nonlinearity and complexity are inherent natures of DDF, e.g., bifurcation solutions exist. The instabilities are highly sensitive to the heterogeneity in porous media properties and boundary conditions, and model discretization.

(2) The occurrence of fingering patterns in DDF problems depends on a series of variations, including the density contrast, the loading rate of dense contaminant, the horizontal groundwater flow velocity. This may be explained by the interactions (or competitions) of DDF with the hydraulically-driven flow (forced convection or advection) and dispersion and diffusion processes, which could be quantified by using dimensionless numbers, e.g., *Ra* and *M*.

(3) A tsunami is a short-term event, while its impacts on groundwater quality and water supply is long-term. Impacts of TSWI on coastal aquifers are very likely associated with multiple factors, including tsunami inundation condition and local hydrogeological properties.

The remaining issues in research on DDF and TSWI problems are summarized as:

(1) Most of the experiments on DDF assumed hydrostatic water table, i.e., no horizontal groundwater flow conditions. However, contaminant transport in natural aquifers is usually accompanied with horizontal groundwater movement. Few physical experiments that considered the horizontal groundwater low, including Schincariol and Schwartz (1990), Oostrom et al. (1992), and Hogan (2006) were high idealized

and limited to lab scales that may not be representative for DDF problems with field settings, e.g., a TSWI problem in a coastal aquifer.

(2) Most of the studies on DDF evaluates the plume behavior in their numerical and physical simulation results based on the concepts of “stable” and “unstable”, “stability” and “instability”, “lobe-shaped instability”, or “fingering”. However, questions remain whether these definitions are sufficient to describe the plume morphology in a mixed system of density-driven convection, groundwater advection, and dispersion and diffusion processes.

(3) Most of the previous works studied TSWI by numerically reproducing the TSWI processes based on the past tsunamis in 2004 and 2011. Unfortunately, little work has been done to assess TSWI in advance in the tsunami-prone zones, which may related to that a comprehensive understating of the model uncertainties that arise from tsunami inundation scenarios, aquifer properties, rainfall recharge, and anthropogenic activities have not been achieved.

(4) The unsaturated zone and bedrock structure were not fully simulated and discussed through previous studies of TSWI, which may have posed large uncertainties on their simulation results and conclusions.

(5) It is necessary to plan for alternative water supply with an adequate amount and a safe quality for emergency uses during the days after the tsunami as well as for a long-term recovery period.

Therefore, this thesis is expected to have contributions with respect to:

(1) Chapter 4 provides numerical simulations of dense plume behavior in a hypothetical unconfined aquifer under various conditions of solute injection, aquifer properties, and horizontal groundwater flow, with the assumptions of constant boundary conditions and homogeneous media. In addition to plume stability, criteria

including streamline patterns and mass concentration distribution are considered for classification of flow patterns. A system integrating the modified dimensionless *Ra* and *M* are used for analyzing the flow regimes.

(2) Chapter 6 provides an example of predicting future TSWI at a tsunami-threatened island by using a 2-D modeling approach, in which the roles of unsaturated zone and bedrock structure are discussed. The impacts of model uncertainties including tsunami inundation conditions and aquifer properties are analyzed.

(3) Chapter 7 presents a 3-D model, in which the unpolluted portion of groundwater resources in the island is discovered and the feasibility of pumping this unpolluted groundwater for supplying freshwater in the post-disaster period is numerically tested.

CHAPTER 3: FUNDAMENTAL THEORY FOR NUMERICAL MODELING OF DENSITY-DRIVEN FLOW IN UNSATURATED-SATURATED MEDIA

3.1 Analytical Solution for Saltwater-Freshwater Interface

The earliest analyses of the saltwater-freshwater interface were carried out by Ghyben (1888) and Herzberg (1901), namely the famous Ghyben-Herzberg principle. Assuming simple hydrostatic conditions in a homogeneous, unconfined coastal aquifer (Figure 3.1a), the principle can be obtained as:

$$\rho_s z_s = \rho_f \left(z_s + z_w \right) \qquad \text{Eq 3.1}$$

or

$$z_s = \frac{\rho_f}{\rho_s - \rho_f} z_w \qquad \text{Eq 3.2}$$

where z_s is the depth of the interface below the datum; z_w is the elevation of the water table; ρ_s and ρ_f are the densities of seawater and freshwater, respectively.

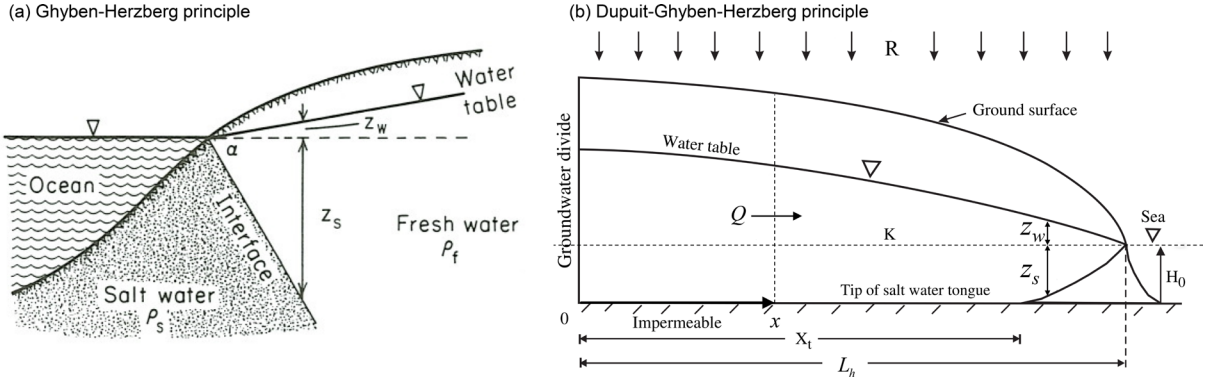

Figure 3.1 The saltwater-freshwater interface in a homogeneous, unconfined coastal aquifer: (a) the Ghyben-Herzberg principle (modified after Freeze and Cherry (1979)); (b) the Dupuit-Ghyben-Herzberg principle considering an impermeable bottom of the aquifer (modified after Guo and Jiao (2007)).

Consider a symmetrical cross-section for a homogeneous island with a horizontal impermeable bottom. Assuming that uniform vertical rainfall recharge *R* under the steady state condition (Figure 3.1b), the saltwater-freshwater interface interacts the aquifer bottom at x_t.

The total horizontal flux Q at the position x should be the same as the recharge in between x and the center of the island ($x = 0$), and hence, is given by

$$Q = Rx \qquad \text{Eq 3.3}$$

Assuming that the groundwater flow occurs horizontally, Q should be equal to the Darcy flux, and hence,

$$\begin{cases} Q = -K(H_0 + z_w)\dfrac{dz}{dx}, & 0 \le x \le x_t \\ Q = -K(z_s + z_w)\dfrac{dz}{dx}, & x_t \le x \le L_h \end{cases} \qquad \text{Eq 3.4}$$

where K is the hydraulic conductivity of the aquifer; H_0 is the depth of the impermeable bottom of the aquifer; and L_h is the distance from the groundwater divide to the coastline. By introducing the Ghyben-Herzberg principle (Eq 3.2) and equating Eq 3.3 and Eq 3.4 for Q, a Dupuit-type differential equation

$$\begin{cases} Rx = -K(H_0 + z_w)\dfrac{dz}{dx}, & 0 \le x \le x_t \\ Rx = -K\left(\dfrac{\rho_f}{\rho_s - \rho_f} + 1\right) z_w \dfrac{dz}{dx}, & x_t \le x \le L_h \end{cases} \qquad \text{Eq 3.5}$$

can be obtained, which is integrated into the form

$$\begin{cases} z_w = \sqrt{\dfrac{R}{K}\left(L_h^{\,2} - x^2\right) + \dfrac{\rho_s}{\rho_f} H_0^{\,2}} - H_0, & 0 \le x \le x_t \\ z_w = \sqrt{\dfrac{R}{K}\dfrac{\left(\rho_s - \rho_f\right)}{\rho_s}\left(L_h^{\,2} - x^2\right)}, & x_t \le x \le L_h \end{cases} \qquad \text{Eq 3.6}$$

which is known as the Dupuit-Ghyben-Herzberg (D-G-H) principle. The location of the tip of the saltwater tongue can be obtained as

$$x_t = \sqrt{L_h^{\,2} - \frac{K}{R}\frac{\left(\rho_s^{\,2} - \rho_s\rho_f\right)}{\rho_f^{\,2}} H_0^{\,2}} \qquad \text{Eq 3.7}$$

Instead of the description by a sharp interface between saltwater and freshwater, a more realistic image can be described by a transition zone where mixing of seawater and fresh groundwater occurs due to dispersion and diffusion. The benchmark Henry problem (Henry, 1964) delineated the development process of the saltwater-freshwater mixing zone in a confined aquifer which was initially saturated with freshwater (Figure 3.2a). The top and bottom of the domain were impermeable boundaries. Hydrostatic pressure with respect to seawater was assumed along the vertical boundary representing the seaside on the right, while the freshwater was recharged by the constant flux of which concentration to be zero from the left side. At the coastal side, the seawater concentration was imposed on the lower half of the vertical boundary, where was assumed that seawater can enter the aquifer and no freshwater exited. Henry (1964) developed a semi-analytical solution for the steady state condition for this problem, and obtained the concentration distribution as shown in Figure 3.2b. The Henry problem (Henry, 1964) has been widely used as a benchmark for validating the numerical models of saltwater-freshwater mixing zones (Abarca et al., 2007; Lee and Cheng, 1974; Pinder and Cooper, 1970; Segol et al., 1975; Yang et al., 2013). Since then, it has become common practice to utilize numerical modeling approaches to understand coastal groundwater processes, which have been introduced by many widely-used instrumental books (Bear et al., 1999; Zheng and Bennett, 2002).

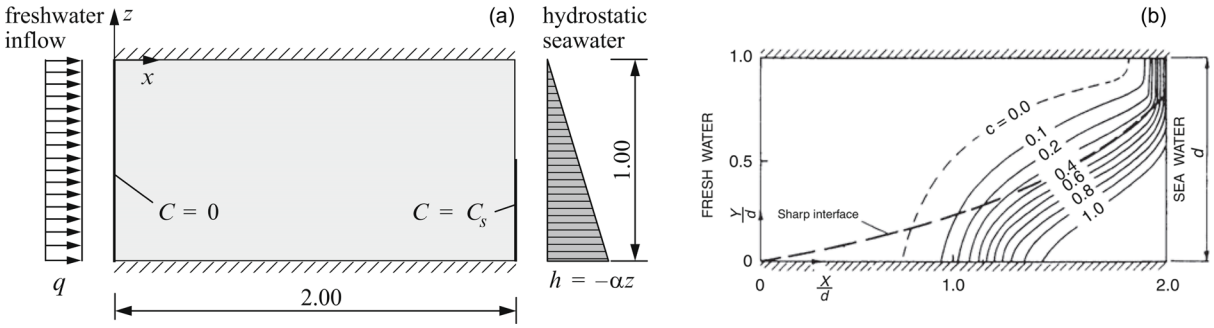

Figure 3.2 (a) Definition of the Henry problem; (b) Concentration distribution obtained by Henry (1964) from his semianalytical solution compared with the Ghyben-Herzberg solution of the sharp interface (modified after Diersch (2013)).

3.2 Governing Equations of Numerical Modeling

3.2.1 Heads in Groundwater for DDF

Lusczynski (1961) introduced the concepts of point-water head, fresh-water head, and environmental-water head, which have been useful in studying groundwater flow of variable-density environment. Point-water head H_p at any point *P* in groundwater of variable-density condition is defined as the water level measured from the datum in a well filled with the water at the assumed point to balance the pressure at the point (Figure 3.3a). From this definition,

$$H_p = \frac{p}{\rho g} + Z \qquad \text{Eq 3.8}$$

where *p* is the pressure at point *P*; ρ is the density of water at *P*; *g* is gravitational acceleration; and *Z* is the elevation of *P* measured positively upward.

Fresh-water head H_f at any point *P* in groundwater of variable-density condition is defined as the water level measured from the datum, in a well filled with freshwater to balance the pressure at the point (Figure 3.3b). From this definition,

$$H_f = \frac{p}{\rho_f g} + Z = \psi + Z \qquad \text{Eq 3.9}$$

where ψ is the pressure head at any point *P*.

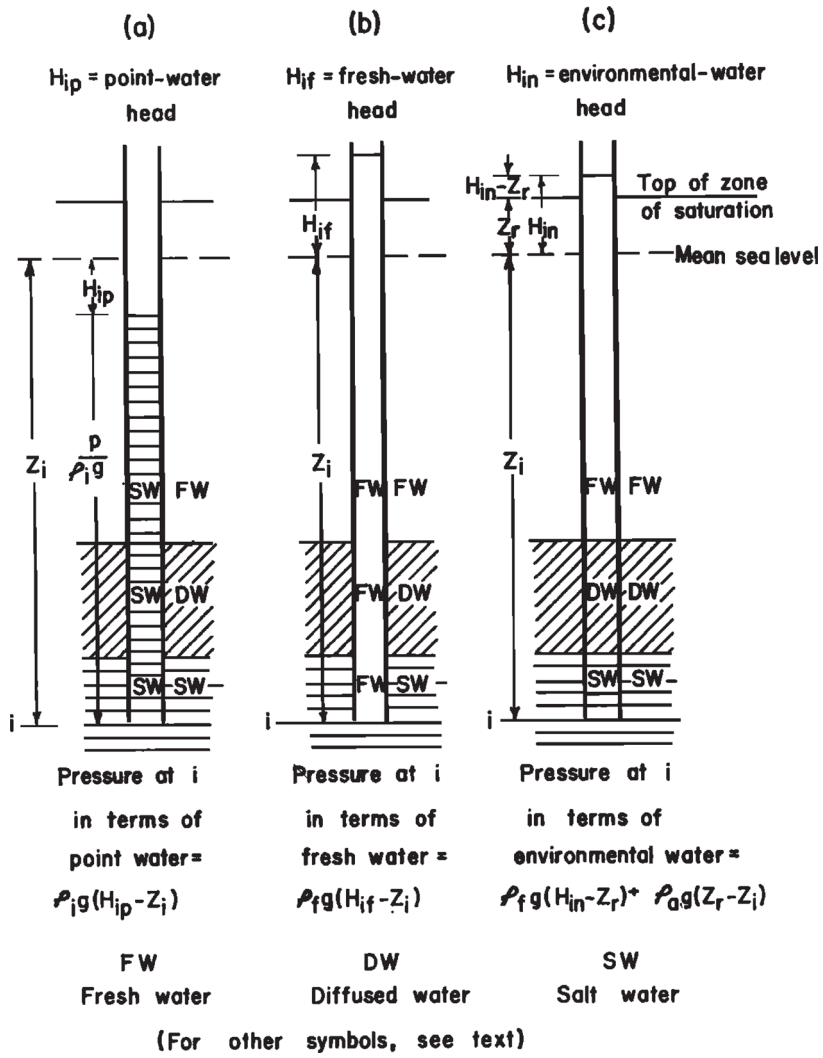

Figure 3.3 Heads in groundwater for variable-density condition modified after Lusczynski (1961).

Environmental-water head H_n at any point P in groundwater of variable-density condition is defined as a fresh-water head reduced by an amount corresponding to the difference of salt mass in freshwater and that in the environmental water between that point and the top of the zone of saturation (Figure 3.3c). From this definition,

$$H_n = H_f - \left(1 - \frac{\rho_a}{\rho_f}\right)\left(Z - Z_r\right) \qquad \text{Eq 3.10}$$

where ρ_a is the average density of water between Z_r and Z, as defined by

$$\rho_a = \frac{1}{Z - Z_r}\int_{Z}^{Z_r} \rho dz \qquad \text{Eq 3.11}$$

and Z_r is the elevation of reference point from which the average density of water to P is determined and above which water is fresh (elevation measured positively upward). When the reference point is the datum, $Z_r = 0$, Eq 3.10 becomes

$$H_n = H_f - Z\left(1 - \frac{\rho_a}{\rho_f}\right) \quad \text{Eq 3.12}$$

where

$$\rho_a = \frac{1}{Z}\int_0^Z \rho dz \quad \text{Eq 3.13}$$

The hydraulic gradient of Eq 3.8 is

$$\frac{\nabla p}{g} + \rho \mathbf{k} = \nabla\left(\rho H_p\right) - Z\nabla\rho \quad \text{Eq 3.14}$$

where ∇ is the gradient operator; and $\mathbf{k}$ is the unit vector directed upward along vertical. Inserting Eq 3.9, Eq 3.10, and Eq 3.11 to Eq 3.14, we can obtain

$$\rho_f \nabla H_n - Z\left(\frac{\partial(\rho_a)}{\partial x}\mathbf{i} + \frac{\partial(\rho_a)}{\partial y}\mathbf{j}\right) = \rho_f \nabla H_f + \left(\rho - \rho_f\right)\mathbf{k} \quad \text{Eq 3.15}$$

where **i** and **j** are the unit vectors normal to one another in a horizontal plane.

Darcy equation in homogenous material is written as

$$\boldsymbol{q} = -\frac{k}{\mu}\left(\nabla p + \rho g \mathbf{k}\right) \quad \text{Eq 3.16}$$

where $\boldsymbol{q}$ is the Darcy flux vector; k is the permeability; and μ is the viscosity.

Considering Eq 3.14 and Eq 3.15, the components of Darcy flux in Eq 3.16 can be written as

$$\begin{cases} q_x = -k_{xx}\dfrac{g}{\mu}\left(\rho_f \dfrac{\partial H_f}{\partial x}\right) - k_{xy}\dfrac{g}{\mu}\left(\rho_f \dfrac{\partial H_f}{\partial y}\right) - k_{xz}\dfrac{g}{\mu}\left(\rho_f \dfrac{\partial H_n}{\partial z}\right) \\ q_y = -k_{yx}\dfrac{g}{\mu}\left(\rho_f \dfrac{\partial H_f}{\partial x}\right) - k_{yy}\dfrac{g}{\mu}\left(\rho_f \dfrac{\partial H_f}{\partial y}\right) - k_{yz}\dfrac{g}{\mu}\left(\rho_f \dfrac{\partial H_n}{\partial z}\right) \\ q_z = -k_{zx}\dfrac{g}{\mu}\left(\rho_f \dfrac{\partial H_f}{\partial x}\right) - k_{zy}\dfrac{g}{\mu}\left(\rho_f \dfrac{\partial H_f}{\partial y}\right) - k_{zz}\dfrac{g}{\mu}\left(\rho_f \dfrac{\partial H_n}{\partial z}\right) \end{cases} \quad \text{Eq 3.17}$$

where q_x, q_y, and q_z are the components of Darcy flux along the x, y, and z coordinates, respectively.

When *x* and *y* are horizontal, *z* is vertical, and when the coordinates coincide with the axes of the principal directional permeabilities, Eq 3.17 can be simplified to

$$\begin{cases} q_x = -k_x \dfrac{g}{\mu}\left(\rho_f \dfrac{\partial H_f}{\partial x}\right) \\ q_y = -k_y \dfrac{g}{\mu}\left(\rho_f \dfrac{\partial H_f}{\partial y}\right) \\ q_z = -k_z \dfrac{g}{\mu}\left(\rho_f \dfrac{\partial H_n}{\partial z}\right) \end{cases} \quad \text{Eq 3.18}$$

Replacing the environmental-water head H_n in Eq 3.18 with the fresh-water head H_f by introducing Eq 3.10, we can obtain

$$\begin{cases} q_x = -k_x \dfrac{\rho_f g}{\mu}\dfrac{\partial H_f}{\partial x} \\ q_y = -k_y \dfrac{\rho_f g}{\mu}\dfrac{\partial H_f}{\partial y} \\ q_z = -k_z \dfrac{\rho_f g}{\mu}\left(\dfrac{\partial H_f}{\partial z} + \dfrac{\rho_a}{\rho_f} - 1\right) \end{cases} \quad \text{Eq 3.19}$$

Considering hydraulic conductivity $K = \rho_f g k / \mu$, Eq 3.19 becomes

$$\begin{cases} q_x = -K_x \dfrac{\partial H_f}{\partial x} \\ q_y = -K_y \dfrac{\partial H_f}{\partial y} \\ q_z = -K_z \left(\dfrac{\partial H_f}{\partial z} + \dfrac{\rho_a}{\rho_f} - 1 \right) \end{cases} \qquad \text{Eq 3.20}$$

Eq 3.20 defines the components of Darcy flux by using fresh-water head, which will contribute to the derivation of governing equation for variable-density, unsaturated-saturated flow and mass transport in the following sections.

3.2.2 Parameters for Variably Saturated Porous Media

An unsaturated media is defined as a zone where the wetting phase (usually water) has a saturation less than 100%. As shown in Figure 3.4a, the macroscopic representation of the equilibrium with the pressure difference between adjacent nonwetting and wetting fluid phases at the interface of the two fluids in the void space of a porous medium is recorded by the capillary pressure head ψ, as defined as in Table 3.1, where *s* is the saturation (fluid volume per void volume), s_r is the residual saturation (fluid volume per void volume when $ds/d\psi = 0$ with $s < 1$), and K^r is the relative permeability.

Table 3.1 Unsaturated versus saturated porous media conditions.

Unsaturated media	Saturated media
$\psi < 0$, $\psi = \psi(s)$, $s_r < s < 1$	$\psi \geq 0$, $s = 1$
$K^r = K^r(s)$	$K^r = 1$

Typical relations in the form of retention $\psi = \psi(s)$ and $K^r = K^r(s)$ are depicted in Figure 3.4b. The relation between hydraulic conductivity for unsaturated (K) and saturated media (K^s) can be expressed as

$$K = K^s K^r(s) \qquad \text{Eq 3.21}$$

The present thesis introduced the van Genuchten model (van Genuchten, 1980) for variably-saturated porous media. The van Genuchten model defines effective saturation s_e

$$s_e = \left(\frac{s - s_r}{s_s - s_r} \right) = \begin{cases} \left[1 + \left(-\alpha \psi \right)^n \right]^{-m} & , \psi < 0 \\ 1 & , \psi \geq 0 \end{cases} \quad \text{Eq 3.22}$$

and

$$K^r = s_e^{0.5} \left[1 - \left(1 - s_e^{\frac{1}{m}} \right)^m \right]^2 \quad \text{Eq 3.23}$$

where s_s is maximum saturation (i.e., $s = 1$); α is the fitting parameter; n is the pore size distribution index; m is the fitting parameters, and $m = 1 - 1/n$.

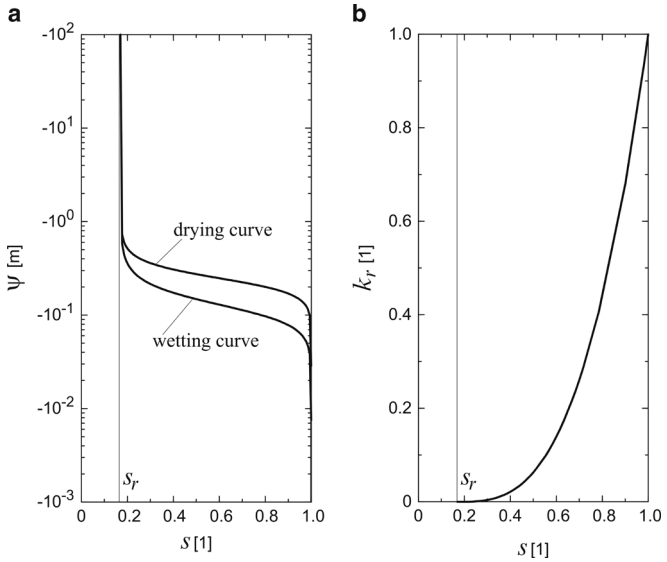

Figure 3.4 Typical plots of (a) retention cure, and (b) relative permeability curve (Diersch, 2013).

3.2.3 Governing Equations for Fluid Flow

At microscopic level, groundwater flows through small pore openings in soil. However, in order to make the quantities measurable, the microscopic process should be scaled up to macroscopic level. Figure 3.5 illustrates a hypothetical plot of the porosity of a porous media as it may be measured on samples of increasing volume V_1, V_2,… (Hubbert, 1940), and V_3 was defined as the representative elementary volume (REV) (Bear, 1972). The REV is the volume

that must be larger than a single pore and include a sufficient number of pores to permit the meaningful statistical average required at macroscopic level (Freeze and Cherry, 1979).

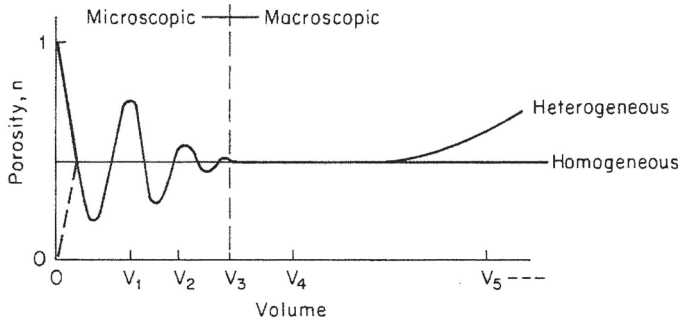

Figure 3.5 Microscopic and macroscopic domains and the representative elementary volume V_3 (Freeze and Cherry, 1979).

Simulation of groundwater flow through porous media can be attained by assuming mass conservation through a series of REVs. Essentially, an influx of mass into an REV must be equivalent to the sum of the outflux mass and changes in storage (Figure 3.6).

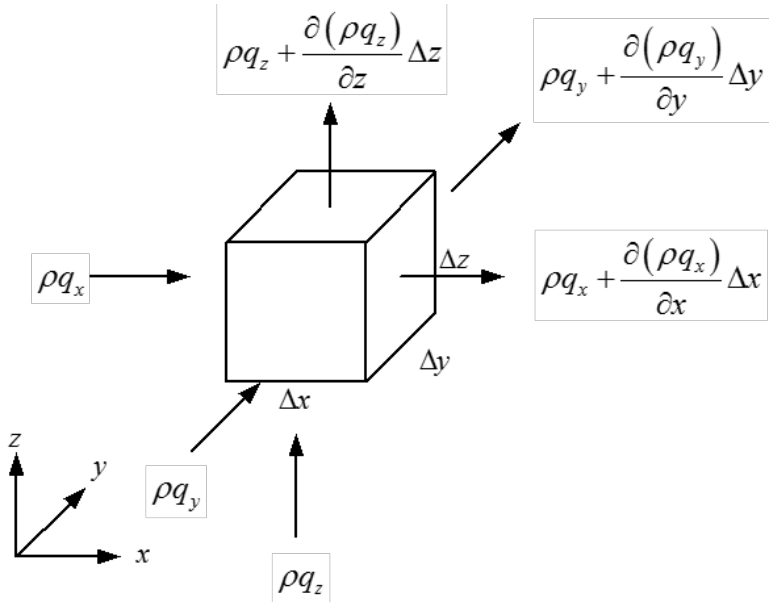

Figure 3.6 Representative elementary volume (REV).

The equation of continuity, shown in Figure 3.6, can be written as

$$\frac{\partial}{\partial t}(\rho \varepsilon s) + \frac{\partial \rho q_x}{\partial x} + \frac{\partial \rho q_y}{\partial y} + \frac{\partial \rho q_z}{\partial z} = 0 \qquad \text{Eq 3.24}$$

where ε is the porosity; and t is the time.

Introducing the volumetric water content $\theta = \varepsilon s$ and combining Eq 3.9, Eq 3.20 and Eq 3.24, we can obtain

$$\frac{\partial}{\partial t}(\rho\theta) = \frac{\partial}{\partial x}\left(\rho K_x \frac{\partial \psi}{\partial x}\right) + \frac{\partial}{\partial y}\left(\rho K_y \frac{\partial \psi}{\partial y}\right) + \frac{\partial}{\partial z}\left[\rho K_z \left(\frac{\partial \psi}{\partial z} + \frac{\rho_a}{\rho_f}\right)\right] \qquad \text{Eq 3.25}$$

where $\frac{\partial}{\partial t}(\rho\theta)$ can be written as

$$\frac{\partial}{\partial t}(\rho\theta) = \theta\frac{\partial \rho}{\partial t} + \rho\frac{\partial \theta}{\partial t} \qquad \text{Eq 3.26}$$

Suppose a linear concentration-density relationship is hold as

$$\rho = \rho_f\left(1 + \chi_s \frac{c - c_f}{c_m - c_f}\right) \qquad \text{Eq 3.27}$$

where $\chi_s = \left(\rho_s - \rho_f\right)/\rho_f$ is the fluid density ratio between the seawater and freshwater, c is the mass concentration of fluid, c_f is the mass concentration of freshwater, c_m is the mass concentration of seawater. Then, the terms in the right-hand side of the Eq 3.26 becomes

$$\theta\frac{\partial \rho}{\partial t} = \theta\frac{\partial\left[\rho_f\left(1 + \chi_s \frac{c - c_f}{c_m - c_f}\right)\right]}{\partial t} = \frac{\rho_f \theta \chi_s}{c_m - c_f}\frac{\partial c}{\partial t} \qquad \text{Eq 3.28}$$

and

$$\rho\frac{\partial \theta}{\partial t} = \rho\frac{d\theta}{d\psi}\frac{\partial \psi}{\partial t} = \rho\frac{d(\varepsilon s)}{d\psi}\frac{\partial \psi}{\partial t} = \rho\left(s\frac{d\varepsilon}{d\psi} + \varepsilon\frac{ds}{d\psi}\right)\frac{\partial \psi}{\partial t} \qquad \text{Eq 3.29}$$

respectively.

For unsaturated flow, since the coupling of deformation of soil is not considered in the present problem, it is assumed that $d\varepsilon / d\psi = 0$. For saturated flow (s = 1), the specific storage coefficient $S_s = ds / d\psi$ becomes constant. Therefore, Eq 3.29 can be written as

$$\rho\left(s\frac{d\varepsilon}{d\psi}+\varepsilon\frac{ds}{d\psi}\right)\frac{\partial\psi}{\partial t}=\rho\left[C_s(\theta)+\beta S_s\right]\frac{\partial\psi}{\partial t} \qquad \text{Eq 3.30}$$

where $C_s(\theta)=\partial\theta/\partial\psi$ is the specific moisture capacity, and

$$\beta=\begin{cases}1, & s=1\\ 0, & s<0\end{cases} \qquad \text{Eq 3.31}$$

Inserting Eq 3.28 and Eq 3.30 to Eq 3.26, the equation can be rewritten as

$$\frac{\partial}{\partial t}(\rho\theta)=\frac{\rho_f\theta\chi_s}{c_m-c_f}\frac{\partial c}{\partial t}+\rho\left[\beta S_s+C_s(\theta)\right]\frac{\partial\psi}{\partial t} \qquad \text{Eq 3.32}$$

Inserting Eq 3.32 and Eq 3.21 into the mass balance Eq 3.25, the governing equation for variable-density, unsaturated-saturated fluid flow can be obtained as

$$\begin{aligned}\frac{\rho_f\theta\chi_s}{c_m-c_f}\frac{\partial c}{\partial t}+\rho\left[\beta S_s+C_s(\theta)\right]\frac{\partial\psi}{\partial t}=&\frac{\partial}{\partial x}\left(\rho K_x{}^s K^r(s)\frac{\partial\psi}{\partial x}\right)\\ &+\frac{\partial}{\partial y}\left(\rho K_y{}^s K^r(s)\frac{\partial\psi}{\partial y}\right)\\ &+\frac{\partial}{\partial z}\left[\rho K_z{}^s K^r(s)\left(\frac{\partial\psi}{\partial z}+\frac{\rho_a}{\rho_f}\right)\right]\end{aligned} \qquad \text{Eq 3.33}$$

3.2.4 Governing Equations for Mass Transport

An equation for advective transport can be obtained by considering an REV shown in Figure 3.7.

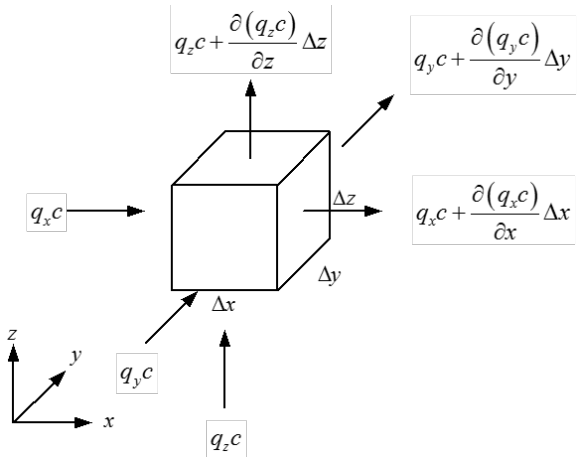

Figure 3.7 REV for development of the advective transport equation.

Applying the mass balance concept used in developing Eq 3.24, the total net inflow minus outflow of solute mass for the REV by advection can be expressed as

$$-\left[\frac{\partial}{\partial x}(q_x c)+\frac{\partial}{\partial y}(q_y c)+\frac{\partial}{\partial z}(q_z c)\right]\Delta x\Delta y\Delta z \qquad \text{Eq 3.34}$$

The rate of accumulation of solute mass within the REV is given by $\Delta x\Delta y\Delta z\partial(\theta c)/\partial t$. Equating this rate of accumulation to the expression in term Eq 3.34 yields

$$-\frac{\partial}{\partial x}(q_x c)-\frac{\partial}{\partial y}(q_y c)-\frac{\partial}{\partial z}(q_z c)=\frac{\partial(\theta c)}{\partial t} \qquad \text{Eq 3.35}$$

where it is assumed that any change in the volume of water within the element $\Delta x\Delta y\Delta z$ can be neglected.

In addition to the advective transport described by term Eq 3.34, some mixing or dilution of solute occurs due to the variations in flow velocity, and it is called dispersive process. The microscopic dispersive processes are understood by considering flow within a single pore as shown in Figure 3.8a. The velocity increases from near the pore wall to the centerline of the pore. Also, the flow in a porous medium is tortuous around the grains, which leads to velocity variation (Figure 3.8b). Each fluid particle must experience a sequence of velocities as it moves through the porous media, which results in the variation in position and travel time of particles, as illustrated by the tracer movement in Figure 3.8c. As shown in Figure 3.8d, the tracer transport problem is the combination of (1) advective transport which advances the tracer at the average linear velocity vector and (2) dispersive transport which causes the spreading of tracer in both transversely and longitudinally.

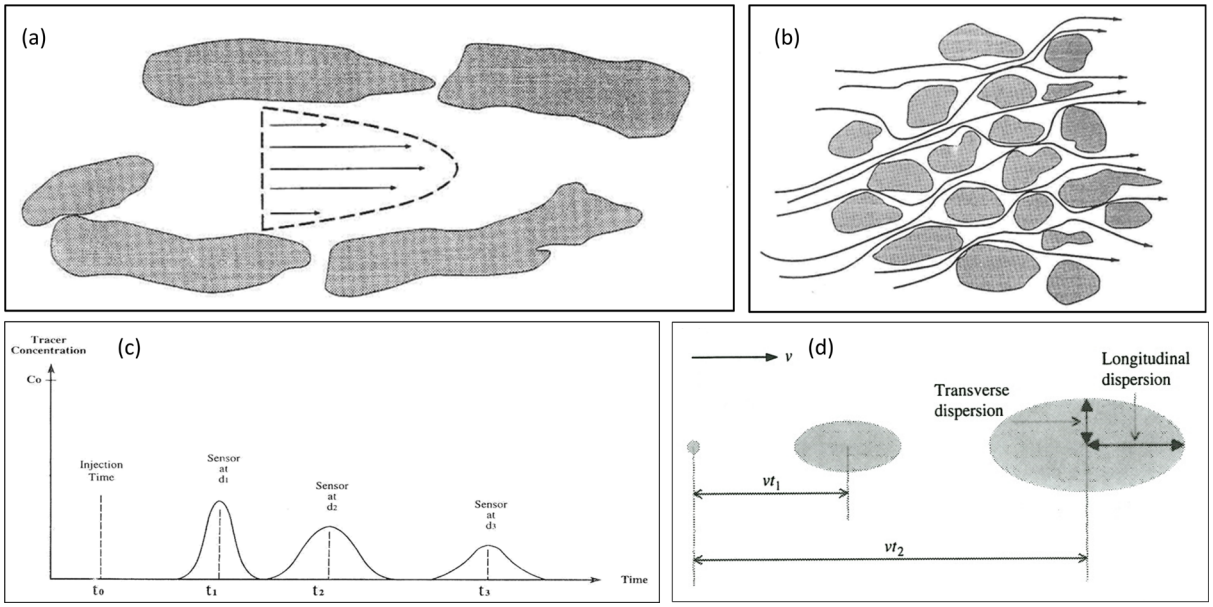

Figure 3.8 (a) Schematic figure showing theoretical variation of velocity within an individual pore; (b) Schematics showing tortuous branching and reconnection of microscopic flow path in a porous media; (c) Results of tracer movement; (d) Tracer transport showing as the sum of advective and dispersive components. Figures were modified after Zheng and Bennett (2002).

It is noted that dispersive transport includes the combined effect of both mechanical dispersion and molecular diffusion, which is described by the dispersion coefficient tensor D_{ij} (Zheng and Bennett, 2002):

$$\begin{cases} D_{xx} = \alpha_L \dfrac{v_x^2}{|v|} + \alpha_T \dfrac{v_y^2}{|v|} + \alpha_T \dfrac{v_z^2}{|v|} + D_d \\ D_{yy} = \alpha_L \dfrac{v_y^2}{|v|} + \alpha_T \dfrac{v_x^2}{|v|} + \alpha_T \dfrac{v_z^2}{|v|} + D_d \\ D_{zz} = \alpha_L \dfrac{v_z^2}{|v|} + \alpha_T \dfrac{v_x^2}{|v|} + \alpha_T \dfrac{v_y^2}{|v|} + D_d \\ D_{xy} = D_{yx} = (\alpha_L - \alpha_T) \dfrac{v_x v_y}{|v|} \\ D_{xz} = D_{zx} = (\alpha_L - \alpha_T) \dfrac{v_x v_z}{|v|} \\ D_{yz} = D_{zy} = (\alpha_L - \alpha_T) \dfrac{v_y v_z}{|v|} \end{cases} \quad \text{Eq 3.36}$$

where α_L and α_T are longitudinal and transverse dispersivities, respectively; the average linear velocity vector $\boldsymbol{v}$ is defined as $\boldsymbol{v} = v_x\mathbf{i} + v_y\mathbf{j} + v_y\mathbf{k}$ and $|\boldsymbol{v}| = \sqrt{{v_x}^2 + {v_y}^2 + {v_y}^2}$; and D_d is the coefficient of molecular diffusion for the solute in porous medium.

Gelhar et al. (1992) suggested that there is a trend of increase of the longitudinal dispersivity along with the increase of observation scale (Figure 3.9).

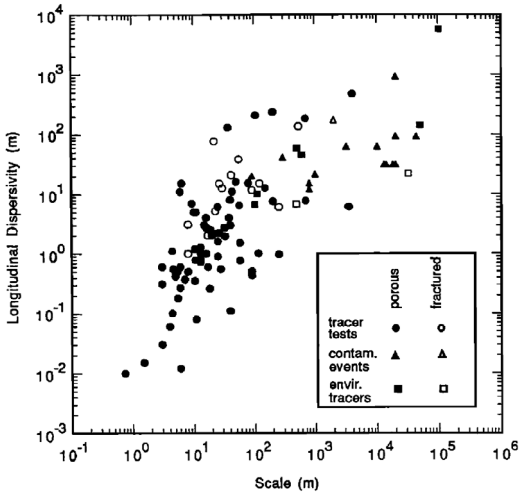

Figure 3.9 Longitudinal dispersivity versus scale of observation reported by Gelhar et al. (1992).

Equations for the components of the dispersive flux W_i can be expressed as

$$\begin{pmatrix} W_x \\ W_y \\ W_z \end{pmatrix} = -\begin{pmatrix} D_{xx} & D_{xy} & D_{xz} \\ D_{yx} & D_{yy} & D_{yz} \\ D_{zx} & D_{zy} & D_{zz} \end{pmatrix} \begin{pmatrix} \dfrac{\partial c}{\partial x} \\ \dfrac{\partial c}{\partial y} \\ \dfrac{\partial c}{\partial z} \end{pmatrix} \qquad \text{Eq 3.37}$$

Using Eq 3.37, the dispersive transport in x direction in terms of mass per unit time is given by

$$W_x \theta \Delta y \Delta z = -\left(D_{xx}\frac{\partial c}{\partial x} + D_{xy}\frac{\partial c}{\partial y} + D_{xz}\frac{\partial c}{\partial z} \right)\theta \Delta y \Delta z \qquad \text{Eq 3.38}$$

The difference between inflow and outflow of mass due to dispersion in x, y, and z direction for $\Delta x \Delta y \Delta z$ is given, respectively

$$\begin{cases} \dfrac{\partial}{\partial x}\left(\varepsilon D_{xx}\dfrac{\partial c}{\partial x}+\varepsilon D_{xy}\dfrac{\partial c}{\partial y}+\varepsilon D_{xz}\dfrac{\partial c}{\partial z}\right)\Delta x\Delta y\Delta z \\ \dfrac{\partial}{\partial y}\left(\varepsilon D_{yx}\dfrac{\partial c}{\partial x}+\varepsilon D_{yy}\dfrac{\partial c}{\partial y}+\varepsilon D_{yz}\dfrac{\partial c}{\partial z}\right)\Delta x\Delta y\Delta z \\ \dfrac{\partial}{\partial z}\left(\varepsilon D_{zx}\dfrac{\partial c}{\partial x}+\varepsilon D_{zy}\dfrac{\partial c}{\partial y}+\varepsilon D_{zz}\dfrac{\partial c}{\partial z}\right)\Delta x\Delta y\Delta z \end{cases} \quad \text{Eq 3.39}$$

When x and y are horizontal, z is vertical, and when the coordinates coincide with the axes of the principal directional dispersive flux. By summing up the advective terms Eq 3.34 and dispersive terms Eq 3.39, the rate of solute mass accumulation in the volume, $\Delta x\Delta y\Delta z\partial(\theta c)/\partial t$, is equated as

$$\begin{aligned} \frac{\partial(\theta c)}{\partial t} &= \frac{\partial}{\partial x}\left(\theta D_x\frac{\partial c}{\partial x}\right)-\frac{\partial}{\partial x}(q_x c) \\ &+\frac{\partial}{\partial y}\left(\theta D_y\frac{\partial c}{\partial y}\right)-\frac{\partial}{\partial y}(q_y c) \\ &+\frac{\partial}{\partial z}\left(\theta D_z\frac{\partial c}{\partial z}\right)-\frac{\partial}{\partial z}(q_z c) \end{aligned} \quad \text{Eq 3.40}$$

For the mass transport in the unsaturated zone, the moisture content θ in Eq 3.40 is replaced by $\theta = \varepsilon s$, and by introducing Eq 3.20, the Eq 3.40 becomes

$$\begin{aligned} \frac{\partial(\varepsilon s c)}{\partial t} &= \frac{\partial}{\partial x}\left(\varepsilon s D_x\frac{\partial c}{\partial x}\right)+\left(K_x\frac{\partial H_f}{\partial x}\right)\frac{\partial c}{\partial x} \\ &+\frac{\partial}{\partial y}\left(\varepsilon s D_y\frac{\partial c}{\partial y}\right)+\left(K_y\frac{\partial H_f}{\partial y}\right)\frac{\partial c}{\partial y} \\ &+\frac{\partial}{\partial z}\left(\varepsilon s D_z\frac{\partial c}{\partial z}\right)+K_z\left(\frac{\partial H_f}{\partial z}+\frac{\rho_a}{\rho_f}-1\right)\frac{\partial c}{\partial z} \end{aligned} \quad \text{Eq 3.41}$$

which is the equation to be solved for the advective-dispersive processes in unsaturated-saturated media.

3.3 General Descriptions of Boundary Conditions (BCs) and Initial Conditions (ICs)

The BCs required for solving the fluid flow problem include Dirichlet-type (1st kind) BCs which applies a pre-defined constant hydraulic head h_c at any given time as

$$h = h_c \qquad \text{Eq 3.42}$$

In the case of the seabed boundary or the boundary under tsunami inundation, the piezometric head related to seawater $h_s = p / \rho_s g + z$ has to be transferred into the hydraulic head *h*. To accomplish this, the equivalent hydraulic head derived from Eq 3.12 is introduced for Eq 3.42:

$$h = h_s + \chi_s \left(h_s - z \right) \qquad \text{Eq 3.43}$$

A seepage face is defined as a boundary where the flow can freely drain out from the saturated porous medium. This seepage face definition can be applied to the case that some intruded saltwater may discharge out through the land surface immediately after tsunami water retreats back to the sea. Since a seepage face is exposed to the atmosphere, p = 0 is set. The seepage face BC is activated only under the condition of outflow ($Q_n < 0$), where Q_n is the integral boundary balance flux of liquid summed-up at discrete points to which the corresponding boundary values are related. Therefore, the seepage BC can be written as

$$\begin{cases} p = 0 \\ Q_n < 0 \end{cases} \qquad \text{Eq 3.44}$$

In order to specify the boundary flux such as recharge by rainfall, Neumann-type (2nd kind) BCs are introduced as

$$q = q_p \qquad \text{Eq 3.45}$$

where q_p is the prescribed fluxes.

For mass transport, Dirichlet-type BCs are introduced

$$C = C_c \qquad \text{Eq 3.46}$$

which assigns a fixed mass concentration C_c at a boundary, such as the groundwater recharge boundary or the seabed boundary. In addition, as discussed by Smith (2004), this fixed mass

concentration BC at seabed should be switched off in the case of outflow ($Q_n < 0$). Therefore, a system-dependent mass transport BC at seabed can be better specified as

$$\begin{cases} C = C_c \\ Q_n > 0 \end{cases} \quad \text{Eq 3.47}$$

The ICs required for transient fluid flow and mass transport problems are, respectively:

$$h = h_0 \quad \text{Eq 3.48}$$

$$s = s_0 \quad \text{Eq 3.49}$$

and

$$c = c_0 \quad \text{Eq 3.50}$$

where h_0, s_0 and c_0 are known spatially varying functions of initial distribution at initial time $t = 0$.

3.4 Criteria for Model Discretization

In order to avoid numerical oscillations, the spatial discretization should make the element size fine enough to keep the mesh Peclet number $Pe_m < 4$ (Voss and Souza, 1987), where the mesh Peclet number is defined as

$$Pe_m = \frac{|v| \Delta_s L}{D_d + \alpha_L |v|} \quad \text{Eq 3.51}$$

where $|v|$ is the magnitude of local velocity; $\Delta_s L$ is the local distance between sides of an element measured along the local flow direction. When, as in most field cases, the coefficient of molecular diffusion D_d is small relative to mechanical dispersion, and the mesh Peclet number is

$$Pe_m \approx \frac{\Delta l}{\alpha_L} \quad \text{Eq 3.52}$$

where Δl is mesh size. Pe_m can be used as the criteria to estimate the mesh size while planning for model discretization.

3.5 Numerical Modeling Code

The numerical code FEFLOW (Diersch, 2013) was chosen here because it is capable of simulating transient processes of DDF in unsaturated-saturated porous media, and has been previously used in studying saltwater-freshwater mixing zone in coastal aquifers (Hu et al., 2008; Smith, 2004) and density-driven fingering phenomenon (Liu et al., 2015; Xie et al., 2010). Based on continuum mechanics, a conceptual model can be developed with a numerical model possessing balance statements for physical quantities and a set of constitutive relations (Figure 3.10). FEFLOW employs the finite element method to solve the numerical model. FEFLOW can closely work with ArcGIS, which was very useful in organizing hydrogeological data, creating numerical model and analyzing simulations results. The user-friendly interface of FEFLOW works efficiently for assigning ICs, BCs, and media properties and virtualizing simulations results. Additional information about FEFLOW is available at the website http://www.feflow.com.

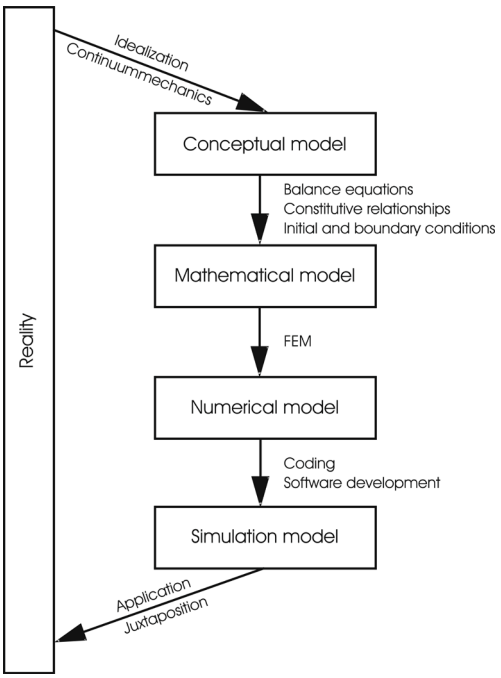

Figure 3.10 Stages of model development using the code FEFLOW (Diersch, 2013).

3.6 Validation of the FEFLOW Code (Modeling Sandbox Experiments)

Modeling approach taken in this thesis was validated in FEFLOW environment by comparing numerical simulations with existing sandbox experiments. Two sandbox experiments were selected: Sandbox Experiment I by Simmons et al. (2002): sinking plume with the static water table, and Sandbox Experiments II by Hogan (2006): sinking plume with horizontal groundwater flow.

3.6.1 Sandbox Experiment I (Sinking Plume with Static Water Table)

Simmons et al. (2002) carried out laboratory experiments of DDF in unsaturated-saturated porous media. In this sandbox experiment, a static water table without horizontal water flow was maintained by keeping the same water head at both sides of the sandbox, while the $CaCl_2$ solution was injected at a constant rate from the top of the porous media (Figure 3.11a). In the present thesis, FEFLOW code was applied to develop a 2-D model for simulating this sandbox experiment. The whole model domain was discretized into 99,852 quadrilateral elements with grid cell size of 0.38 cm, which fulfilled $Pe_m < 4$. Figure 3.11b illustrates the model domain and BCs corresponding to Sandbox Experiment I. Detailed parameters of Sandbox Experiment I and the 2-D numerical model by FEFLOW are summarized in Table 3.2.

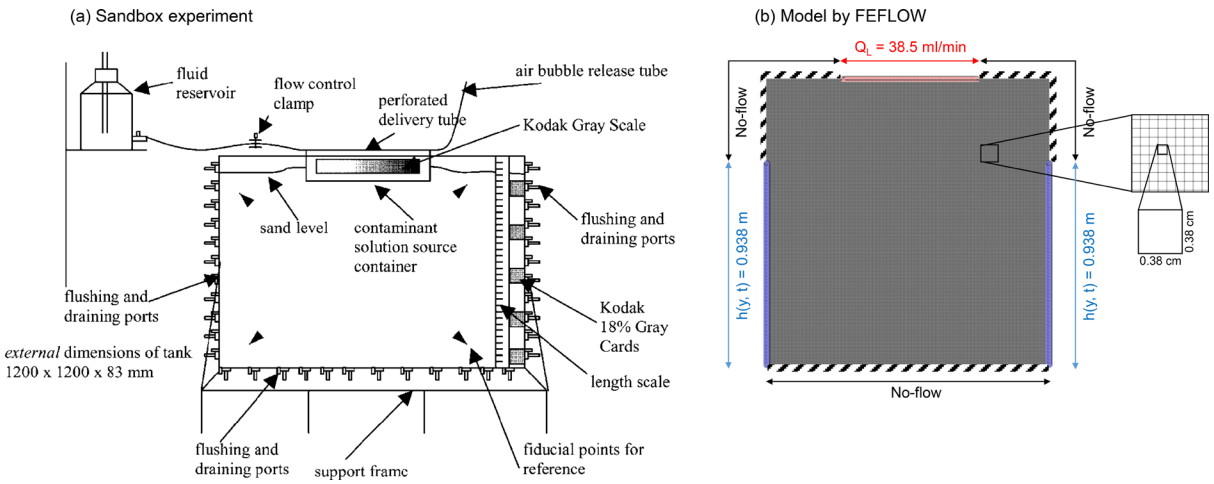

Figure 3.11 (a) Setups of Sandbox Experiment I (Simmons et al., 2002); (b) Model domain and BCs using FEFLOW.

Table 3.2 Summary of parameters of Sandbox Experiment I and numerical model by FEFLOW.

Parameter	Value	Parameter	Value
Hydraulic conductivity	106 m/d	Parameters for van Genuchten model	
Porosity	0.36	Residual saturation (s_r)	0.0025
Loading rate (Q_L)	38.5 mL/min	Maximum saturation (s_s)	1
Mass concentration of injected solution ($CaCl_2$)	62.61 mg/L	Fitting parameters α	57 1/m
Constant head BCs	0.938 m	Fitting parameters n	1.3

Figure 3.12 compares the results by Sandbox Experiment I with the corresponding numerical modeling results by FEFLOW. The modeling results relatively well reproduced the plume migration in the unsaturated zone. However, some discrepancy was observed between the actual and modeled fingering patterns in the saturated zone, which may due to the heterogeneity of the sand material.

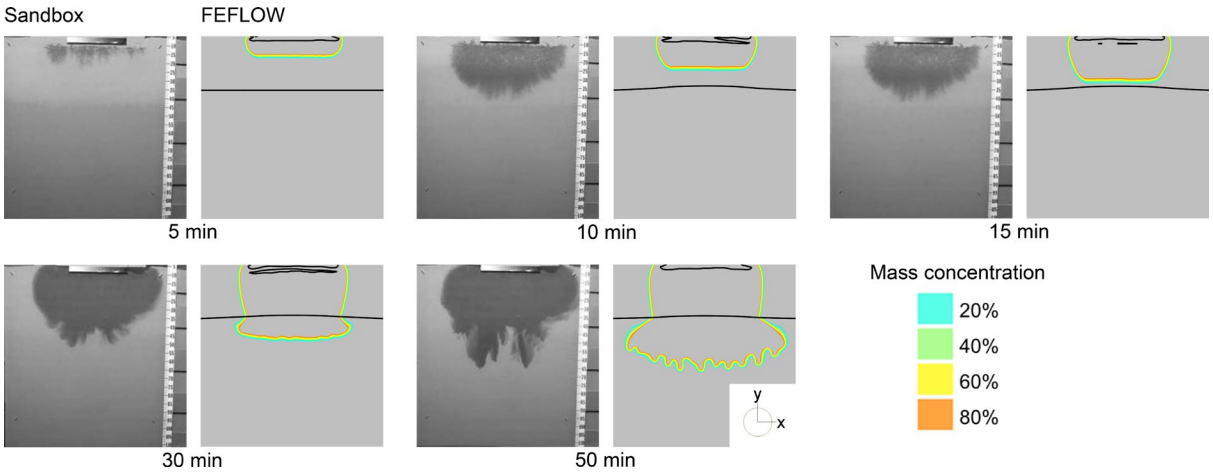

Figure 3.12 Comparisons between Sandbox Experiment I and FEFLOW modeling results (black line indicating the water table or the line of pressure zero).

3.6.2 Sandbox Experiment II (Sinking Plume with Lateral Water Flow)

The Sandbox Experiment II by Hogan (2006) (Figure 3.13a) considered the horizontal groundwater flow created by the hydraulic head gradient between two sides of the sandbox. A numerical model was developed by using the FEFLOW code for modeling this physical experiment. The domain of sandbox was discretized into 39,642 triangular elements of near 0.4 cm in element size, where the elements near the injection source were refined into the size

of about 0.2 cm, which ensured $Pe_m < 4$. Figure 3.13 (b) illustrates the model domain and BCs corresponding to Sandbox Experiment II. Table 3.3 summarizes the setups of the sandbox experiment and the corresponding numerical model parameters. The model was run for a simulation time of 60 mins.

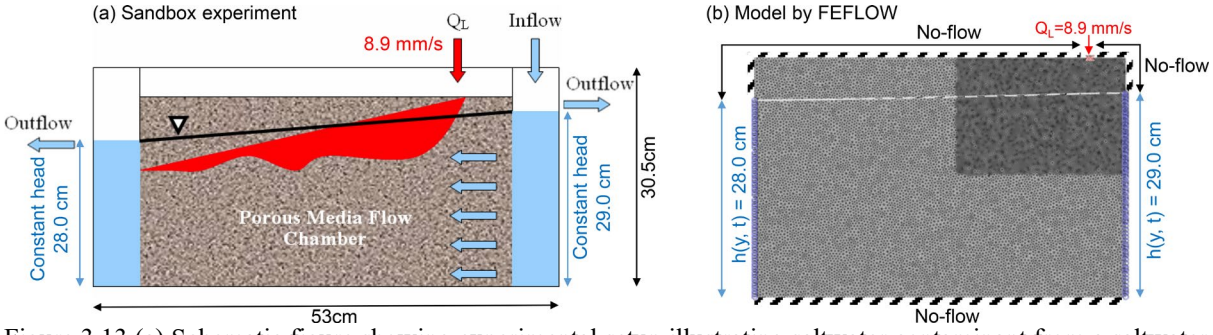

Figure 3.13 (a) Schematic figure showing experimental setup illustrating saltwater contaminant from a saltwater plume infiltrating into a porous medium (modified after Hogan, 2006); (b) Model domain and BCs by FEFLOW for simulating the sandbox experiments (white line indicating the water table).

Table 3.3 Summary of sandbox experiment setups and parameters in FEFLOW model.

Parameter	**Value**	**Parameter**	**Value**
Hydraulic conductivity	1130 m/d	Parameters for van Genuchten model	
Porosity	0.385	Residual saturation (s_r)	0.079
Loading rate (Q_L)	8.9 mm/s	Maximum saturation (s_s)	1
Density of injected saltwater (NaCl)	1025 mg/L	Fitting parameters α	15.2 1/m
Constant head BCs (H_L)	28.0 cm	Fitting parameters n	7.5
Constant head BSs (H_R)	28.8 cm		

In Figure 3.14, the numerical solution obtained from FEFLOW are illustrated next to photographs of the physical experiments by Hogan (2006). The modeling results showed a reasonable match with the sinking saltwater plume movement observed from the sandbox experiments.

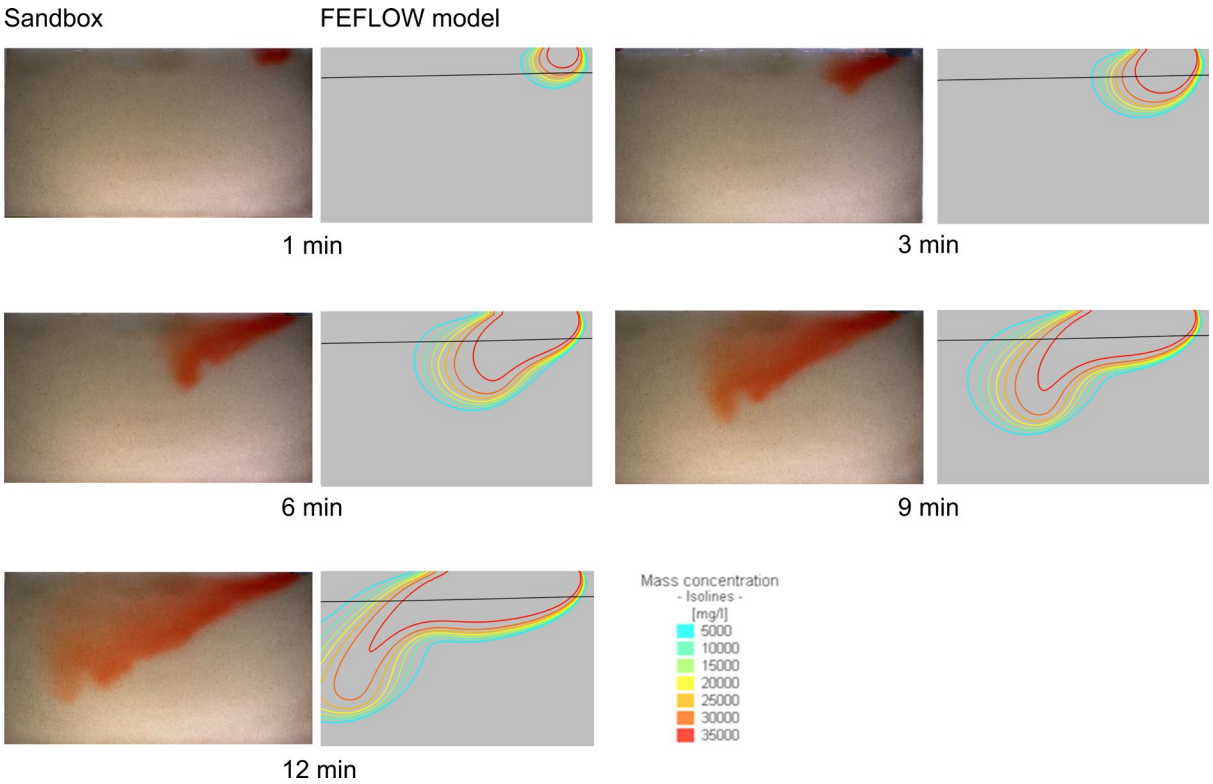

Figure 3.14 Comparison between Sandbox Experiment II and FEFLOW modeling results (black line indicating the water table or the line of pressure zero).

CHAPTER 5: THE STUDY SITE: THE NIIJIMA ISLAND, JAPAN[1]

5.1 Location and Climate

The Niijima Island is situated at around 150 km south of Tokyo, Japan (Figure 5.1a). It has a land area of about 24 km^2 with its north-south distance of around 11.5 km and east-west distance of around 2.5 km (Niijima Village Office, 2015). The Niijima Island has a warm and temperate climate characterized by the average annual temperature of 17.7 °C with the highest monthly temperature in August (26.4 °C) and the lowest in February (9.1 °C) (Niijima Village Office, 2015) (Figure 5.2). The average annual rainfall on the island is 2207 mm (Japan Meteorological Agency, 2017).

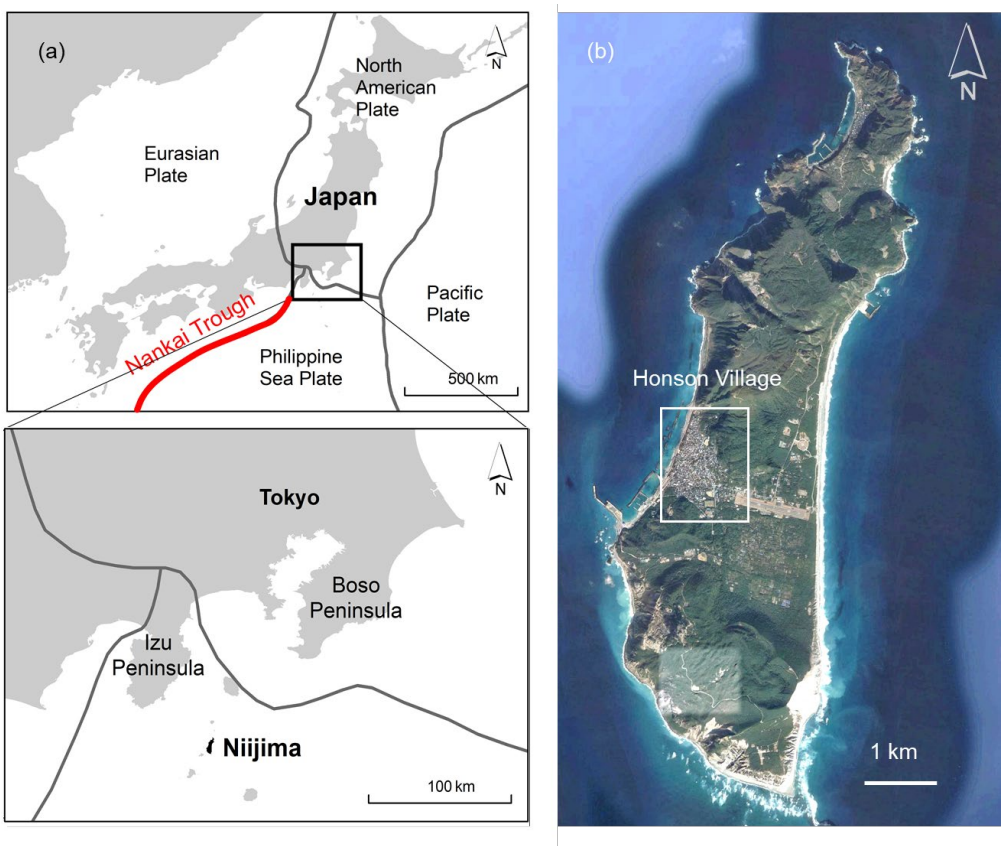

Figure 5.1 (a) A location map of the Niijima Island; (b) Satellite image of Niijima Island showing the location of the Honson Village (by Google Earth).

[1] The content of chapter appears in: a) Liu, J., & Tokunaga, T. (2019). Future Risks of Tsunami - Induced Seawater Intrusion Into Unconfined Coastal Aquifers: Insights From Numerical Simulations at Niijima Island, Japan. *Water Resources Research*, 55. https://doi.org/10.1029/2019WR025386 and b) Liu, J., & Tokunaga, T. (2020). 3D modeling of tsunami-induced seawater intrusion and aquifer recovery in Niijima Island, Japan, under the future tsunami scenario. *Journal of Groundwater Hydrology*. (in press as of Jan 30, 2020)

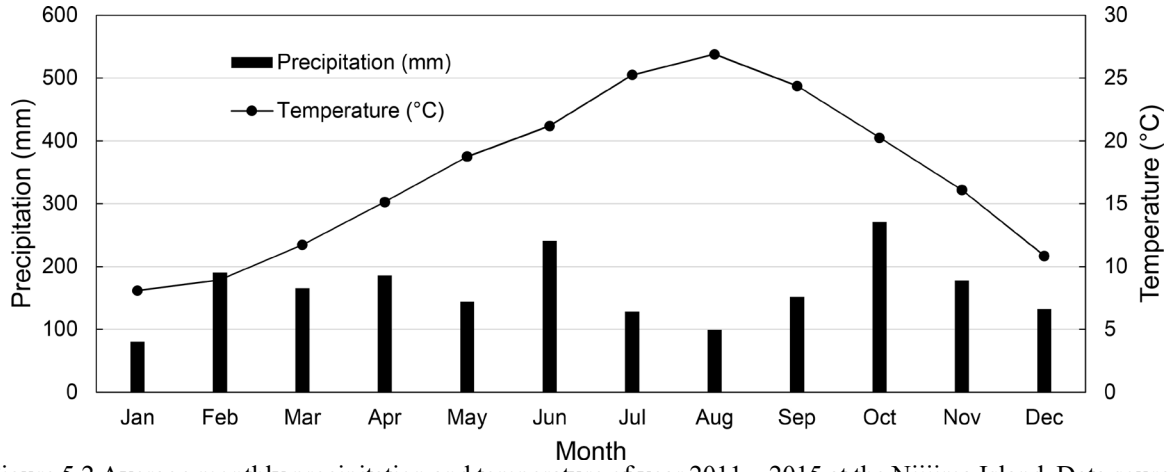

Figure 5.2 Average monthly precipitation and temperature of year 2011 ~ 2015 at the Niijima Island. Data source: Japan Meteorological Agency (2017).

5.2 Social Background

The population on the Niijima Island is 2734 in the year of 2015. Most of the population are residing in the Honson Village that is located in the mid-west part of the island (Figure 5.1b). In addition, in the years 1960 ~ 2015, compared with the average level in Japan, Niijima Island has been showing a large percentage of the old-age groups (65+) in its population structure with a faster ageing trend (Figure 5.3).

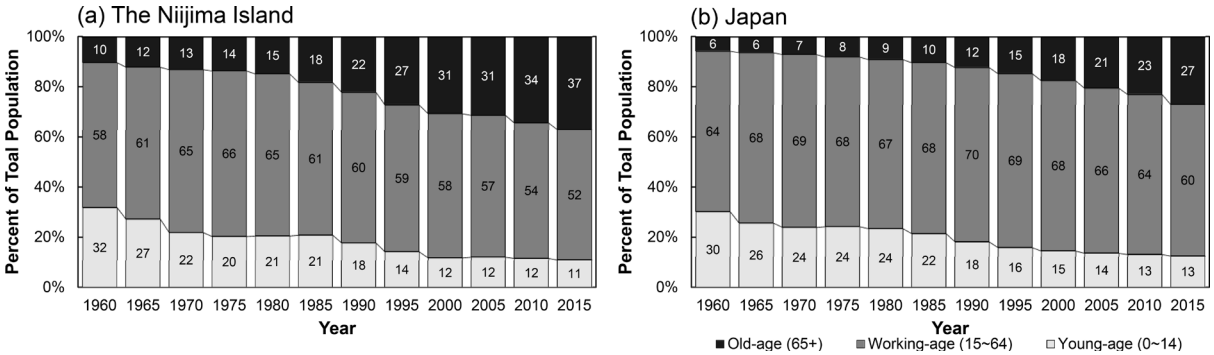

Figure 5.3 (a) Trends in population by age of Niijima Island 1960-2015; (b) Trends in Population by Age of Japan, 1960-2015 (data source: http://www.stat.go.jp).

As a tourist resort, the island attracts around 46,000 visitors annually (Oshima Subprefecture of Tokyo, 2014). May, July, August, and September are the months when the number of visitors is high (Figure 5.4).

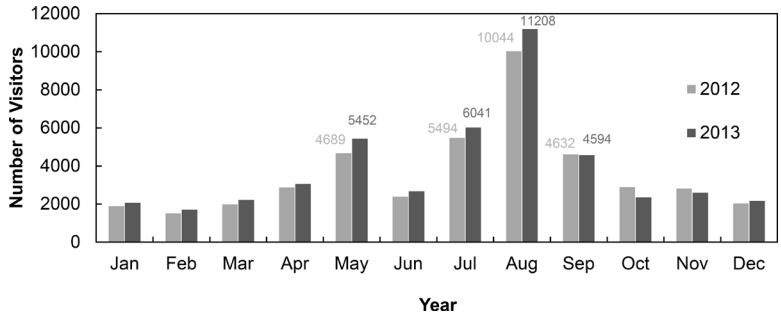

Figure 5.4 Number of visitors to the Niijima Island by month, 2012 and 2013. Data from Oshima Subprefecture of Tokyo (2014).

5.3 Geological Settings

The Niijima Island is a Quaternary volcanic island. It is composed of rhyolite lava domes in the northern and southern regions, and a low-lying plain in the central part (Figure 5.5a). Before 886 AD, the Mt. Minejiyama, Mt. Setoyama, and Mt. Marujimamine were above the sea-level and others were below the sea-level (Nakaoka and Suzuki-Kamata, 2015). In 886 AD, the latest eruption of the Mukaiyama Volcano occurred with a phreatomagmatic explosion of rhyolite magma at the southern part of the Niijima Island (Koyaguchi, 1986). It then released a pyroclastic flow and pyroclastic surge settling in the central part of the island that formed a single-layered unconfined aquifer (Figure 5.5b). The rhyolite lava from the Mukaiyama Volcano spreaded and overlaid the pyroclastic cone in the southern part of the island, as illustrated in Figure 5.5. All the aquifer materials below the sea-level were initially submerged by seawater, then, the fresh groundwater system was gradually developed by receiving and storing freshwater from rainfall. The seafloor depth within a horizontal distance of 1000 m from the coastline of the Niijima Island is less than 30 m (Nakaoka and Suzuki-Kamata, 2015). According to the estimated bedrock surface (aquifer bottom) topography by electrical survey (Shindo, 1980), there is a structural high of the bedrock surface in the central area of the island (Figures 5.5b and c). In order to confirm the bedrock surface elevations in the Niijima Island, microtremor survey was carried out. The field investigation and data analysis were supported by Geo-X Consultants Corporation, Japan. The microtremor survey results suggested that

depths to bedrock surface differed from the those Shindo (1980) (Figure 5.6). The microtremor survey results indicated a local depression of the bedrock surface in the western area of the island, and two structural lows of the bedrock surface in the eastern area. The detailed measurement data of the microtremor survey is presented in Appendix-A.

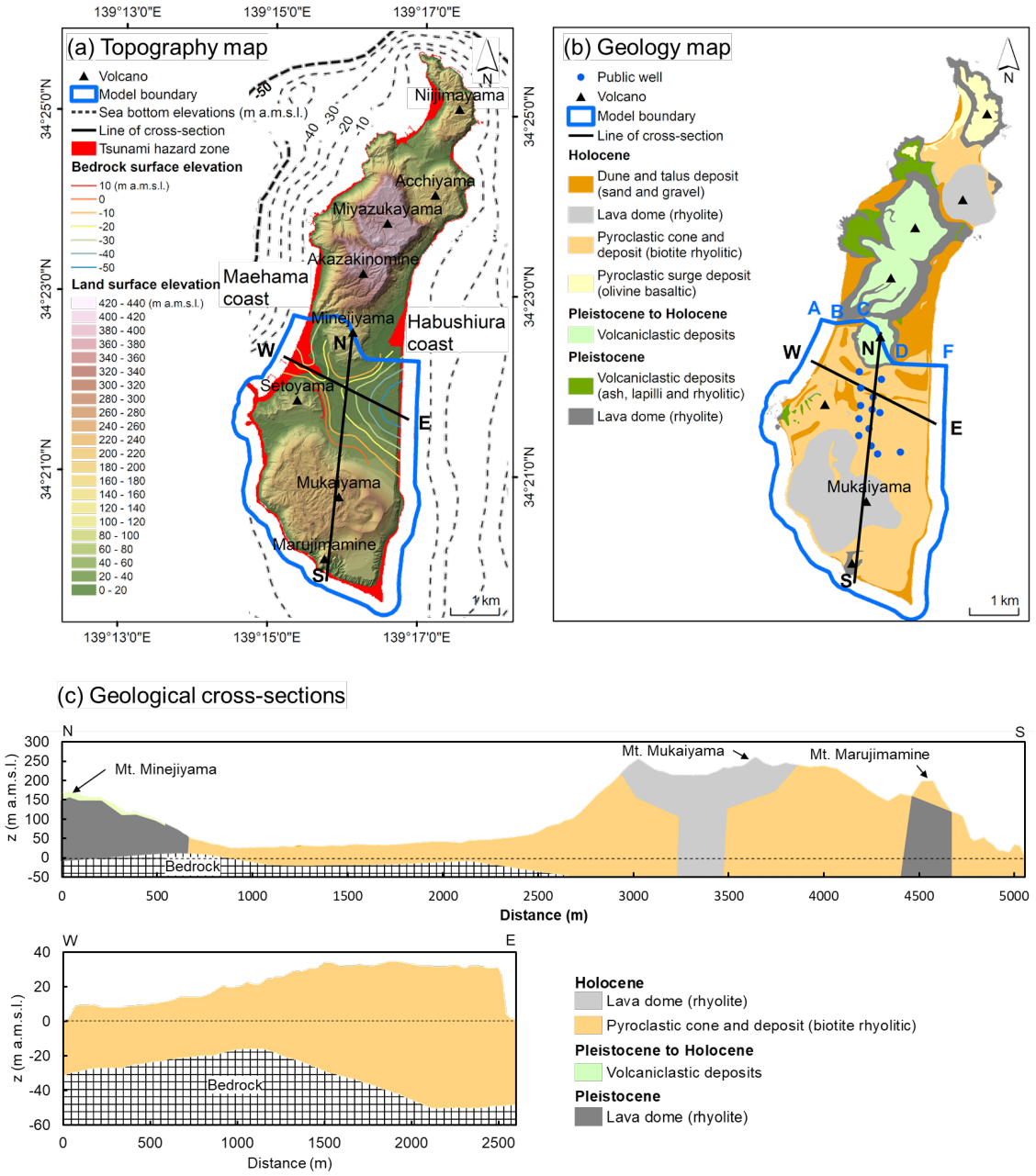

Figure 5.5 Geology of the Niijima Island: (a) topography map showing land surface elevations (Ministry of Land, Infrastructure, Transport and Tourism, 2015), bedrock surface elevations (Construction Section of Niijima Village, 2001; Isobe and Nakashima, 2001; Shindo, 1980), sea bottom elevations (Nakaoka and Suzuki-Kamata, 2015) and anticipated tsunami hazard zone (Tokyo Disaster Management Council, 2013); (b) geologic map with the location of public water supply wells; (c) schematic geologic cross-sections of N-S (vertical exaggeration by a factor of 2) and W-E (vertical exaggeration by a factor of 10). Modified from Shindo (1980) and Isshiki (1987).

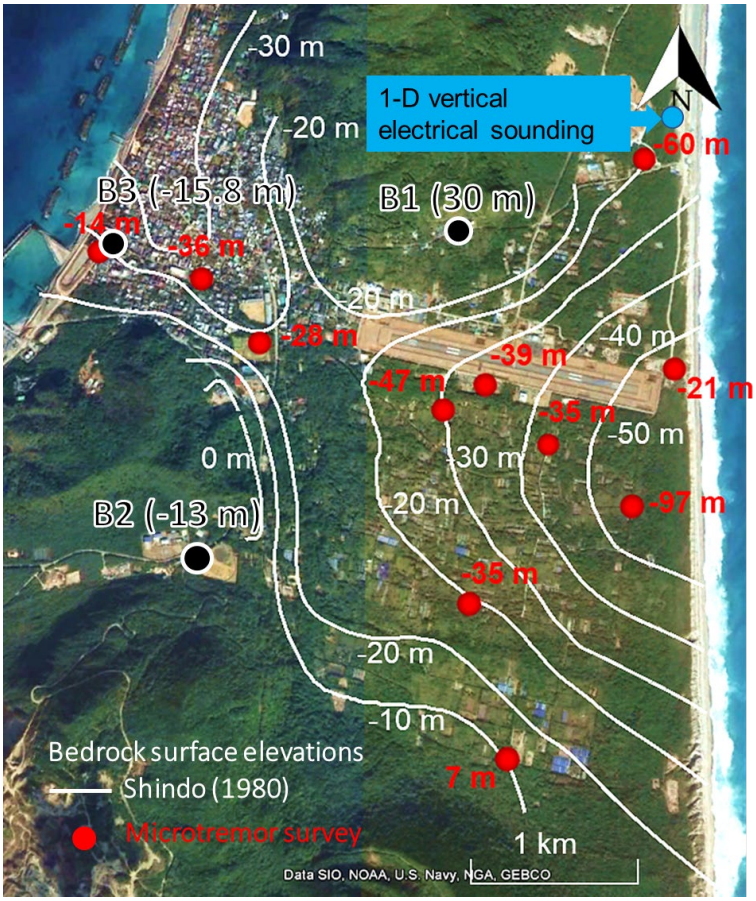

Figure 5.6 The bedrock surface elevations of the Niijima Island based on the resistivity survey results by Shindo (1980) (white lines), the ones based on the microtremor survey results (red points), and the ones based on borehole data by Niijima Village Office (2015) (B1 and B2) and by Construction Section of Niijima Village (2001) (B3).

5.4 Hydrogeological Settings

Holocene pyroclastic surge deposits form a single-layered unconfined aquifer in the study area. The measured hydraulic conductivity (K) of the aquifer was reported to be varied between 1×10^{-6} and 6×10^{-3} m/s (Construction Section of Niijima Village, 2001; Honma et al., 1974; Shindo, 1980). Aichi et al. (2011) estimated K to be 3.0×10^{-4} to 3.4×10^{-2} m/s based on the water level fluctuation of wells by tidal signals. Previous studies (Aichi et al., 2011; Honma et al., 1974) indicated that water table elevations ranged from about 0.5 m a.m.s.l. near the coast to 1.3 m a.m.s.l. in the central plain of the island, and had about ± 0.3 m fluctuations throughout the year. The groundwater system is recharged by direct infiltration of rainfall. The recharge of the aquifer was estimated to be around 30% to 50% of the annual rainfall (Honma et al., 1974). To estimate the subsurface structure, a 1-D electrical sounding survey was carried

out at the location approximately 75 m away from the eastern coastline with a surface elevation of 11 m a.m.s.l.. According to the inversion result (Figure 5.7), the groundwater table was at 0.8 m a.m.s.l., the interface between fresh groundwater and saltwater was at around -15.4 m a.m.s.l.. Groundwater is abstracted from the public wells that were constructed in 1980s in the central plain of the island (5.5b), supplying about 3.7×10^5 m^3 of freshwater annually for domestic purposes (Oshima Subprefecture of Tokyo, 2014; Shindo, 1992). Note that there is no surface water, and hence, groundwater is the only freshwater source on the island.

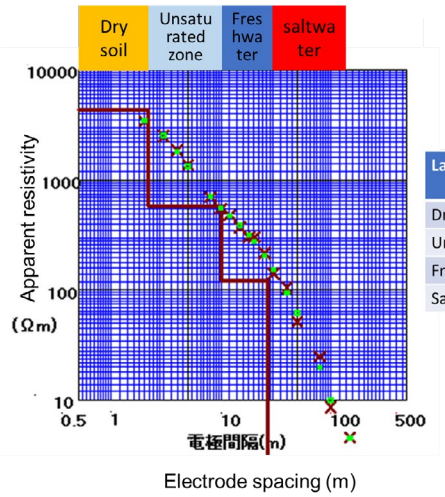

Surface elevation: 11 m a.m.s.l.

Layer	Resistivity (Ωm)	Depth (m)
Dry soil	4409.6	2.18
Unsaturated zone	577.6	10.19
Freshwater	121.4	26.4
Saltwater	0.6	

Figure 5.7 The results of 1-D electrical sounding. See the location of the measurement in Figure 5.6. The data was analyzed and provided by Kiso-jiban Consultants Co.,Ltd., Japan.

5.5 Tsunami Disaster Risks

5.5.1 The Anticipated Nankai Earthquake and Tsunami Scenarios

The Niijima Island is located in a seismically active zone surrounded by plate boundaries (Figure 5.8a). Along the Nankai Trough (Figure 5.8b), a series of devastating earthquakes have occurred historically with the intervals of about 100 to 150 years, including 1605 Keichō Nankaido earthquake (7.9 M_w), 1707 Hōei earthquake (8.6 M_w), 1854 Ansei-Nankai earthquake (8.4 M_w), and 1946 Nankaidō earthquake (8.1 M_w), with the generated tsunami waves of 6 to 28 m a.m.s.l. in height (National Geophysical Data Center, 2015; Utsu, 2004). According to the Cabinet Office of Japan (2011), there is a high possibility that a

massive earthquake of 9.0 M_W will occur along the Nankai Trough on the Pacific side of Japan during the year 2011 to 2040. Under this earthquake scenario, the Niijima Island is anticipated to be one of the most vulnerable coastal zones which will face tsunami waves of up to about 30 m a.m.s.l. (Figure 5.8c). According to the simulation results by Tokyo Disaster Management Council (2013) (Figure 5.9a), under the worst tsunami scenario, the low-lying area near the Maehama coast of the Niijima Island would be inundated by seawater up to about 15 m a.m.s.l. in elevation. Figure 5.9b shows the temporal changes of the simulated tsunami wave heights at the sea surface near the western coast of the Niijima Island by Tokyo Metropolitan Government (2013), which indicated that the tsunami waves would keep affecting the western coast significantly for around 60 to 120 minutes.

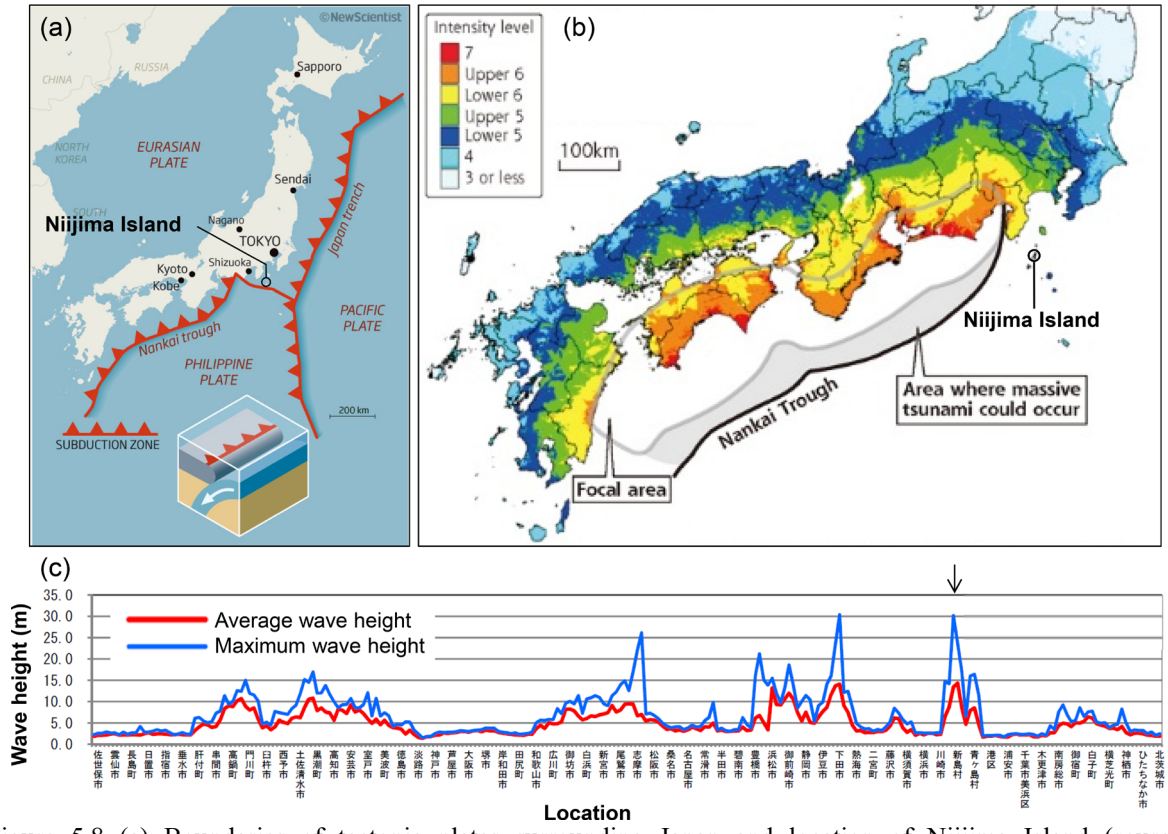

Figure 5.8 (a) Boundaries of tectonic plates surrounding Japan and location of Niijima Island (source: https://www.newscientist.com); (b) Estimated maximum seismic intensity by the Nankai earthquake and location of Niijima Island (intensity level in Japan Meteorological Agency seismic intensity scale) (source: http://www.forbes.com); (c) Average wave height and maximum wave height in different coastal sites in the worst scenario of the estimated Nankai Earthquake. Black arrow indicates the condition of Niijima Island (Cabinet Office of Japan, 2011).

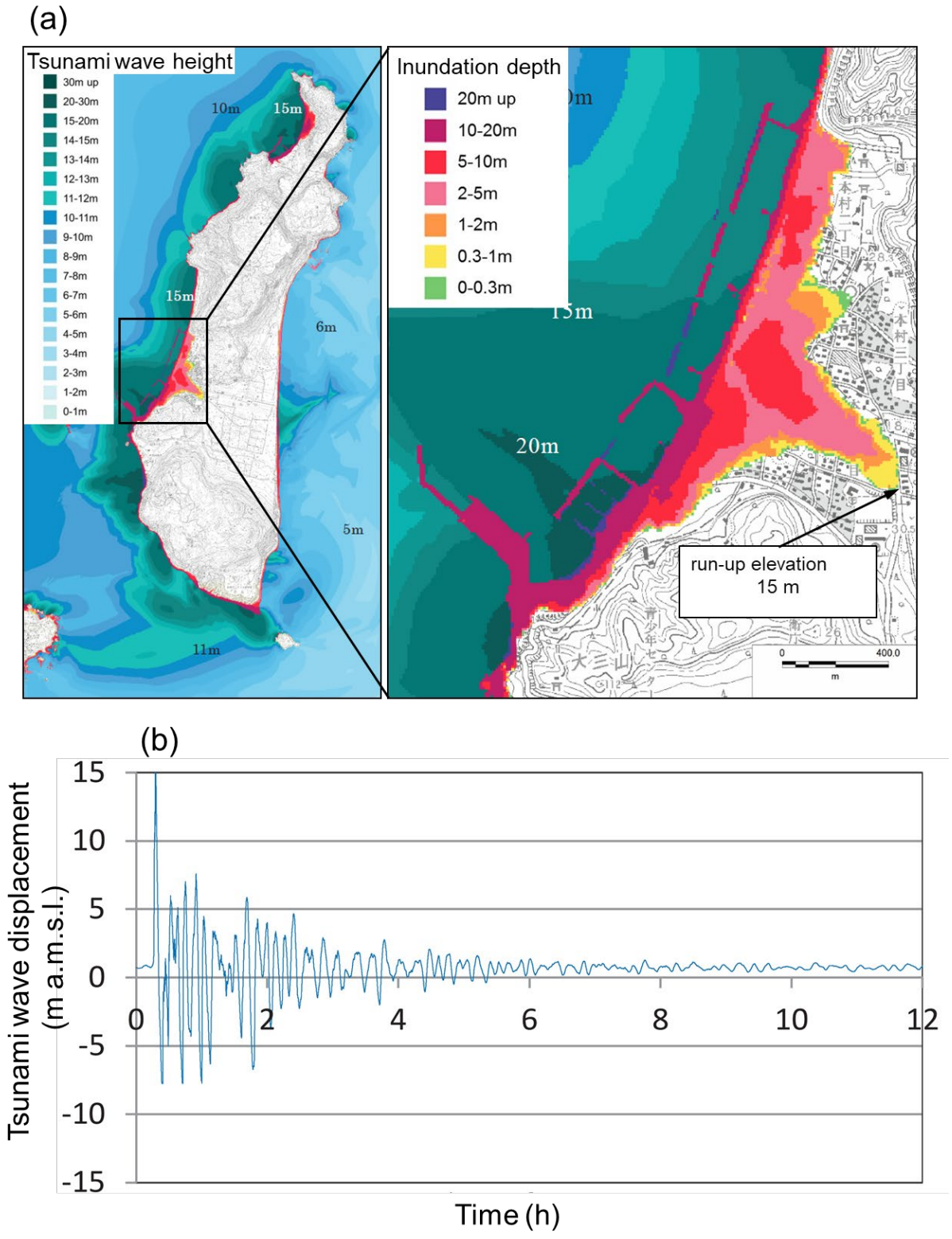

Figure 5.9 The scenario of tsunami inundation at the Niijima Island: (a) simulated height of tsunami waves and inundation area (b) Tsunami wave displacement at the sea surface near the Maehama coast of the Niijima Island under the Nankai earthquake and tsunami scenario simulated by Tokyo Metropolitan Government (2013). A tide level of 0.73 m a.m.s.l. was considered in the simulation.

5.5.2 Local Preparedness

Under the Nankai earthquake and tsunami scenario, groundwater, the only freshwater source for the locals living on the Niijima Island, will face the problem of TSWI. According to Central Disaster Management Council (2014), the bottled drinking-water has been prepared for emergency situations by local organizations and convenience stores. As for remote areas, small islands like the Niijima Island, it is recommended that they should prepare water stock for 1-week use with the anticipation of no rescue from others (Central Disaster Management Council, 2014). According to the interview with one officer of the local government of the Niijima Island, bottled drinking-water has been reserved to the local residents with about 3 L water per person per day for 3-days emergency. However, this 3 L of water is only for drinking purpose, while water demands for other daily activities such as washing and showering were not considered. Furthermore, this plan does not take into account the number of tourists who may be on the island at the time of disaster. The demands for freshwater could be much higher if the earthquake and tsunami occurs in the peak tourist seasons. In addition, it is demonstrated by the tsunami disasters in 2004 and 2011 that the groundwater deterioration can last for years, hence, long-term water supply should be considered for the efficient and proper recovery planning from the disaster.

CHAPTER 6: 2-D MODEL OF THE NIIJIMA ISLAND: PROCESSES AND UNCERTAINTIES[1]

6.1 Introduction

The main objective of this chapter is to improve the understanding of TSWI processes in coastal unconfined aquifers and model uncertainties based on the case of the Niijima Island. A vertical cross-section was modeled to represent the groundwater system of the island. The settings of the tsunami inundation scenarios, the rainfall recharge conditions, and the aquifer properties were varied to investigate their impacts on the simulation results.

6.2 Methods

6.2.1 ICs and BCs

The vertical cross-section along the line W-E (Figure 5.5) was selected as the model domain (Figure 6.1) which was located in the tsunami inundation zone under the Nankai tsunami scenario. After several trials, the seafloors with a horizontal distance of 150 m (0 m < $x \leq$ 150 m and 2730 m < $x \leq$ 2880 m) were decided to be included in the model, which ensured all the important seawater-freshwater interactions to be captured throughout the whole simulation stages. The landside part in the west (150 m < x < 960 m) was below 15 m a.m.s.l. and was subject to tsunami inundation risks while that in the east (960 m < x < 2730 m) was above 15 m a.m.s.l. that was extended to a cliff of about 30 m a.m.s.l. near the eastern coast.

Figure 6.1 shows the BCs different simulation stages, i.e., ST-1: the development of fresh groundwater system since the deposition of pyroclastic materials in 886 AD until it reached to the quasi-steady-state; ST-2: the SWI processes during the tsunami inundation period; ST-3: the days after the tsunami inundation until the arrival of the first rainfall; and ST-

[1] The content of chapter appears in Liu, J., & Tokunaga, T. (2019). Future Risks of Tsunami‐Induced Seawater Intrusion Into Unconfined Coastal Aquifers: Insights From Numerical Simulations at Niijima Island, Japan. *Water Resources Research*, 55. https://doi.org/10.1029/2019WR025386

4: the years of the post-tsunami aquifer recovery processes. The ICs of each simulation stage (except for ST-1) were directly imported from the end of the previous stage.

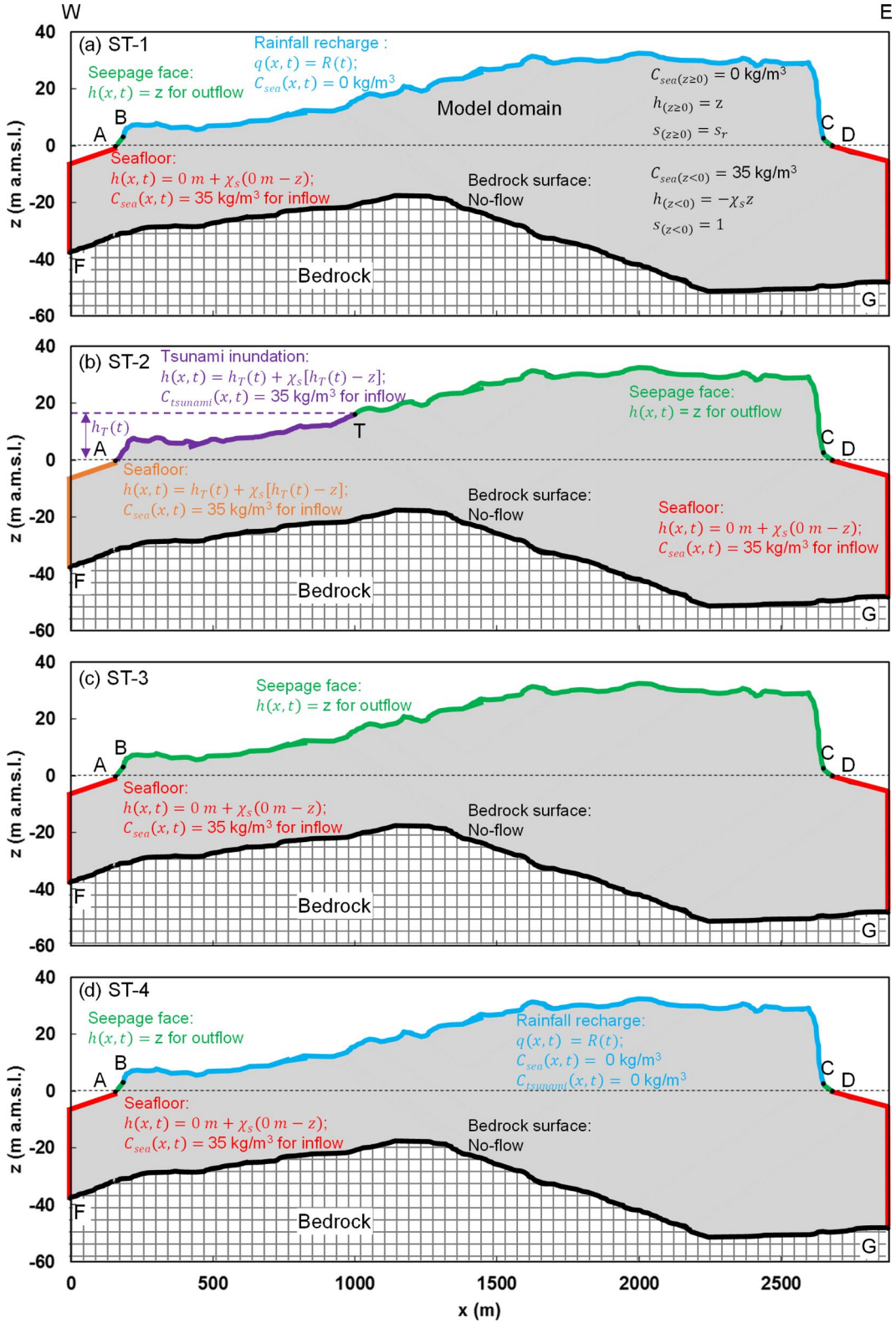

Figure 6.1 ICs of ST-1, and BCs of ST-1 to ST-4. Vertical exaggeration is by a factor of 10.

For ST-1 (Figure 6.1a), the ICs were set to reflect the time when the island was formed in 886 AD as described in Section 5.3. All the media above the sea-level were set to contain residual water in the concentration of 0 kg/m^3 while the media below the sea-level was fully saturated with seawater with a concentration C_{sea} = 35 kg/m^3 (NaCl). Along the seafloors A-F and D-G where groundwater was in contact with seawater, a constant seawater head BC of sea-level h_s = 0 m a.m.s.l. was assigned. A system-dependent BC was applied to A-F and D-G, in which the constant concentration of C_{sea} = 35 kg/m^3 was set for seawater inflow from the sea to aquifer while no constraints were set in the case of groundwater discharge from the aquifer to the sea. At the beach zones A-B and C-D where groundwater may discharge out from the surface, a seepage face BC was applied. The height of this seepage face boundary was decided to be 5 m a.m.s.l., above which no obvious groundwater discharge was observed in the field. By running several trial models, the current settings of seepage face BCs were proved to be sufficient to simulate the discharges of groundwater at the beach zones. A constant mass concentration of C_{sea} = 0 kg/m^3 with a time-variable flux $R(t)$, representing the rainfall recharge, was applied along the land surface B-C. Like the land surface B-C, the seepage face A-B and C-D should also receive freshwater recharge from rainfall unless active discharge happened, however, the contribution of recharge from A-B and C-D was negligible compared with that from B-C. This was proved by using a more complicated setting of BCs at A-B-C-D which applied the rainfall recharge to the nodes except those if the discharges of groundwater occurred. The surface of bedrock F-G was set to be a no-flow boundary through all the simulation stages. The transient simulation was run for a period of 200 years to ensure the model reached to the quasi-steady-state.

During ST-2 (Figure 6.1b), the tsunami inundation event was considered as a constant sea-level rise (constant in space but variable in time) of $h_T(t)$ in elevation at the Maehama coast. The seawater heads along A-F and the inundated land surface A-T became $h_T(t)$ which

represented the tsunami-induced sea-level rise. Though the solute entered to the aquifer through A-F boundary and the one through A-T boundary were considered to be the same chemical composition in this model (35 kg/m^3 of NaCl), they were labeled as two species C_{sea} and $C_{Tsunami}$, respectively, which allowed the calculation of the total mass introduced to subsurface by tsunami, as described in Section 6.2.4. This setting of BCs with two chemical species produced consistent simulation results with those using the setting of single chemical species. The eastern coast was assumed not to be directly inundated by the tsunami, and hence, the BCs along D-G stayed the same for all the simulation stages. For the uninundated land surface D-C-T, a seepage face BC was set. The duration of ST-2 was varied in the range of 10 to 120 minutes depending on the simulation cases.

ST-3 was designed to represent the dry days (1 to 30 days depending on the cases) before the first rainfall event arrived after the tsunami. During this period, the sea-level near the Maehama coast had descended back to the normal status (0 m a.m.s.l.) while some intruded seawater in the domain which was initially unsaturated would discharge out from the soil medium. Therefore, the land surface A-B-C-D became a seepage face boundary (Figure 6.1c).

During ST-4 (Figure 6.1d), the freshwater recharge $R(t)$ with 0 kg/m^3 concentration from the rainfall began to flush the salinized groundwater system. Other BCs were the same as the ones in ST-3. The simulation ST-4 was continued for 15 to 25 years depending on the cases.

6.2.2 Spatial and Temporal Discretization

The spatial discretization was set to minimize numerical dispersion and avoid numerical oscillation. In order to determine how sensitive the simulation results were to the mesh size, additional simulations were performed at different levels of discretization. The results showed that when the mesh size Δl was smaller than 2.56 m, the saltwater movement and the budget of fluid flow and mass transport were very similar. However, a finer mesh design would cause higher computational burden, e.g., reducing the mesh size from $\Delta l \approx 1.68$ m to $\Delta l \approx 0.43$ m

tremendously raised the CPU time from approximately 3 days to 10 days with two 2.50 GHz processors to simulate an ST-4 period of 15 years. Therefore, the model domain was first discretized into triangular elements with the element size $\Delta l \approx 1.68$ m. Then, at the coastal areas and tsunami inundation zones where the simulation required higher stability and accuracy, the elements were refined to $\Delta l \approx 0.25$ m. In total, the model contained 186,278 elements with 98,148 nodes. This mesh design fulfilled $Pe_m < 4$ (Voss and Souza, 1987). The automatic time-step control with the time-integration scheme of Forward Euler/Backward Euler (FE/BE) was applied for the temporal discretization (Diersch, 2013). The initial time step was set to be 1×10^{-6} day for ST-1 and ST-4, 1×10^{-6} second for ST-2, and 1×10^{-6} hour for ST-3. The maximum growth factor between subsequent time steps was restricted to be 1.1, and the maximum time step be one day for ST-1 and ST-4, 1 second for ST-2, and 0.1 hour for ST-3.

6.2.3 Parameterization of Simulation Cases

The present model assumed that the aquifer of the Niijima Island was single-layered and homogeneous. A baseline case was designed with the parameters summarized in Table 6.1. The parameters for the van Genuchten model (Eq 3.22 and Eq 3.23) were obtained by fitting the water retention curve with the measured data by Shindo (1980) (Figure 6.2a). The longitudinal dispersivity α_L of 5 m was chosen here based on the relationship between dispersivity and observation scale that was suggested by Gelhar et al. (1992) (Figure 3.9), and the ratio between longitudinal and transverse dispersivities was set to be 10. The porosity of 0.34 was obtained from Shindo (1980). According to Honma et al. (1974), the recharge rate of the groundwater system in the Niijima Island was equivalent to 30 to 50% of the annual rainfall amount. Therefore, a constant recharge rate $R(t) = 883$ mm/yr was adopted in the baseline case, which was derived from 40% of the average annual rainfall amount of 2207 mm/yr (Japan Meteorological Agency, 2017). Aichi et al. (2011) estimated the ratio R/K to be 3.0×10^{-5} by fitting the Dupuit-Ghyben-Herzberg analytical solution (Vacher, 1988) to the measured

groundwater table elevations in the Niijima Island. By several trials using the present numerical model, the ratio R/K was calibrated to be 2.55×10^{-5}, and K be 1.1×10^{-3} m/s, which resulted in rather good fits with the measured groundwater table elevations (Figure 6.2b). The simulated elevations of the groundwater table and the transition zone between fresh groundwater and saltwater were in good agreement with the 1-D electrical sounding result (Figure 5.7). Based on the tsunami simulation results by Tokyo Disaster Management Council (2013), a tsunami inundation event lasting for 120 minutes with a constant inundation elevation $h_T(t)$ = 15 m a.m.s.l. was assumed in the baseline case. The duration of ST-3 was chosen to be five days. Other parameters were selected according to the typical literature values (Diersch, 2013; Vithanage et al., 2012; Yu et al., 2016) and are listed in Table 1.

Table 6.1 Summary of simulation parameters in the baseline case

	Symbol	Value	Unit	Data source
Parameters obtained from literature of the Niijima Island				
Porosity	ε	0.34	-	(Shindo, 1980)
Net recharge rate	$R(t)$	883	mm/yr	(Honma et al., 1974; Japan Meteorological Agency, 2017)
Parameters obtained by calibration				
Residual saturation	s_r	0.209	-	Calibrated by fitting van Genuchten model (van Genuchten, 1980) with measured data by Shindo (1980)
van Genuchten parameter	α	3.6	1/m	
Pore size distribution index	n	2.3	-	
Horizontal hydraulic conductivity	K_x	1.1×10^{-3}	m/s	Calibrated based on the measured groundwater table elevations
Parameters obtained from typical literature values				
Longitudinal dispersivity	α_L	5	m	(Gelhar et al., 1992)
Transverse dispersivity	α_T	0.5	m	
Anisotropy ratio of hydraulic conductivity	K_z/K_x	1	-	(Diersch, 2013; Vithanage et al., 2012; Yu et al., 2016)
Freshwater concentration	C_0	0	kg/m^3	
Seawater concentration	C_s	35	kg/m^3	
Density ratio	χ_s	0.025	-	
Gravitational acceleration	g	9.8	m/s^2	
Dynamic viscosity	μ	0.001	kg/(m·s)	
Molecular diffusion coefficient	D_0	1×10^{-9}	m^2/s	

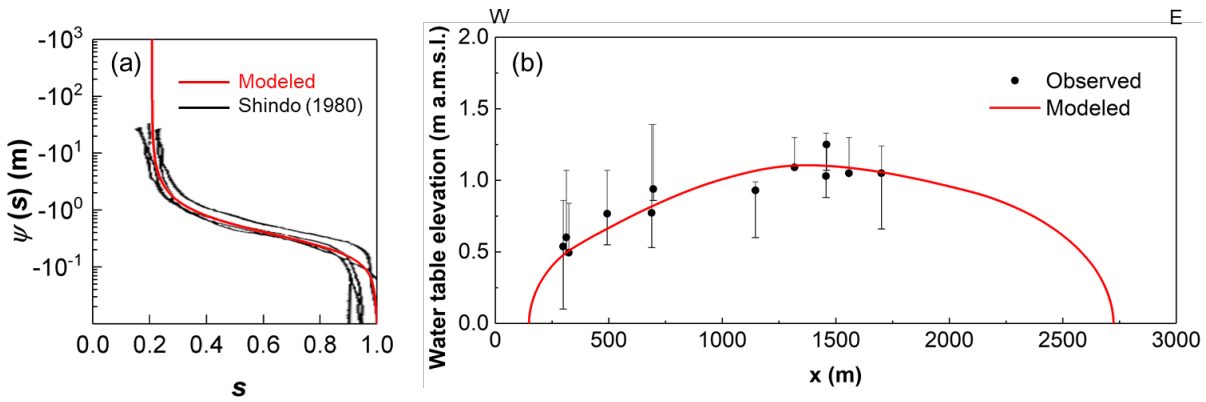

Figure 6.2 Fitting results for parameterization: (a) The modeled water retention curve using the van Genuchten model (van Genuchten, 1980) based on the measured data by Shindo (1980). (b) Comparison of the simulated results (at the end of ST-1) and observed water table elevations. The observed data are projected positions to the line W-E. The measured data are plotted with the fluctuation ranges based on the historical records of water table elevations provided by the Niijima Office and by Aichi et al. (2011).

Besides the baseline case, additional simulation cases were designed to investigate the effects of parameter uncertainties that could arise from the tsunami inundation scenarios, the rainfall recharge settings, and the configurations of the aquifer properties, and numerical parameters (Table 6.2). The cases T-H1 to T-H4 were designed with $h_T(t)$ varied from 5 to 25 m a.m.s.l. while $h_T(t)$ was kept constant over time in each case. Based on the simulation results of ST-2 in the baseline case, two representative tsunami inundation durations, 10 and 40 minutes (with constant $h_T(t)$ = 15 m a.m.s.l.) were simulated in the cases T-D1 and T-D2, respectively, to examine their effects on the post-tsunami recovery processes. As shown in Figure 6.3a, the cases T-HD1 to T-HD3 with $h_T(t)$ linearly decreasing from 15 to 0 m a.m.s.l. in a period of 30, 60, and 120 minutes, and the case T-HD4 representing a second tsunami wave arrival were tested. The case T-HD5 was designed by setting the $h_T(t)$ (Figure 6.3a) to be equal to the wave displacement that simulated by Tokyo Metropolitan Government (2013) (Figure 5.9b). To study how the length of ST-3 would affect the simulation results, the cases R-D1 and R-D2 with the period of ST-3 of 1 and 30 days, respectively, were simulated. According to Honma et al. (1974), the main aquifer of the Niijima Island received freshwater recharge of 30 to 50% of the annual rainfall. Therefore, keeping the R/K ratio constant, besides

the baseline case which set $R(t)$ to be 40 % of the annual rainfall, two additional cases with $R(t)$ of 30% and 50% of the annual rainfall were designed, namely $R(t)$ = 662 mm/yr with K = 8.1 × 10^{-4} m/s for the case R-R1 and $R(t)$ = 1104 mm/yr with K = 1.3 × 10^{-3} m/s for R-R2. To investigate the effect of time-variable (annually cyclic) rainfall recharge BCs, keeping the same annual recharge of 883 mm/yr, two settings were designed, i.e., the case R-R3: a daily-variable recharge setting by assigning $R(t)$ according to the daily rainfall patterns on the Niijima Island in 2017 (Figure 6.3b); and the case R-R4: a seasonally-variable recharge setting of half year of dry ($R(t)$ = 0 mm/month) and half year of wet ($R(t)$ =147 mm/month). Keeping the same K_x, the uncertainty of anisotropic aquifer properties was analyzed in the cases A-Kz1 to A-Kz3 with the ratio K_z/K_x of 0.1, 0.2 and 0.5. The case A-K1 represented a hypothetical aquifer system with K = 1.1 × 10^{-4} m/s which is one order of magnitude lower than that of the Niijima Island but had a same R value as that of the Niijima Island. As stated in Section 5.3, the estimation of the bedrock surface elevations shown in Figure 5.5a could include large uncertainties, and the microtremor survey indicated a different pattern of bedrock surface elevations (Figure 5.6). Therefore, in comparison to the bedrock setting with a dome structure in the baseline case, an arbitrary bedrock surface with a local depression structure in the central area of the island was designed (Figure 6.3c), and were simulated in the cases A-BS1 and A-BS2 with $h_T(t)$ of 15 and 25 m a.m.s.l., respectively. Compared with the baseline case that specified no-flow BCs (impermeable) at the bottom boundary, the cases A-BK1 and A-BK2 included a low-permeable bedrock layer (K = 1 × 10^{-13} m/s and ε = 0.05) and a semi-permeable bedrock layer (K = 1 × 10^{-7} m/s and ε = 0.05), respectively, into the model domain (Figure 6.3d). The bedrock layers in the cases A-BK1 and A-BK2 were assumed to be fresh at the beginning of ST-2 (C = 0 kg/m^3). Considering that low permeability layers at the land surface could possibly be formed by tsunami deposits after the inundation, the cases A-T1 and A-T2 included several low-permeable tsunami deposits layers (K = 1 × 10^{-13} m/s and ε = 0.05) and

Table 6.2 Configurations of the simulation cases for uncertainty analysis

ID	Tsunami inundation scenarios		Rainfall recharge settings		Aquifer properties					Numerical parameters	
	$h_T(t)$ (m a.m.s.l.)	ST-2 duration (min)	ST-3 Duration (d)	$R(t)$ (mm/yr)	K_x (m/s)	K_z/K_x	Bedrock structure	Bedrock layers K (m/s)	Tsunami deposits layers K (m/s)	Seawater density ρ_s (kg/m^3)	Element size Δl (m)
baseline	**15**	**120**	**5**	**883**	**1.1×10^{-3}**	**1**	**Concave down**	**Impermeable**	**No**	**1025**	**1.68***
T-H1	5	120	5	883	1.1×10^{-3}	1	Concave down	Impermeable	No	1025	1.68*
T-H2	10	120	5	883	1.1×10^{-3}	1	Concave down	Impermeable	No	1025	1.68*
T-H3	20	120	5	883	1.1×10^{-3}	1	Concave down	Impermeable	No	1025	1.68*
T-H4	25	120	5	883	1.1×10^{-3}	1	Concave down	Impermeable	No	1025	1.68*
T-D1	15	10	5	883	1.1×10^{-3}	1	Concave down	Impermeable	No	1025	1.68*
T-D2	15	40	5	883	1.1×10^{-3}	1	Concave down	Impermeable	No	1025	1.68*
T-HD1	Linear decrease from 15 to 0	30	5	883	1.1×10^{-3}	1	Concave down	Impermeable	No	1025	1.68*
T-HD2	Linear decrease from 15 to 0	60	5	883	1.1×10^{-3}	1	Concave down	Impermeable	No	1025	1.68*
T-HD3	Linear decrease from 15 to 0	120	5	883	1.1×10^{-3}	1	Concave down	Impermeable	No	1025	1.68*
T-HD4	Linear decrease from 15 to 0	30 × 2	5	883	1.1×10^{-3}	1	Concave down	Impermeable	No	1025	1.68*
T-HD5	Tsunami wave displacement	120	5	883	1.1×10^{-3}	1	Concave down	Impermeable	No	1025	1.68*
R-D1	15	120	1	883	1.1×10^{-3}	1	Concave down	Impermeable	No	1025	1.68*
R-D2	15	120	30	883	1.1×10^{-3}	1	Concave down	Impermeable	No	1025	1.68*
R-R1	15	120	5	662	8.1×10^{-4}	1	Concave down	Impermeable	No	1025	1.68*
R-R2	15	120	5	1104	1.3×10^{-3}	1	Concave down	Impermeable	No	1025	1.68*
R-R3	15	120	5	Daily variation	1.1×10^{-3}	1	Concave down	Impermeable	No	1025	1.68*
R-R4	15	120	5	Seasonal variation	1.1×10^{-3}	1	Concave down	Impermeable	No	1025	1.68*
A-Kz1	15	120	5	883	1.1×10^{-3}	0.1	Concave down	Impermeable	No	1025	1.68*
A-Kz2	15	120	5	883	1.1×10^{-3}	0.2	Concave down	Impermeable	No	1025	1.68*
A-Kz3	15	120	5	883	1.1×10^{-3}	0.5	Concave down	Impermeable	No	1025	1.68*
A-K1	15	120	5	883	1.1×10^{-4}	1	Concave down	Impermeable	No	1025	1.68*
A-BS1	15	120	5	883	1.1×10^{-3}	1	Concave up	Impermeable	No	1025	1.68*
A-BS2	25	120	5	883	1.1×10^{-3}	1	Concave up	Impermeable	No	1025	1.68*
A-BK1	15	120	5	883	1.1×10^{-3}	1	Concave down	1.1×10^{-13}	No	1025	1.68*
A-BK2	15	120	5	883	1.1×10^{-3}	1	Concave down	1.1×10^{-7}	No	1025	1.68*
A-T1	15	120	5	883	1.1×10^{-3}	1	Concave down	Impermeable	1.1×10^{-13}	1025	1.68*
A-T2	15	120	5	883	1.1×10^{-3}	1	Concave down	Impermeable	1.1×10^{-7}	1025	1.68*
M-S1	25	120	5	883	1.1×10^{-3}	1	Concave up	Impermeable	No	1000	1.68*
M-S2	25	120	5	883	1.1×10^{-3}	1	Concave up	Impermeable	No	1002.5	1.68*
M-S3	25	120	5	883	1.1×10^{-3}	1	Concave up	Impermeable	No	1250	1.68*
M-E1	15	120	5	883	1.1×10^{-3}	1	Concave down	Impermeable	No	1025	0.43
M-E2	15	120	5	883	1.1×10^{-3}	1	Concave down	Impermeable	No	1025	0.86
M-E3	15	120	5	883	1.1×10^{-3}	1	Concave down	Impermeable	No	1025	1.68
M-E4	15	120	5	883	1.1×10^{-3}	1	Concave down	Impermeable	No	1025	2.56
M-E5	15	120	5	883	1.1×10^{-3}	1	Concave down	Impermeable	No	1025	4.44
M-E6	15	120	5	883	1.1×10^{-3}	1	Concave down	Impermeable	No	1025	6.29
M-E7	15	120	5	883	1.1×10^{-3}	1	Concave down	Impermeable	No	1025	9.93

The settings varied from the ones in the baseline case are shaded in grey.

*The element size Δl = 1.68 was set for most of the model domain, except for the zones near the land surface and the coastal areas with a finer element size (Δl = 0.25 m).

several semi-permeable tsunami deposits layers ($K = 1 \times 10^{-7}$ m/s and $\varepsilon = 0.05$), respectively, into the model domain at the beginning of ST-4 (Figure 6.3e). These tsunami deposits layers were assumed to have a vertical thickness of about 0.3 m and to cover 50% of the total inundated land surface. In order to discuss the effect of density ratio on saltwater movement in the aquifer, the cases M-S1 to M-S3 assumed the density of seawater ρ_s to be 1000 kg/m^3, 1002.5 kg/m^3, and 1250 kg/m^3, respectively, and adopted the model domain with the concave up shape of the bedrock surface (Figure 6.3c). The cases M-E1 to M-E7 tested the effects of different levels of model discretization with the element size ranging from 0.42 m to 9.93 m. Except for the description above, other configurations of the simulation cases remained the same as those in the baseline case. Note that, except for the case A-K1, all these simulation cases produced water table elevations at the end of ST-1 very similar to the ones in the baseline model and in good agreements with the measured ones.

6.2.4 Measurable Indicator and Element-Based Dimensionless Numbers

The indicator *TM* was selected to quantitively evaluate the TSWI processes. *TM* was defined as the total mass of the solute ($C_{tsunami}$) that entered into the groundwater system from land surface (A-T in Figure 6.1b) by the tsunami inundation. *TM* was calculated for the vertical cross-section with a thickness of 1 m.

The Element-based dimensionless numbers M_x^E, M_z^E, and Ra_d^E defined in Section 4.2.4 were also used in this chapter to analyze the temporal changes of the flow patterns.

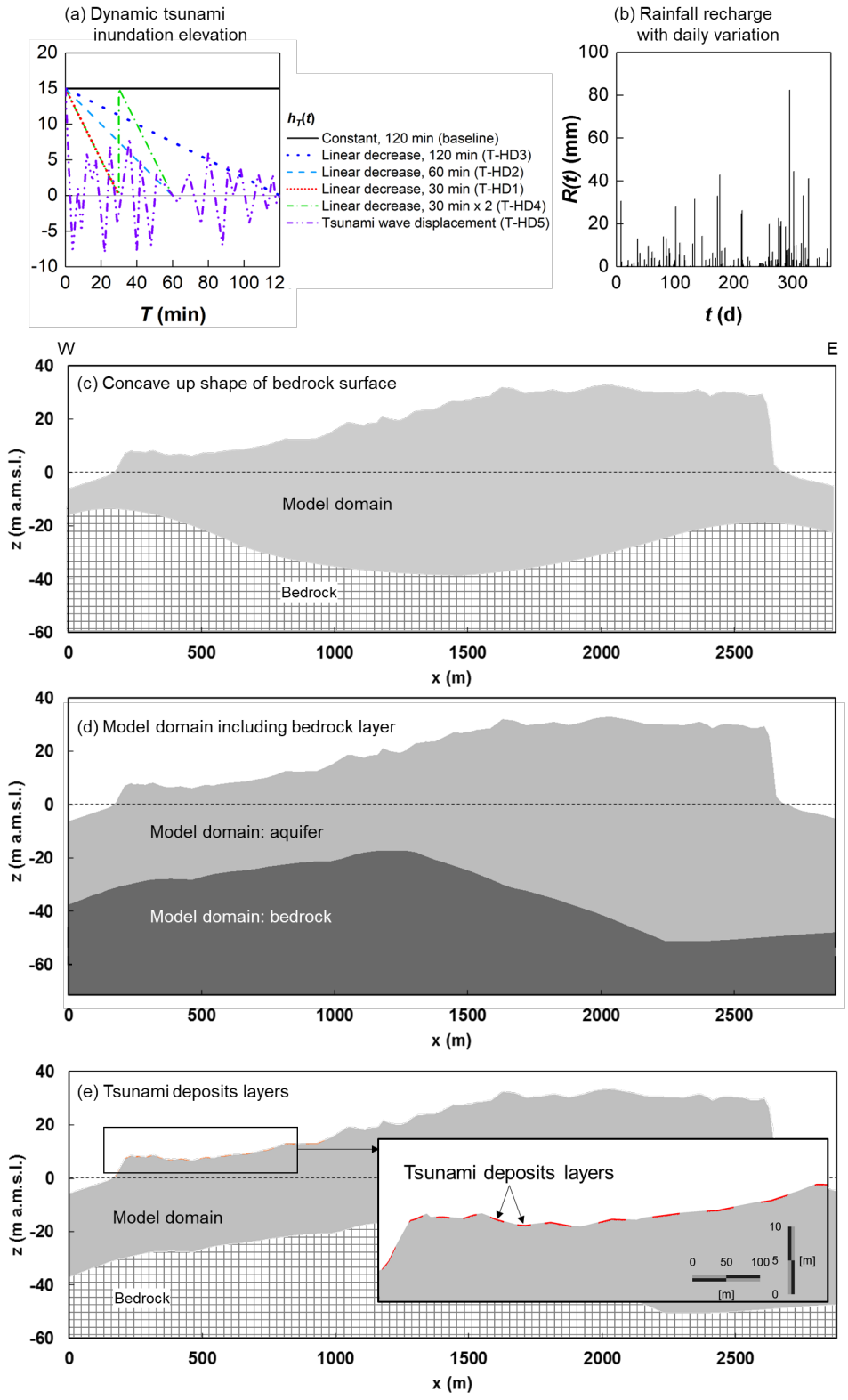

Figure 6.3 Varied settings for uncertainty analysis: (a) The settings of time-variable tsunami inundation elevation $h_T(t)$ during ST-2. (b) The setting of the recharge rate $R(t)$ with daily variances (annually cyclic). Keeping the annual recharge of 883 mm/yr, $R(t)$ was set to be proportional to the daily rainfall amount on the Niijima Island in 2017 (Japan Meteorological Agency, 2017). (c) The model domain showing the scenario of the bedrock with the concave up shape. (d) The model domain included the aquifer layer and the bedrock layer. (d) The model domain included the tsunami deposits layers at land surface at the beginning of ST-4.

6.3 Results and Discussions

6.3.1 TSWI Processes

The simulation results at representative time steps of the baseline case are illustrated in Figure 6.4. The temporal changes of *TM* from ST-2 to ST-4 in the baseline case are shown in Figure 6.5. After the transient simulation period of 200 years from the start of the flushing of seawater by the rainfall recharge, the model reached to the quasi-steady-state (Figure 6.4a), which reflected the groundwater conditions before the tsunami arrival. The streamlines indicated that fresh groundwater was recharged by the vertical infiltration of rainfall, then, flowed sub-horizontally from inland to the coast and met with seawater at the seawater-freshwater mixing zone, and finally discharged out near the coastline. The overall travel time of fresh groundwater to be discharged out was found to be at around 5 to 20 years.

In ST-2, the tsunami inundation event of 15 m a.m.s.l. started to affect the coastal zone for two hours. Three sub-stages can be distinguished via the temporal changes of *TM* (Figure 6.5a). During the first 10 minutes, *TM* showed a rapid increase, which corresponded to the invasion of seawater into the unsaturated zone (Figure 6.4b). This downward infiltration process occurred rather fast because of the following reasons: infiltration was driven by the large downward hydraulic head gradients, i.e., much larger than unity, caused by the tsunami-induced seawater-level rise; and the aquifer materials were formed by pyroclastic surge deposits with a high hydraulic conductivity value of $K = 1.1 \times 10^{-3}$ m/s. However, the simulated infiltration process in the unsaturated zone may remain uncertain and have limitations because the possible increase of air pressure in the remained air pockets was not calculated in our unsaturated-saturated flow modeling. For example, according to our simulation results at T = 10 min (Figure 6.4b), an unsaturated air pocket was observed in the model domain at around x = 300 m, which may be a pressurized air pocket in reality, but was set to be atmospheric pressure in the calculations. This process should be studied by a two-phase fluid flow approach

which allows the pressurization of air phase fluid. The infiltration of total salt mass slowed down in between 10 to 40 minutes (Figure 6.5a). The vertically infiltrated seawater reached to the water table, and the unsaturated zone beneath the inundated area became fully saturated with saltwater (Figure 6.4c), during which the vertical hydraulic head gradients became much reduced. During 40 min < T < 120 min, the increase of TM became rather small because the unsaturated zone beneath the inundated area had already been fully saturated with saltwater which prevented further saltwater intrusion (Figure 6.4d). These results implied that the unsaturated zone had the role of temporarily storing the intruded seawater during ST-2, and the vertical thickness and porosity of the unsaturated zone determined the maximum amount of seawater that could be possibly infiltrated into subsurface. The slight increase of TM was mainly caused by the seawater infiltration at around x = 1000 m where saltwater flowed horizontally towards the central area of the island.

In ST-3, the groundwater system entered the period of five days with seepage face BC at the land surface after the tsunami inundation event. Two sub-stages can be distinguished via the temporal changes of TM (Figure 6.5b). Before T = 24 h, TM showed a relatively fast decrease, which corresponded to the time when saltwater in the domain which was initially unsaturated was discharged out from the beach zone (at around x = 150 m) and from the depressions in the land surface (e.g., at around x = 500 m). After T = 24 h, TM continued to decrease with a slower rate because of the lowering of the spatial gradient of water table, which reduced the discharge flux through the beach zone (Figures 6.4f and g). The decrease of TM during ST-3 was equivalent to a small portion (about 4%) of the overall increase of TM in ST-2. However, this period was still important but was not fully represented in this study, because after the tsunami retreated to the sea, seawater would remain at local depressions of the land surface and became seawater ponds that would continuously be supplying salt mass into

subsurface. This process should be studied by a 3-D modeling approach with coupled surface and subsurface water flow.

In ST-4, the fresh rainfall recharge started to flush the salinized aquifer. Three sub-stages can be distinguished via the temporal changes of *TM* (Figure 6.5c). Within the first year after the tsunami inundation event, *TM* showed a rapid decrease to about 70%. During this period (Figures 6.4g to i), groundwater table descended to its normal level as the one at the quasi-steady-state. The vertical density-driven flow was dominant during the process. For example, density-driven fingering patterns with the wave-like streamlines were observed at T = 80 d (Figure 6.5h). During the period of 1 yr < T < 10 yr, *TM* was reduced with a nearly linear rate. As time proceeded, unstable fingers began to mix each other by horizontal groundwater flow, and then, dissolved salt migrated horizontally and was discharged out near the coastline (Figures 6.4h to j). Because of the density effect, the saltwater plume had the tendency to descend to the aquifer bottom and migrated along the impermeable bedrock surface towards the seawater-freshwater mixing zone. This implied that the bedrock surface topography may have affected the migration of the saltwater plume. The effects of bedrock structure are further discussed in Section 6.3.5. The modeling results indicated that the groundwater salinity beneath the tsunami inundated area became greater than the Japanese drinking water standard of 0.2 kg/m^3 of Cl^-, which lasted for more than 10 years (Figure 6.4k) while the groundwater salinity in the eastern half domain remained unaffected. After 10 years, about 10% of *TM* still remained at near the saltwater-freshwater mixing zone (Figure 6.4k), and was continued to be discharged out at a slower rate. The full recovery of the tsunami-induced groundwater salinization by natural rainfall recharge in the baseline case required a period of about 15 years (Figure 6.4l), which was consistent with the range of the travel time (5 to 20 years) of fresh groundwater under the normal conditions in the island. This is because the flushing of intruded saltwater was driven mainly by seaward groundwater flow.

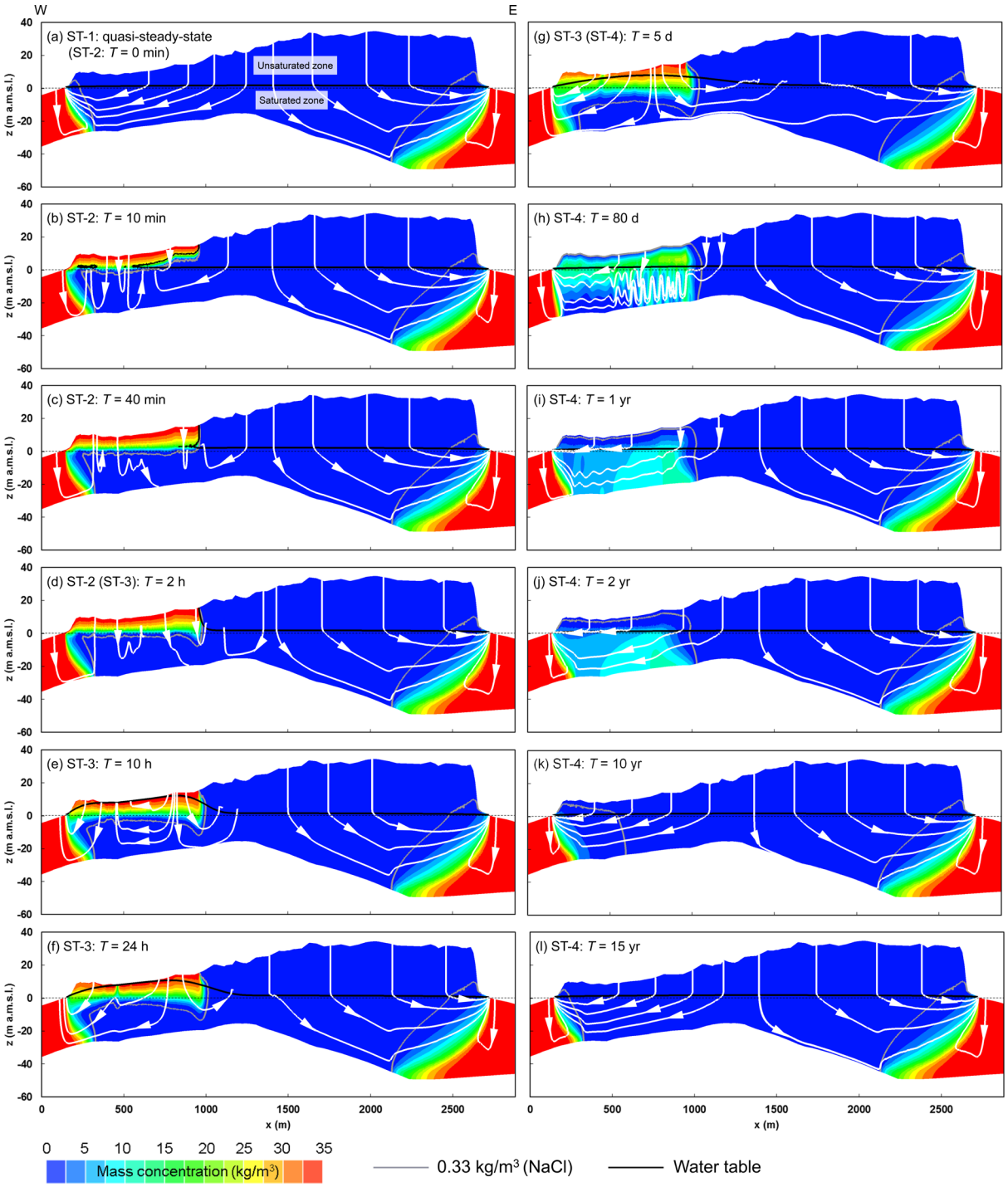

Figure 6.4 The simulation results showing the temporal changes of mass concentrations, water table, and streamlines in the baseline case: (a) ST-1, (a) to (d) ST-2, (d) to (g) ST-3, and (g) to (l) ST-4. The white lines with arrows are streamlines. Note that the streamlines in (a) show the route of water flows at the quasi-steady-state while the ones in (b) to (l) illustrate the directions of flow at the given time during the transient simulation period. The grey lines are the concentration isoline of 0.33 kg/m^3 NaCl which is equivalent to the concentration limit of 0.2 kg/m^3 Cl^- in Japanese drinking water standards (Ministry of Health, Labor and Welfare, 2015) . *T* indicates the time elapsed from the beginning of ST-2 when the tsunami inundation event started. Vertical exaggeration is by a factor of 10.

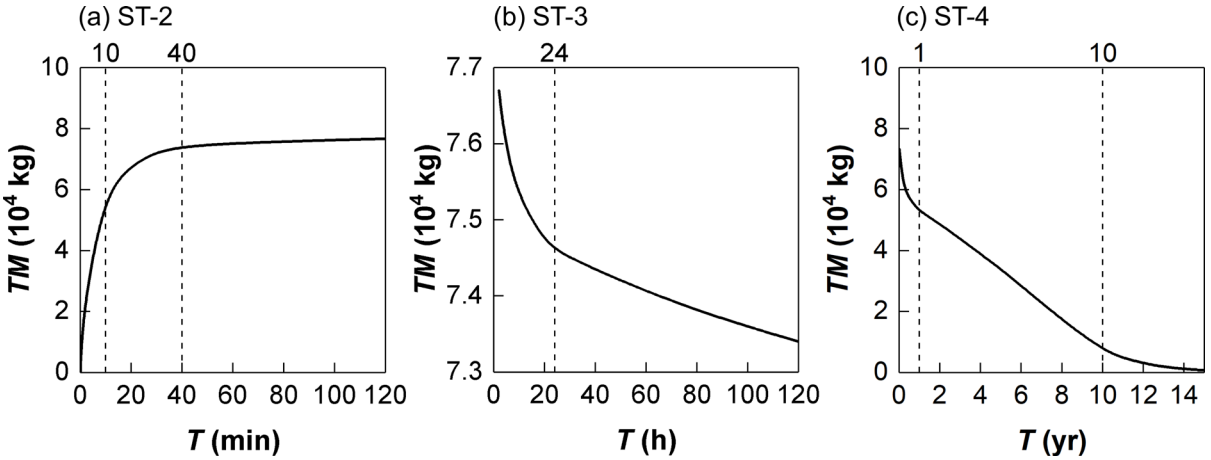

Figure 6.5 The temporal changes of *TM* during (a) ST-2, (b) ST-3, and (c) ST-4 in the baseline case. Note the scale of the *TM* axis in (b) is different from those in (a) and (c).

6.3.2 Element-Based Dimensionless Number Analysis

Figure 6.6 shows the spatial and temporal changes of the element-based dimensionless numbers M_x^E, M_z^E, Ra_d^E, and the locations of the plume cores for the baseline case. At 10 minutes, due to the large downward hydraulic gradients, the vertical hydraulically-driven flow was dominant in the process, and hence, the plume showed a low range of M_z^E (Figure 6.6b), which was similar to the flow regime VH as discussed in Chapter 4. At 80 days, Ra_d^E showed high values at the locations inside of the fingers, i.e., the plume cores, which indicated the vertical density-driven flow was dominant, which was similar to the flow regime VD i as discussed in Chapter 4. M_x^E showed high values at the locations surrounding the fingers, because the vertical density-driven flow was stronger than the horizontal groundwater flow. At two years, though the plume showed a larger area of high Ra_d^E values than that at 80 days, the plume showed a stable pattern which was similar to the flow regime HH as discussed in Chapter 4.

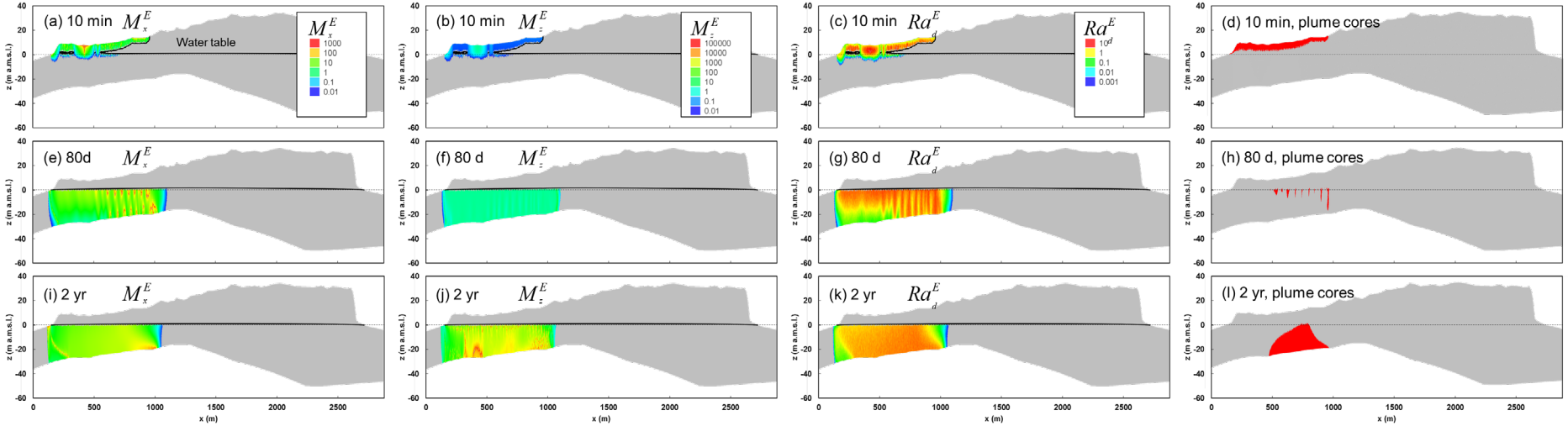

Figure 6.6 Spatial distributions of the element-based dimensionless numbers M_x^E, M_z^E, Ra_d^E, and the plume cores for the simulations results of the baseline case at 10 minutes, 80 days, and 2 years. See the corresponding simulation results in Figure 6.4.

Figure 6.7 showed the plot of the element-based dimensionless numbers at the plume cores on the diagram of M_x^E, M_z^E, and Ra_d^E. The transition from 10 minutes to 80 days showed a similar trend of flow regime shift from VH to VD (Figure 4.4), i.e., increases of M_z^E. However, the plume cores at 2 years had a high range of M_z^E than 80 days but showed a stable pattern. This was mainly because that the plume core could not penetrate into a deeper part of the aquifer, e.g., M_z^E showed high values at the plume cores near the aquifer bottom where the downward velocities were reduced. These results may imply that, if the aquifer had a large thickness than that in the baseline case, fingers, rather than the stable patterns, could have occurred at 2 years.

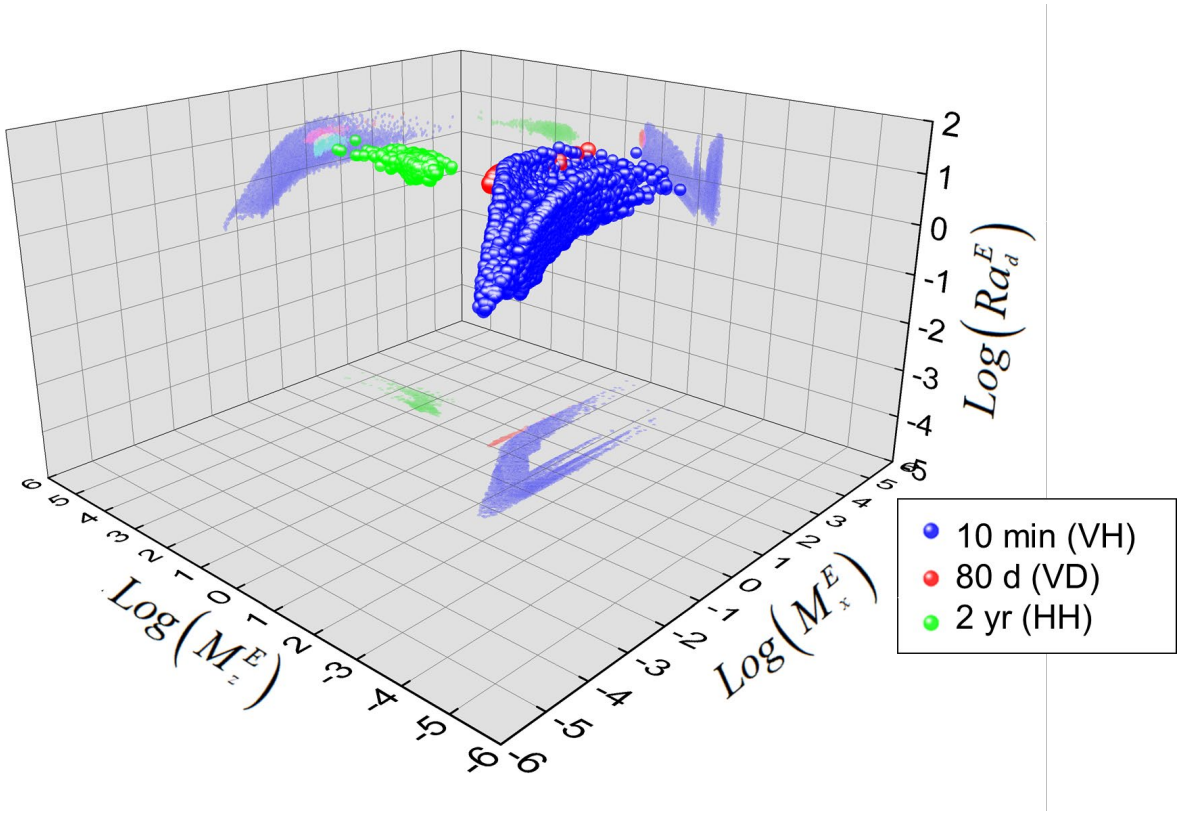

Figure 6.7 The plots of the element dimensionless numbers at the plume cores for the simulation results of the baseline case at 10 minutes, 80 days, and 2 years on the diagram of M_x^E, M_z^E, and Ra_d^E.

6.3.3 Uncertainties of Tsunami Inundation Scenarios

The temporal changes of *TM* in ST-2 and ST-4 when $h_T(t)$ was varied from 5 to 25 m a.m.s.l. are shown in Figure 6.8a. The scenario with a higher $h_T(t)$ showed a larger *TM* with a greater increasing rate in ST-2 (Figure 6.9a1) because of the larger downward hydraulic head gradients and the larger area of the inundated land surface. The tsunami of $h_T(t)$ = 5 m a.m.s.l. inundated the land surface of about only 40 m in horizontal distance from the coastline, and hence, it caused limited impacts on the groundwater system. *TM* in the cases with $h_T(t)$ of 10 and 20 m a.m.s.l. decreased rapidly within the first year after the tsunami, and then, began to decrease with a slower rate in ST-4 (Figure 6.9a2), which was similar to the decreasing pattern of *TM* in the baseline case. This is because the tsunami with $h_T(t)$ of 10, 15, and 20 m a.m.s.l. induced groundwater salinization only in the western half domain (x < 1050 m). However, under the extreme scenario of $h_T(t)$ = 25 m a.m.s.l., the tsunami inundation was extended to further inland area up to about x = 1300 m, and a portion of the saltwater plume crossed the structural high of the bedrock surface at the central part of the island and migrated along the slopes of the bedrock surface towards east (Figure 6.9). Though the eastern half domain was not directly inundated by the tsunami, it became salinized by the migration of saltwater that originated from the tsunami event at the western half domain. This phenomenon was driven mainly by the fact that some saltwater entered the eastern half domain where groundwater flowed towards east, and the dome-like bedrock structure contributed to the movement of the dense plume towards east. After 20 years, the majority of the groundwater resources became salinized and was not appropriate for drinking purpose (Figure 6.9e). The overall freshening process of the polluted groundwater system by rainfall recharge required a period more than 25 years.

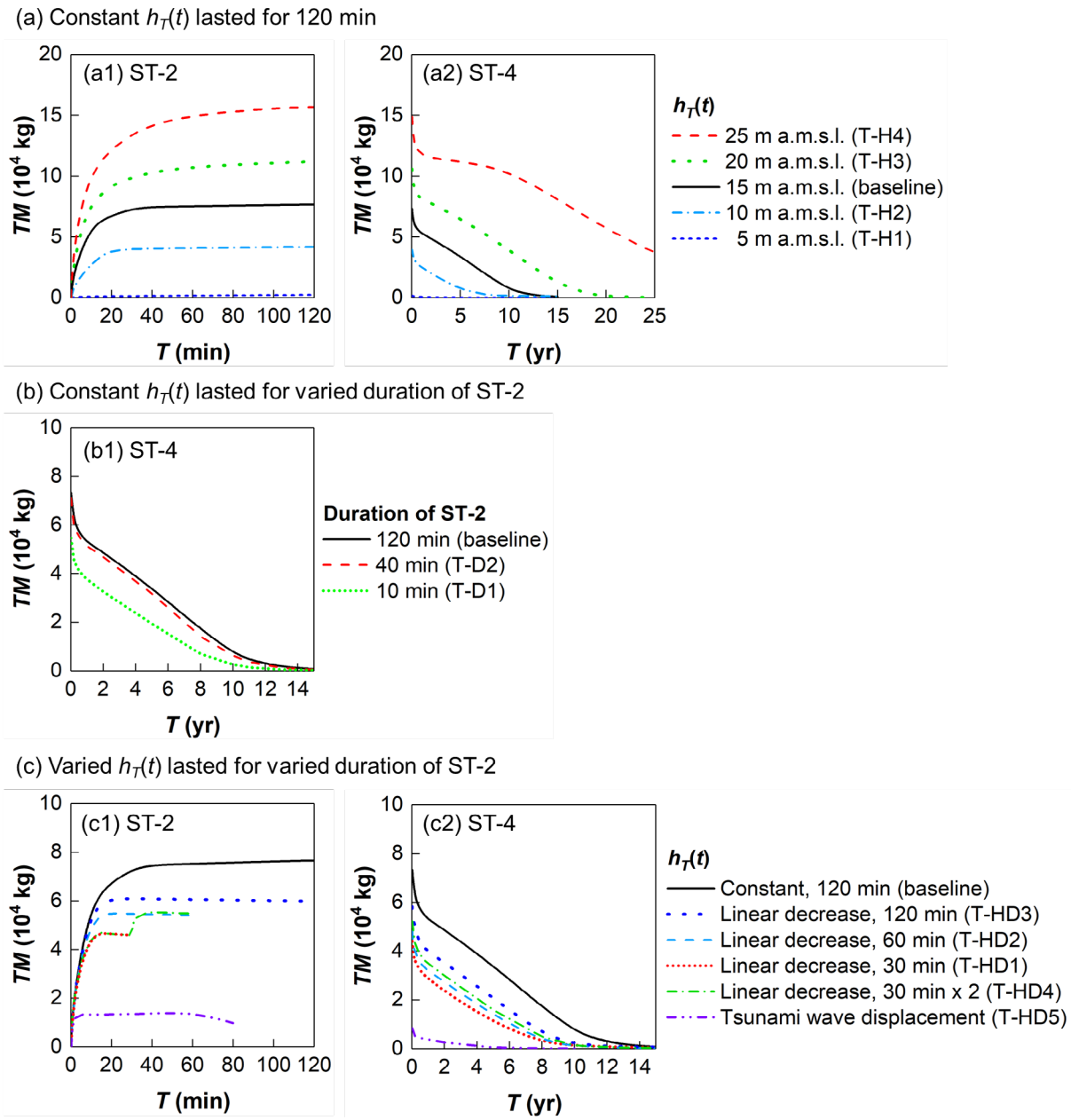

Figure 6.8 The temporal changes of *TM* during ST-2 and ST-4 for the simulation cases with varied settings of tsunami inundation scenarios: (a) $h_T(t)$ was varied from 5 m a.m.s.l. to 25 m a.m.s.l. while $h_T(t)$ was kept constant over time in each case; and (b) $h_T(t)$ of 15 m a.m.s.l. was kept constant for 10, 40, and 120 minutes; and (c) $h_T(t)$ was temporally varied over time during ST-2 (see details in Figure 6.3a).

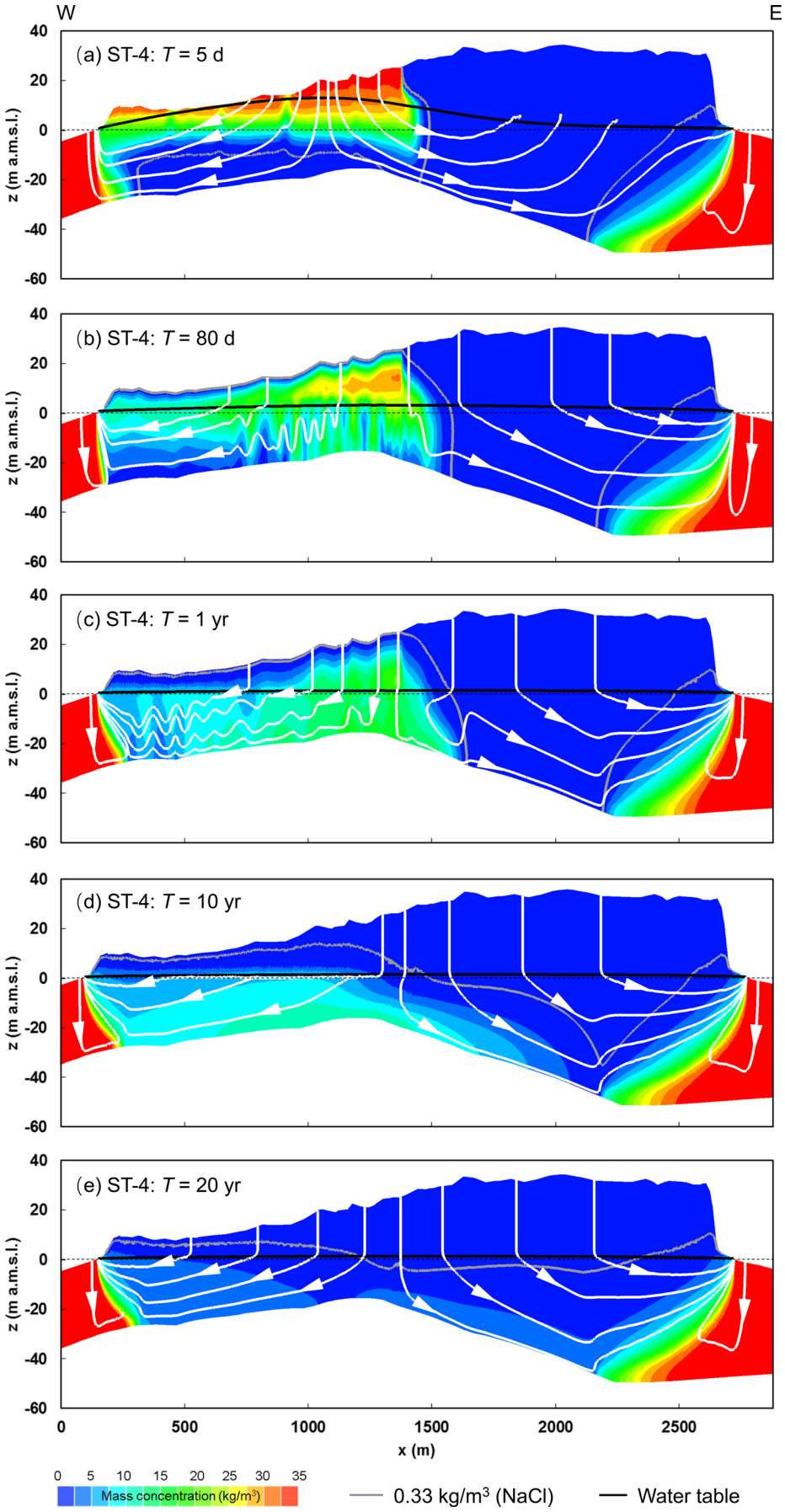

Figure 6.9 The simulation results showing the temporal changes of concentrations, water table, and streamlines in ST-4 for the case of $h_T(t)$ = 25 m a.m.s.l. (the case T-H4). Vertical exaggeration is by a factor of 10.

The temporal changes of *TM* in ST-4 when the duration of ST-2 was varied from 10 to 120 minutes are shown in Figure 6.8b. Reducing the duration of ST-2 from 120 to 40 minutes caused minimal differences of the *TM* curves in ST-4 because the vertical infiltration of seawater became much smaller after 40 minutes (Figure 6.5a). Though the duration of ST-2 was significantly reduced to 10 minutes, a period of more than eight years was still required for the salinized aquifer to be freshened by the rainfall recharge. This is because the tsunami of $h_T(t)$ = 15 m a.m.s.l. for 10 minutes supplied about 70% of *TM* in the baseline case.

Figure 6.8c shows the temporal changes of *TM* during ST-2 and ST-4 of the simulation cases that adopted the settings of temporally varied $h_T(t)$ (see the detailed settings in Figure 6.3a). Compared with the baseline case in ST-2, when $h_T(t)$ became temporally varied (the cases T-HD1 to T-HD4), the increase of *TM* became smaller, but a period of more than seven years was still required for the polluted aquifer to be recovered by the rainfall recharge. In the case T-HD5, after the inundation by the first tsunami wave of 15 m a.m.s.l. for about two minutes, the tsunami started to inundate that area mainly below 8 m a.m.s.l in the rest of the inundation period. Therefore, compared with the baseline case, the case T-HD5 resulted in less infiltration of seawater into subsurface, and the period for its full recovery was about four years. However, according to Figure 6.10, the case T-HD5 still produced a considerably large model domain with a concentration higher than the drinking water standards (0.33 kg/m^3 of NaCl), which affected the western part of the aquifer for about two to four years. The amount of seawater infiltration in the case T-HD5 was likely to be underestimated because the spatially constant $h_T(t)$ was assumed to be equal to the wave displacement at the ocean surface, however, in an actual tsunami inundation event, seawater could remain at the land surface and continue to infiltrate after the retreat of tsunami waves. Therefore, reducing the model uncertainties from tsunami scenarios would require the coupling of surface and subsurface flow processes together with tsunami inundation modeling.

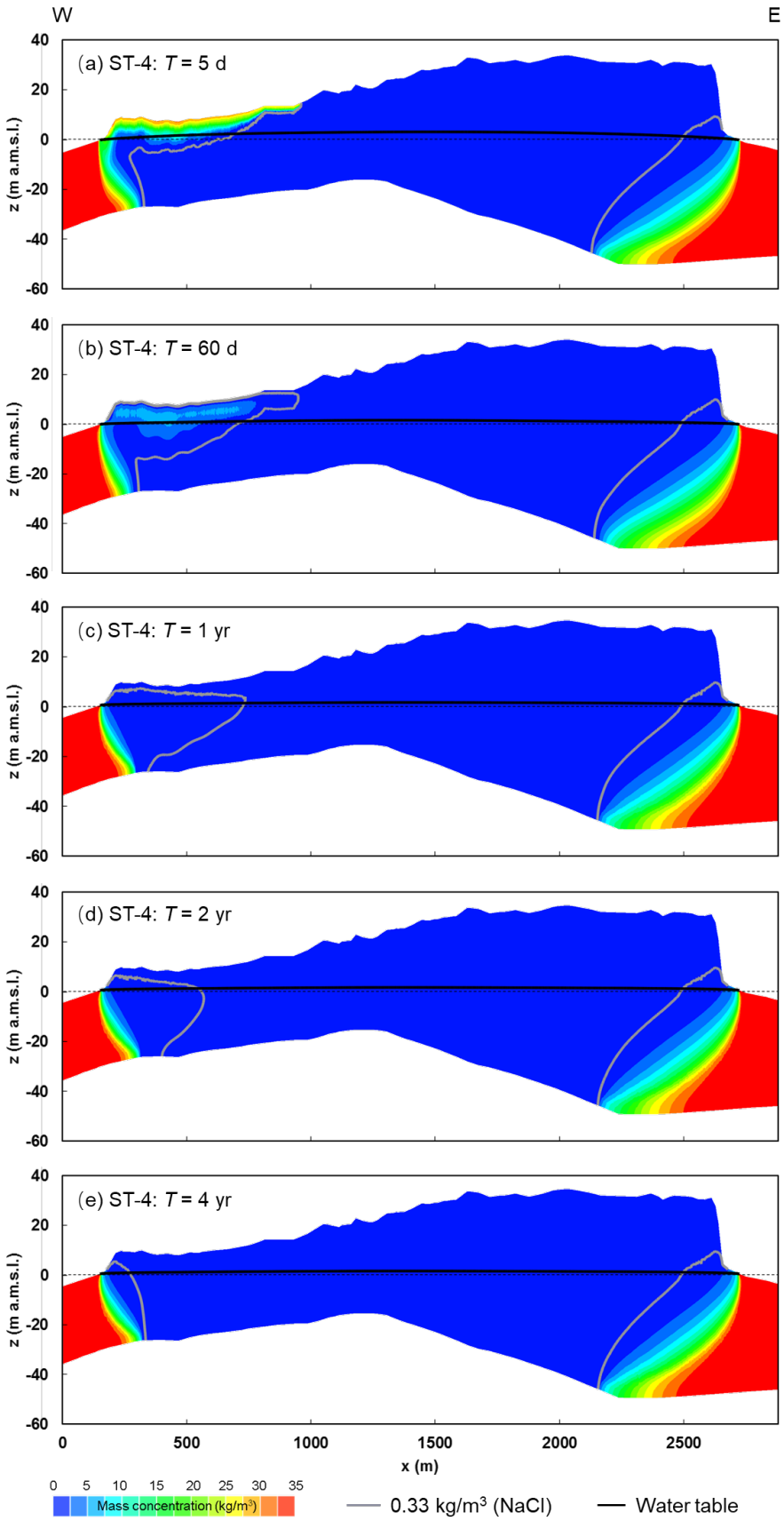

Figure 6.10 The simulation results showing the temporal changes of mass concentrations and water table in ST-4 for the case T-HD5 which set $h_T(t)$ according to the tsunami wave displacement that was simulated by Tokyo Metropolitan Government (2013) (Figure 5.9b). Vertical exaggeration is by a factor of 10.

6.3.4 Uncertainties of Rainfall Recharge BCs

The temporal changes of *TM* in ST-4 when the duration of ST-3 was varied from 1 to 30 days are shown in Figure 6.11a. The variations of the duration of ST-3 within this range showed no significant impacts on the *TM* curve in ST-4. This reflected that the duration of ST-3 (the period from the end of tsunami inundation event to the arrival of first rainfall event) was not likely to significantly influence the modeling results of ST-4. However, these results may remain uncertain if the evaporation and infiltration processes of ponded seawater at land surface was simulated. This should also be further studied by a coupled surface and subsurface water model.

The temporal changes of *TM* in ST-2 and ST-4 when the setting of $R(t)$ were varied are shown in Figure 6.11b. In ST-2, the uncertainties of $R(t)$ within the range of 662 to 1104 mm/yr, i.e., K of 8.1×10^{-4} to 1.3×10^{-3} m/s, showed no significant influence on the increase of *TM*. In ST-4, the case with a higher $R(t)$ (and a higher K) showed a faster decrease of *TM*, i.e., faster removal of intruded saltwater in the groundwater system. This is because the increase of $R(t)$ enhanced the freshening of the polluted aquifer, and the increase of K allowed faster transport of the intruded salt mass from the inland to the coast. However, the case with a relatively high recharge rate $R(t)$ = 1104 mm/yr still required a period of more than eight years for the polluted aquifer to be recovered. There were basically no differences in the *TM* curves of the cases with daily and seasonal variations of $R(t)$ compared with that of the baseline case. These results implied that, with the current setting of the Niijima Island, whether the tsunami occurred in a rainy or dry season was not like to cause large differences in the aquifer recovery process. This is perhaps because these temporal variations of $R(t)$ caused only minor fluctuations of groundwater table of about 0.7 m at maximum, and did not significantly affect the horizontal groundwater flow rate which controlled the flushing of salt mass.

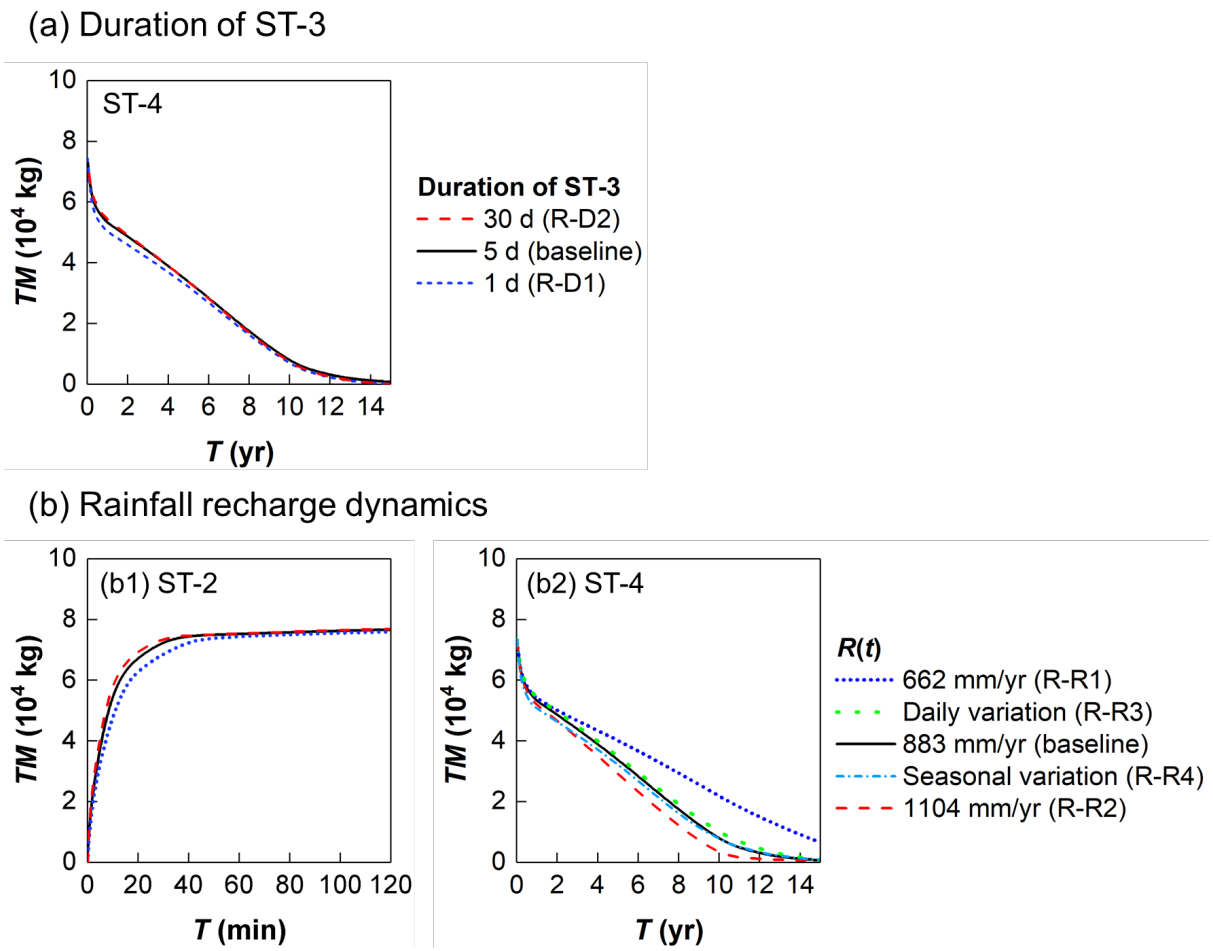

Figure 6.11 The temporal changes of *TM* during ST-2 and ST-4 for the simulation cases with varied settings: (a) the duration of ST-3 was varied from 1 to 30 days; and (b) $R(t)$ was varied from 662 to 1104 mm/yr while the ratio R/K was kept constant, and $R(t)$ with daily and seasonal variation.

6.3.5 Uncertainties of Aquifer properties

The uncertainties of K with the isotropic setting ($K_z/K_x = 1$) are discussed together with $R(t)$ in Section 6.3.4 while uncertainties of the ratio K_z/K_x (K_x was kept constant) are presented in this section. The temporal changes of *TM* in ST-2 and ST-4 when K_z/K_x was varied from 0.1 to 1 are shown in Figure 6.12a. When K_z/K_x was decreased by one order of magnitude, the increase of *TM* at early time steps (before T = 40 min) in ST-2 became slower. As time proceeded in ST-2, the discrepancy among *TM* curves of the cases with varied K_z/K_x became smaller. This is because lower ratios of K_z/K_x (i.e., a lower K_z) reduced the vertical infiltration rate of seawater during the tsunami inundation event, which prolonged the process for the unsaturated zone to be filled up with intruded seawater. For example, the unsaturated zone had

not been fully saturated by the intruded seawater at T = 120 min in the case with K_z/K_x = 0.1 (Figure 6.13), compared with that of the baseline case with K_z/K_x = 1 (Figure 6.4d). In the case with K_z/K_x = 0.1, though *TM* at the end of ST-2 was reduced to be about 70% of that in the baseline case, the recovery of the aquifer system required a period of more than eight years. The *TM* curves with varied K_z/K_x showed a similar decreasing rate after about one year in ST-4 (Figure 6.12a2) because changes of K_z did not influence horizontal groundwater flow and mass transport which was the dominant process for removing the intruded saltwater from the aquifer. With a lower K_z, the vertical density effect in ST-4 was reduced. For example, the saltwater plume was rather stable in the case with K_z = 0.1 (Figure 6.13) compared with that in the baseline case (Figure 6.4h).

The temporal changes of *TM* in ST-2 and ST-4 when K was varied from 1.1×10^{-3} m/s to 1.1×10^{-4} m/s are shown in Figure 6.12b. Though the case A-K1 with $K = 1.1 \times 10^{-4}$ m/s resulted in a rise of groundwater table at the normal condition (at the end of ST-1) and a thinner unsaturated zone compared with that of the baseline case with $K = 1.1 \times 10^{-3}$ m/s, this case may represent an island setting with K that was one order magnitude lower than that of the Niijima Island. This decrease in K reduced both vertical and horizontal flux with respect to: (1) a lower infiltration rate of seawater during ST-2 and about 36% decrease of *TM* at the end of ST-2; (2) a slower recovery process of the aquifer during ST-4; and (3) a rather stable flow pattern (Figure 6.14). These results suggested that a coastal unconfined aquifer with a lower K may be less vulnerable in terms of a less amount of seawater infiltration under the same tsunami inundation condition during ST-2, however, may require a longer recover period given the same amount of rainfall recharge during ST-4.

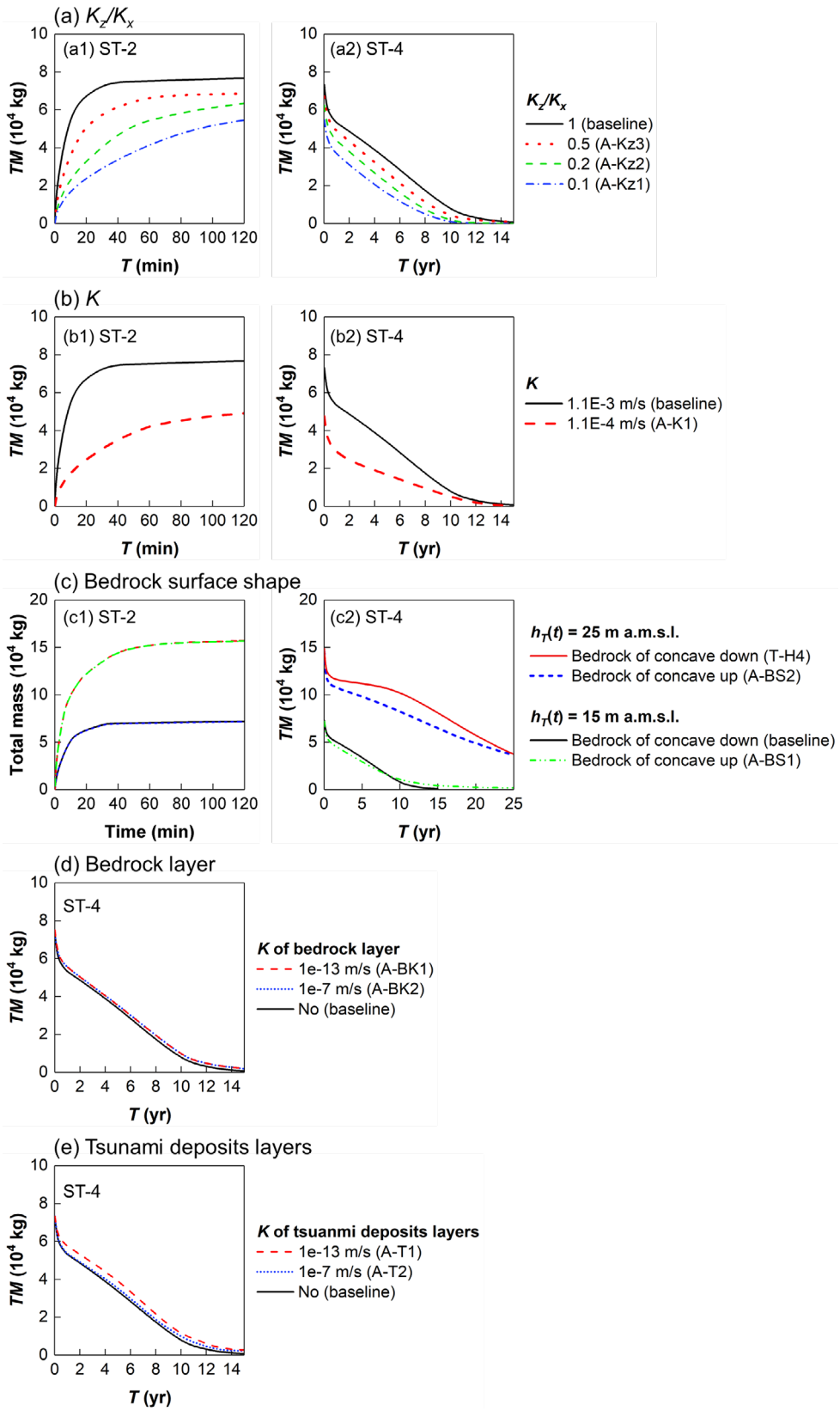

Figure 6.12 The temporal changes of *TM* during ST-2 and ST-4 for the simulation cases with varied settings of aquifer properties: (a) the ratio K_z/K_x was varied from 0.1 to 1; (b) K of the aquifer materials was varied from 1.1 × 10^{-3} m/s to 1.1 × 10^{-4} m/s; (c) the bedrock surface topography in a concave up shape with $h_T(t)$ of 15 and 25 m a.m.s.l.; (d) the effect of a bedrock layer with K of 1.1 × 10^{-13} m/s and 1.1 × 10^{-7} m/s; and (e) the effect of the tsunami deposits layers with K of 1.1 × 10^{-13} m/s and 1.1 × 10^{-7} m/s.

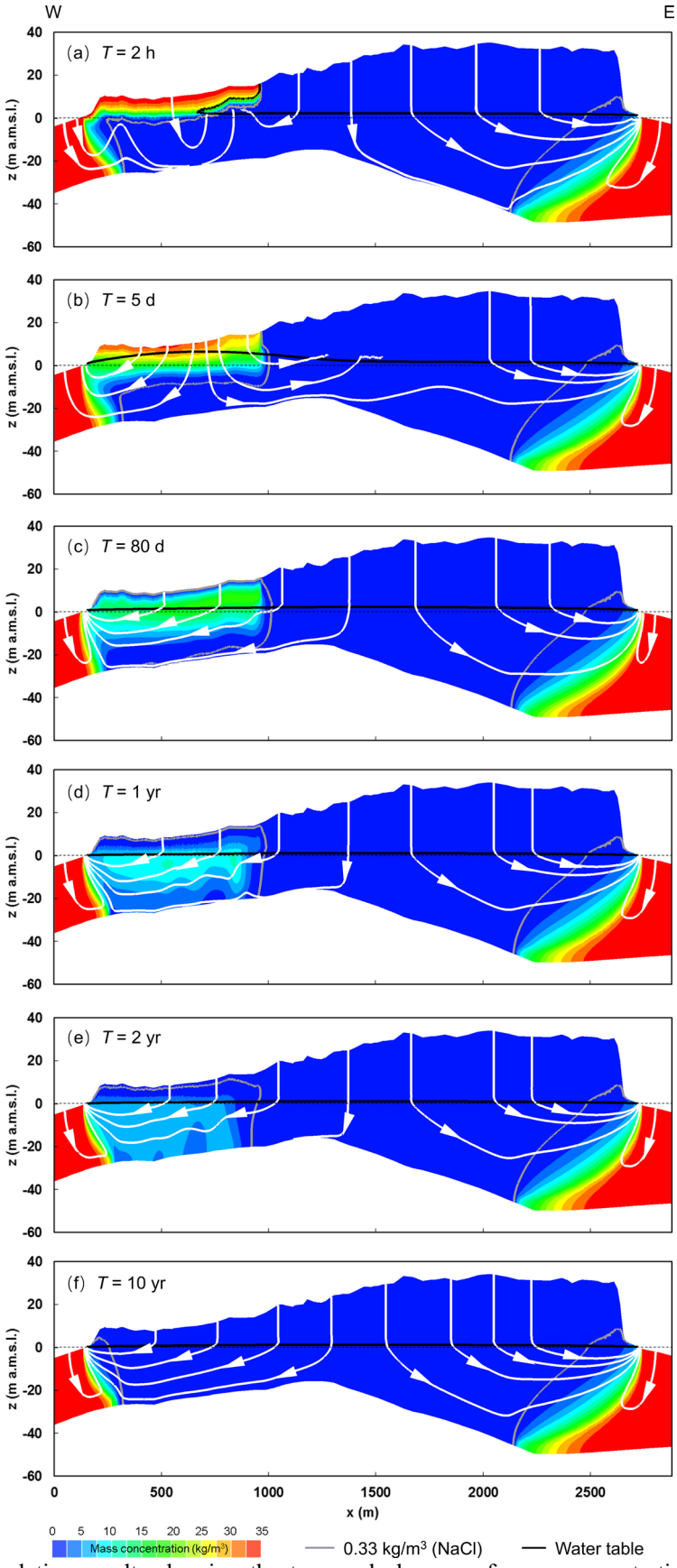

Figure 6.13 The simulation results showing the temporal changes of mass concentrations, water table, and streamlines in (a) ST-2, and (b) to (f) ST-4 for the case with K_z/K_x = 0.1 (the case A-Kz1). Vertical exaggeration is by a factor of 10.

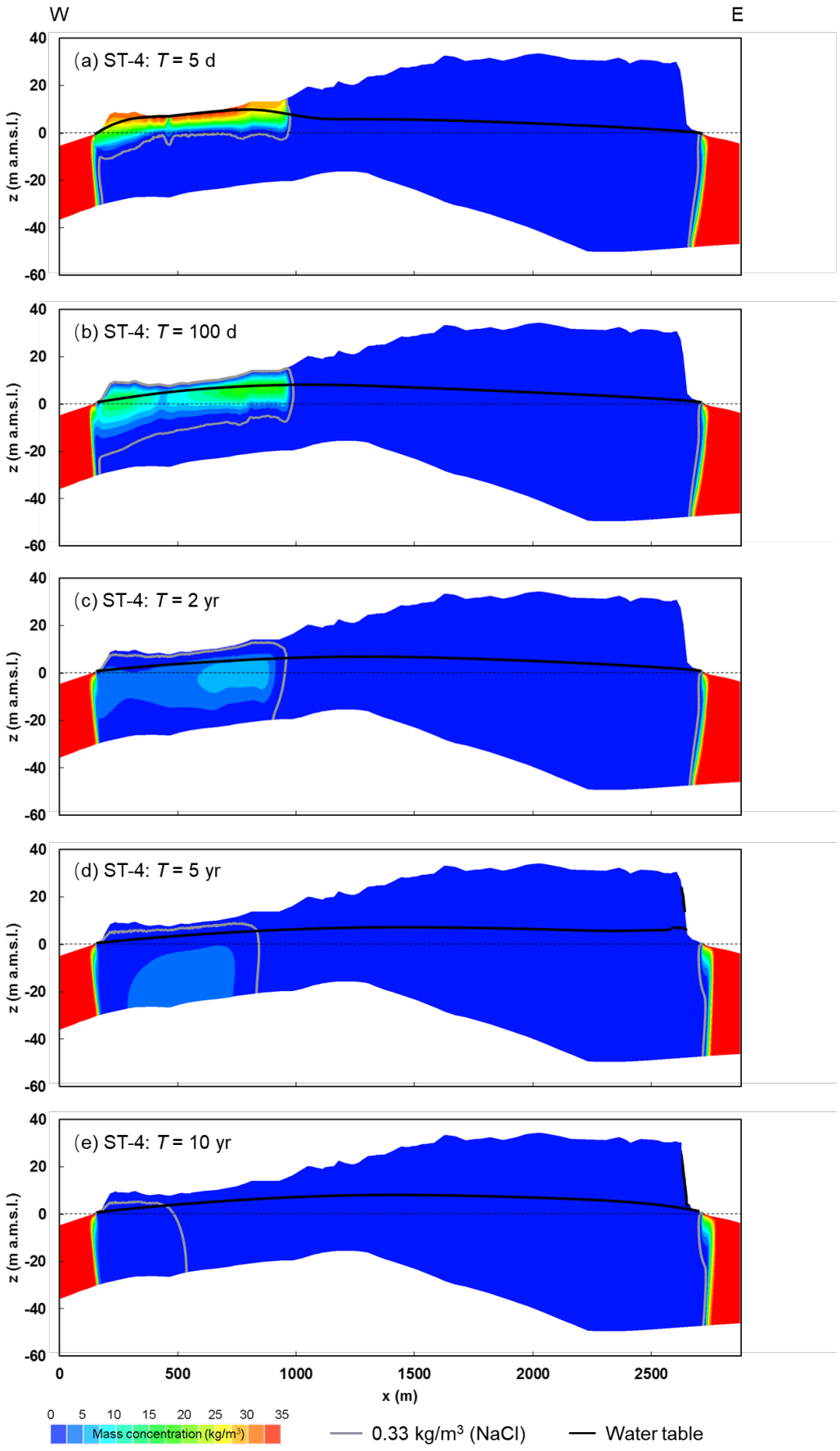

Figure 6.14 The simulation results showing the temporal changes of mass concentrations and water table during ST-4 for the case with $K = 1.1 \times 10^{-4}$ (the case A-K1). Vertical exaggeration is by a factor of 10.

The temporal changes of *TM* in ST-2 and ST-4 when varied settings of the bedrock surface are shown in Figure 6.12c. The distinct bedrock settings showed no difference in the increase of the *TM* curves in ST-2, when comparing the case A-BS1 with the baseline, and A-BS2 with T-H4. When $h_T(t)$ was set to be 15 m a.m.s.l., the discrepancy between the *TM* curve of the case A-BS1 and that of the baseline case in ST-4 was rather small. However, for plume behavior in the case A-BS1 during ST-4 (Figure 6.15a), compared with that in the baseline case (Figure 6.15c), the fingers reached to a lower depth at around x = 900 m at T = 80 d, and the seaward movement of the 0.33 kg/m^3 isoline was delayed. When $h_T(t)$ was set to be 25 m a.m.s.l., the effects of bedrock structure became more noticeable in ST-4. For example, during the period of 10 yr < T < 25 yr in ST-4, *TM* showed a higher decreasing rate in the case T-H4 than that in A-BS2 (Figure 6.12b). This is because, during this period, the dense salt mass tended to remain in the central bottom part of the bowl-like bedrock structure in the case A-BS2, and intruded saltwater was discharged out mainly through the western coast (Figure 6.15b5) while the salt mass began to be flushed out from both the western and eastern coasts in the case T-H4 (Figure 6.9d). The overall impacts of the bedrock structure on the modeling results were moderate, probably because the bedrock surface was inclined with a small slope (around 2 m over a horizontal distance of 100 m in average) in both cases. However, it is still reasonable to emphasize the importance of bedrock structures that may strongly affect the transport of salt mass in an aquifer with a much steeper bedrock surface topography than that in this paper. Sensitivity analysis should be further carried out with a variety of bedrock structure settings in 3-D domains.

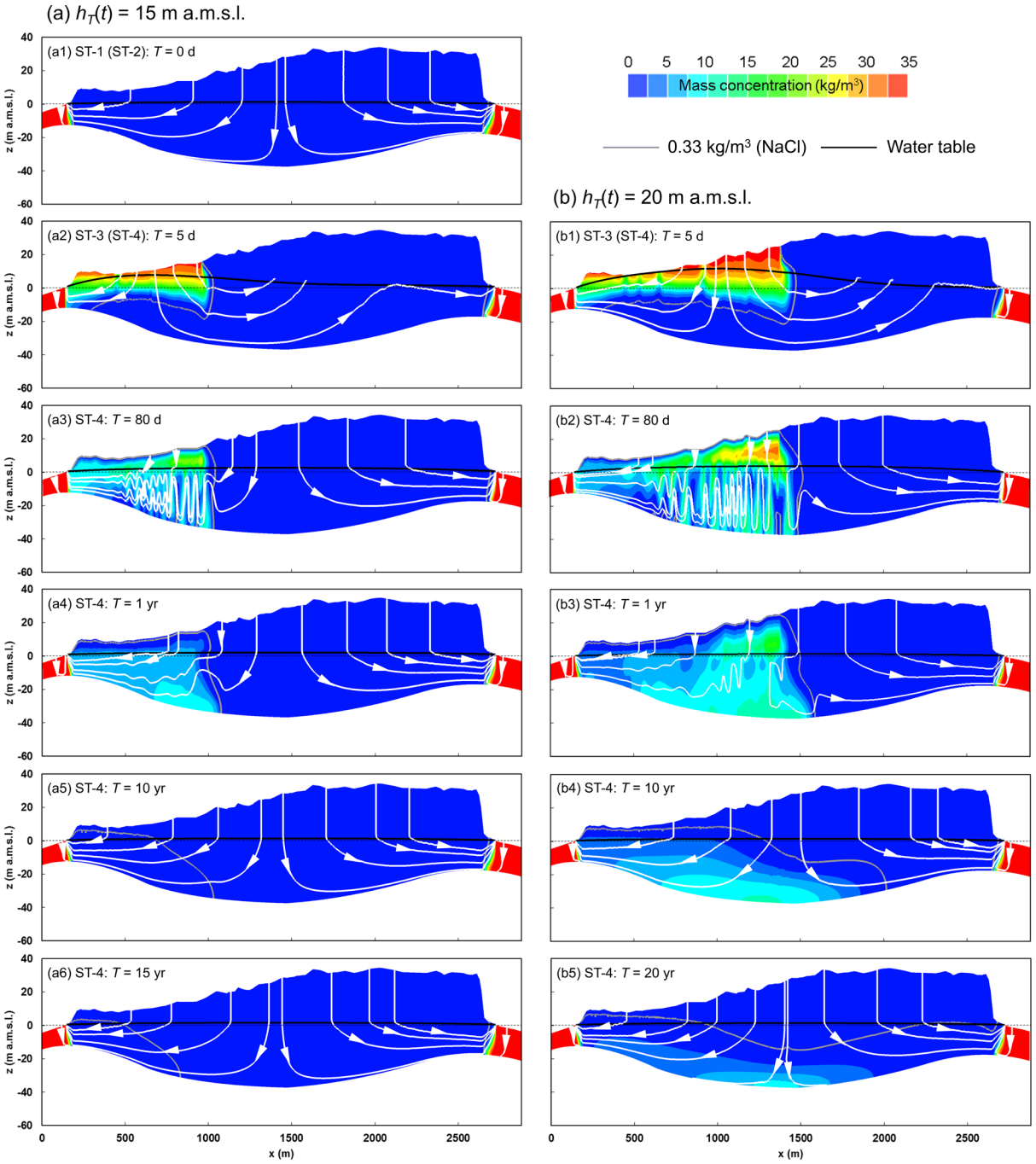

Figure 6.15 The simulation results showing the temporal changes of mass concentrations, water table, and streamlines with the setting of in a concave up bedrock shape with (a) $h_T(t)$ = 15 m a.m.s.l. (the case A-BS1) and (b) $h_T(t)$ = 25 m a.m.s.l. (the case A-BS2). Vertical exaggeration is by a factor of 10.

The settings of a bedrock layer with $K = 1.1 \times 10^{-13}$ m/s and $K = 1.1 \times 10^{-7}$ m/s showed very similar aquifer recovery processes in terms of the decreases of *TM* compared to the setting of an impermeable bottom of the aquifer in the baseline case (Figure 6.12d). This is because these bedrock layers (K of 1.1×10^{-13} m/s to 1.1×10^{-7} m/s) had negligible influence on the

groundwater flow patterns in the aquifer layer (K of 1.1×10^{-3} m/s), which can be observed by comparing the streamlines in Figure 6.16 with those in Figure 6.4. During ST-4, most of the intruded saltwater migrated along with the horizontal groundwater flow in the aquifer layer towards the coastal zone, while only a small amount of seawater could enter the bedrock layer from the aquifer layer. This can be further proved by Figure 6.17 which shows that at the interface between the aquifer layer and the bedrock layer, the horizontal fluid velocities (towards $x = 0$) were generally one order magnitude larger than the downwards velocity and that the majority of the velocity directions were in coincidence with the bedrock surface slope.

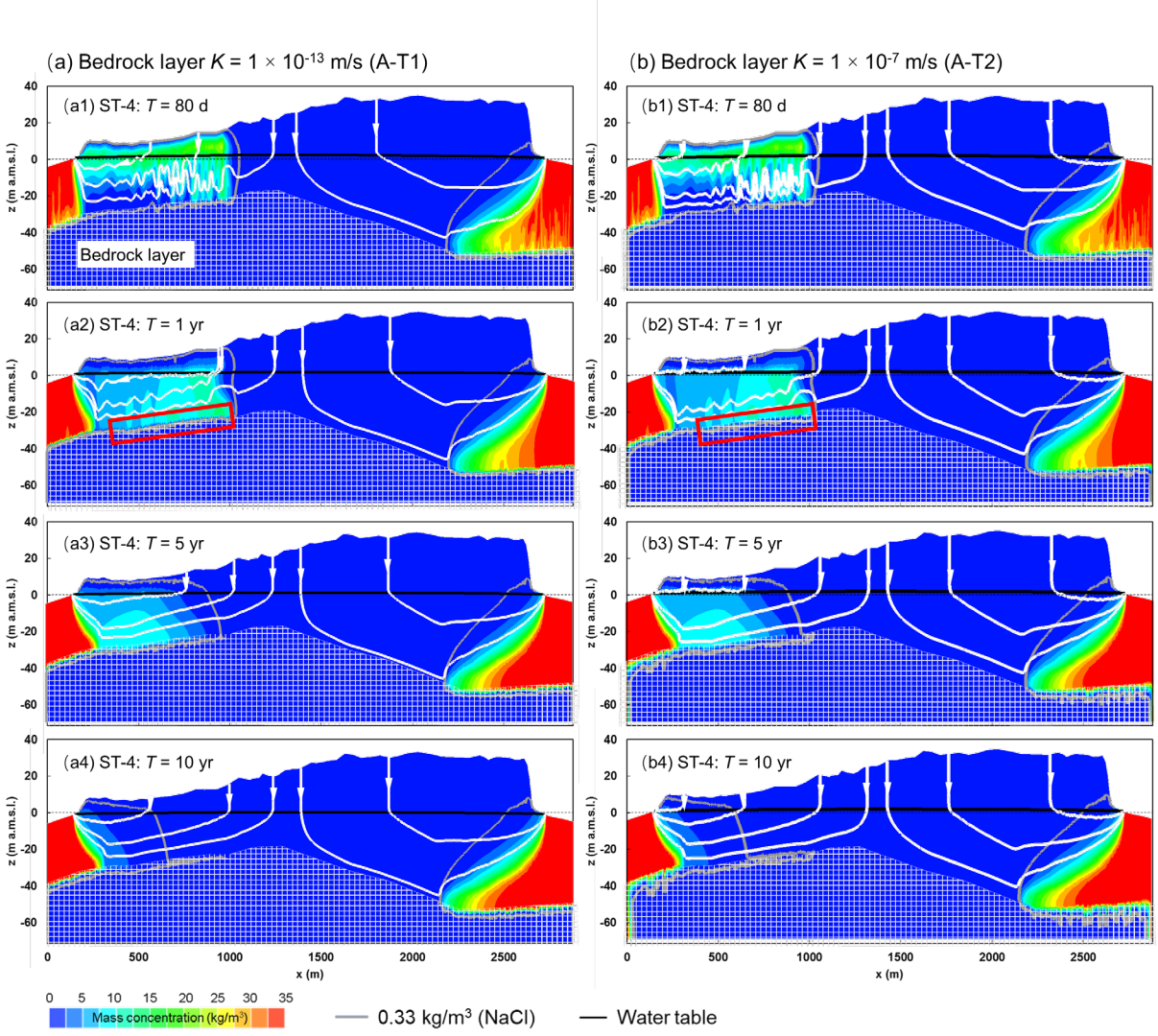

Figure 6.16 The simulation results showing the temporal changes of mass concentrations, water table, and streamlines during ST-4: (a) a bedrock layer with $K = 1.1 \times 10^{-13}$ m/s (the case A-BK1); and (b) a bedrock layer with $K = 1.1 \times 10^{-7}$ m/s (the case A-BK2). Vertical exaggeration is by a factor of 10.

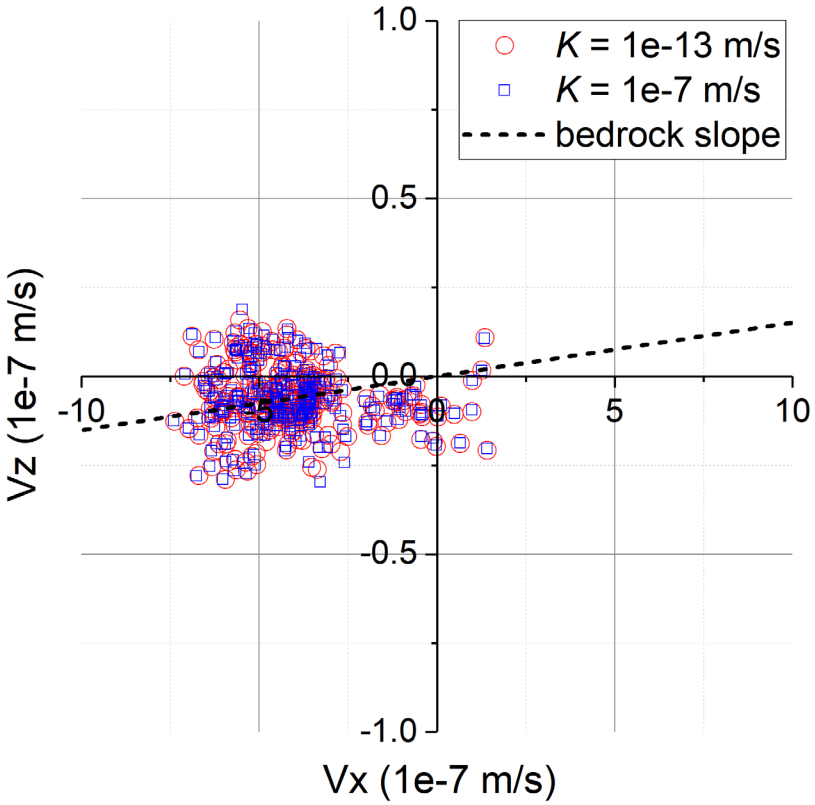

Figure 6.17 Plots of horizontal and vertical fluid velocity v_x and v_z of the nodes at the interface between the aquifer layer and the bedrock layer for the simulation cases A-BK1 and ABK2 at 1 year after the tsunami. See the location of the selected interface at the red frame in Figure 6.16. The plots were compared with the average slope of the selected interface.

The cases A-T1 and A-T2 considered the tsunami deposits layers with K of 1.1×10^{-13} m/s and 1.1×10^{-7} m/s, respectively, at the inundated land surface since the beginning of ST-4. Compared with the baseline case (Figure 6.4), the tsunami layers with $K = 1.1 \times 10^{-13}$ m/s prevented the saltwater in the unsaturated zone to be freshened by the rainfall recharge up to about 5 years after the tsunami (Figure 6.18a). This effect was less significant in the case with the tsunami deposits layers of $K = 1.1 \times 10^{-7}$ m/s. In general, the overall decrease of *TM* was not significantly influenced by these tsunami deposits layers (Figure 6.12e). However, after an actual tsunami inundation event, some seawater may remain above the low-permeability layers of tsunami deposits and continuously infiltrate into subsurface and prolong the aquifer recover processes. This phenomenon should be further studied by coupling surface and subsurface flow modeling.

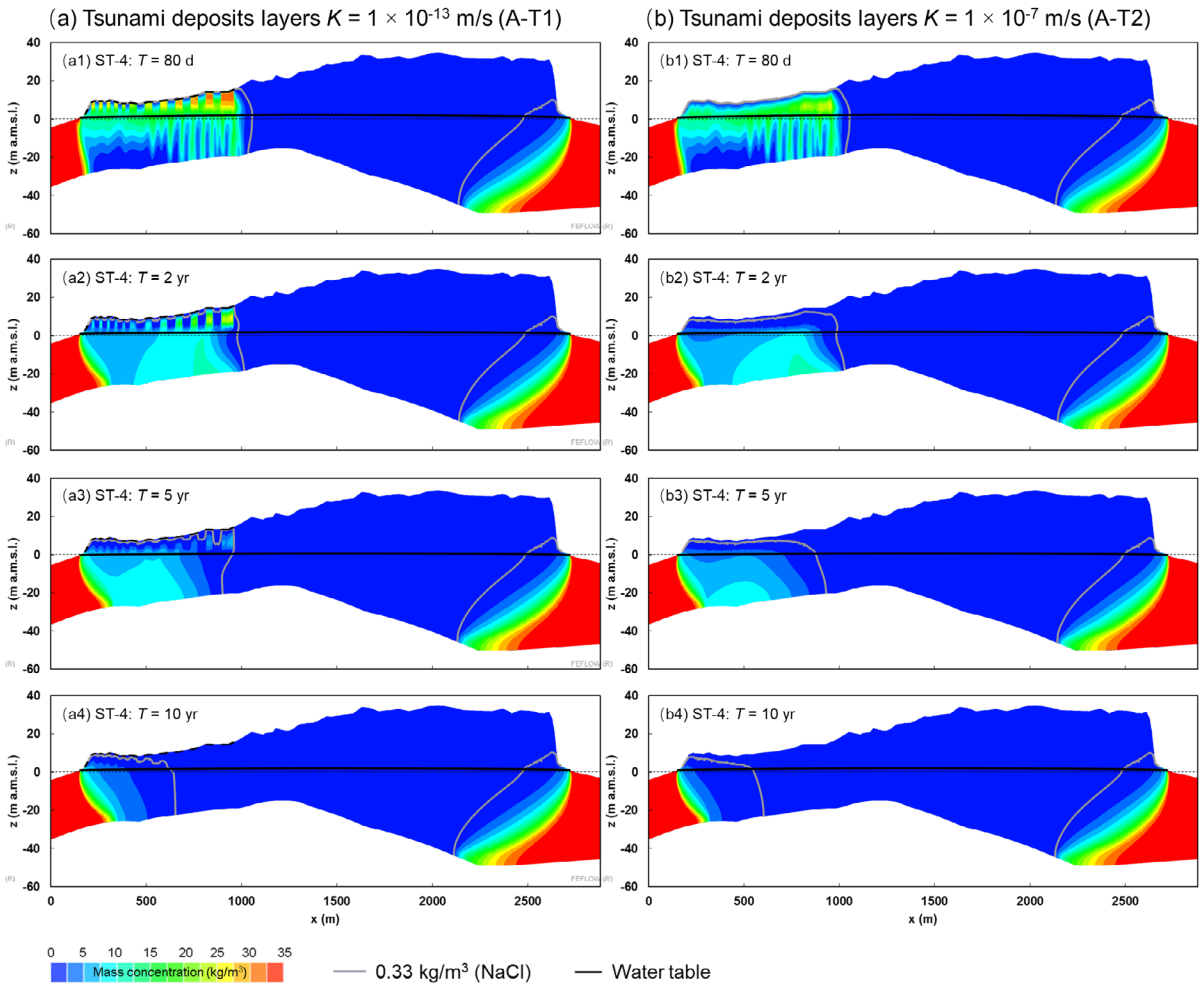

Figure 6.18 The simulation results showing the temporal changes of mass concentrations and water table during ST-4: (a) tsunami deposits layers with $K = 1.1 \times 10^{-13}$ m/s (the case A-T1); and (b) tsunami deposits layers with $K = 1.1 \times 10^{-7}$ m/s (the case A-T2). Vertical exaggeration is by a factor of 10.

6.3.6 Uncertainties of Numerical Parameters

Figure 6.19 shows the simulation results that assumed seawater density ρ_s to be 1000 kg/m^3 (no density contrast), 1002.5 kg/m^3 (low density contrast), and 1250 kg/m^3 (extremely high density contrast), respectively. When no density contrast was assumed, no fingering pattern was observed during ST-4, and the mass concentration distributions showed no influence on the streamlines. With a higher density contrast, the fingering flow patterns became stronger and occurred in an earlier stage. When assuming the extremely high seawater density (ρ_s = 1250 kg/m^3), the saltwater plume remained in the depression of the bedrock surface and became rather stagnant (see the circulation of streamlines near the aquifer bottom in Figure

6.19c4). With a higher seawater density assumed, the decrease of ST-4 showed an earlier turning point, which resulted in a longer recovery period (Figure 6.20). This was because the majority of the intruded saltwater descended to the aquifer bottom within a shorter period in the high density contrast case, while in the later stage (around 5 to 25 years) *TM* decreased with a similar rate among the different seawater density cases. These results proved that groundwater flow could flush the intruded saltwater remained in the depression of bedrock surface even when an extremely high density contrast was assumed. This is because for flow and mass transport processes in porous media, dispersion causes the spreading of mass both transversely and longitudinally along the flow direction (Figure 3.8d in Section 3.2.4). Moreover, the bedrock surface in the cases A-BS1 and A-BS2 was inclined with a relatively small slope (around 2 m over a horizontal distance of 100 m in average) in this study (Figure 6.3c).

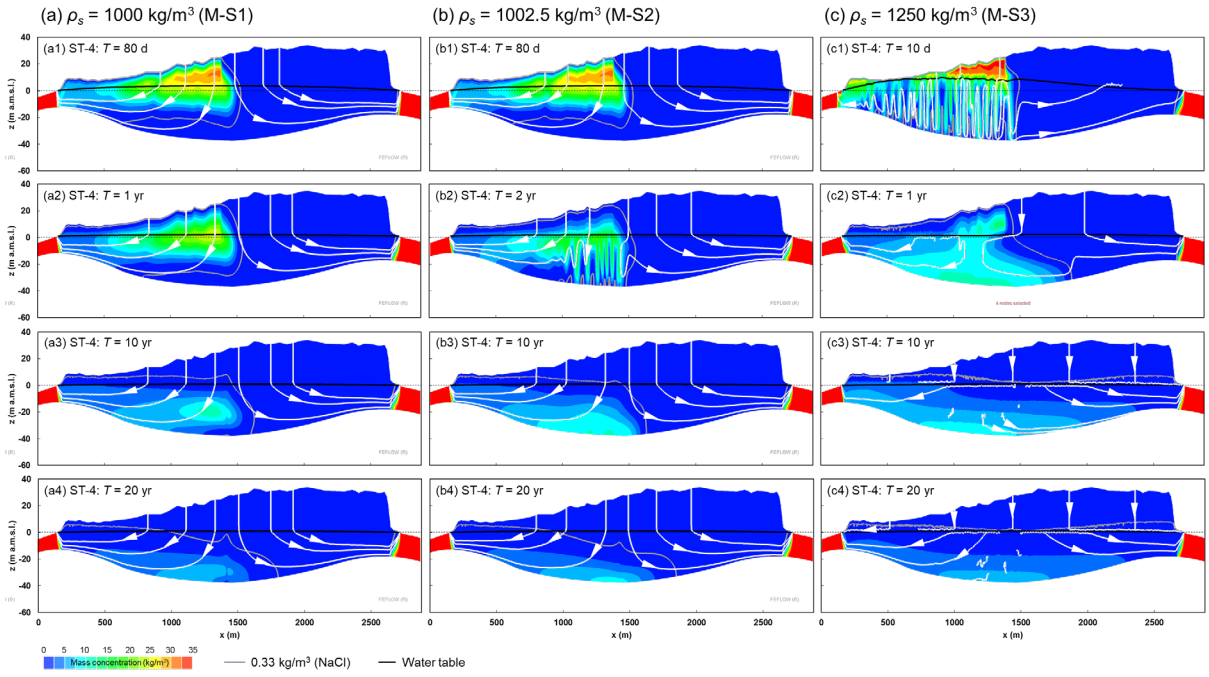

Figure 6.19 The simulation results showing the temporal changes of mass concentrations, water table, and streamlines during ST-4 with varied settings of seawater density: (a) ρ_s = 1000 kg/m^3 (M-S1), (b) ρ_s = 1002.5 kg/m^3 (M-S2), and (c) ρ_s = 1250 kg/m^3 (M-S3). The white lines with arrows are streamlines. Vertical exaggeration is by a factor of 10.

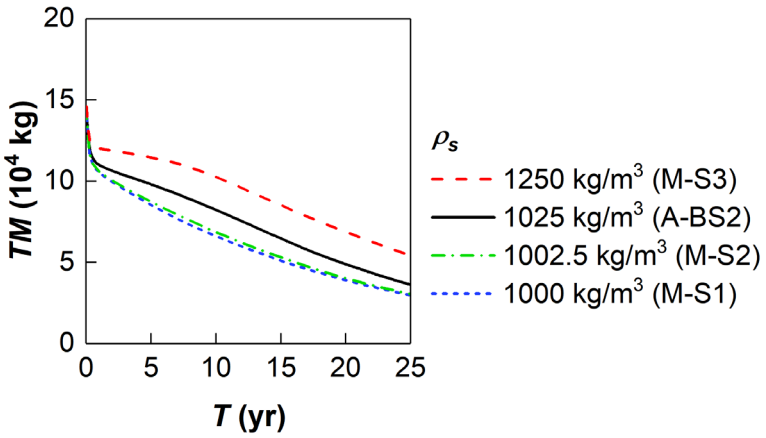

Figure 6.20 The temporal changes of *TM* during ST-4 for the simulation cases with varied seawater density settings from 1000 kg/m^3 to 1250 kg/m^3.

Figure 6.21 shows the simulation results obtained by using different levels of model discretization. When the element size Δl was in the range of 0.43 m to 2.56 m, the simulation results were consistent and showed strong fingering flow patterns at 100 days after the tsunami. The finger pattern became weakened when Δl was increased to 4.44 m (mesh Peclet number Pe_m = 0.88) and 6.29 m (Pe_m = 1.26). No convergence was obtained by using the model with Δl = 9.93 m. Figure 6.22 shows the comparisons of downwards velocities at the plume cores with different Δl. The 25 to 75 percentiles of the elemental velocities were in comparable ranges when Δl was varied from 0.43 m to 6.29 indicating that the movement of the overall plume was consistent. However, there was a decreasing trend of 75 to 99 percentiles of the downward velocities when Δl was increased, indicating that the finger pattern became weakened.

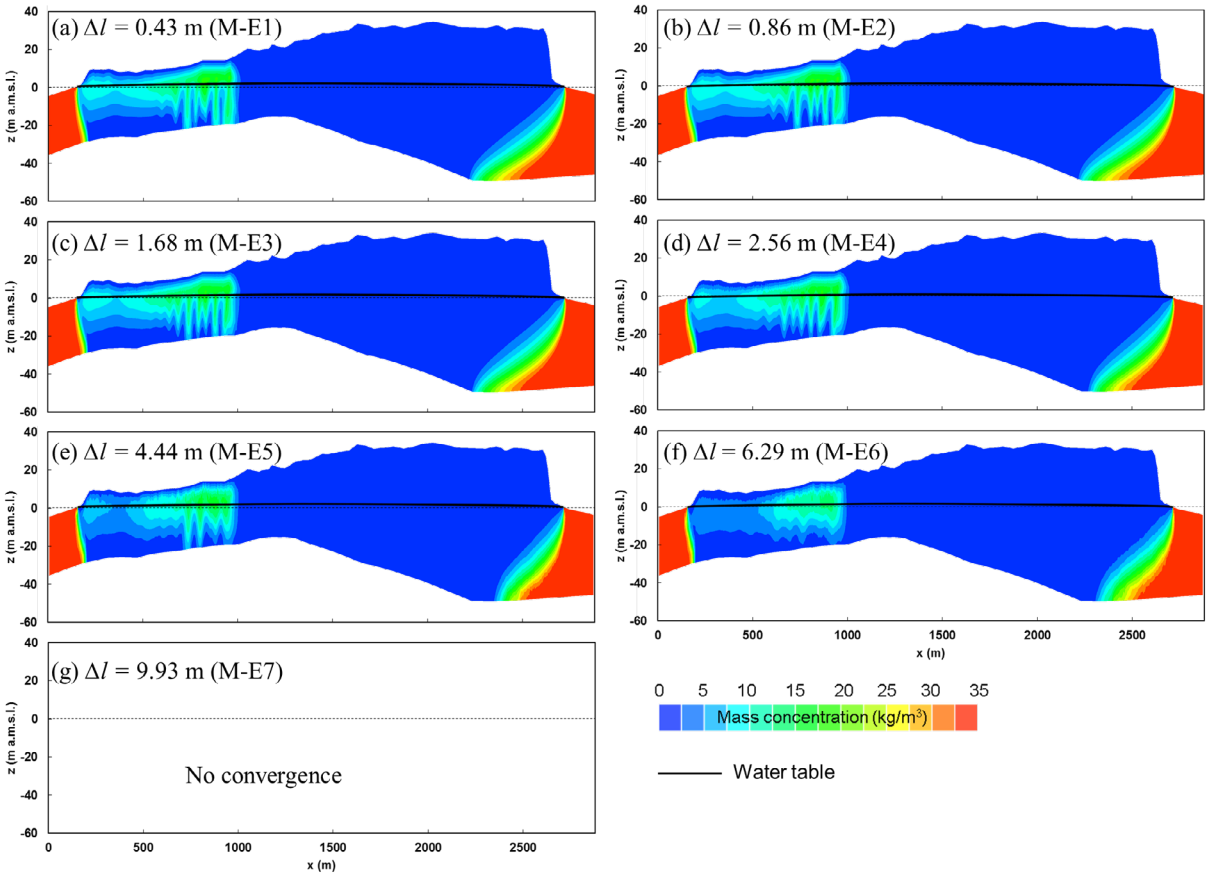

Figure 6.21 Comparison of the simulation results showing mass transport patterns at 100 days after the tsunami with element size Δl that ranged from 0.43 m to 9.93 m. No convergence was obtained in the case M-E7. Vertical exaggeration is by a factor of 10.

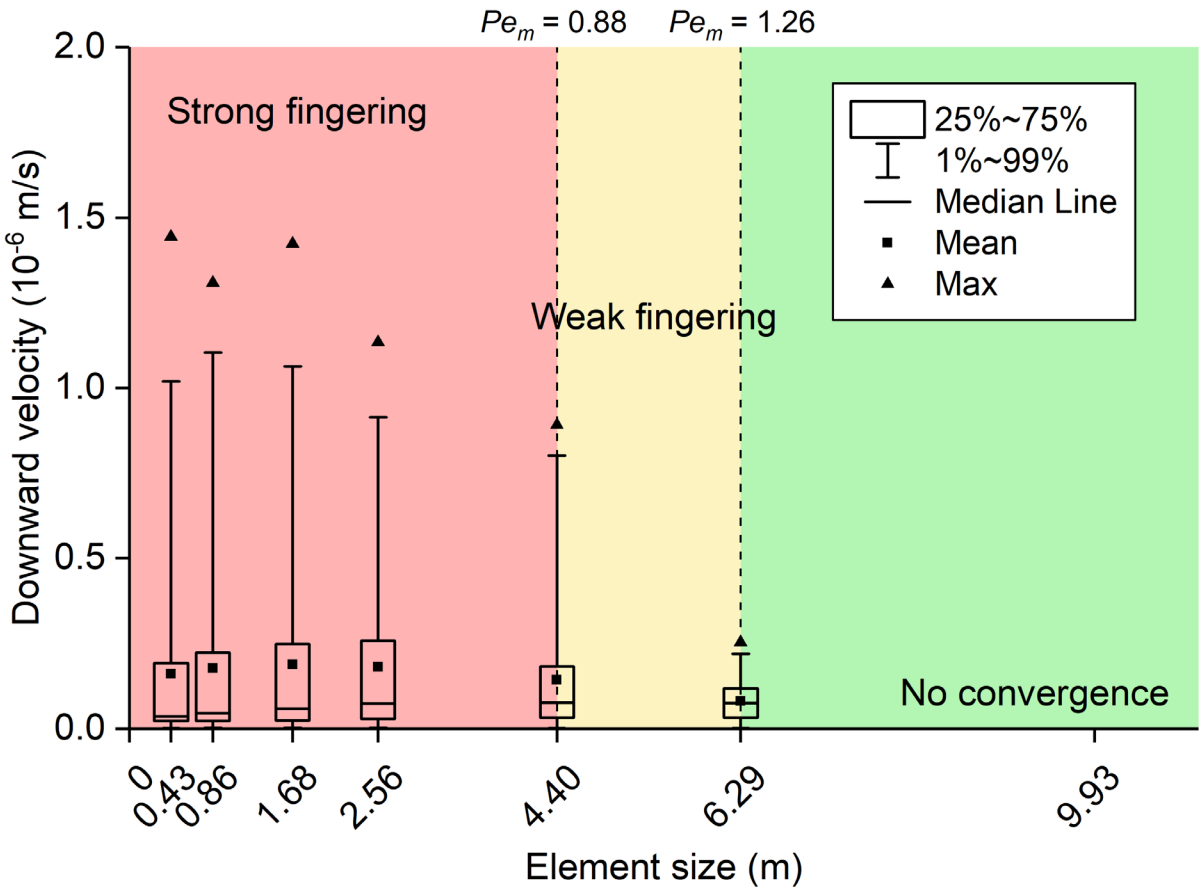

Figure 6.22 Box and whisker plots of downward velocities of the elements at the plume cores at 100 days after the tsunami with element size Δl that ranged from 0.43 m to 9.93 m. The plume cores were defined as the regions where the concentration was higher than 50% of the maximum concentration of the plume in the saturated zone.

Based on these numerical simulation results of TSWI, the density effect showed important roles during two different periods in ST-4: the period after the tsunami and before saltwater reached to the aquifer bottom (around 80 to 100 days after the tsunami in the case of the Niijima Island), and the period since the majority of the saltwater settled down at the aquifer bottom (around one to two years in the case of the Niijima Island). During the former period, the density effect produced fingering flow patterns accelerating the vertical mixing of the intruded saltwater with fresh groundwater (Figure 6.21). During the later period, the density effect leaded the saltwater plume to migrate along the decreasing slope of the bedrock surface (Figure 6.9 and Figure 6.15). Therefore, when applying numerical modeling approaches to predict TSWI or similar density-dependent contaminant overtopping problem in an aquifer with similar geological setting with the ones of the Niijima Island, the following parameters

are important to reduce model uncertainties that could arise from the density effect: the parameters that determined the occurrence of fingering, including hydraulic conductivity (Figure 6.14) and its could (Figure 6.13), density contrast (Figure 6.19), and grid size (Figure 6.22); the parameters that determined the extent of vertical mixing, e.g., aquifer thickness; and the parameters that determine the preferential path of dense plume migration, e.g., the bedrock structure (Figure 6.15).

6.4 Summary

This chapter numerically simulated TSWI on a 2-D vertical cross-section of the Niijima Island, Japan, under the future Nankai earthquake and tsunami scenarios. A series of transient simulations for DDF in unsaturated-saturated media were carried out to examine the model uncertainties associated with the tsunami inundation scenarios, the rainfall recharge conditions, the aquifer properties, and numerical parameters. The main findings are as follows:

(1) In the baseline case, during the two-hour period with the tsunami inundation of 15 m a.m.s.l., seawater infiltrated into soil media and reached to the water table in 10 minutes and saturated the entire unsaturated zone beneath the inundation area in 40 minutes, which afterwards caused groundwater salinization over 0.2 kg/m^3 of Cl^- (Japanese drinking water standards) that persisted more than 10 years in the Niijima Island. Under the extreme tsunami inundation scenario of 25 m a.m.s.l., saltwater migrated to the eastern part of the aquifer of which surface was not directly affected by the tsunami inundation, and the overall flushing time became more than 25 years.

(2) Vertical seawater infiltration was significantly slowed down after the intruded seawater reached to the water table and filled up the unsaturated zone. Therefore, the vertical thickness and porosity of the unsaturated zone determined the maximum volume of saltwater that could possibly intrude into subsurface during the tsunami inundation.

(3) The element-based dimensionless numbers at the plume cores could explain the temporal changes of the patterns of saltwater movement.

(4) The density effect was important for producing fingering flow patterns and leading saltwater migration towards the decreasing slope of the bedrock surface. The parameters including hydraulic conductivity, grid size, density contrast, aquifer thickness, and bedrock structure were important for reducing the model uncertainties associated with the density effect.

The simulation approach taken in this study is potentially useful for vulnerability assessment of coastal aquifers in other tsunami-prone zones with comparable geological and hydrological settings. The modeling method adopted in this study should be further extended to integrate the calculation of coupled surface-subsurface processes and two-phase fluid flow in 3-D domains, which could provide more physically plausible simulations of TSWI problems.

CHAPTER 7: 3-D MODEL OF THE NIIJIMA ISLAND: PREDICTION OF TSWI AND POST-DISASTER WATER SUPPLY[1]

7.1 Introduction

The main objectives of this chapter were: (1) to simulate TSWI using a 3-D numerical model; and (2) to seek for secure and long-term water supply sources in response to tsunami disasters. A 3-D numerical model of the main aquifer in the Niijima Island was developed and calibrated to solve DDF processes in unsaturated-saturated media. The model was applied to predict the TSWI processes in the Niijima Island under future Nankai earthquake and tsunami scenarios. Based on the simulation results, the reliability of the unpolluted portion of groundwater as freshwater resource in the post-disaster period was tested.

7.2 Methods

7.2.1 ICs and BCs

The model boundary was determined based on the following considerations: (1) inclusion of important groundwater flow and freshwater-seawater mixing zones in the island, (2) correspondence with natural hydraulic boundaries, and (3) minimization of model scale to reduce computational demands. Therefore, a trial model, covering the entire island and the seafloor with a horizontal distance of 500 m from the coastline, was developed to simulate the hydraulic head distributions and freshwater-seawater mixing zones. Based on this preliminary simulation, the model domain (Figures 5.5 and 7.1a) was decided to be narrowed down to mainly include the major tsunami-prone zone near the western coast, the main aquifer in the central plain, and the southern part of the island where the potential groundwater stock may be reserved. As shown in Figure 5.5b, the northern boundary of the model was set perpendicular to the coastline (A-B and D-F), along a seasonal stream (B-C), and along mountain ridges (C-

[1] The content of chapter appears in Liu, J., & Tokunaga, T. (2020). 3D modeling of tsunami-induced seawater intrusion and aquifer recovery in Niijima Island, Japan, under the future tsunami scenario. *Journal of Groundwater Hydrology*. (in press as of Jan 30, 2020)

D) assuming no-flow BCs. The model boundary at the seaside (A-F) was adjusted to be located at a horizontal distance of 300 m from the coastline, which sufficiently ensured all the important seawater-freshwater interactions to be captured throughout the whole simulation stages.

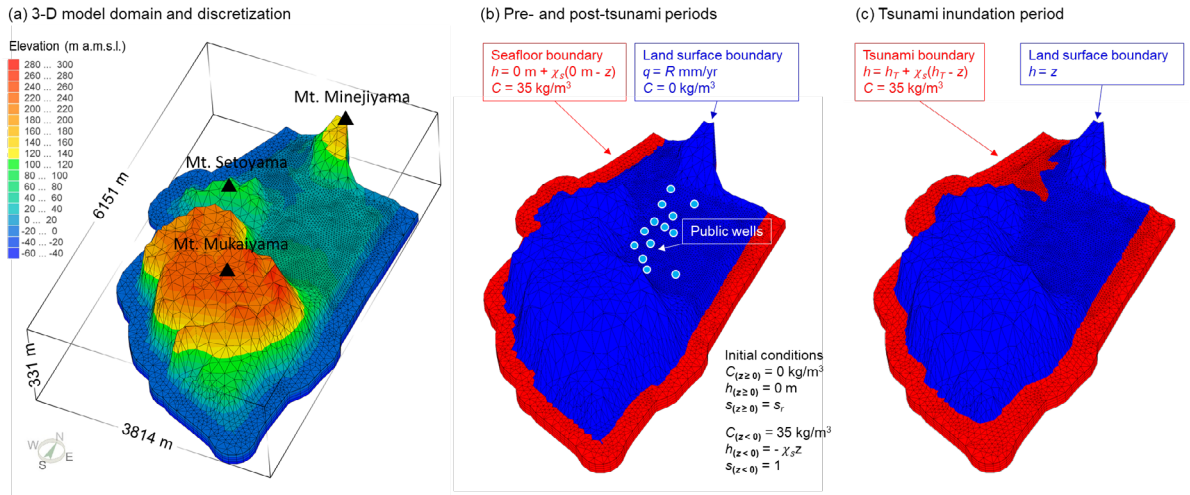

Figure 7.1 (a) Domain and discretization of the 3-D model; BCs and ICs for simulation of (b) the pre- and post-tsunami periods and (c) the tsunami inundation period. Vertical exaggeration is by a factor of 5.

The ICs and BCs were varied for three simulations stages: the development of fresh groundwater system since the deposition of pyroclastic materials in 886 AD until it reached to the quasi-steady-state; the SWI processes during the tsunami inundation period; and the years of the post-tsunami aquifer recovery processes.

To obtain the quasi-steady state, the ICs and BCs were set to reflect the time when the island was formed in 886 AD (Figure 7.1b). All the media above the sea-level were set to contain residual water in the concentration of 0 kg/m^3 while the media below the sea-level was fully saturated with seawater with a concentration of 35 kg/m^3 (NaCl). Along the seafloors where groundwater was in contact with seawater, a constant seawater head BC of 0 m a.m.s.l. with a fixed concentration C = 35 kg/m^3 was assigned. A constant mass concentration BC of C = 0 kg/m^3 with a constant flux R, representing the rainfall recharge, was applied along the land surface. Strictly speaking, this BCs design was not perfectly representative due to its simplification for the discharge of groundwater at coastal zones which indeed required a

system-dependent strategy including: at the seafloor, the constant concentration of 35 kg/m^3 should be set for seawater inflow from the sea to aquifer while no constraints should be set in the case of groundwater discharge from the aquifer to the sea; and at the beach surface, rainfall recharge should be applied to the nodes except for the nodes where groundwater discharges out. However, this system-dependent BCs setting was not adopted in this paper due to the fact that the system-dependent BCs caused serious numerical oscillations and tremendously raised the CPU time, probably due to the complexity of such BCs; and the system-dependent BCs produced only limited influence on the position of freshwater-seawater mixing zones. No-flow boundary was specified at the aquifer bottom. The transient simulation was run for a period of 200 years to ensure the model to reach to a quasi-steady-state, and then, groundwater abstraction was introduced by specifying well BCs at public wells pumping a total amount of freshwater of 3.7×10^5 m^3/yr. After the transient simulation of 30 years, another quasi-steady state was achieved which was regarded as the normal condition of the groundwater system in the Niijima Island before the tsunami.

The obtained quasi-steady state was used as the ICs for simulating the SWI process during the tsunami inundation period. For simplification, the tsunami-induced seawater flooding was simulated as a spatially and temporally constant sea-level rise event lasting for a certain period of time. This assumption was intended to produce a higher degree of SWI than that could happen in the actual disaster. At the seafloor and the land surface below the inundation elevation h_T, a constant seawater head BC of $h_{sw} = h_T$ with C = 35 kg/m^3 were assigned. The land surface that was high than h_T was set to be seepage face boundary. The well BCs were disabled during this simulation stage considering the temporary power failure due to the earthquake and tsunami. Other BCs were assumed to be the same as those in the previous simulation stage.

The simulation results at the final time step of the tsunami inundation period was used as the ICs for simulating the aquifer recovery process. After the tsunami, the sea-level was recovered to 0 m a.m.s.l., and the rainfall recharge began to freshen the salinized aquifer, and hence the BCs at the seafloor and land surface were resumed to be the same as those in the pre-tsunami simulation stage. The aquifer recovery processes during the post-disaster period were compared for two different scenarios: no groundwater abstraction at all, and pumping groundwater from unpolluted wells to supply freshwater. The simulation of this stage was continued for a period of 15 to 25 years, depending on the scenarios.

7.2.2 Spatial and Temporal Discretization

To determine the spatial discretization of the model, two criteria were considered: (1) to avoid numerical oscillations, the mesh size Δl at the places where groundwater flow and mass transport were significant were kept to ensure the Peclet number $Pe_m \approx \Delta l/\alpha_L < 4$ (Voss and Souza, 1987), where α_L is the longitudinal dispersivity; (2) to reduce the computing demands to an acceptable level, the total number of elements were limited. As illustrated in Figure 7.1a, the aquifer system of Niijima Island was discretized into 25,578 nodes with 41,970 prismatic elements with a triangular base. For the sake of avoiding numerical oscillations and improving the accuracy of modeling results, a higher degree of refinement ($\Delta l \approx 60$ m) was adopted in important local areas, including the coast (freshwater-saltwater interaction zones) and the central plain (the estimated tsunami inundation zone and the groundwater abstraction zone) of the island. One big limitation was that the current degree of spatial discretization was not fine enough to simulate the fingering pattern like that observed in previous laboratory experiments (Illangasekare et al., 2006; Simmons et al., 2002) and numerical simulations (Vithanage et al., 2012). This fingering pattern could accelerate the vertical mixing of intruded saltwater with fresh groundwater (Simmons et al., 2001). However, further mesh refinement was not carried out because of the following reasons: the current simulation involves complex

flow and mass transport processes featured with variable-density, unsaturated-saturated conditions, transient simulations, and a 3-D domain, which required large computational efforts, and hence, further mesh refinement dramatically raised the CPU time; and instead of simulating local-scale fingering flows nicely and extensively, identifying the most vulnerable part of the overall groundwater system and seeking for the possibility to supply freshwater for the island were of the main interest in this paper.

In the vertical direction, the model contained five layers with six slices (Figure 7.2). At the top slice (Slice 1), the elevations of the land surface and seafloor obtained from Ministry of Land (2015) and Nakaoka and Suzuki-Kamata (2015), respectively, were assigned. The bedrock depth under the central plain of the island (Figure 5.5a) based on the information provided by Shindo (1980), Isobe and Nakashima (2001), and Construction Section of Niijima Village (2001), was specified at the bottom model slice (Slice 6 in Figure 7.2). However, bedrock depth information at the southern part of the island is currently not available. Isshiki (1987) indicated that aquifer materials exist under the lava layer of the Mukaiyama Volcano (Figure 5.5a), hence, the bedrock surface elevation of -50 m a.m.s.l. at the southern island was assumed in the model. The elements corresponding to the impermeable lava layer and the lava dome were specified as inactive (Figure 7.2). All the elements in the uppermost layer (Layer 1) with a vertical thickness of 2 m were set to be active to receive rainfall recharge.

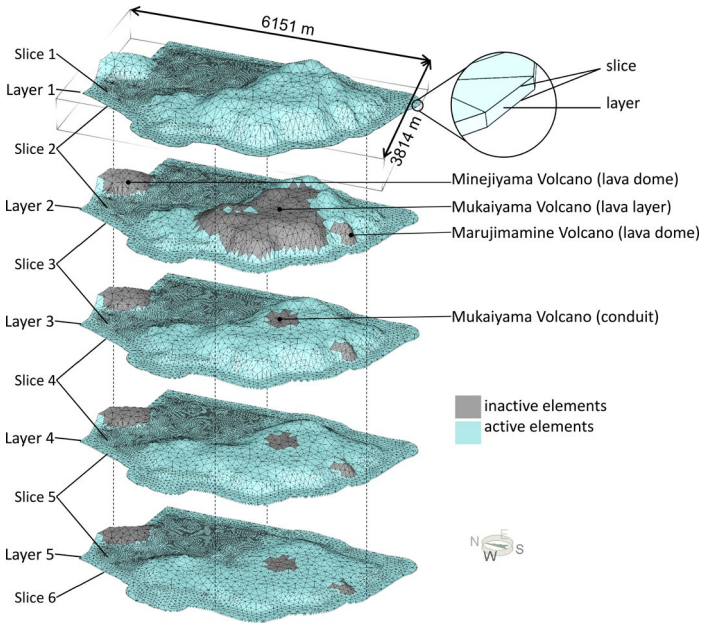

Figure 7.2 Layer configurations of the 3-D model.

For each of the three simulation stages (the pre-, during, and post-tsunami period), the corresponding initial time step was set to be 1×10^{-6} day, 1×10^{-6} second, and 1×10^{-6} day, and the maximum time step be one day, one second, and one day, respectively. The maximum growth factor between subsequent time steps was restricted to be 1.1.

7.2.3 Parameterization

The present model assumed that the aquifer of the Niijima Island was single-layered, homogeneous, and isotropic. Model parameters were summarized in Table 7.1. The parameters for the van Genuchten model (Eq 3.22 and Eq 3.23) were obtained by fitting the saturation curve with the measured data by Shindo (1980) (Figure 7.3a). The longitudinal dispersivity α_L of 50 m was chosen here based on the relationship between dispersivity and observation scale that was suggested by Gelhar et al. (1992), and the ratio between longitudinal and transverse dispersivities was set to be 10. The porosity of 0.34 was obtained from Shindo (1980). According to Honma et al. (1974), the recharge rate of the groundwater system in the Niijima Island was equivalent to 30 to 50% of the annual rainfall amount. Therefore, a constant recharge rate $R(t)$ = 883 mm/yr was adopted, which was derived from 40% of the average annual rainfall amount of 2207 mm/yr (Japan Meteorological Agency, 2017). Aichi et al. (2011)

estimated the ratio R/K to be 3.0×10^{-5} by fitting the Dupuit-Ghyben-Herzberg analytical solution (Vacher, 1988) to the measured groundwater table elevations. By several trials using the present numerical model, the ratio R/K was calibrated to be 2.1×10^{-5}, and K be 1.3×10^{-3} m/s, which resulted in rather good fits with the measured groundwater table elevations (Figures 7.3b and c). Based on the tsunami simulation results by Tokyo Disaster Management Council (2013), a tsunami inundation event lasting for 120 minutes with a constant inundation elevation h_T = 15 m a.m.s.l. was assumed. An extreme tsunami inundation scenario of h_T = 20 m a.m.s.l. was also simulated. Other parameters listed in Table 7.1 were selected based on the typical literature values (Diersch, 2013; Vithanage et al., 2012; Yu et al., 2016).

Table 7.1 Summary of simulation parameters in the baseline case

	Symbol	Value	Unit	Data source
Parameters obtained from literature of the Niijima Island				
Porosity	ε	0.34	-	(Shindo, 1980)
Net recharge rate	$R(t)$	883	mm/yr	(Honma et al., 1974; Japan Meteorological Agency, 2017)
Parameters obtained by calibration				
Residual saturation	s_r	0.209	-	Calibrated by fitting van Genuchten model (van Genuchten, 1980) with measured data by Shindo (1980)
van Genuchten parameter	α	3.6	1/m	
Pore size distribution index	n	2.3	-	
Horizontal hydraulic conductivity	K_x	1.3×10^{-3}	m/s	Calibrated based on the measured groundwater table elevations
Parameters obtained from typical literature values				
Longitudinal dispersivity	α_L	50	m	(Gelhar et al., 1992)
Transverse dispersivity	α_T	5	m	
Anisotropy ratio of hydraulic conductivity	K_z/K_x	1	-	(Diersch, 2013; Vithanage et al., 2012; Yu et al., 2016)
Freshwater concentration	C_0	0	kg/m^3	
Seawater concentration	C_s	35	kg/m^3	
Density ratio	χ_s	0.025	-	
Gravitational acceleration	g	9.8	m/s^2	
Dynamic viscosity	μ	0.001	kg/(m·s)	
Molecular diffusion coefficient	D_0	1×10^{-9}	m^2/s	

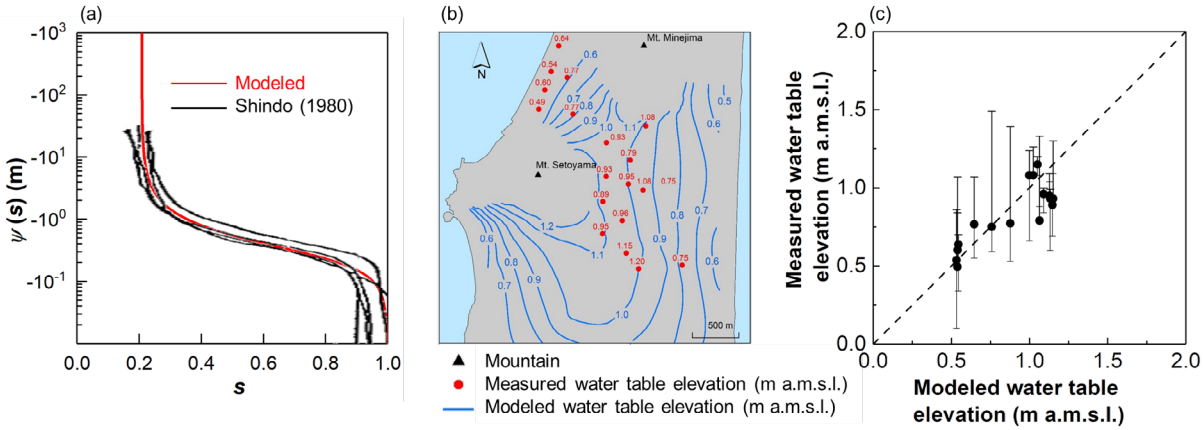

Figure 7.3 Comparison of measured and computed data: (a) The modeled saturation curve using the van Genuchten model (van Genuchten, 1980) based on the measured data by Shindo (1980); (b) Spatial distribution of computed hydraulic head contours and measured hydraulic heads; (c) Comparison of computed and measured hydraulic heads. The measured data are plotted with the fluctuation ranges based on the historical records of water table elevations provided by the Niijima Office and by Aichi et al. (2011).

7.3 Results and Discussions

7.3.1 Prediction of TSWI

Figure 7.4 illustrates the modeling results of the SWI processes during the tsunami inundation of 15 m a.m.s.l. on the W-E vertical cross-section (Figure 5.5). The cliff of about 30 m a.m.s.l. at the eastern coast prevented the eastern half domain from being directly inundated by the tsunami. However, in the western half domain, the tsunami caused seawater flooding along a horizontal distance of about 870 m inland. Due to the tsunami inundation event, seawater infiltrated vertically into soil media and reached to the groundwater table within 10 minutes. Within 30 minutes, the domain which was initially unsaturated became fully saturated with intruded seawater. This vertical infiltration process took place rapidly because of the large downwards hydraulic gradients and the highly permeable sands (Table 7.1).

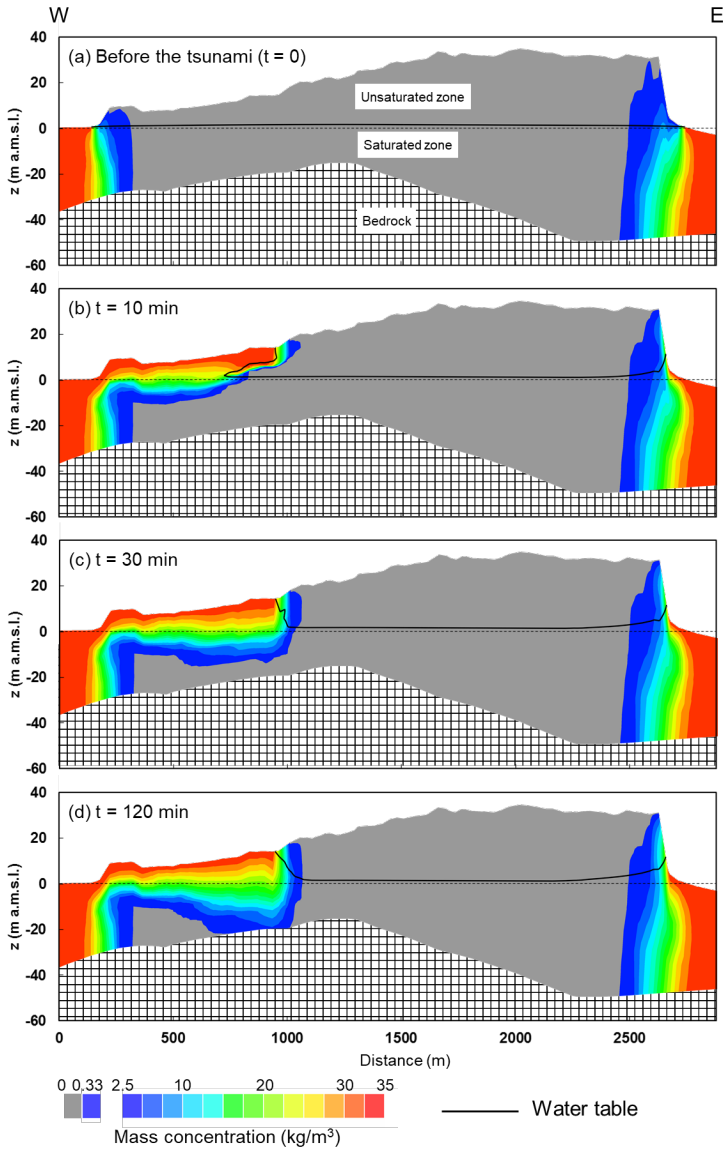

Figure 7.4 Cross-sections showing temporal changes of mass concentration distributions under the condition that prior to the arrival of the tsunami, and at 10, 30, and 120 minutes during tsunami inundation of h_T = 15 m a.m.s.l.. Vertical exaggeration of the cross-sections is by a factor of 10. See the location of the cross-section in Figure 5.5. The mass concentration of 0.33 kg/m^3 NaCl is equivalent to the concentration limit of 0.2 kg/m^3 Cl^- in Japanese drinking water standards (Ministry of Health, Labor and Welfare, 2015).

Figure 7.5 shows the growth of accumulated volume of intruded seawater along with time. In the case of h_T = 15 m a.m.s.l., the volume of intruded seawater increased with a rapid rate in the first 30 minutes and reached to a level about 1.2 ×10^6 m^3. After 30 minutes, the increase of intruded seawater volume became rather small compared with that during the first 30minutes. This is because the domain which was initially unsaturated became fully saturated with intruded seawater at around 30 minutes (Figure 7.4c), which prevented further seawater

infiltration. This result suggested that the void space of the soil media in the unsaturated zone provided a room for storing seawater during the early stage of tsunami inundation.

The extreme scenario of tsunami inundation of 20 m a.m.s.l. caused a larger amount of seawater infiltration (Figure 7.5). Both simulations of 15 and 20 m a.m.s.l. indicated an intruded seawater volume with a magnitude of 10^6 m^3. Considering the assumption of constant tsunami inundation elevation in the 3-D model, these simulation results represented an upper bound of the total amount of seawater that could possibly enter the groundwater system in the Niijima Island during the actual tsunami inundation event.

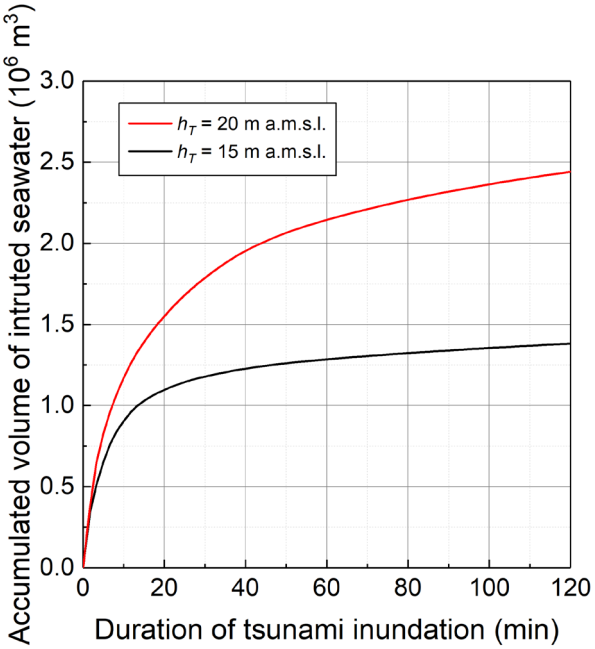

Figure 7.5 Temporal changes of accumulated volume of seawater that was intruded through land surface during the tsunami inundation of 15 and 20 m a.m.s.l..

The 3-D simulation results of the SWI processes during the tsunami inundation period were similar with the 2-D simulation results in Chapter 6 with respect to the plume behavior (comparing Figure 7.4 with Figure 6.4) and the increasing volume of intruded saltwater (comparing Figure 7.5 with Figure 6.5a).

Figure 7.6b shows the 3-D views of the simulated aquifer recovery processes by the natural rainfall recharge after the tsunami of 15 m a.m.s.l.. During the first year after the

tsunami, though the concentration of saltwater plume was reduced due to the mixing with fresh groundwater, an maximum amount of about 4.5 $\times 10^6$ m^3 fresh groundwater resource was lost (Figure 7.7), which was an striking volume scale when comparing with the annual water supply of 3.7 $\times$ 10^5 m^3 on the island. After one year, the rainfall recharge continuously kept flushing the intruded saltwater out through the west coast, and the groundwater system was recovered to the pre-tsunami condition after eight years (Figures 7.6b and 7.7).

The saltwater migration showed a distinct trend after the tsunami of 20 m a.m.s.l. (Figure 7.6c), compared with that after the tsunami of 15 m a.m.s.l. (Figure 7.6b). The case of h_T = 20 m a.m.s.l. caused larger areas of seawater flooding at both the western and eastern coastal zones. In addition, the saltwater plume which originated from the western side traveled towards the east, some public wells became not appropriate to provide drinking water due to their salinity to become over 200 mg/L Cl^- standard. This extreme tsunami scenario caused a maximum loss of fresh groundwater resource about 7.2 $\times 10^6$ m^3, and the recovery of groundwater quality required more than 18 years. This distinct saltwater intrusion pattern was associated with two factors: (1) the tsunami of 20 m a.m.s.l. from the western coast traveled further inland and caused SWI to cross the groundwater divide and reached to the eastern part of the island where groundwater normally flowed eastwards (Figure 7.6a2); (2) the dense saltwater plume had the tendency to sink to aquifer bottom and to move along the slopes of the bedrock surface, and hence, the convex upward shape of the bedrock surface under the Niijima Island may had facilitated dense saltwater moving only westwards in the case of h_T = 15 m a.m.s.l., while both westwards and eastwards in the case of h_T = 20 m a.m.s.l. (Figure 7.8). This eastern movement of intruded saltwater was also observed in 2-D numerical simulations of the case with h_T = 25 m a.m.s.l. in Chapter 6 (Figure 6.9).

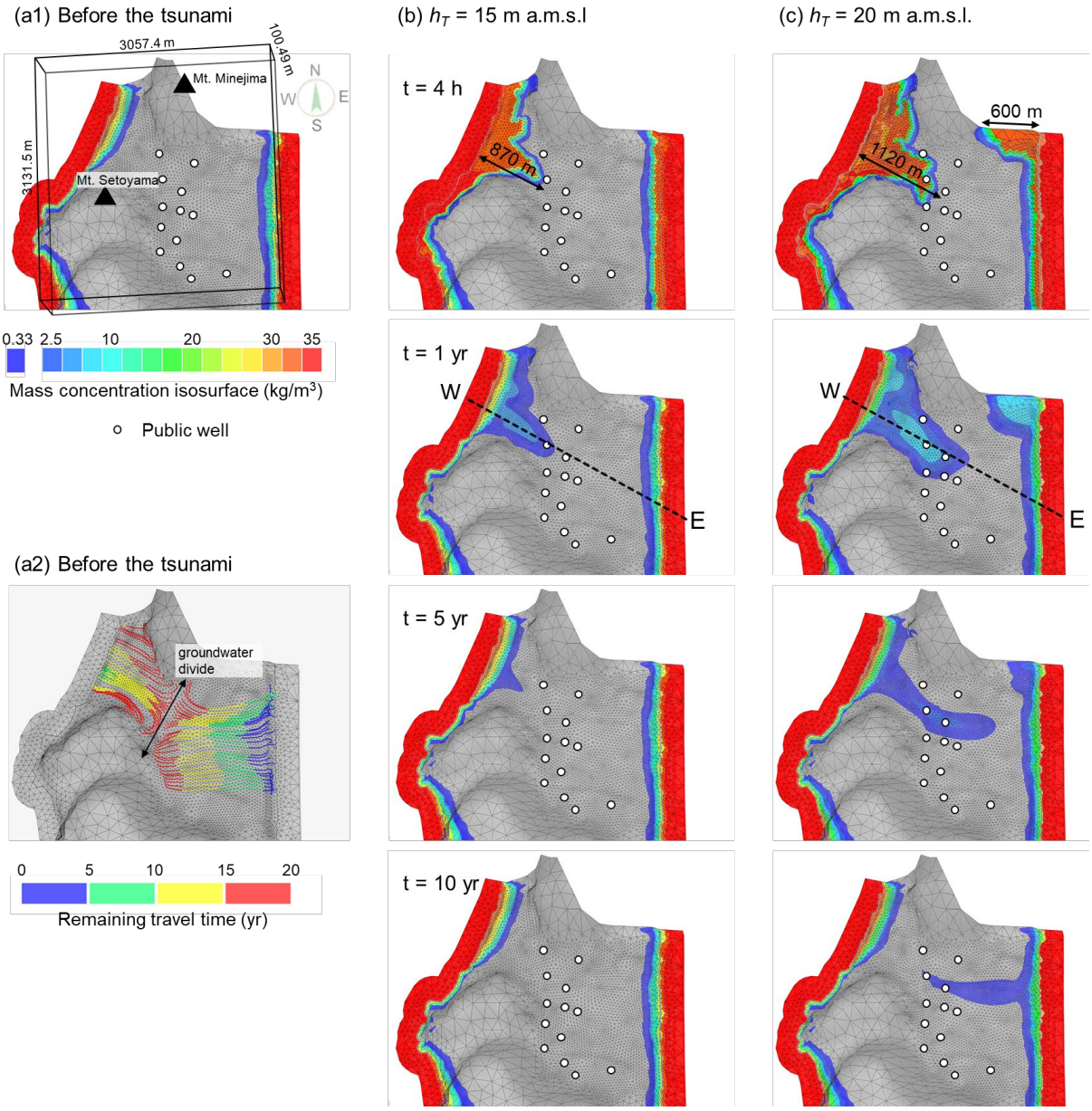

Figure 7.6 3-D views of modeling results: (a1) mass concentration distributions and (a2) flowlines showing directions and remaining travel time of groundwater which discharges out to the sea at the normal quasi-steady state (before the tsunami) of the Niijima Island. The aquifer recovery process after the tsunami of (b)15 m a.m.s.l. and (c) 20 m a.m.s.l.. Dashed lines show the location of the vertical cross-sections in Figure 11. Vertical exaggeration is by a factor of 10.

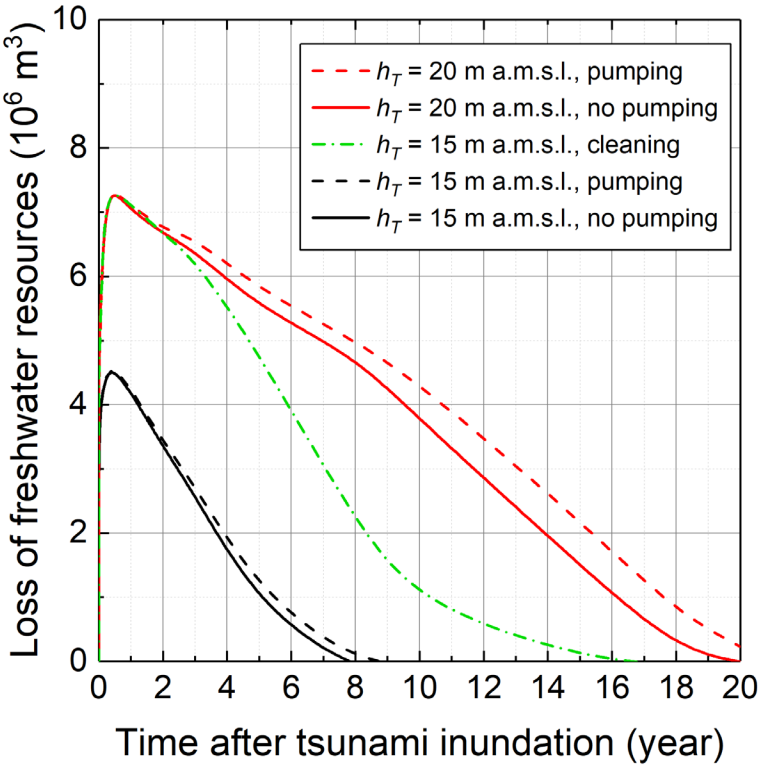

Figure 7.7 Temporal changes of the loss of freshwater resource with time after tsunami of 15 and 20 m a.m.s.l. under pumping and no pumping conditions.

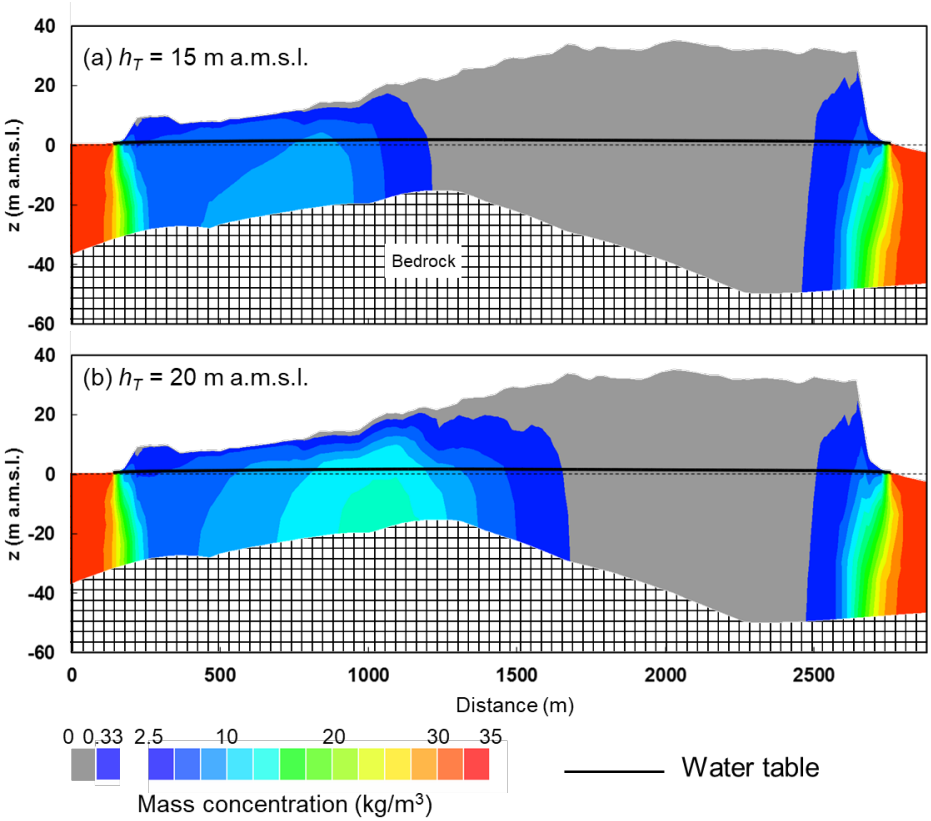

Figure 7.8 Vertical cross-sections comparing the distribution of mass concentration at one year after the tsunami of (a) 15 m a.m.s.l. and (b) 20 m a.m.s.l.. See the locations of the cross-section in Figure 7.6. Vertical exaggeration of the cross-sections is by a factor of 10.

It was observed that the overall flushing time of the intruded saltwater was basically similar to the groundwater travel time (Figure 7.6a2). For example, the overall flushing time was about eight years after the tsunami of 15 m a.m.s.l., compared with the remaining groundwater travel time of 10 to 15 years in the inundation zone. The recovery of the groundwater system after the tsunami of 20 m a.m.s.l. required a period of about 19 years while the inundation zone at inland had a remaining groundwater travel time ranging from 15 to 20 years.

The fingering patterns observed in the 2-D simulation results of aquifer recovery processes in Chapter 6 (Figure 6.4) were not found in the 3-D simulations (Figure 7.6). This is probably due to the insufficient vertical discretization of the 3-D model. However, in the later stage of the aquifer recovery processes (after one year), both 2-D and 3-D simulations indicated a stable plume.

7.3.2 Long-Term Water Supply in Response to Tsunami Disasters

According to the simulation results (Figure 7.6), groundwater survived from the TSWI was found in the southeastern part of the aquifer in the Niijima Island. Therefore, the feasibility of pumping this survived groundwater for post-disaster water supply was numerically investigated. Figure 7.9 showed the recovery processes with pumping the survived groundwater from the four wells located in the southeastern part of the island. The pumping rate of each well was 253 m^3/d (maximum capacity was 300 m^3/d) so that they can provide the equivalent total amount of water supply as that before the disaster. Compared with no-pumping conditions, this pumping behavior had very negligible impacts on the migration of saltwater plume (Figure 7.9) and the recovery of freshwater resource (Figure 7.7) in both cases of the tsunami with 15 and 20 m a.m.s.l.. Furthermore, this centralized pumping behavior did not produce any noticeable groundwater drawdown or SWI from the eastern coast, probably because that the aquifer materials are highly permeable and that the groundwater resources

underneath the lava dome of the Mukaiyama Volcano (Figure 5.5c) supplied enough amount of water to this pumping activity.

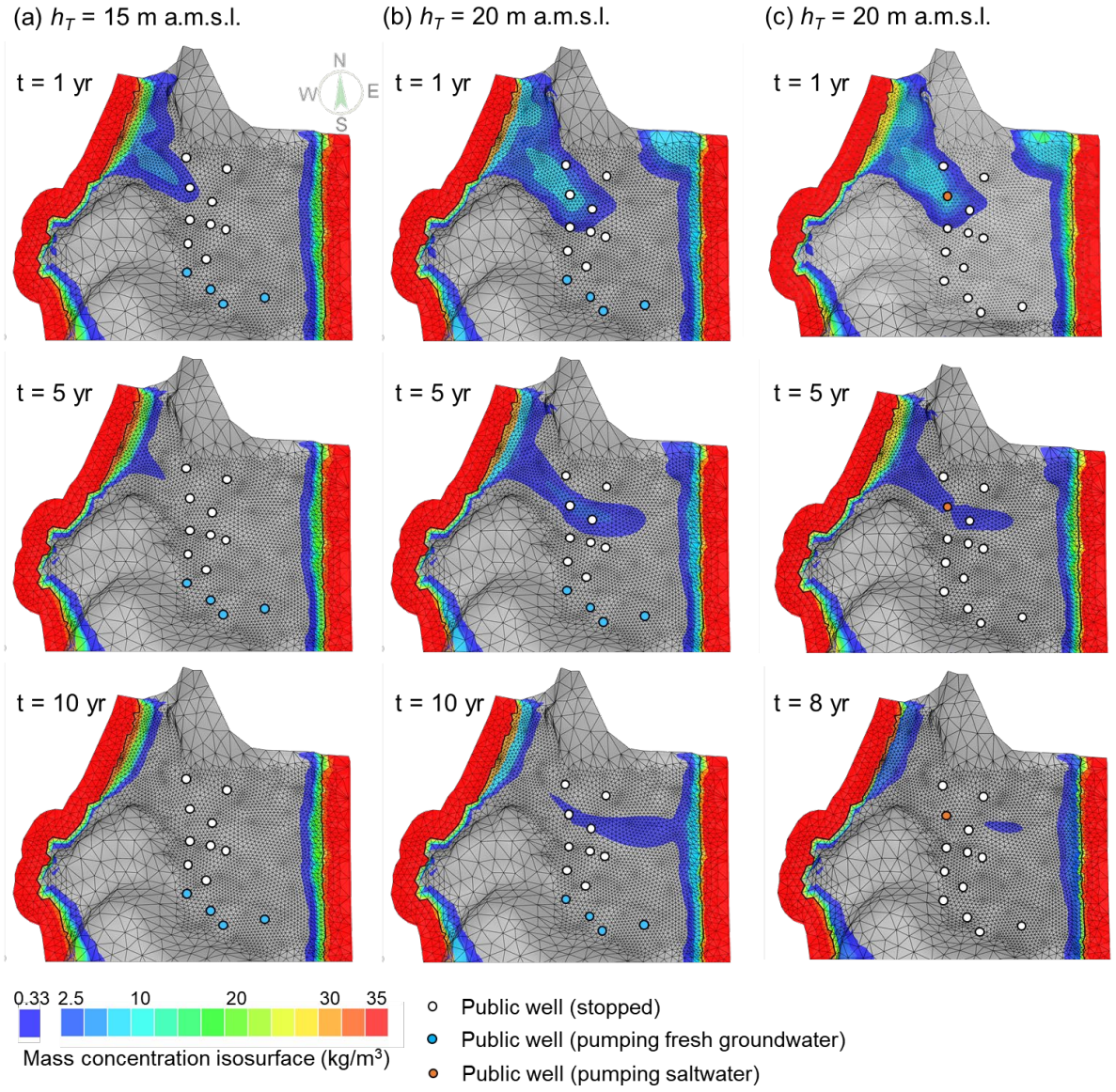

Figure 7.9 Simulations results of pumping fresh groundwater after (a) h_T = 15 m a.m.s.l. tsunami and (b) h_T = 20 m a.m.s.l. tsunami and pumping the intruded saltwater after (c) h_T = 20 m a.m.s.l. tsunami.

7.3.3 Effect of Pumping Saltwater Out

Figure 7.9 showed the simulations results of pumping the intruded saltwater out from the aquifer. The pumping activity was set to be carried out at one tsunami-affected well that was located in the central area of the island. The pumping rate was set to be 300 m^3/d (the maximum pumping capacity of the well). Compared with the aquifer recovery only by natural

rainfall recharge (Figure 7.6b), this pumping behavior showed the effect of reducing the volume of saltwater intrusion to the east half of the groundwater system. As shown in Figure 7.7, removing the intruded saltwater from the aquifer facilitated the recovery process and shortened the recovery period for about five years at maximum.

7.4 Recommendations and Implications

7.4.1 Field Indicators for Assessing the Vulnerability of Coastal Aquifers to TSWI

The modeling results indicated that the unsaturated zone in the Niijima Island had the role of storing intruded seawater during the tsunami inundation period (Figure 7.4). This implies that the vertical thickness and porosity of the unsaturated zone underneath the inundation area would determine the maximum volume of seawater infiltration during the tsunami inundation. That is, given the same tsunami inundation scenario, fresh groundwater resource would be more vulnerable in the case of a thicker unsaturated zone with a larger porosity which would store larger amount of intruded seawater to be mixed with fresh groundwater after tsunami.

The modeling results also indicated that the direction of post-tsunami saltwater migration and flushing time were generally agreed with the pre-tsunami groundwater flow path and travel time, respectively (Figure 7.6a2). An aquifer would be more vulnerable if its groundwater divide is located within or nearby the tsunami hazard zone, and saltwater intrusion would affect groundwater quality not only in the tsunami inundation area but also in no-inundation areas depending on the relative position between the area of tsunami inundation and the groundwater divide. Therefore, obtaining general groundwater flow directions using field measurement techniques and numerical modeling can substantially assist to evaluate the vulnerability of groundwater resource to tsunami disasters. Moreover, knowing groundwater

flow velocity and its travel time may provide rough estimations of flushing time of intruded saltwater.

The modeling results showed that the intruded saltwater had the tendency to sink to the aquifer bottom and migrated along the slopes of the bedrock surface, which may have contributed to the eastward movement of saltwater in the case of h_T = 20 m a.m.s.l. (Figure 7.6a2c and Figure 7.8b). In this study, the bedrock surface was inclined with a small slope (around 2 m over a horizontal distance of 100 m in average). It can be inferred that the transport of salt mass in an aquifer would be more strongly influenced by a much steeper bedrock surface topography than that in this study. As mentioned in Section 5.2, the current convex upwards bedrock structure assumed in this paper remained uncertain, and it can be inferred that a convex downward bedrock setting would result in the retention of the saltwater plume in the depression of bedrock surface and prolong the aquifer recovery process (Figure 7.10). Therefore, it is necessary to further confirm the bedrock condition of the Niijima Island by using more reliable investigation techniques. As for other coastal areas with more complicated geological structures than the single-layered unconfined aquifer in the Niijima Island, it is also important to have a clear image of the aquifer system, especially the existence of the low permeable layers.

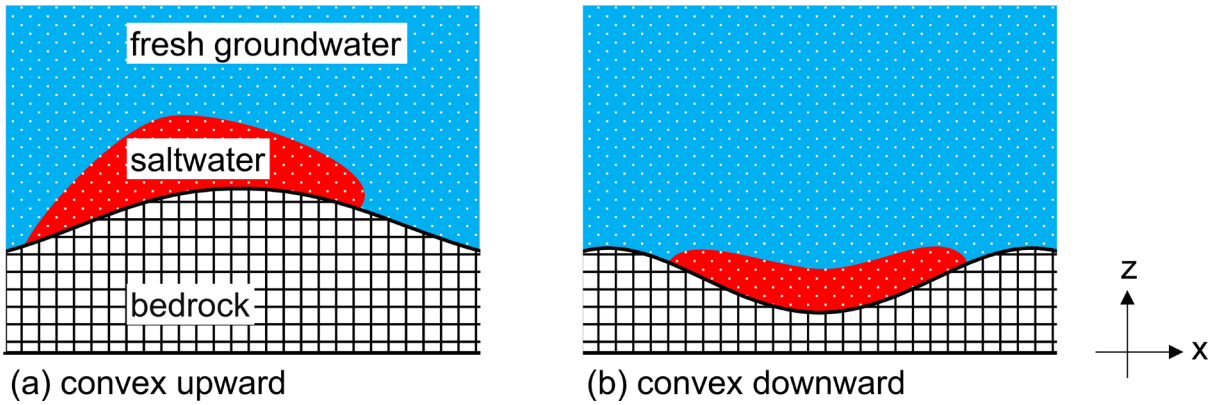

Figure 7.10 Conceptual vertical cross-sections showing the patterns of saltwater plume with bedrock structures (a) convex upward and (b) convex downward, respectively.

7.4.2 Strategies for Securing Water Supply in Post-Disaster Period

According to the simulation results, the southeastern part of the aquifer will very likely be survived from the TSWI caused by the anticipated Nankai earthquake, and the survived portion of the aquifer will have great potential to provide groundwater supply for the island in the post-tsunami recovery period. Strategies and plans for utilizing those unpolluted groundwater resources can improve the resilience of local water supply to tsunami disasters in terms of water quantity and quality on a long-term basis. Currently, groundwater is abstracted from those public wells by using electric pumps on the Niijima Island. However, at the time of earthquake and tsunami, electricity failure can happen. Therefore, in order to ensure the pumping capacity immediately after the tsunami, backups of pumps, generators, fuels, and relevant equipment, should be prepared in advance.

Our simulations were conducted for pumping groundwater from four wells in the Niijima Island after the tsunami disaster. However, for other coastal zones, there are still risks caused by intensive pumping from a few wells, such as the possible upconing of seawater. Therefore, it is suggested that the pumping of survived groundwater should be carried out in wells in different locations in turns with careful monitoring of the groundwater level and water quality.

Removing the intruded saltwater from the aquifer may contribute to preventing saltwater invading to the eastern region of the groundwater system and may facilitate the aquifer recovery processes. However, the continuous intensive pumping activity may require a large energy supply and may cause possible upconing of seawater.

Problems arose after the 2004 Indian Ocean earthquake and tsunami that there was a lack of proper information about where and how people will get freshwater (Shaw et al., 2006). Therefore, it is important to distribute information to the local residents and the visitors about the emergency water supply. Another experience from the 2004 Indian Ocean tsunami was that

there was not enough quantity of clean vessel for people to get water from the water distributions sites (Shaw et al., 2006). Hence, the preparation of water containers and appropriate water treatment methods is also highly recommended.

7.5 Summary

In this chapter, a 3-D numerical groundwater model of the Niijima Island was developed and calibrated to simulate TSWI processes, and was applied to examine the possibility of pumping the unpolluted portion of groundwater to supply freshwater in the post-disaster period. The main simulation results are:

(1) A tsunami inundation of 15 m a.m.s.l. would cause seawater, with a volume scale of 10^6 m^3, to infiltrate into subsurface within several tens of minutes, which caused groundwater salinization that would persist for about eight years in the western low-lying coastal zone of the Niijima Island. An extreme tsunami of 20 m a.m.s.l. could cause a broader seawater flooding that extends to the central area of the island, and as a result, some intruded saltwater may migrate eastwards and deteriorate the groundwater quality even in uninundated zones, which required a period of more than 18 years to be recovered by the natural rainfall recharge.

(2) Some groundwater in the southeastern part of the island would be survived from SWI, and this survived portion of groundwater resource had the potential to provide post-disaster water supply in an equivalent amount of the pre-tsunami level (3.7×10^5 m^3/year), and at the same time, did not worsen the recovery processes.

(3) Pumping the intruded saltwater out had the effect of reducing the risks of saltwater intrusion in the eastern part of the groundwater system and facilitating the aquifer recovery process.

These simulation results provide the following recommendations and implications for the Niijima Island, and they are potentially transferable to other coastal zones, especially the remote islands where they face tsunami risks:

(1) The field indicators including unsaturated zone properties, groundwater flow path and travel time, bedrock surface topography, can provide important information for tsunami risk assessment with respect to the estimation of the total amount of seawater infiltration, migration direction, and flushing time of saltwater intrusion.

(2) In order to activate the utilization of the unpolluted portion of groundwater as water supply in the post-disaster period, necessities such as pumps, generators, fuels, and clean containers, should be prepared in advance. The abstract of groundwater should be accompanied with careful monitoring of groundwater quality. Information on the emergency plan for water supply should be distributed to the local residents and the visitors to avoid chaos.

The modeling method adopted in this study should be further improved with respect to spatial discretization, system-dependent BCs, and heterogeneity, which could provide more robust and physically plausible simulations of TSWI processes.

CHAPTER 8: CONCLUSIONS

This thesis numerically simulates tsunami-induced seawater intrusion (TSWI) in coastal aquifers under future tsunami scenarios and studies the impacts of model uncertainties on simulation results. A numerical model approach using the code FEFLOW is adopted to solve variable-density flow and mass transport processes in unsaturated-saturated porous media.

In Chapter 4, a series of numerical experiments were conducted based on the conceptual problem where the saltwater behavior under various conditions was studied. Three end-member flow regimes were identified that they were dominated by the horizontal hydraulically-driven flow, the vertical hydraulically-driven flow, and the vertical density-driven flow, respectively. The driving forces and regime shifts were explained by both the BCs-based and element-based dimensionless numbers, which are potentially applicable to real field cases.

In Chapters 6 and 7, numerical simulations of TSWI in the Niijima Island under the future Nankai earthquake scenarios were conducted in 2-D and 3-D domains, respectively. The simulated tsunami inundation of 15 m a.m.s.l. (above mean sea-level) would cause seawater, with a volume scale of 10^6 m^3, to infiltrate into subsurface within several tens of minutes, which afterwards caused groundwater salinization over 0.2 kg/m^3 of Cl^- (Japanese drinking water standards) that persisted more than eight years in the Niijima Island. The vertical thickness and porosity of the unsaturated zone determined the maximum volume of seawater that could intrude into subsurface during the tsunami inundation. The dense saltwater plume showed a tendency to migrate along the slopes of the bedrock surface during the post-tsunami period. The migration pattern and flushing time of intruded saltwater would be different with the different bedrock structures. The occurrence of fingering flow patterns was associated with hydraulic conductivity, grid size, and density contrast. Some groundwater in the southeastern part of the island would be survived from TSWI, and this survived portion of groundwater resource had the potential to provide post-disaster water supply in an equivalent amount of the

pre-tsunami level (3.7×10^5 m^3/year), and at the same time, did not worsen the recovery processes. Pumping the intruded saltwater had the effect of reducing the risks of saltwater migration to the eastern part of groundwater system and accelerating the recovery process.

To sum up, the problem of TSWI is a transient process that related to dynamic interactions of density-driven convection, vertical and horizontal hydraulically-driven advection, and dispersion. As a result, the flow patterns in a TSWI problem would be temporarily varied, which is more complicated than fingering patterns only. Numerical modeling is a promising tool for assessing the vulnerability of coastal aquifers to TSWI, while special attention should be paid to the model uncertainties that arise from site-specific geologic setting, particularly the bedrock surface structure, considering the density effect.

These simulation results and implications based on the Niijima Island are potentially transferable to other coastal zones worldwide, especially the remote islands where they face tsunami risks. The modeling method adopted in this study should be further improved with respect to coupled surface-subsurface processes, two-phase fluid flow, and spatial discretization of a 3-D domain with a higher resolution and heterogeneity, which could provide more physically plausible simulations of TSWI problem.

CITED REFERENCES

Abarca, E., Carrera, J., Sánchez-Vila, X., & Dentz, M. (2007). Anisotropic dispersive Henry problem. *Advances in Water Resources*, *30*(4), 913-926.

Aichi, M., Shiokari, M., & Tokunaga, T. (2011). A new analytical solution of water table response to tidal fluctuations and its application to estimate aquifer properties at the Niijima Island, Japan. *Journal of Groundwater Hydrology*, *53*(3), 249-265. https://doi.org/10.5917/jagh.53.249 (in Japanese with English abstract)

Alsumaiei, A. A., & Bailey, R. T. (2018). Quantifying threats to groundwater resources in the Republic of Maldives Part II: Recovery from tsunami marine overwash events. *Hydrological Processes*, *32*(9), 1154-1165. https://doi.org/10.1002/hyp.11473

Bear, J. (1972). *Dynamics of fluids in porous media*: Courier Corporation.

Bear, J., Cheng, A. H. D., Sorek, S., Ouazar, D., & Herrera, I. (1999). *Seawater Intrusion in Coastal Aquifers: Concepts, Methods and Practices*: Springer Science & Business Media.

Cabinet Office of Japan. (2011). *Tsunami height and distribution of seismic intensity from the Huge Nankai Trough Earthquake.* Retrieved from http://www.bousai.go.jp/jishin/nankai/taisaku/pdf/1_1.pdf (in Japanese)

Central Disaster Management Council. (2014). *Nankai Trough Earthquake disaster prevention countermeasures promotion area.* Retrieved from http://www.bousai.go.jp/jishin/nankai/pdf/nankaitrough_keikaku.pdf (in Japanese)

Chidambaram, S., Ramanathan, A. L., Prasanna, M. V., Karmegam, U., Dheivanayagi, V., Ramesh, R., et al. (2010). Study on the hydrogeochemical characteristics in groundwater, post- and pre-tsunami scenario, from Portnova to Pumpuhar, southeast coast of India. *Environmental Monitoring and Assessment*, *169*(1-4), 553-568. https://doi.org/10.1007/s10661-009-1196-y

Construction Section of Niijima Village. (2001). *Niijima Village Specific Environment Conservation, Public Sewage System Design and Geological Survey Report*.

Cremer, C. J., & Graf, T. (2015). Generation of dense plume fingers in saturated-unsaturated homogeneous porous media. *Journal of Contaminant Hydrology*, *173*, 69-82. https://doi.org/10.1016/j.jconhyd.2014.11.008

Diersch, H. J. G. (2013). *FEFLOW: Finite element modeling of flow, mass and heat transport in porous and fractured media*: Springer, Berlin, Heidelberg.

Diersch, H. J. G., & Kolditz, O. (2002). Variable-density flow and transport in porous media: Approaches and challenges. *Advances in Water Resources*, *25*(8-12), 899-944. https://doi.org/10.1016/S0309-1708(02)00063-5

Elder, J. W. (1967). Transient convection in a porous medium. *Journal of Fluid Mechanics*, *27*(03), 609-623. https://doi.org/10.1017/S0022112067000576

Essink, G. H. P. O. (2005). *Impact of the 26-12-04 Tsunami on Groundwater Systems and Groundwater Based Water Supplies*.

Freeze, R. A., & Cherry, J. A. (1979). *Groundwater*: Prentice Hall.

Gehlin, S. E. A., & Hellstrom, G. (2003). Influence on thermal response test by groundwater flow in vertical fractures in hard rock. *Renewable energy*, *28*(14), 2221-2238. https://doi.org/10.1016/S0960-1481(03)00128-9

Gelhar, L. W., Welty, C., & Rehfeldt, K. R. (1992). A critical review of data on field-scale dispersion in aquifers. *Water Resources Research*, *28*(7), 1955-1974. https://doi.org/10.1029/92WR00607

Ghyben, B. W. (1888). Notes on the probable results of well drilling near Amsterdam. *Tijdschrift van het Koninklijk Inst. van Ingenieur, The Hague*, *9*, 8-22.

Guo, H., & Jiao, J. J. (2007). Impact of Coastal Land Reclamation on Ground Water Level and the Sea Water Interface. *Ground Water*, *45*(3), 362-367. https://doi.org/10.1111/j.1745-6584.2006.00290.x

Guo, W., & Langevin, C. D. (2002). *User's guide to SEAWAT; a computer program for simulation of three-dimensional variable-density ground-water flow.*

Gvirtzman, H., Garven, G., & Gvirtzman, G. (1997). Hydrogeological modeling of the saline hot springs at the Sea of Galilee, Israel. *Water Resources Research*, *33*(5), 913-926. https://doi.org/10.1029/96wr03191

Henry, H. R. (1964). *Effects of dispersion on salt encroachment in coastal aquifers*: US Geological Survey.

Herzberg, D. (1901). *Die Wasserversorgung Einiger Nordseebäder*.

Hogan, M. (2006). *Understanding the flow and mixing dynamics of saline water discharged into coastal freshwater aquifers.* (Doctoral dissertation), Auburn University, Auburn, Alabama. Retrieved from http://etd.auburn.edu/handle/10415/672

Honma, J., Hagiwara, G., & Shindo, S. (1974). Observation and analysis of the ground water in Niijima Island. *Proceedings of the Japan Society of Civil Engineers*, *1974*(222), 79-92. https://doi.org/10.2208/jscej1969.1974.222_79 (in Japanese)

Horton, C. W., & Rogers, F. T. (1945). Convection Currents in a Porous Medium. *Journal of Applied Physics*, *16*(6), 367-370. https://doi.org/10.1063/1.1707601

Hu, L. T., Jiao, J. J., & Guo, H. P. (2008). Analytical studies on transient groundwater flow induced by land reclamation. *Water Resources Research*, *44*(11), W11427. https://doi.org/10.1029/2008wr006926

Hubbert, M. K. (1940). The theory of ground-water motion. *The Journal of Geology*, 785-944.

Illangasekare, T., Tyler, S. W., Clement, T. P., Villholth, K. G., Perera, A. P. G. R. L., Obeysekera, J., et al. (2006). Impacts of the 2004 tsunami on groundwater resources in Sri Lanka. *Water Resources Research*, *42*(5), W05201. https://doi.org/10.1029/2006wr004876

Inui, T., Yasutaka, T., Endo, K., & Katsumi, T. (2012). Geo-environmental issues induced by the 2011 off the Pacific Coast of Tohoku Earthquake and tsunami. *Soils and Foundations*, *52*(5), 856-871. https://doi.org/10.1016/j.sandf.2012.11.008

Isobe, I., & Nakashima, R. (2001). Molluscan fossil found from pyroclastic of the Niijima volcano and its basement rocks. *Bulletin of the Geological Survey of Japan*, *52*(1), 41-48. (in Japanese with English abstract)

Isshiki, N. (1987). *Geology of the Niijima Island with Geological Sheet Map at 1:50,000*. Geological Survey of Japan, National Institute of Advanced Industrial Science and Technology, Tokyo. (in Japanese)

Japan Meteorological Agency. (2017). *Historical Weather Data.* Retrieved from http://www.data.jma.go.jp/ (in Japanese)

Ketabchi, H., Mahmoodzadeh, D., Ataie-Ashtiani, B., & Simmons, C. T. (2016). Sea-level rise impacts on seawater intrusion in coastal aquifers: Review and integration. *Journal of Hydrology*, *535*, 235-255. https://doi.org/10.1016/j.jhydrol.2016.01.083

Kimmel, G. E., & Braids, O. C. (1980). *Leachate plumes in ground water from Babylon and Islip landfills, Long Island, New York*: US Government Printing Office.

Koyaguchi, T. (1986). Evidence for two-stage mixing in magmatic inclusions and rhyolitic lava domes on Niijima Island, Japan. *Journal of Volcanology and Geothermal Research*, *29*(1–4), 71-98. https://doi.org/10.1016/0377-0273(86)90040-5

Kume, T., Umetsu, C., & Palanisami, K. (2009). Impact of the December 2004 tsunami on soil, groundwater and vegetation in the Nagapattinam district, India. *Journal of*

Environmental Management, *90*(10), 3147-3154. https://doi.org/http://dx.doi.org/10.1016/j.jenvman.2009.05.027

Lapwood, E. (1948). *Convection of a fluid in a porous medium.* Paper presented at the Mathematical Proceedings of the Cambridge Philosophical Society.

Lee, C. H., & Cheng, R. T. S. (1974). On seawater encroachment in coastal aquifers. *Water Resources Research*, *10*(5), 1039-1043.

Lemke, L. D., Abriola, L. M., & Goovaerts, P. (2004). Dense nonaqueous phase liquid (DNAPL) source zone characterization: Influence of hydraulic property correlation on predictions of DNAPL infiltration and entrapment. *Water Resources Research*, *40*(1). https://doi.org/10.1029/2003wr001980

List, E. J. (1965). *The stability and mixing of a density-stratified horizontal flow in a saturated porous medium.* (Doctoral dissertation), California Institute of Technology, Retrieved from https://core.ac.uk/download/pdf/4890980.pdf

Liu, H., & Dane, J. (1996). A criterion for gravitational instability in miscible dense plumes. *Journal of Contaminant Hydrology*, *23*(3), 233-243.

Liu, P. L., Lynett, P., Fernando, H., Jaffe, B. E., Fritz, H., Higman, B., et al. (2005). Observations by the international tsunami survey team in Sri Lanka. *Science*, *308*(5728), 1595. https://doi.org/10.1126/science.1110730

Liu, Y., Kuang, X., Jiao, J. J., & Li, J. (2015). Numerical study of variable-density flow and transport in unsaturated-saturated porous media. *Journal of Contaminant Hydrology*, *182*, 117-130. https://doi.org/10.1016/j.jconhyd.2015.09.001

Lusczynski, N. J. (1961). Head and flow of ground water of variable density. *Journal of Geophysical Research*, *66*(12), 4247-4256. https://doi.org/10.1029/JZ066i012p04247

Lyllon, L. (2008). Deep impact: why post-tsunami wells need a measured approach. *Proceedings of the Institution of Civil Engineers-Civil Engineering*, *161*(1), 42-48. https://doi.org/10.1680/cien.2008.161.1.42

Mahmoodzadeh, D., & Karamouz, M. (2019). Seawater intrusion in heterogeneous coastal aquifers under flooding events. *Journal of Hydrology*, *568*, 1118-1130. https://doi.org/10.1016/j.jhydrol.2018.11.012

Marohn, C., Distel, A., Dercon, G., Wahyunto, Tomlinson, R., von Noordwijk, M., & Cadisch, G. (2012). Impacts of soil and groundwater salinization on tree crop performance in post-tsunami Aceh Barat, Indonesia. *Natural Hazards and Earth System Sciences*, *12*(9), 2879-2891. https://doi.org/10.5194/nhess-12-2879-2012

Mazzia, A., Bergamaschi, L., & Putti, M. (2001). On the reliability of numerical solutions of brine transport in groundwater: Analysis of infiltration from a salt lake. *Transport in Porous Media*, *43*(1), 65-86. https://doi.org/10.1023/A:1010665609617

Ministry of Agriculture, Forestry and Fisheries. (2011). *The Damage and Measure of The 2011 off the Pacific coast of Tohoku Earthquake.* Retrieved from http://www.maff.go.jp/e/quake/press_110313-1.html

Ministry of Agriculture, Forestry and Fisheries. (2017). *Report of groundwater survey in coastal area "Tohoku area" (H23-H26).* (in Japanese)

Ministry of Health, Labor and Welfare. (2015). *Drinking Water Quality Standards.* Retrieved from http://www.mhlw.go.jp/stf/seisakunitsuite/bunya/topics/bukyoku/kenkou/suido/kijun/kijunchi.html (in Japanese)

Ministry of Land, Infrastructure, Transport and Tourism. (2015). *National Land Numerical Information (Elevation Data).* Retrieved from http://nlftp.mlit.go.jp/ksj/old/old_datalist.html (in Japanese)

Mori, K., Takahashi, T., Okaniwa, N., Shibasaki, N., & Ouchi, T. (2012). Change in groundwater environment caused by the 2011 off the Pacific Coast of Tohoku Earthquake in the southern part of Sendai Plain. *Journal of Groundwater Hydrology*, *54*(1), 11-23. https://doi.org/10.5917/jagh.54.11 (in Japanese with English abstract)

Nakagawa, K., Wada, N., Kaihotsu, I., Tokunaga, T., Kondo, A., Onodera, S., et al. (2013). Effect of Tsunami induced by the 2011 off the Pacific coast of Tohoku Earthquake on groundwater. *Journal of Groundwater Hydrology*, *55*(1), 21-28. https://doi.org/10.5917/jagh.55.21 (in Japanese)

Nakaoka, R., & Suzuki-Kamata, K. (2015). Rock-magnetic evidence for the low-temperature emplacement of the Habushiura pyroclastic density current, Niijima Island, Japan. *Geological Society, London, Special Publications*, *396*(1), 51-66. https://doi.org/10.1144/SP396.7

National Geophysical Data Center, NOAA. (2015). *World Data Service (NGDC/WDS): Global Historical Tsunami Database*. Retrieved from: http://www.ngdc.noaa.gov/metadata/published/NOAA/NESDIS/NGDC/MGG/Hazards/iso/

Nield, D. A., & Bejan, A. (2006). *Convection in porous media* (Vol. 3): Springer.

Niijima Village Office. (2015). *Introduction of Niijima Island*.

Oldenburg, C. M., & Pruess, K. (1999). Plume separation by transient thermohaline convection in porous media. *Geophysical Research Letters*, *26*(19), 2997-3000. https://doi.org/10.1029/1999GL002360

Olivieri, A., Eisenberg, D., Kurtovich, M., & Pettegrew, L. (1985). Ground-water contamination in Silicon Valley. *Journal of Water Resources Planning and Management*, *111*(3), 346-358. https://doi.org/10.1061/(ASCE)0733-9496(1985)111:3(346)

Oostrom, M., Hayworth, J. S., Dane, J. H., & Guven, O. (1992). Behavior of dense aqueous phase leachate plumes in homogeneous porous-media. *Water Resources Research*, *28*(8), 2123-2134. https://doi.org/10.1029/92wr00711

Oshima Subprefecture of Tokyo. (2014). *Overview of administration*.

Paschke, N. W., & Hoopes, J. A. (1984). Buoyant contaminant plumes in groundwater. *Water Resources Research*, *20*(9), 1183-1192.

Pinder, G. F., & Cooper, H. H. (1970). A numerical technique for calculating the transient position of the saltwater front. *Water Resources Research*, *6*(3), 875-882.

Piyadasa, R. U. K., Weerasinghe, K., Liyanage, J. A., & Wijayawardhana, L. M. J. R. (2009). *Coastal aquifer management after the Asian tsunami in Sri Lanka.* Paper presented at the 1st Asia-Pacific Coastal Aquifer Management Meeting, Bangkok, Thailand.

Post, V. E. A., & Kooi, H. (2003). Rates of salinization by free convection in high-permeability sediments: insights from numerical modeling and application to the Dutch coastal area. *Hydrogeology Journal*, *11*(5), 549-559. https://doi.org/10.1007/s10040-003-0271-7

Pruess, K., Oldenburg, C. M., & Moridis, G. (1999). TOUGH2 user's guide version 2.

Schincariol, R. A., & Schwartz, F. W. (1990). An experimental investigation of variable density flow and mixing in homogeneous and heterogeneous media. *Water Resources Research*, *26*(10), 2317-2329. https://doi.org/10.1029/WR026i010p02317

Schoeman, J. J., Steyn, A., & Makgae, M. (2005). Evaluation of electrodialysis for the treatment of an industrial solid waste leachate. *Desalination*, *186*(1-3), 273-289. https://doi.org/10.1016/j.desal.2005.04.061

Segol, G., Pinder, G. F., & Gray, W. G. (1975). A Galerkin-finite element technique for calculating the transient position of the saltwater front. *Water Resources Research*, *11*(2), 343-347.

Shaw, R., Clasen, T., Smith, L., Albert, J., Bastable, A., & Fesselet, J. F. (2006). The drinking water response to the Indian Ocean tsunami, including the role of household water treatment. *Disaster Prevention and Management: An International Journal*, *15*(1), 190-201.

Shindo, S. (1980). *Research on Groundwater Balance on Volcanic Islands: Examples of Izu Islands.* (in Japanese)

Shindo, S. (1992). Problems related to the development and conservation of groundwater in volcanic islands: The case studies of Izu Islands. *Journal of Groundwater Hydrology*, *34*(3), 137-152. https://doi.org/10.5917/jagh1987.34.137 (in Japanese)

Simmons, C. T. (2005). Variable density groundwater flow: From current challenges to future possibilities. *Hydrogeology Journal*, *13*(1), 116-119. https://doi.org/10.1007/s10040-004-0408-3

Simmons, C. T., Bauer-Gottwein, P., Graf, T., Kinzelbach, W., Kooi, H., Li, L., et al. (2010). Variable density groundwater flow: From modelling to applications. In *Groundwater Modelling in Arid and Semi-Arid Areas* (pp. 87-117): Cambridge University Press.

Simmons, C. T., Fenstemaker, T. R., & Sharp, J. M., Jr. (2001). Variable-density groundwater flow and solute transport in heterogeneous porous media: Approaches, resolutions and future challenges. *Journal of Contaminant Hydrology*, *52*(1-4), 245-275. https://doi.org/10.1016/S0169-7722(01)00160-7

Simmons, C. T., & Narayan, K. A. (1997). Mixed convection processes below a saline disposal basin. *Journal of Hydrology*, *194*(1-4), 263-285. https://doi.org/10.1016/S0022-1694(96)03204-0

Simmons, C. T., Narayan, K. A., & Wooding, R. A. (1999). On a test case for density-dependent groundwater flow and solute transport models: The Salt Lake Problem. *Water Resources Research*, *35*(12), 3607-3620.

Simmons, C. T., Pierini, M. L., & Hutson, J. L. (2002). Laboratory investigation of variable-density flow and solute transport in unsaturated–saturated porous media. *Transport in Porous Media*, *47*(2), 215-244. https://doi.org/10.1023/a:1015568724369

Sivakumar, C., & Elango, L. (2010). Application of solute transport modeling to study tsunami induced aquifer salinity in India. *Journal of Environmental Informatics*, *15*(1), 33-41. https://doi.org/10.3808/jei.201000164

Smith, A. J. (2004). Mixed convection and density-dependent seawater circulation in coastal aquifers. *Water Resources Research*, *40*(8), W08309. https://doi.org/10.1029/2003wr002977

Sugita, F. (2012). Impact of Tsunami caused by the 2011 off the Pacific coast of Tohoku Earthquake on groundwater usage and quality in Asahi-city, Chiba Prefecture Japan. *Journal of Groundwater Hydrology*, *54*(1), 25-37. https://doi.org/10.5917/jagh.54.25 (in Japanese)

Therrien, R., McLaren, R., Sudicky, E., Panday, S., DeMarco, D., Mantanga, G., & Huyakorn, P. (2004). HydroGeoSphere: a three-dimensional numerical model describing fully integrated subsurface and overland flow and solute transport. *User's guide, Groundwater Simulations Group, Waterloo, ON*.

Tokyo Disaster Management Council. (2013). *Report of Estimations of Damage in Tokyo by Nankai Earthquake.* Retrieved from https://www.bousai.metro.tokyo.lg.jp/taisaku/torikumi/1000902/1000402.html (in Japanese)

Tokyo Metropolitan Government. (2013). *Simulated damages in Tokyo by Nankai Trough earthquakes.* Retrieved from URL: https://www.bousai.metro.tokyo.lg.jp/_res/projects/default_project/_page_/001/000/402/20130514gaiyou.pdf (in Japanese)

United Nations Office for Disaster Risk Reduction (UNISDR). (2009). *Risk and poverty in a changing climate: Invest today for a safer tomorrow.* Retrieved from https://www.preventionweb.net/english/hyogo/gar/report/index.php?id=9413

Utsu, T. (2004). *Catalog of Damaging Earthquakes in the World (Through 2002)*. Retrieved from: http://iisee.kenken.go.jp/utsu/index.html

Vacher, H. (1988). Dupuit-Ghyben-Herzberg analysis of strip-island lenses. *Geological Society of America Bulletin*, *100*(4), 580-591. https://doi.org/10.1130/0016-7606(1988)100<0580:DGHAOS>2.3.CO;2

van Genuchten, M. T. (1980). A closed-form equation for predicting the hydraulic conductivity of unsaturated soils. *Soil Science Society of America Journal*, *44*(5), 892-898. https://doi.org/10.2136/sssaj1980.03615995004400050002x

van Reeuwijk, M., Mathias, S. A., Simmons, C. T., & Ward, J. D. (2009). Insights from a pseudospectral approach to the Elder problem. *Water Resources Research*, *45*(4). https://doi.org/10.1029/2008wr007421

Villholth, K. G. (2007). Tsunami impacts on groundwater and water supply in eastern Sri Lanka. *Waterlines*, *26*(1), 8-11. https://doi.org/10.3362/0262-8104.2007.033

Villholth, K. G., Amerasinghe, P., Jeyakumar, P., Panabokke, C., Woolley, O., Weerasinghe, M., et al. (2005). *Tsunami impacts on shallow groundwater and associated water supply on the East Coast of Sri Lanka.* Retrieved from http://s3-us-west-2.amazonaws.com/ucldc-nuxeo-ref-media/464e0d92-2e21-4211-a0dd-b10a9d45327c

Violette, S., Boulicot, G., & Gorelick, S. M. (2009). Tsunami-induced groundwater salinization in southeastern India. *Comptes Rendus Geoscience*, *341*(4), 339-346. https://doi.org/10.1016/j.crte.2008.11.013

Vithanage, M., Engesgaard, P., Villholth, K. G., & Jensen, K. H. (2012). The effects of the 2004 tsunami on a coastal aquifer in Sri Lanka. *Ground Water*, *50*(5), 704-714. https://doi.org/10.1111/j.1745-6584.2011.00893.x

Vithanage, M., Villholth, K. G., Mahatantila, K., Engesgaard, P., & Jensen, K. H. (2009). Effect of well cleaning and pumping on groundwater quality of a tsunami-affected coastal aquifer in eastern Sri Lanka. *Water Resources Research*, *45*, 5. https://doi.org/10.1029/2008wr007509

Voss, C. I., & Provost, A. M. (1984). Sutra. *US Geological Survey Water Resources Investigation Reports*, 84-4369.

Voss, C. I., & Souza, W. R. (1987). Variable density flow and solute transport simulation of regional aquifers containing a narrow freshwater-saltwater transition zone. *Water Resources Research*, *23*(10), 1851-1866. https://doi.org/10.1029/WR023i010p01851

Vrba, J., & Salamat, A. (2007). *Groundwater for Emergency Situations.*: UNESCO.

Werner, A. D., Bakker, M., Post, V. E. A., Vandenbohede, A., Lu, C., Ataie-Ashtiani, B., et al. (2013). Seawater intrusion processes, investigation and management: Recent advances and future challenges. *Advances in Water Resources*, *51*, 3-26. https://doi.org/https://doi.org/10.1016/j.advwatres.2012.03.004

Werner, A. D., & Simmons, C. T. (2009). Impact of Sea-Level Rise on Sea Water Intrusion in Coastal Aquifers. *Groundwater*, *47*(2), 197-204. https://doi.org/10.1111/j.1745-6584.2008.00535.x

WHO. (2004). *Guidelines for drinking-water quality: recommendations*: World Health Organization.

Wood, M., Simmons, C. T., & Hutson, J. L. (2004). A breakthrough curve analysis of unstable density-driven flow and transport in homogeneous porous media. *Water Resources Research*, *40*(3), W03505. https://doi.org/10.1029/2003wr002668

Wooding, R. A. (1989). Convective regime of saline groundwater below a 'dry'lake bed. In *CSIRO Center for Environmental Mechanics, Technical Report* (Vol. 27, pp. 1-20).

Wooding, R. A., Tyler, S. W., & White, I. (1997). Convection in groundwater below an evaporating salt lake: 1. Onset of instability. *Water Resources Research*, *33*(6), 1199-1217. https://doi.org/10.1029/96wr03533

Xie, Y. Q., Simmons, C. T., Werner, A. D., & Diersch, H. J. G. (2012). Prediction and uncertainty of free convection phenomena in porous media. *Water Resources Research*, *48*(2), W02535. https://doi.org/10.1029/2011wr011346

Xie, Y. Q., Simmons, C. T., Werner, A. D., & Ward, J. D. (2010). Effect of transient solute loading on free convection in porous media. *Water Resources Research*, *46*(11), W11511. https://doi.org/10.1029/2010wr009314

Yang, J., Graf, T., Herold, M., & Ptak, T. (2013). Modelling the effects of tides and storm surges on coastal aquifers using a coupled surface-subsurface approach. *Journal of Contaminant Hydrology*, *149*, 61-75. https://doi.org/10.1016/j.jconhyd.2013.03.002

Yu, X., Yang, J., Graf, T., Koneshloo, M., O'Neal, M. A., & Michael, H. A. (2016). Impact of topography on groundwater salinization due to ocean surge inundation. *Water Resources Research*, *52*(8), 5794-5812. https://doi.org/10.1002/2016wr018814

Zhang, H. B., & Schwartz, F. W. (1995). Multispecies contaminant plumes in variable-density flow systems. *Water Resources Research*, *31*(4), 837-847. https://doi.org/10.1029/94wr02567

Zheng, C., & Bennett, G. D. (2002). *Applied Contaminant Transport Modeling*: Wiley-Interscience New York.

APPENDIX

In order to confirm the bedrock surface topography in Niijima Island, microtremor survey was carried out at 11 measurements points, as shown in Figure A1. The field investigation and data analysis were supported by Geo-X Consultants Corporation, Japan. The results of the measurements data by microtremor survey at each point are showed in Figure A2.

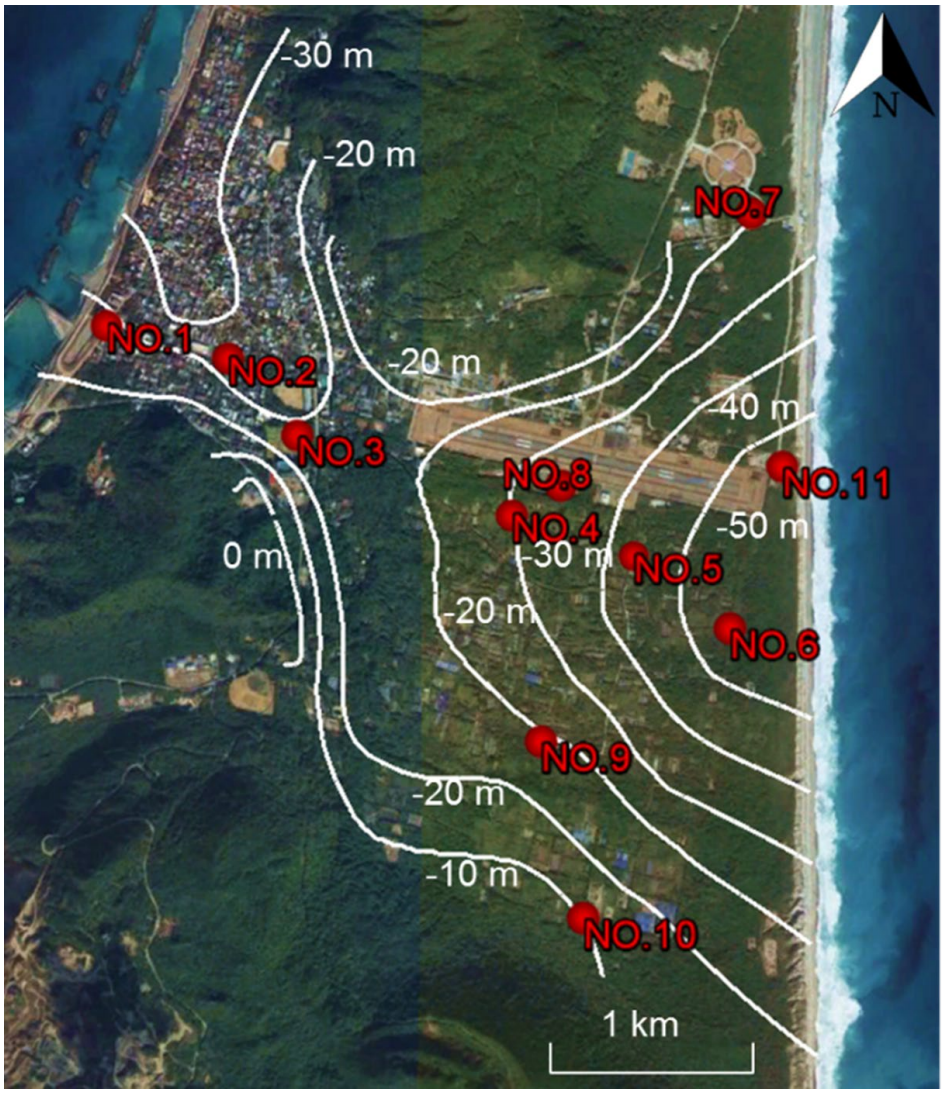

Figure A1 Bedrock surface elevation of Niijima Island based on the resistivity survey results by Shindo (1980) (white lines) with (a) the locations of measurements using microtremor survey (red points).

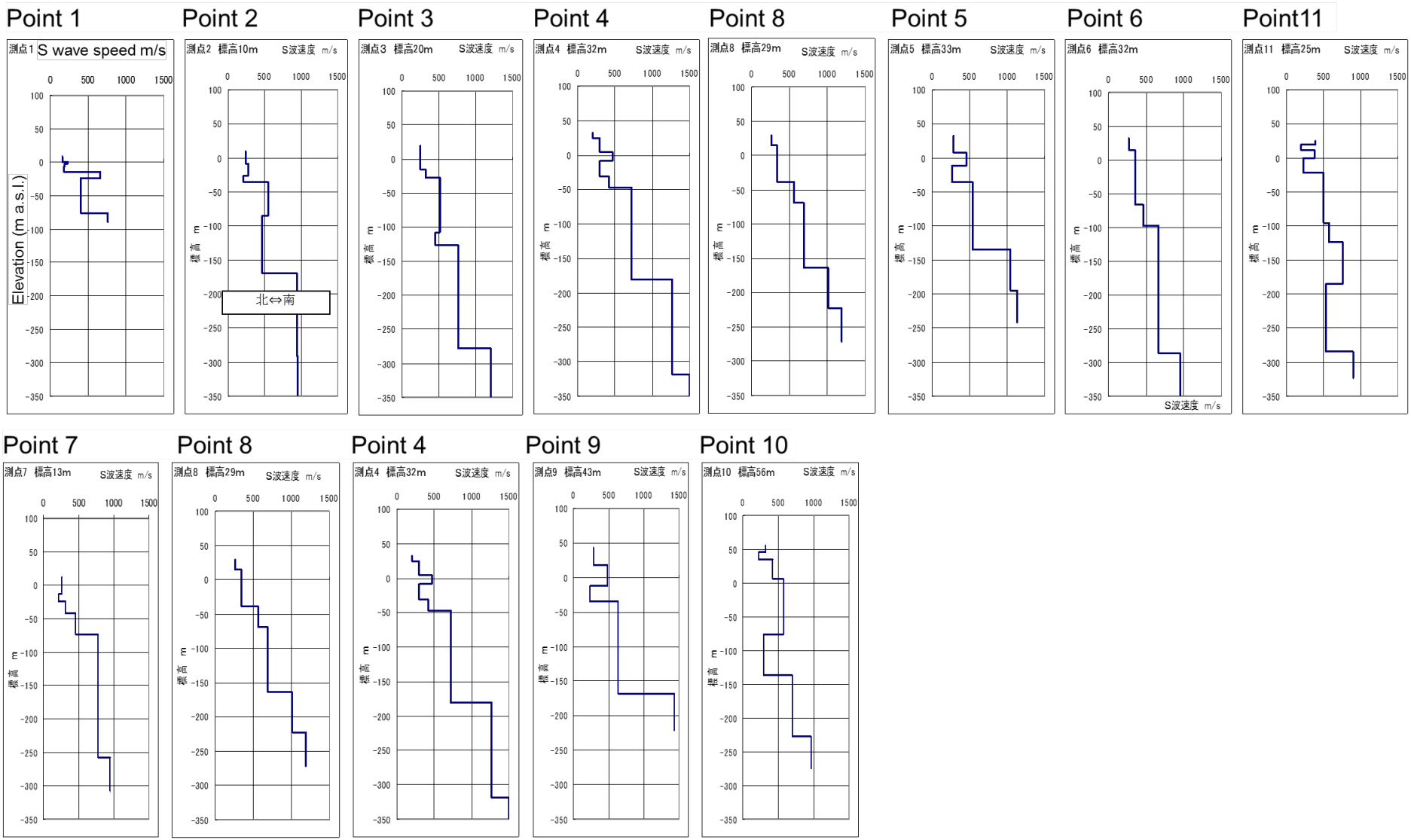

Figure A2 Analyzing results of the measurements data by microtremor survey (see Figure A1 for the locations of measurements point. The data was analyzed and provided by Geo-X Consultants Corporation, Japan.

Table A1 Configurations, BC-based dimensionless numbers and flow and transport regimes of the simulation cases in Chapter 4.

No.	Simulation time (d)	Groundwater flow condition	Settings of solute injection			Aquifer properties			Dispersivity	BC-based dimensionless numbers			Flow and transport Regime
		J^{BC}	q_z^{BC} (m/s)	C_s^{BC} (kg/m^3)	L^{BC} (m)	K_x (m/s)	K_z/K_x	H^{BC} (m)	α_L (m)	$Log\left(M_x^{BC}\right)$	$Log\left(M_z^{BC}\right)$	$Log\left(Ra_d^{BC}\right)$	
1	9855	1×10^{-3}	5.79×10^{-9}	3.5	2	1.13×10^{-6}	0.1	18	0.2	-1.56	-1.31	1.22	HH-VH
2	5475	1×10^{-3}	5.79×10^{-9}	3.5	2	1.13×10^{-6}	1	18	0.2	-0.56	-0.31	2.22	HH-VH
3	2555	1×10^{-3}	5.79×10^{-9}	3.5	2	1.13×10^{-3}	0.1	18	0.2	-1.56	1.69	2.35	HH
4	2920	1×10^{-3}	5.79×10^{-9}	3.5	2	1.13×10^{-3}	1	18	0.2	-0.56	2.69	3.35	HH
5	1825	1×10^{-3}	5.79×10^{-9}	3.5	100	1.13×10^{-6}	0.1	18	0.2	0.14	-1.31	1.22	VH
6	2555	1×10^{-3}	5.79×10^{-9}	3.5	100	1.13×10^{-6}	1	18	0.2	1.14	-0.31	2.22	VH
7	500	1×10^{-3}	5.79×10^{-9}	3.5	100	1.13×10^{-3}	0.1	18	0.2	0.14	1.69	2.35	HH
8	365	1×10^{-3}	5.79×10^{-9}	3.5	100	1.13×10^{-3}	1	18	0.2	1.14	2.69	3.35	HH
9	8395	1×10^{-3}	5.79×10^{-9}	100	2	1.13×10^{-6}	0.1	18	0.2	-0.10	0.14	2.67	HH-VH
10	1460	1×10^{-3}	5.79×10^{-9}	100	2	1.13×10^{-6}	1	18	0.2	0.90	1.14	3.67	VH-VD
11	2555	1×10^{-3}	5.79×10^{-9}	100	2	1.13×10^{-3}	0.1	18	0.2	-0.10	3.14	3.80	HH
12	1825	1×10^{-3}	5.79×10^{-9}	100	2	1.13×10^{-3}	1	18	0.2	0.90	4.14	4.80	HH
13	1825	1×10^{-3}	5.79×10^{-9}	100	100	1.13×10^{-6}	0.1	18	0.2	1.60	0.14	2.67	VH
14	3285	1×10^{-3}	5.79×10^{-9}	100	100	1.13×10^{-6}	1	18	0.2	2.60	1.14	3.67	VH-VD
15	365	1×10^{-3}	5.79×10^{-9}	100	100	1.13×10^{-3}	0.1	18	0.2	1.60	3.14	3.80	HH-VD
16	365	1×10^{-3}	5.79×10^{-9}	100	100	1.13×10^{-3}	1	18	0.2	2.60	4.14	4.80	VD
17	1460	1×10^{-3}	5.47×10^{-8}	3.5	2	1.13×10^{-6}	0.1	18	0.2	-1.56	-2.09	1.22	VH
18	1460	1×10^{-3}	5.47×10^{-8}	3.5	2	1.13×10^{-6}	1	18	0.2	-0.56	-1.09	2.22	VH
19	730	1×10^{-3}	5.47×10^{-8}	3.5	2	1.13×10^{-3}	0.1	18	0.2	-1.56	0.91	2.35	HH
20	365	1×10^{-3}	5.47×10^{-8}	3.5	2	1.13×10^{-3}	1	18	0.2	-0.56	1.91	3.35	HH
21	365	1×10^{-3}	5.47×10^{-8}	3.5	100	1.13×10^{-6}	0.1	18	0.2	0.14	-2.09	1.22	VH
22	220	1×10^{-3}	5.47×10^{-8}	3.5	100	1.13×10^{-6}	1	18	0.2	1.14	-1.09	2.22	VH
23	365	1×10^{-3}	5.47×10^{-8}	3.5	100	1.13×10^{-3}	0.1	18	0.2	0.14	0.91	2.35	HH
24	365	1×10^{-3}	5.47×10^{-8}	3.5	100	1.13×10^{-3}	1	18	0.2	1.14	1.91	3.35	HH-VD
25	8395	1×10^{-3}	5.47×10^{-8}	100	2	1.13×10^{-6}	0.1	18	0.2	-0.10	-0.63	2.67	VH
26	730	1×10^{-3}	5.47×10^{-8}	100	2	1.13×10^{-6}	1	18	0.2	0.90	0.37	3.67	VH-VD
27	365	1×10^{-3}	5.47×10^{-8}	100	2	1.13×10^{-3}	0.1	18	0.2	-0.10	2.37	3.80	HH
28	2920	1×10^{-3}	5.47×10^{-8}	100	2	1.13×10^{-3}	1	18	0.2	0.90	3.37	4.80	HH-VD
29	365	1×10^{-3}	5.47×10^{-8}	100	100	1.13×10^{-6}	0.1	18	0.2	1.60	-0.63	2.67	VH
30	280	1×10^{-3}	5.47×10^{-8}	100	100	1.13×10^{-6}	1	18	0.2	2.60	0.37	3.67	VH
31	200	1×10^{-3}	5.47×10^{-8}	100	100	1.13×10^{-3}	0.1	18	0.2	1.60	2.37	3.80	VD
32	100	1×10^{-3}	5.47×10^{-8}	100	100	1.13×10^{-3}	1	18	0.2	2.60	3.37	4.80	VD

No.	Simulation time (d)	Groundwater flow condition	Settings of solute injection			Aquifer properties			Dispersivity	BC-based dimensionless numbers			Flow and transport Regime
		J^{BC}	q_z^{BC} (m/s)	C_s^{BC} (kg/m^3)	L^{BC} (m)	K_x (m/s)	K_z/K_x	H^{BC} (m)	α_L (m)	$Log\left(M_x^{BC}\right)$	$Log\left(M_z^{BC}\right)$	$Log\left(Ra_d^{BC}\right)$	
33	2920	1×10^{-2}	5.79×10^{-9}	3.5	2	1.13×10^{-6}	0.1	18	0.2	-2.56	-1.31	1.00	HH
34	2555	1×10^{-2}	5.79×10^{-9}	3.5	2	1.13×10^{-6}	1	18	0.2	-1.56	-0.31	2.00	HH
35	2555	1×10^{-2}	5.79×10^{-9}	3.5	2	1.13×10^{-3}	0.1	18	0.2	-2.56	1.69	1.35	HH
36	2555	1×10^{-2}	5.79×10^{-9}	3.5	2	1.13×10^{-3}	1.0	18	0.2	-1.56	2.69	2.35	HH
37	4015	1×10^{-2}	5.79×10^{-9}	3.5	100	1.13×10^{-6}	0.1	18	0.2	-0.86	-1.31	1.00	VH
38	2920	1×10^{-2}	5.79×10^{-9}	3.5	100	1.13×10^{-6}	1.0	18	0.2	0.14	-0.31	2.00	VH
39	200	1×10^{-2}	5.79×10^{-9}	3.5	100	1.13×10^{-3}	0.1	18	0.2	-0.86	1.69	1.35	HH
40	200	1×10^{-2}	5.79×10^{-9}	3.5	100	1.13×10^{-3}	1	18	0.2	0.14	2.69	2.35	HH
41	4380	1×10^{-2}	5.79×10^{-9}	100	2	1.13×10^{-6}	0.1	18	0.2	-1.10	0.14	2.45	HH
42	1460	1×10^{-2}	5.79×10^{-9}	100	2	1.13×10^{-6}	1	18	0.2	-0.10	1.14	3.45	HH-VD
43	8030	1×10^{-2}	5.79×10^{-9}	100	2	1.13×10^{-3}	0.1	18	0.2	-1.10	3.14	2.81	HH
44	2920	1×10^{-2}	5.79×10^{-9}	100	2	1.13×10^{-3}	1	18	0.2	-0.10	4.14	3.81	HH
45	3285	1×10^{-2}	5.79×10^{-9}	100	100	1.13×10^{-6}	0.1	18	0.2	0.60	0.14	2.45	VH
46	2160	1×10^{-2}	5.79×10^{-9}	100	100	1.13×10^{-6}	1	18	0.2	1.60	1.14	3.45	VH-VD
47	365	1×10^{-2}	5.79×10^{-9}	100	100	1.13×10^{-3}	0.1	18	0.2	0.60	3.14	2.81	HH
48	150	1×10^{-2}	5.79×10^{-9}	100	100	1.13×10^{-3}	1	18	0.2	1.60	4.14	3.81	HH
49	4015	1×10^{-2}	5.47×10^{-8}	3.5	2	1.13×10^{-6}	0.1	18	0.2	-2.56	-2.09	1.00	HH-VH
50	3285	1×10^{-2}	5.47×10^{-8}	3.5	2	1.13×10^{-6}	1	18	0.2	-1.56	-1.09	2.00	HH-VH
51	730	1×10^{-2}	5.47×10^{-8}	3.5	2	1.13×10^{-3}	0.1	18	0.2	-2.56	0.91	1.35	HH
52	730	1×10^{-2}	5.47×10^{-8}	3.5	2	1.13×10^{-3}	1	18	0.2	-1.56	1.91	2.35	HH
53	365	1×10^{-2}	5.47×10^{-8}	3.5	100	1.13×10^{-6}	0.1	18	0.2	-0.86	-2.09	1.00	VH
54	470	1×10^{-2}	5.47×10^{-8}	3.5	100	1.13×10^{-6}	1	18	0.2	0.14	-1.09	2.00	VH
55	70	1×10^{-2}	5.47×10^{-8}	3.5	100	1.13×10^{-3}	0.1	18	0.2	-0.86	0.91	1.35	HH
56	70	1×10^{-2}	5.47×10^{-8}	3.5	100	1.13×10^{-3}	1	18	0.2	0.14	1.91	2.35	HH
57	2920	1×10^{-2}	5.47×10^{-8}	100	2	1.13×10^{-6}	0.1	18	0.2	-1.10	-0.63	2.45	HH-VH
58	1460	1×10^{-2}	5.47×10^{-8}	100	2	1.13×10^{-6}	1	18	0.2	-0.10	0.37	3.45	VH-VD
59	700	1×10^{-2}	5.47×10^{-8}	100	2	1.13×10^{-3}	0.1	18	0.2	-1.10	2.37	2.81	HH
60	150	1×10^{-2}	5.47×10^{-8}	100	2	1.13×10^{-3}	1	18	0.2	-0.10	3.37	3.81	HH
61	560	1×10^{-2}	5.47×10^{-8}	100	100	1.13×10^{-6}	0.1	18	0.2	0.60	-0.63	2.45	VH
62	410	1×10^{-2}	5.47×10^{-8}	100	100	1.13×10^{-6}	1	18	0.2	1.60	0.37	3.45	VH
63	70	1×10^{-2}	5.47×10^{-8}	100	100	1.13×10^{-3}	0.1	18	0.2	0.60	2.37	2.81	HH
64	50	1×10^{-2}	5.47×10^{-8}	100	100	1.13×10^{-3}	1	18	0.2	1.60	3.37	3.81	HH
65	110	2×10^{-3}	1.16×10^{-6}	35	20	1.13×10^{-4}	1	18	0.2	1.14	0.39	4.02	VH-VD
66	150	2×10^{-2}	1.16×10^{-6}	35	20	1.13×10^{-4}	1	18	0.2	0.14	0.39	3.05	HH-VH-VD

No.	Simulation time (d)	Groundwater flow condition	Settings of solute injection			Aquifer properties			Dispersivity	BC-based dimensionless numbers			Flow and transport Regime
		J^{BC}	q_z^{BC} (m/s)	C_s^{BC} (kg/m^3)	L^{BC} (m)	K_x (m/s)	K_z/K_x	H^{BC} (m)	α_L (m)	$Log\left(M_x^{BC}\right)$	$Log\left(M_z^{BC}\right)$	$Log\left(Ra_d^{BC}\right)$	
67	365	2×10^{-3}	1.16×10^{-7}	3.5	20	1.13×10^{-4}	1	18	0.2	0.14	0.39	3.02	HH-VH-VD
68	70	2×10^{-3}	1.16×10^{-7}	70	20	1.13×10^{-4}	1	18	0.2	1.44	1.69	4.33	VD
69	100	5×10^{-3}	1.16×10^{-7}	70	20	1.13×10^{-4}	1	18	0.2	1.05	1.69	3.94	VD
70	260	2×10^{-2}	1.16×10^{-7}	3.5	20	1.13×10^{-4}	1	18	0.2	-0.86	0.39	2.05	HH
71	560	2×10^{-3}	1.16×10^{-7}	35	20	1.13×10^{-5}	1	18	0.2	1.14	0.39	3.84	VH-VD
72	220	2×10^{-3}	1.16×10^{-7}	35	20	2.25×10^{-5}	1	18	0.2	1.14	0.69	3.93	VH-VD
73	365	1×10^{-2}	5.79×10^{-8}	70	20	1.13×10^{-4}	1	18	0.2	0.74	1.99	3.65	HH-VD
74	270	1×10^{-2}	5.79×10^{-7}	7	20	1.13×10^{-4}	1	18	0.2	-0.26	-0.01	2.65	HH-VH-VD
75	80	1×10^{-2}	5.79×10^{-7}	17.5	20	1.13×10^{-4}	1	18	0.2	0.14	0.39	3.05	HH-VH-VD
76	170	1×10^{-2}	1.16×10^{-6}	3.5	20	1.13×10^{-4}	1	18	0.2	-0.56	-0.61	2.35	HH-VH
77	70	1×10^{-2}	1.16×10^{-6}	17.5	20	1.13×10^{-4}	1	18	0.2	0.14	0.09	3.05	HH-VH
78	365	1×10^{-2}	5.79×10^{-8}	35	40	1.13×10^{-4}	1	18	0.2	0.74	1.69	3.35	HH-VD
79	300	1×10^{-2}	5.79×10^{-7}	35	4	1.13×10^{-4}	1	18	0.2	-0.26	0.69	3.35	HH-VD
80	300	1×10^{-2}	1.16×10^{-6}	35	2	1.13×10^{-4}	1	18	0.2	-0.56	0.39	3.35	HH-VD
81	365	1×10^{-2}	1.16×10^{-7}	10	2	1.13×10^{-4}	1	18	0.2	-1.10	0.84	2.80	HH
82	200	1×10^{-2}	1.16×10^{-7}	10	10	1.13×10^{-4}	1	18	0.2	-0.40	0.84	2.80	HH-VH-VD
83	730	1×10^{-2}	1.16×10^{-7}	17.5	20	1.13×10^{-5}	1	18	0.2	0.14	0.09	3.00	HH-VH
84	365	2×10^{-3}	1.16×10^{-8}	70	20	1.13×10^{-4}	1	18	0.2	1.44	2.69	4.33	VD
85	200	2×10^{-3}	5.79×10^{-8}	70	20	1.13×10^{-4}	1	18	0.2	1.44	1.99	4.33	VD
86	220	2×10^{-3}	5.79×10^{-7}	17.5	20	1.13×10^{-4}	1	18	0.2	0.84	0.39	3.72	VH-VD
87	50	2×10^{-3}	5.79×10^{-7}	70	20	1.13×10^{-4}	1	18	0.2	1.44	0.99	4.33	VD
88	70	2×10^{-3}	1.16×10^{-6}	3.5	20	1.13×10^{-4}	1	18	0.2	0.14	-0.61	3.02	VH
89	140	5×10^{-3}	5.79×10^{-8}	70	20	1.13×10^{-4}	1	18	0.2	1.05	1.99	3.94	VD
90	130	5×10^{-3}	5.79×10^{-7}	17.5	20	1.13×10^{-4}	1	18	0.2	0.44	0.39	3.34	VH-VD
91	365	5×10^{-3}	5.79×10^{-7}	3.5	20	1.13×10^{-4}	1	18	0.2	-0.26	-0.31	2.64	HH-VH
92	130	5×10^{-3}	1.16×10^{-6}	17.5	20	1.13×10^{-4}	1	18	0.2	0.44	0.09	3.34	VH
93	365	1.5×10^{-2}	5.79×10^{-8}	70	20	1.13×10^{-4}	1	18	0.2	0.57	1.99	3.47	HH-VD
94	260	2×10^{-2}	5.79×10^{-7}	3.5	20	1.13×10^{-4}	1	18	0.2	-0.86	-0.31	2.05	HH-VH
95	220	2×10^{-2}	5.79×10^{-7}	10	20	1.13×10^{-4}	1	18	0.2	-0.40	0.14	2.50	HH-VH-VD
96	220	2×10^{-2}	5.79×10^{-7}	17.5	20	1.13×10^{-4}	1	18	0.2	-0.16	0.39	2.75	HH-VH-VD
97	80	2×10^{-2}	5.79×10^{-7}	70	20	1.13×10^{-4}	1	18	0.2	0.44	0.99	3.35	HH-VD
98	260	2×10^{-2}	1.16×10^{-6}	3.5	20	1.13×10^{-4}	1	18	0.2	-0.86	-0.61	2.05	HH-VH
99	100	2×10^{-3}	5.79×10^{-7}	35	40	1.13×10^{-4}	1	18	0.2	1.44	0.69	4.02	VH-VD
100	100	5×10^{-3}	5.79×10^{-7}	35	40	1.13×10^{-4}	1	18	0.2	1.05	0.69	3.64	VH-VD

No.	Simulation time (d)	Groundwater flow condition	Settings of solute injection			Aquifer properties			Dispersivity	BC-based dimensionless numbers			Flow and transport Regime
		J^{BC}	q_z^{BC} (m/s)	C_s^{BC} (kg/m^3)	L^{BC} (m)	K_x (m/s)	K_z/K_x	H^{BC} (m)	α_L (m)	$Log\left(M_x^{BC}\right)$	$Log\left(M_z^{BC}\right)$	$Log\left(Ra_d^{BC}\right)$	
101	60	5×10^{-3}	1.16×10^{-6}	35	10	1.13×10^{-4}	1	18	0.2	0.44	0.39	3.64	VH-VD
102	200	5×10^{-3}	1.16×10^{-7}	17.5	40	1.13×10^{-4}	1	18	0.2	0.74	1.09	3.34	VD
103	100	2×10^{-3}	1.16×10^{-7}	70	40	1.13×10^{-4}	1	18	0.2	1.74	1.69	4.33	VD
104	365	1×10^{-2}	1.16×10^{-8}	70	2	1.13×10^{-4}	1	18	0.2	-0.26	2.69	3.65	HH
105	200	1×10^{-2}	1.16×10^{-8}	70	40	1.13×10^{-4}	1	18	0.2	1.05	2.69	3.65	HH
106	260	1×10^{-2}	5.79×10^{-8}	17.5	2	1.13×10^{-4}	1	18	0.2	-0.86	1.39	3.05	HH
107	300	1×10^{-2}	5.79×10^{-8}	70	40	1.13×10^{-4}	1	18	0.2	1.05	1.99	3.65	HH-VD
108	365	1×10^{-2}	5.79×10^{-7}	7	4	1.13×10^{-4}	1	18	0.2	-0.95	-0.01	2.65	HH
109	210	5×10^{-3}	1.16×10^{-7}	70	20	1.13×10^{-5}	1	18	0.2	1.05	0.69	3.86	VH-VD
110	300	2×10^{-3}	1.16×10^{-8}	70	40	1.13×10^{-4}	1	18	0.2	1.74	2.69	4.33	VD
111	200	2×10^{-3}	5.79×10^{-8}	70	40	1.13×10^{-4}	1	18	0.2	1.74	1.99	4.33	VD
112	100	2×10^{-3}	5.79×10^{-7}	3.5	40	1.13×10^{-4}	1	18	0.2	0.44	-0.31	3.02	VH
113	250	2×10^{-3}	1.16×10^{-6}	3.5	4	1.13×10^{-4}	1	18	0.2	-0.56	-0.61	3.02	HH-VH
114	100	5×10^{-3}	5.79×10^{-7}	3.5	40	1.13×10^{-4}	1	18	0.2	0.05	-0.31	2.64	VH
115	30	5×10^{-3}	5.79×10^{-7}	70	4	1.13×10^{-4}	1	18	0.2	0.35	0.99	3.94	VH-VD
116	365	2×10^{-2}	5.79×10^{-8}	70	2	1.13×10^{-4}	1	18	0.2	-0.56	1.99	3.35	HH
117	365	2×10^{-2}	5.79×10^{-8}	70	10	1.13×10^{-4}	1	18	0.2	0.14	1.99	3.35	HH
118	300	2×10^{-2}	5.79×10^{-7}	3.5	4	1.13×10^{-4}	1	18	0.2	-1.56	-0.31	2.05	HH
119	40	2×10^{-2}	5.79×10^{-7}	70	10	1.13×10^{-4}	1	18	0.2	0.14	0.99	3.35	HH-VD
120	300	2×10^{-2}	1.16×10^{-6}	3.5	2	1.13×10^{-4}	1	18	0.2	-1.86	-0.61	2.05	HH
121	200	2×10^{-3}	1.16×10^{-7}	17.5	40	1.13×10^{-5}	1	18	0.2	1.14	0.09	3.54	VH
122	365	2×10^{-3}	1.16×10^{-7}	70	2	5.64×10^{-4}	1	18	0.2	0.44	2.39	4.35	HH
123	30	2×10^{-3}	1.16×10^{-7}	70	10	5.64×10^{-4}	1	18	0.2	1.14	2.39	4.35	VD
124	30	2×10^{-3}	1.16×10^{-7}	70	40	5.64×10^{-4}	1	18	0.2	1.74	2.39	4.35	VD
125	80	5×10^{-3}	1.16×10^{-7}	70	4	5.64×10^{-4}	1	18	0.2	0.35	2.39	3.95	HH
126	40	2×10^{-2}	5.79×10^{-7}	3.5	10	2.25×10^{-4}	1	18	0.2	-1.16	-0.01	2.05	HH-VH
127	365	2×10^{-3}	5.79×10^{-7}	17.5	10	1.13×10^{-5}	1	18	0.2	0.54	-0.61	3.54	VH
128	150	6×10^{-2}	5.79×10^{-9}	100	0.22	1.13×10^{-2}	0.1	18	2	-2.84	4.14	1.03	HH
129	730	6×10^{-2}	5.79×10^{-9}	300	0.22	1.13×10^{-3}	1	38	0.1	-1.68	4.62	4.13	HH
130	36	1×10^{-3}	5.79×10^{-9}	35	200	1.13×10^{-3}	1	10	100	2.70	3.69	1.40	DD
131	10	1×10^{-3}	1.16×10^{-6}	3.5	200	1.13×10^{-6}	1	2	2	2.40	-2.61	1.04	VH
132	20	1×10^{-3}	1.16×10^{-6}	35	20	1.13×10^{-7}	10	38	0.1	2.12	-1.61	3.57	VH
133	5840	1×10^{-3}	1.16×10^{-6}	3.5	0.22	1.13×10^{-5}	1	38	0.1	-1.84	-1.61	3.43	HH-VH
134	365	1×10^{-2}	1.16×10^{-7}	35	20	1.13×10^{-4}	1	18	0.2	0.44	1.39	3.35	HH-VD

No.	Simulation time (d)	Groundwater flow condition	Settings of solute injection			Aquifer properties			Dispersivity	BC-based dimensionless numbers			Flow and transport Regime
		J^{BC}	q_z^{BC} (m/s)	C_s^{BC} (kg/m^3)	L^{BC} (m)	K_x (m/s)	K_z/K_x	H^{BC} (m)	α_L (m)	$Log\left(M_x^{BC}\right)$	$Log\left(M_z^{BC}\right)$	$Log\left(Ra_d^{BC}\right)$	
135	160	0	1.16×10^{-7}	35	20	1.13×10^{-4}	1	18	0.2	$+\infty$	1.39	5.25	VD
136	160	2×10^{-3}	1.16×10^{-7}	35	20	1.13×10^{-4}	1	18	0.2	1.14	1.39	4.02	VD
137	365	2×10^{-2}	1.16×10^{-7}	35	20	1.13×10^{-4}	1	18	0.2	0.14	1.39	3.05	HH
138	365	1×10^{-2}	1.16×10^{-8}	35	20	1.13×10^{-4}	1	18	0.2	0.44	2.39	3.35	HH
139	100	1×10^{-2}	5.79×10^{-7}	35	20	1.13×10^{-4}	1	18	0.2	0.44	0.69	3.35	VH-VD
140	80	1×10^{-2}	1.16×10^{-6}	35	20	1.13×10^{-4}	1	18	0.2	0.44	0.39	3.35	VH-VD
141	365	1×10^{-2}	1.16×10^{-7}	3.5	20	1.13×10^{-4}	1	18	0.2	-0.56	0.39	2.35	HH
142	365	1×10^{-2}	1.16×10^{-7}	70	20	1.13×10^{-4}	1	18	0.2	0.74	1.69	3.65	HH-VD
143	80	1×10^{-2}	1.16×10^{-7}	300	20	1.13×10^{-4}	1	18	0.2	1.38	2.32	4.28	VD
144	365	1×10^{-2}	1.16×10^{-7}	35	2	1.13×10^{-4}	1	18	0.2	-0.56	1.39	3.35	HH
145	365	1×10^{-2}	1.16×10^{-7}	35	40	1.13×10^{-4}	1	18	0.2	0.74	1.39	3.35	HH-VD
146	220	1×10^{-2}	1.16×10^{-7}	35	150	1.13×10^{-4}	1	18	0.2	1.32	1.39	3.35	VD
147	1095	1×10^{-2}	1.16×10^{-7}	35	20	1.13×10^{-6}	1	18	0.2	0.44	-0.61	3.00	VH
148	700	1×10^{-2}	1.16×10^{-7}	35	20	1.13×10^{-5}	1	18	0.2	0.44	0.39	3.30	VH-VD
149	60	1×10^{-2}	1.16×10^{-7}	35	20	1.13×10^{-3}	1	18	0.2	0.44	2.39	3.35	HH
150	600	1×10^{-2}	1.16×10^{-7}	35	20	1.13×10^{-4}	0.1	18	0.2	-0.56	0.39	2.35	HH
151	365	1×10^{-2}	1.16×10^{-7}	35	20	1.13×10^{-4}	0.2	18	0.2	-0.26	0.69	2.65	HH-VD
152	365	1×10^{-2}	1.16×10^{-7}	35	20	1.13×10^{-4}	0.5	18	0.2	0.14	1.09	3.05	HH-VD
153	200	1×10^{-2}	1.16×10^{-7}	35	20	1.13×10^{-4}	1	3	0.2	1.22	1.39	2.57	HH-VH-VD
154	365	1×10^{-2}	1.16×10^{-7}	35	20	1.13×10^{-4}	1	5	0.2	1.00	1.39	2.79	HH-VD
155	365	1×10^{-2}	1.16×10^{-7}	35	20	1.13×10^{-4}	1	38	0.2	0.12	1.39	3.67	HH-VD
156	365	1×10^{-2}	1.16×10^{-7}	35	20	1.13×10^{-4}	1	18	1	0.44	1.39	2.65	HH
157	365	1×10^{-2}	1.16×10^{-7}	35	20	1.13×10^{-4}	1	18	2	0.44	1.39	2.35	HH
158	365	1×10^{-2}	1.16×10^{-7}	35	20	1.13×10^{-4}	1	18	10	0.44	1.39	1.65	DD

For the cases No.1 ~ 64, the lower and higher values of each parameter are shaded in light and dark grey, respectively.
For the cases No.135 ~ 158, the parameter values that differ from the ones in No.134 are in red.

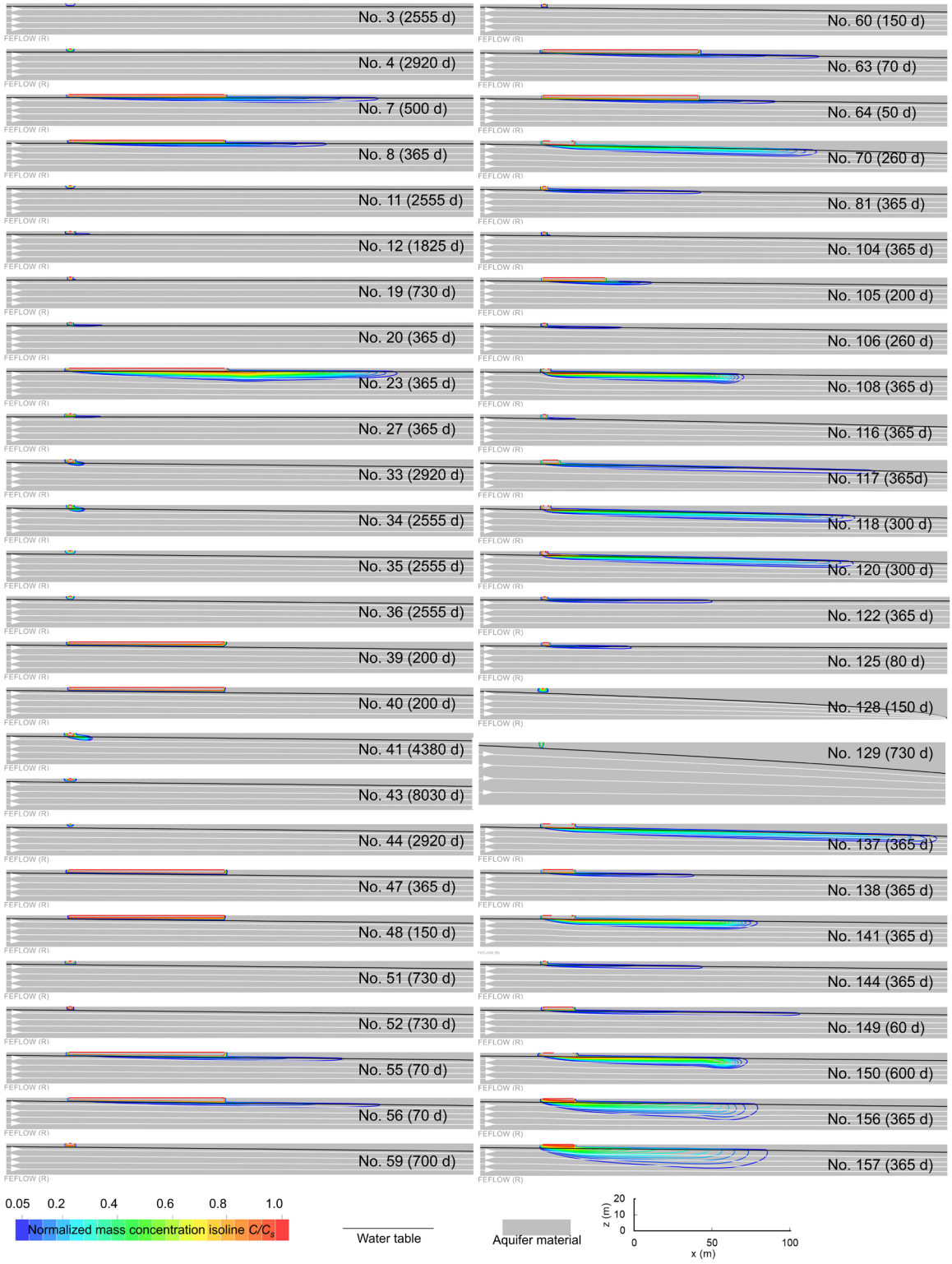

Figure A3 Modeling results of the simulation cases of HH in Chapter 4. Note that no concentration isolines were shown in the saturated zone in the cases No. 3, 4, 11, 35, 36, 43, 44, 51, 52, 59, 60, 104, 128, and 129 because in these cases, once the solute entered the saturated zone, its concentration was quickly diluted to lower than 5% of Cs by the horizontal groundwater flow. The white arrows show the flow directions.

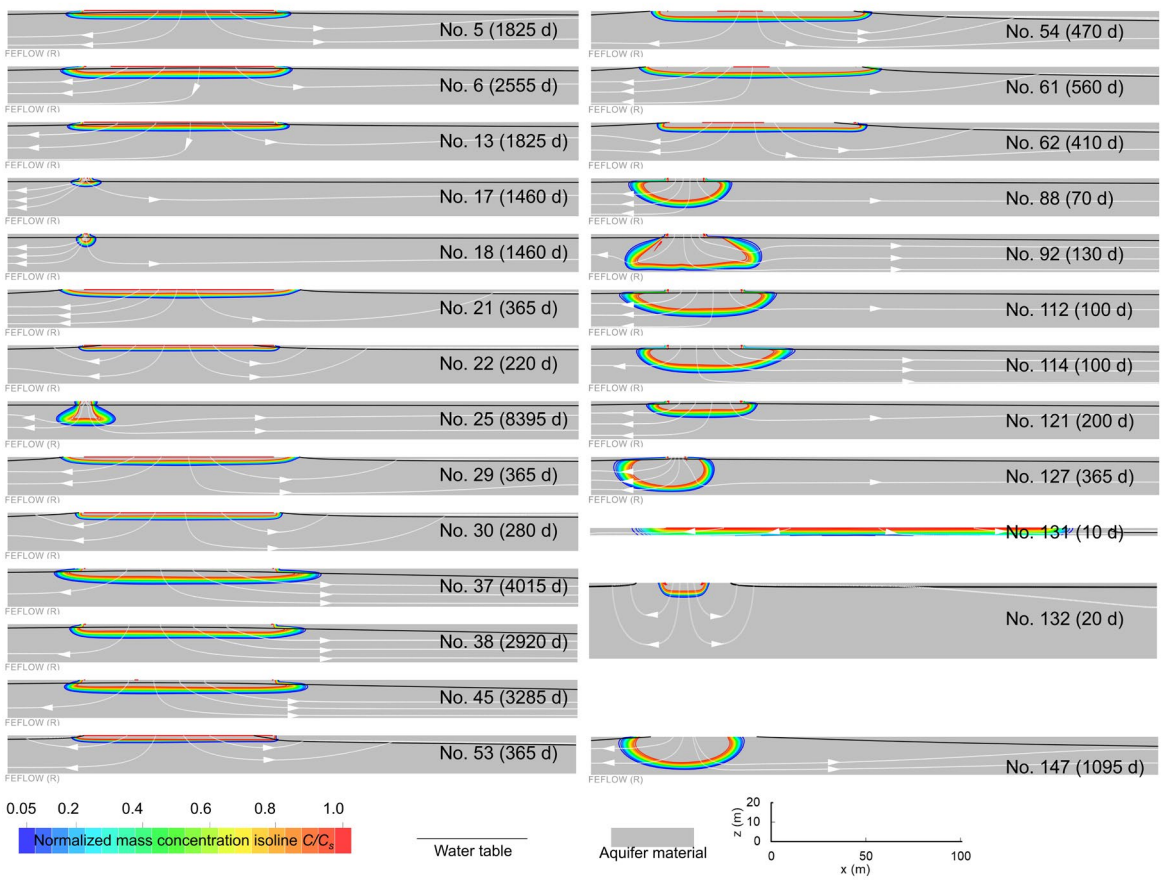

Figure A4 Modeling results of the simulation cases of VH in Chapter 4. The white arrows show the flow directions.

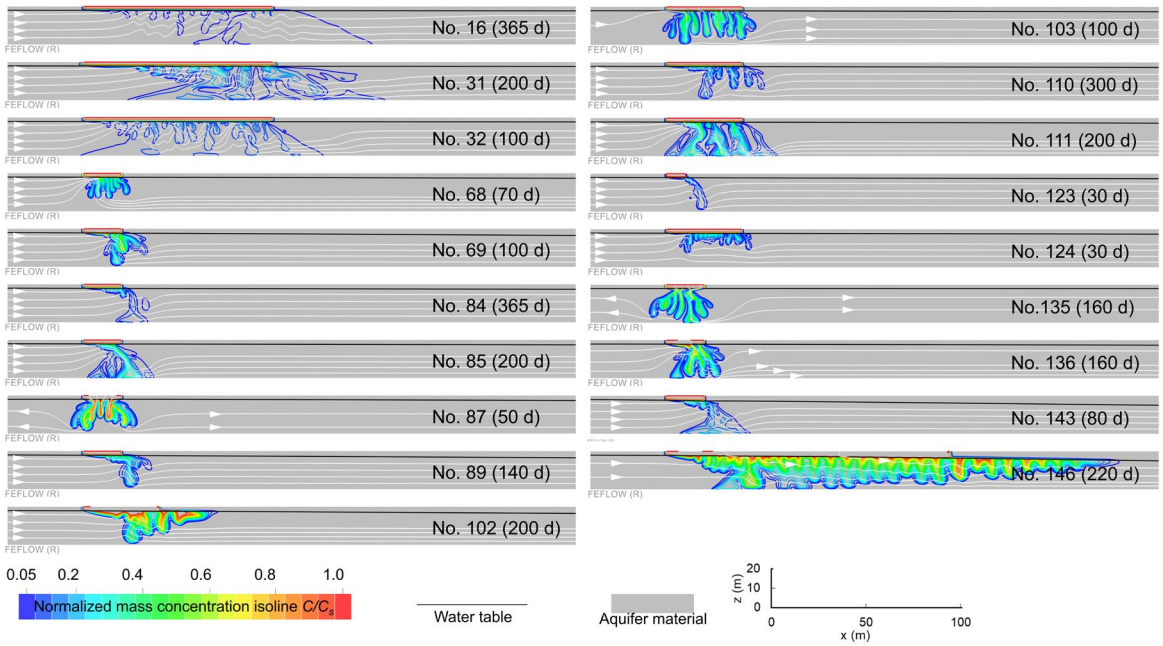

Figure A5 Modeling results of the simulation cases of flow and transport regime VD in Chapter 4. The white arrows show the flow directions.

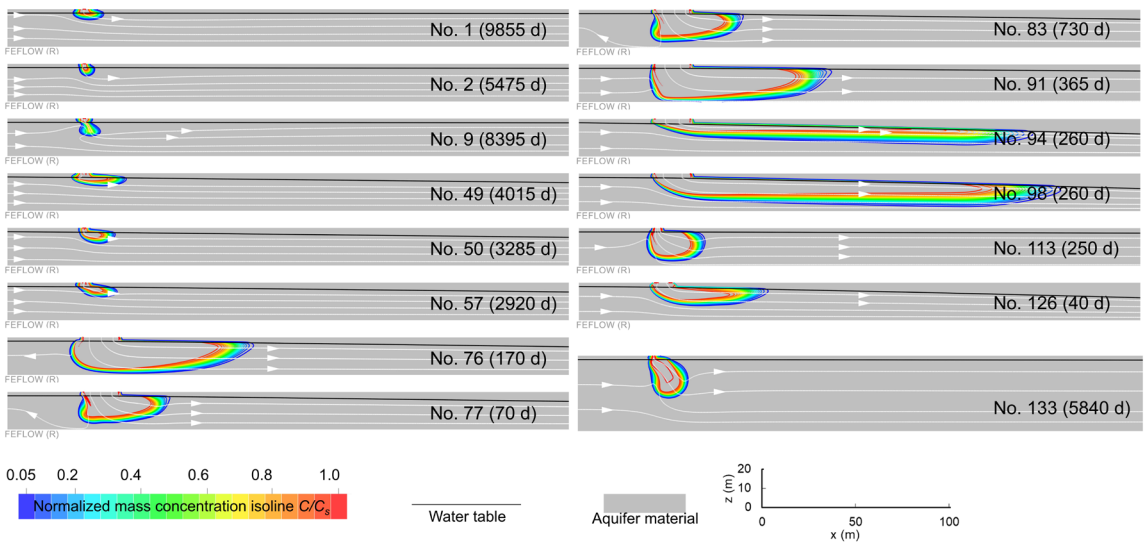

Figure A6 Modeling results of the simulation cases of flow and transport regime HH-VH in Chapter 4. The white arrows show the flow directions.

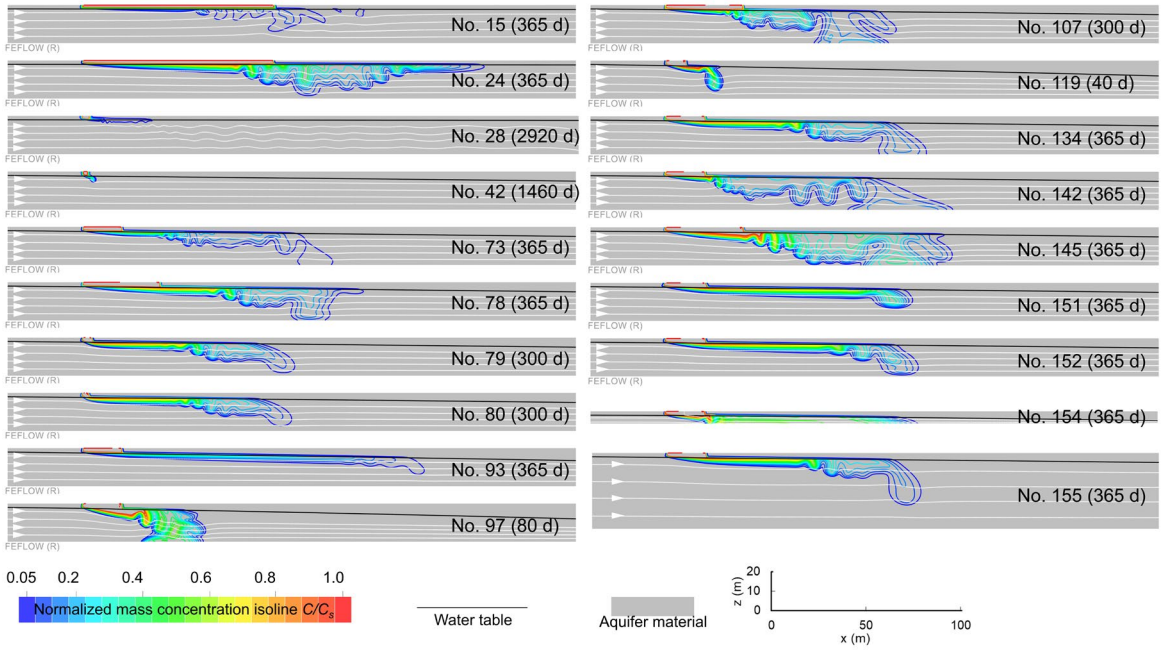

Figure A7 Modeling results of the simulation cases of flow and transport regime HH-VD in Chapter 4. The white arrows show the flow directions.

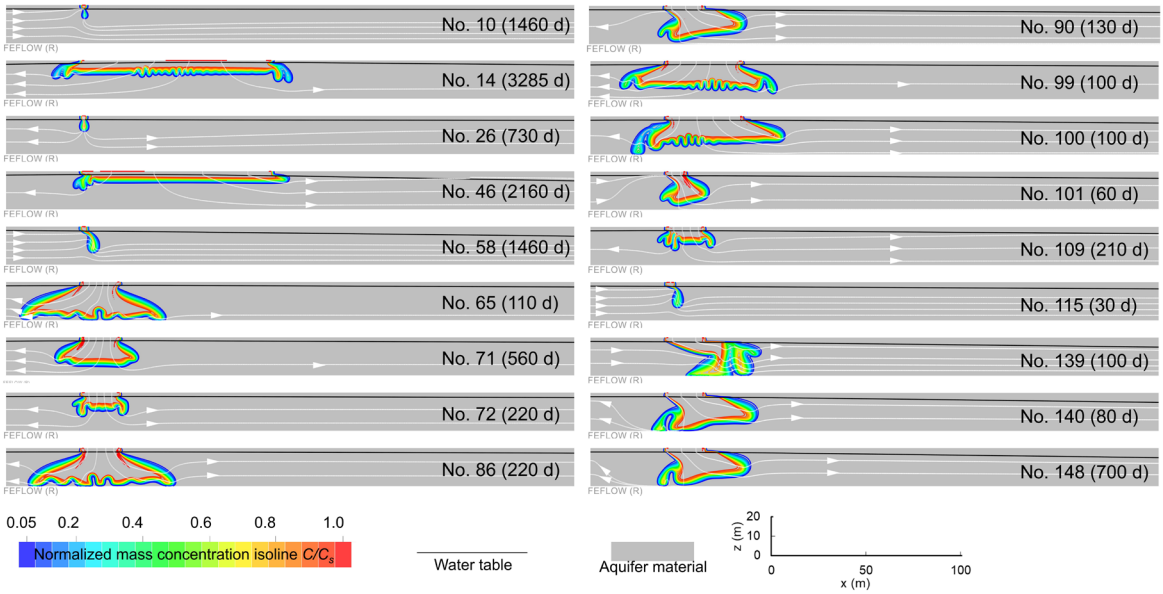

Figure A8 Modeling results of the simulation cases of flow and transport regime VH-VD in Chapter 4. The white arrows show the flow directions.

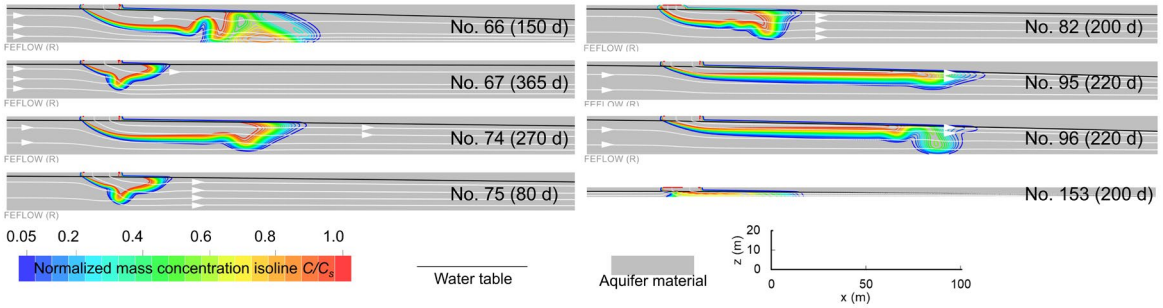

Figure A9 Modeling results of the simulation cases of flow and transport regime HH-VH-VD in Chapter 4. The white arrows show the flow directions.

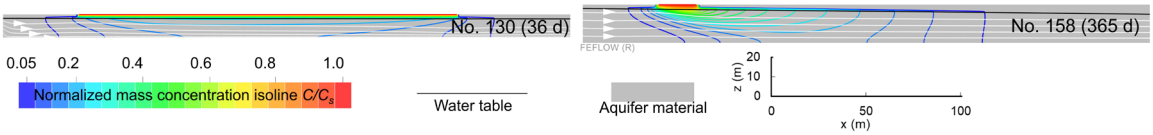

Figure A10 Modeling results of the simulation cases of flow and transport regime DD in Chapter 4. The white arrows show the flow directions.